

Dissertation
submitted to the
Combined Faculties for the Natural Sciences and for Mathematics
of the Ruperto-Carola University of Heidelberg, Germany
for the degree of
Doctor of Natural Science

presented by

Diploma-Biology (Laurea), Marco Salomone-Stagni

Born in: Udine, Italy

Oral-examination: 11.11.2010

**Biochemical and Biophysical Characterization of the Human
Ethylmalonic Encephalopathy non-Heme Sulfur
[Fe]-Dioxygenase ETHE1, and X-ray Absorption Spectroscopy
Applications and Methods Development**

Referees:

Prof. Dr. Irmgard Sinning

Dr. Andreas Ladurner

To my parents and friends

Preface

This Thesis is based on the results presented in the following manuscripts:

1. Dominik Barthelme, Urte Scheele, Stephanie Dinkelaker, Adam Janoschka, Fraser MacMillan, Sonja-Verena Albers, Arnold J. M. Driessen, Marco S. Stagni, Eckhard Bill, Wolfram Meyer-Klaucke, Volker Schünemann and Robert Tampè
Structural organization of essential iron-sulfur clusters in the evolutionarily highly conserved ATP-binding cassette protein ABCE1
Journal of Biological Chemistry, 2007 May 11; 282(19): 14598-607
2. Seigo Shima, Oliver Pilak, Sonja Vogt, Marco S. Stagni, Wolfram Meyer-Klaucke, Eberhard Warkentin, Rudolf K. Thauer, Ulrich Ermler
The crystal structure of [Fe]-hydrogenase reveals the geometry of the active site
Science, 2008 July 25; 321: 572-5
3. Takeschi Hiromoto, Kenichi Ataka, Oliver Pilak, Sonja Vogt, Marco S. Stagni, Wolfram Meyer-Klaucke, Eberhard Warkentin, Rudolf K. Thauer, Seigo Shima, Ulrich Ermler
The crystal structure of C176A mutated [Fe]-hydrogenase suggests an acyl-iron ligation in the active site iron complex
Federation of European Biochemical Societies Letters, 2009 February 4; 583(3): 585-90
4. Stephan Binder, Marco Salomone-Stagni, Roxana Haase, Benjamin Schulz, Andreas Eich, Gerald Henkel, Michael Rübhausen, Sonja Herres-Pawlis, and Wolfram Meyer-Klaucke

Characterization of the optically excited state of a bis (μ -oxo)-dicopper(III) species mimicking the hemocyanin and tyrosinase active sites

Journal of Physics: Conference Series, 2009 November; 190; id: 012197

5. Marco Salomone-Stagni, Sonja Vogt, Rudolf K. Thauer, Seigo Shima, and Wolfram Meyer-Klaucke

Extended X-ray absorption fine structure of the [Fe]-hydrogenase HMD active site

Journal of Physics: Conference Series, 2009 November; 190; id: 012201

6. Marco Salomone-Stagni, Francesco Stellato, Matthew Whaley, Sonja Vogt, Seigo Shima, Eckhard Bill, Thomas B. Rauchfuss, and Wolfram Meyer-Klaucke

The iron-site structure of [Fe]-hydrogenase and model systems: an X-ray Absorption Near Edge Spectroscopy study

Dalton Transactions, 2010; 39: 3057-64. DOI: 10.1039/b922557a

7. Marco Salomone-Stagni, Alexey Kikhney, Eckhard Bill, and Wolfram Meyer-Klaucke

Biochemical and biophysical characterization of the ethylmalonic encephalopathy non-heme sulfur [Fe]-dioxygenase ETHE1 from *Homo sapiens*

In preparation

Own contribution:

1. EXAFS and XANES analysis.
2. XAS measurements; EXAFS analysis.
3. XAS measurements; EXAFS analysis.
4. Pumped-XAS experimental set up, measurement and data evaluation; contribution to the pilot resonance Raman spectroscopy data collection.

5. EXAFS analysis.
6. EXAFS analysis; XANES analysis.
7. Most of the work. I didn't performed the Mössbauer data collection and analysis.
I contributed to the SAXS data analysis and evaluation.

Table of contents

SUMMARY	1
ZUSAMMENFASSUNG	2
1 INTRODUCTION	3
1.1 Ethylmalonic encephalopathy protein 1	3
1.1.1 <i>Homo sapiens</i> ETHE1	4
1.1.2 <i>Hs</i> ETHE1 and hepatocellular carcinoma	5
1.1.3 <i>Hs</i> ETHE1 and ethylmalonic encephalopathy	5
1.1.4 <i>At</i> ETHE1 structure.....	6
1.1.5 <i>Hs</i> ETHE1 activity.....	9
1.1.6 <i>Hs</i> ETHE1 metal binding site(s).....	10
1.2 X-ray Absorption Spectroscopy (XAS)	12
1.2.1 Mononuclear [Fe]-hydrogenases	16
1.2.2 [Cu ₂ L ₂ (μ-O) ₂] ₂	18
1.2.3 The ATP binding cassette protein ABCE1	20
1.3 Aim of the projects	21
1.3.1 ETHE1 project.....	22
1.3.2 XAS project	22
2 MATERIALS AND METHODS	23
2.1 Cloning	23
2.1.1 Material for cloning	24
2.1.1.1 Primers.....	24
2.1.1.2 Kits used for cloning.....	31
2.1.1.3 Plasmid vectors	31
2.1.1.4 Bacterial Strains	31
2.1.1.5 Agarose Gel Electrophoresis (AGE) apparatus.....	32
2.1.1.6 Polymerase Chain Reaction (PCR) apparatus	32
2.1.2 Methods for cloning.....	32
2.1.2.1 Gene amplification.....	32

2.1.2.1.1 Amplification by cell culture	32
2.1.2.1.2 Amplification by PCR	32
2.1.2.2 Agarose Gel Electrophoresis (AGE)	34
2.1.2.3 DNA purification.....	34
2.1.2.4 DNA digestion.....	34
2.1.2.5 DNA ligation.....	35
2.1.2.5.1 Ligase dependent cloning	35
2.1.2.5.2 Ligase Independent Cloning (LIC).....	36
2.1.2.6 Transformation of <i>Escherichia coli</i> strains	40
2.1.2.7 Clones selection.....	40
2.1.2.8 Sequencing	42
2.1.2.9 Clones storage	42
2.2 Protein expression.....	43
2.2.1 Materials for Protein expression	43
2.2.2 Methods for protein expression.....	43
2.2.2.1 Protein expression in Luria-Bertani medium.....	43
2.2.2.2 Protein expression in ultra rich Auto-Inducing Medium (AIM).....	44
2.2.2.3 Protein expression in minimal medium.....	46
2.3 Protein purification.....	47
2.3.1 Materials for protein purification	48
2.3.2 Methods for protein purification	48
2.3.2.1 Sample preparation.....	48
2.3.2.2 Immobilized Metal Affinity Chromatography (IMAC).....	49
2.3.2.3 Estimation of the protein concentration.....	50
2.3.2.4 Digestion with TEV protease	51
2.3.2.5 Purification from the TEV and uncleaved protein.....	51
2.3.2.6 Size Exclusion (SE)/ Gel Filtration (GF) chromatography	52
2.3.2.7 Production of metal-free <i>HsETHE1</i>	53
2.3.2.8 Protein storage.....	53
2.4 Protein characterization.....	53
2.4.1 Poly Acrylamide Gel Electrophoresis (PAGE)	53
2.4.2 Dynamic Light Scattering (DLS).....	55
2.4.3 Protein stability	56
2.4.4 Static Light Scattering (SLS)	58
2.4.5 Crosslinking.....	59

2.4.6 Total X-ray Reflection Fluorescence (TXRF)	60
2.4.7 Isothermal Titration Calorimetry (ITC)	62
2.4.7.1 The ITC experiment	62
2.4.7.2 Solutions used in the ITC experiments	63
2.4.8 Optical absorption spectrophotometry	64
2.4.9 Mass Spectrometry (MS)	66
2.4.10 Circular Dichroism (CD) spectroscopy	66
2.4.11 Crystallization	68
2.4.12 Substrate screening	70
2.4.13 Small Angle X-ray Scattering	73
2.4.14 X-ray Absorption Spectroscopy (XAS)	75
2.4.14.1 Synchrotron beamlines	75
2.4.14.2 XAS measurements	75
2.4.14.3 Data processing (background removal, data reduction, normalization)	76
2.4.14.4 EXAFS analysis	76
2.4.14.5 XANES analysis	78
2.4.14.6 XANES simulations	78
2.4.15 Electron Paramagnetic Resonance (EPR) spectroscopy	78
2.4.16 Mössbauer spectroscopy	80
2.4.17 Molecular visualization tools	82
3 RESULTS	83
3.1 Biochemical and biophysical characterization of <i>Homo sapiens</i> ETHE1	83
3.1.1 Cloning	83
3.1.2 Expression and purification	84
3.1.3 Protein stability	87
3.1.4 Oligomeric state and exact mass determination	90
3.1.4.1 Crosslinking experiment	90
3.1.4.2 Static Light Scattering (SLS)	90
3.1.4.3 Mass Spectrometry (MS)	91
3.1.5 Substrate screening	92
3.1.6 UV-Vis and the interaction with reduced glutathione	94
3.1.7 Total X-ray Reflection Fluorescence (TXRF)	95
3.1.8 Isothermal Titration Calorimetry (ITC)	97
3.1.8.1 Metal titration	97
3.1.8.2 Glutathione titration	98

3.1.9 Small Angle X-ray Scattering (SAXS)	99
3.1.9.1 SAXS on olo- <i>Hs</i> ETHE1	99
3.1.9.2 SAXS on apo- <i>Hs</i> ETHE1	101
3.1.10 X-ray Absorption Spectroscopy (XAS)	103
3.1.10.1 EXAFS on <i>Hs</i> ETHE1	104
3.1.10.2 XANES on <i>Hs</i> ETHE1	111
3.1.11 Electron Paramagnetic Resonance (EPR)	114
3.1.12 Mössbauer spectroscopy	114
3.1.13 Crystallization	116
3.1.14 Hypothetic <i>Hs</i> ETHE1's reaction mechanism.....	117
3.2 X-ray Absorption Spectroscopy applications and methods development.....	120
3.2.1 XAS study of the mononuclear [Fe]-hydrogenases Hmd.....	120
3.2.1.1 jHmd: EXAFS analysis	120
3.2.1.1.1 jHmd EXAFS-model[2]	124
3.2.1.1.2 Revisited jHmd EXAFS-model[4,115].....	126
3.2.1.2 jHmd: XANES analysis[117]	127
3.2.1.2.1 Experimental XANES analysis: model complexes and jHmd.....	128
3.2.1.2.2 XANES simulations: model complexes and jHmd.....	132
3.2.2 [Cu ₂ L ₂ (μ-O) ₂]I ₂ excited state characterization[122]	138
3.2.3 ABCE1 protein: XAS characterization	139
4 CONCLUSIONS AND DISCUSSION	142
4.1 <i>Homo sapiens</i> ETHE1 characterization	142
4.2 X-ray Absorption Spectroscopy applications and methods development.....	144
4.2.1 Mononuclear [Fe]-hydrogenase	144
4.2.2 [Cu ₂ L ₂ (μ-O) ₂]I ₂ excited state	146
4.2.3 ABCE1	147
5 OUTLOOK.....	148
6 APPENDIX A: MATERIAL.....	151
7 APPENDIX B: ABBREVIATIONS	175

8 ACKNOWLEDGEMENTS.....	178
9 REFERENCES	179
PUBLICATIONS.....	187

List of figures

Fig. 1: ETHE1 introduction.....	4
Fig. 2: <i>At</i> ETHE1 structure and metal binding site.....	7
Fig. 3: <i>At</i> ETHE1 active site.....	8
Fig. 4: Model of the mitochondrial sulfide-oxidation system.....	10
Fig. 5: XAS principles.....	13
Fig. 6: Hmd hydride acceptor and cofactor.....	17
Fig. 7: Tyrosinase metal binding site and Cu-based model complex.....	18
Fig. 8: $[\text{Cu}_2\text{L}_2(\mu\text{-O})_2]\text{I}_2$ formation and pumped-XAS experimental set up.....	19
Fig. 9: X-ray diffraction structure of the protein ABCE1 from <i>Pyrococcus abyssi</i> (PDB: BK7).....	21
Fig. 10: <i>Hs</i> ETHE1 cloning vectors.....	31
Fig. 11: Substrate screenings.....	72
Fig. 12: EXAFS sample holder design.....	75
Fig. 13: Agarose gel of <i>Hs</i> ETHE1 and plasmid vectors DNA.....	84
Fig. 14: <i>Hs</i> ETHE1 IMAC.....	86
Fig. 15: <i>Hs</i> ETHE1 TEV cleavage.....	87
Fig. 16: <i>Hs</i> ETHE1 SEC.....	88
Fig. 17: reducing agents test.....	89
Fig. 18: SDS-PAGE of the cross-linking experiment samples.....	90
Fig. 19: SLS spectrum of <i>Hs</i> ETHE1.....	91
Fig. 20: Mass spectrometry spectrum of <i>Hs</i> ETHE1 as isolated.....	92
Fig. 21: Results of a substrate screening test.....	93
Fig. 22: Results of the esterase activity test.....	94
Fig. 23: <i>Hs</i> ETHE1 UV-Vis.....	95

Fig. 24: Results of ITC experiments.....	99
Fig. 25: Results of SAXS experiments.....	101
Fig. 26: <i>Hs</i> ETHE1 EXAFS.....	104
Fig. 27: <i>Hs</i> ETHE1 XANES spectra.....	110
Fig. 28: <i>Hs</i> ETHE1 XANES pre-edge peak analysis.....	113
Fig. 29: Mössbauer spectrum of <i>Hs</i> ETHE1.....	115
Fig. 30: <i>Hs</i> ETHE1 crystallization spherulites.....	117
Fig. 31: Proposed catalytic mechanism for <i>Hs</i> ETHE1.....	118
Fig. 32: Hmd EXAFS analysis.....	124
Fig. 33: Single scatterer contributions to Hmd EXAFS.....	127
Fig. 34: Structural sketches of Hmd model complexes.....	128
Fig. 35: Hmd and model complexes XANES.....	129
Fig. 36: Hmd-wt and Hmd-CN XANES comparison.....	130
Fig. 37: Hmd and model complexes edge positions.....	132
Fig. 38: Hmd metal binding site.....	134
Fig. 39: Hmd XANES simulation.....	135
Fig. 40: Hmd simulated and experimental XANES.....	136
Fig. 41: Hmd-ligands contributions to the XANES.....	137
Fig. 42: Results of EXAFS, XANES and resonance Raman spectroscopy on [Cu ₂ L ₂ (μ-O) ₂] ₂	139
Fig. 43: XAS analysis of ABCE1.....	140

List of tables

Tab. 1: <i>Hs</i> ETHE1 constructs.....	85
Tab. 2: TXRF results of <i>Hs</i> ETHE1 as isolated and metal-free.....	96
Tab. 3: <i>Hs</i> ETHE1 SAXS parameters.....	100
Tab. 4: <i>Hs</i> ETHE1 EXAFS parameters.....	108
Tab. 5: <i>Hs</i> ETHE1 pre-edge peak analysis.....	112
Tab. 6: <i>Hs</i> ETHE1 Mössbauer parameters.....	116
Tab. 7: Hmd EXAFS parameters.....	123

Tab. 8: Edge and pre-edge peak parameters of Hmd and model complexes.....	131
Tab. 9: EXAFS parameters Hmd and model complexes.....	133

Summary

This work focuses on the biochemical and biophysical characterization of highly interesting metallo-proteins and is divided in two main projects. The first project regards the characterization of the iron-based enzyme ETHE1 from *Homo sapiens*, which is fundamental for detoxification from highly reactive persulfide species and whose specific mutations on the structural gene or on its regulatory sequences cause ethylmalonic encephalopathy. Moreover, ETHE1 was reported to be involved in apoptosis and cancer through the interaction with transcription factors such as NF- κ B and p53. The protein has been studied by a number of techniques, noticeably XAS (X-ray absorption spectroscopy), SAXS (Small Angle X-ray Scattering Spectroscopy), Mössbauer spectroscopy and ITC (Iso-Thermal Calorimetry).

The second project is based on XAS analysis and method development applied to metallo-proteins that are likely to have a substantial impact on basic and applied science. The mononuclear [Fe]-hydrogenase Hmd from *Methanocaldococcus jannaschii* has been extensively investigated by XANES and EXAFS analysis in the native and inhibited forms. This study revealed the major determiners of the electronic structure of this unique hydrogenase iron site and shed light on the chemico-physical requirements for the heterolysis of molecular hydrogen. In addition, I contribute to the characterization of the optically excited state of a bis (μ -oxo)-dicopper(III) complex mimicking the potential di-oxo to μ -oxo transition in tyrosinases active site. We took advantage of two cooperative approaches: pumped-XAS and an innovative combination of EXAFS spectroscopy and resonant Raman scattering. I present also the XAS analysis results obtained on the protein ABCE1, which is one of the most conserved proteins in the evolution of eukaryotes and archaea. ABCE1 is essential for cell viability and is a unique ATP-binding-cassette protein bearing iron-sulfur clusters.

Zusammenfassung

Diese Arbeit beschäftigt sich mit der biochemischen und biophysikalischen Charakterisierung von hochinteressanten Metalloproteinen und gliedert sich in zwei Hauptprojekte. Das erste Projekt behandelt das humane eisenabhängige Enzym ETHE1, welches essentiell für die Entgiftung reaktiver Persulfide ist und von dem Mutationen der kodierenden Gensequenz oder regulatorischer Sequenzen für die Entstehung von Ethylmalonsäure-Enzephalopathie verantwortlich sind. Darüber hinaus wurde berichtet, dass ETHE1 durch Interaktion mit den Transkriptionsfaktoren NF- κ B und p53 an Apoptose und der Entstehung von Leber Krebs beteiligt ist. Dieses Protein wurde in *E. coli* überexpression und mittels XAS (Roentgenabsorptionsspektroskopie), SAXS (Roentgenkleinwinkelstreuung), Moessbauerspektroskopie und ITC (Isothermale Titrationskalorimetrie) untersucht.

Das zweite Projekt umfasst die XAS-Analyse und neuartiger Ausweitungs Methoden zum Studium von Metalloproteinen, denen große Bedeutung in der Grundlagenforschung und angewandten Forschung zugeschrieben wird. Die mononukleare [Fe]-Hydrogenase Hmd von *Methanocaldococcus jannaschii* wurde eingehend in ihrer nativen und inhibierten Form durch XANES und EXAFS studiert. Diese Untersuchung deckte die wichtigsten Faktoren für die elektronische Struktur der einzigartigen Hydrogenase-Eisenbindungsstelle auf, und brachte neue Erkenntnisse über die chemisch-physikalischen Bedingungen der Heterolyse von molekularem Wasserstoff. Zusätzlich beschreibe ich die Charakterisierung des optisch angeregten Zustandes einer (μ -oxo)-dicopper(III) Verbindung, die den möglichen "di-oxo zu μ -oxo"-Übergang im aktiven Zentrum von Tyosinasen nachhaffen. Dazu nutzten wir zwei komplementäre Ansätze: pumped XAS und eine innovative Kombination aus EXAFS und resonanter Raman-Streuung. Ich präsentiere desweiterer die Ergebnisse der XAS-Analyse des Proteins ABCE1, das eines der konserviertesten Proteine in der Evolution der *Eukarya* und *Archaea* darstellt. ABCE1 ist wichtig für das Ueberleben der Zelle und enthält eine einzigartige ATP-Bindungskassette, die auf Eisen-Schwefel Clustern basiert.

1 Introduction

Enzymes catalyze a wide range of chemical reactions. The variety of function is achieved partly because proteins can incorporate in their active sites cofactors such as small organic molecules, single metal atoms, or clusters containing metal and non-metal atoms. Strikingly, almost half of all known enzymes require a metal for their activity.[7] Biochemists developed their interest on ‘metalloproteins, particularly since the 1950s, when the first X-ray crystal structure of a protein (sperm whale myoglobin) indicated the presence of an iron atom. A lot has been understood about which metal ions are commonly found in metalloenzymes and their ligand specificity. In addition, we are much closer to understanding the mechanisms by which metalloenzymes catalyze such a wide range of complex chemical reactions. However, after more than half a century of research by chemists, biochemists and cell biologists, many discoveries remain to be made.

In this work, I focus on two related projects. The first concerns the biochemical and biophysical characterization of the human metalloprotein ETHE1, which is fundamental for survival and development of metazoa towards the adult age. The second concerns X-ray Absorption Spectroscopy (XAS) application and method development. XAS is a powerful synchrotron-based technique used for determining the local geometric and/or electronic structure of matter and herein applied to study the metal centers of proteins, and bioinorganic compounds.

1.1 Ethylmalonic encephalopathy protein 1

ETHylmalonic Encephalopathy protein 1 (ETHE1), also known as Hepatoma Subtracted-cDNA library Clone One (HSCO), is a protein with Metallo- β -Lactamase (M β L) superfamily fold (Fig. 1 A). ETHE1 has been found in metazoa and plants. It is not known why is absent in mesozoa and protozoa. Speculations led to the possibility that its codifying sequence might derive from the duplication of an ancient ancestor gene, which evolved gaining a functionality that is not necessary for protozoa and mesozoa.

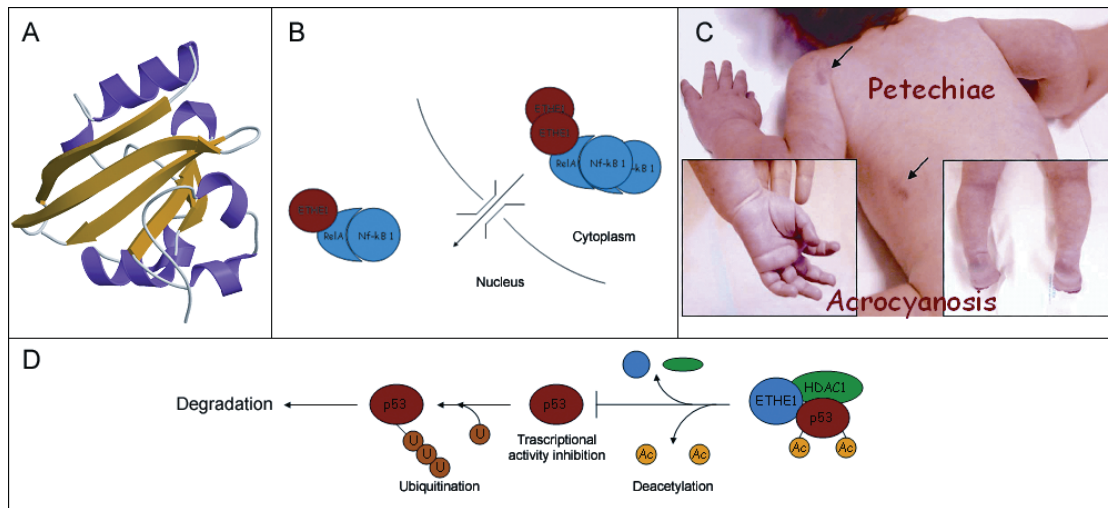


Fig. 1: ETHE1 introduction.

A) Metallo β -lactamase superfamily fold. B) Scheme of NF- κ B1 shuttling model. ETHE1 is able to shuttle NF- κ B1 from the nucleus to the cytoplasm. C) Some symptoms (petechiae and acrocyanosis) characterizing the ethylmalonic encephalopathy phenotype are visible on an affected infant's body. D) Schematics of the ETHE1-stimulated p53 degradation pathway.

Thus, the gene could have been lost by the ancestor organism. Alternatively, it might derive from horizontal genetic transfer virus/viroid mediated.

1.1.1 *Homo sapiens* ETHE1

Homo sapiens ETHE1 (*Hs*ETHE1) is a 254 aminoacids (aa) M β L superfamily protein codified by a gene lying on the long arm of the chromosome 19 (19q13.31). More information can be found on the GeneCards web site (www.genecards.org) under the gene card identifier (GIFtS) = GC19M048702. Studies on human cells highlighted that the protein is localized mainly in the mitochondrial matrix, but can be found also within the cytoplasm and the nucleus.[8,9] The protein is addressed to the mitochondrial matrix by an N-terminal localization sequence.[10] ETHE1 is then thought to be activated as an enzyme through the cleavage of a short peptide at the N-terminus. Recently, exploiting MALDI-TOF mass spectrometry it has been defined that the aminoacids from 1 to 7 are cut away during the translocation into the mitochondrion.[11] There is evidence that *Hs*ETHE1 is often overexpressed in Hepato-Cellular Carcinoma (HCC).[8] Moreover, it is able to inhibit p53 dependent apoptosis by two ways[12] and it is strictly involved in Ethylmalonic Encephalopathy (EE).[9,10] The structure of the homologous enzyme

from *Arabidopsis thaliana* has been reported.[13] Recently, it has been proved that ETHE1 is an essential sulfur dioxygenase involved in the detoxification from highly reactive persulfide species.[11]

1.1.2 *Hs*ETHE1 and hepatocellular carcinoma

Hepato-cellular carcinoma is one of the most frequent carcinomas in the world. It evolves extremely rapidly and it is fatal. Indeed, the expectancy of life is about six months after the first diagnosis. In a work of 2002, Hisako Higashitsuji *et al.*[8] analyzed 30 hepato-cellular carcinomas. In 20 of them, ETHE1 was found over expressed. This work shows that *Hs*ETHE1 binds RelA, which is one of the 2 proteins forming the most common Nf-kB type transcription factors. The interaction takes place in the nucleus. Wherein, *Hs*ETHE1 is able to shuttle Nf-kB to the cytoplasm (Fig. 1 B). As a consequence of the failed transcription by Nf-kB, the caspase 9 is inhibited. Thus, *Hs*ETHE1 blocks p53-dependent apoptosis induced by DNA damage triggering tumorigenesis. Moreover, the protein exhibits anti-apoptotic activity in human cells exposed to DNA-damaging agents by suppressing the transcriptional activity of p53.[12] ETHE1 specifically associates with histone deacetylase 1 (HDAC1) and forms a ternary complex with p53 in the nucleus. This interaction enhances deacetylation of p53 at Lys373/382 by HDAC1 (Fig. 1 D). Deacetylated p53 becomes a facilitated target of the ubiquitin-proteasome system. Thus, ETHE1 increases ubiquitylation and degradation of p53, reducing the protein availability. ETHE1 is therefore a promising target for HCC treatment and its characterization could give a contribution to the development of therapeutic strategies to restore the appropriate p53 response in cancer.

1.1.3 *Hs*ETHE1 and ethylmalonic encephalopathy

Ethylmalonic Encephalopathy (EE) (OMIM #602473) is a devastating infantile autosomal recessive metabolic disorder affecting the brain, the gastrointestinal tracts and the peripheral vessels.[14] It affects mainly Mediterranean people and who bears this disease dies within the first decade of life. In three works, Tiranti *et al.* showed that in all 47 (on the whole) analyzed patients affected by EE, the *ethe1* gene was mutated in

both allelic loci.[9,10,15] Specific mutations in this gene are always associated to the disease. More than thirty independent mutations have been reported to cause the disease.[16] All of them led, or to the loss of the gene's product, or they involved highly conserved aminoacids. Tiranti *et al.* also revealed that *HsETHE1* is a mitochondrial-matrix protein whose N-terminal sequence is processed during its internalization.[9] This cleavage takes place between Arg7 and Val8 and is supposed to turn on the enzymatic activity of the protein.[11] EE is characterized by a specific phenotype and biochemical, metabolic findings. The patients show: a) psychomotor regression and hypotonia due to inhibition of Cytochrome c Oxidase (COX) activity; b) progressive encephalopathy with symmetrical lesions in the basal ganglia and brainstem, eventually leading to global neurological failure; c) vasculopathic petechiae and orthostatic acrocyanosis; d) chronic diarrhoea; e) EthylMalonic Aciduria (EMA) associated with methyl-succinic aciduria, high plasmatic levels of C4-C6 acylglycine and C4-C5 acylcarnitine species; f) lactic aciduria. The latter symptoms (e and f) are also the hallmark of Short Chain Acyl-CoA Dehydrogenase (SCAD) deficiency.[17] The aetiology can presently be entirely explained by the loss of *ETHE1* physiological activity, which was discovered and described by Tiranti *et al.* in 2009.[11,18]

1.1.4 *AtETHE1* structure

In 2006, McCoy *et al.* presented the structure of *ETHE1* from *Arabidopsis thaliana* (*AtETHE1*) (Fig. 2 A).[13] They found that the protein is a homodimer with one iron bound to the active site (B2- M β L; Fig. 2 B), even if the protein, as *HsETHE1*, still keeps conserved all the aminoacids usually responsible of the binding of two metals (B1- and B3-M β L). *AtETHE1* misses a 2 helix bundle present in *AtGLX2-5*. This results in the formation of a dimerization interface. The comparison with the structurally highly related Glyoxalases II from *Arabidopsis thaliana* showed that *AtETHE1* possesses the same highly conserved substrate-binding aminoacids, but they also showed that these are in slightly different positions. Moreover, *AtETHE1* has a smaller cavity for substrate binding, because the C-terminus covers much of the active site leading to reaction chemistry different from Glyoxalase II enzymes. *AtETHE1* and *HsETHE1* share an

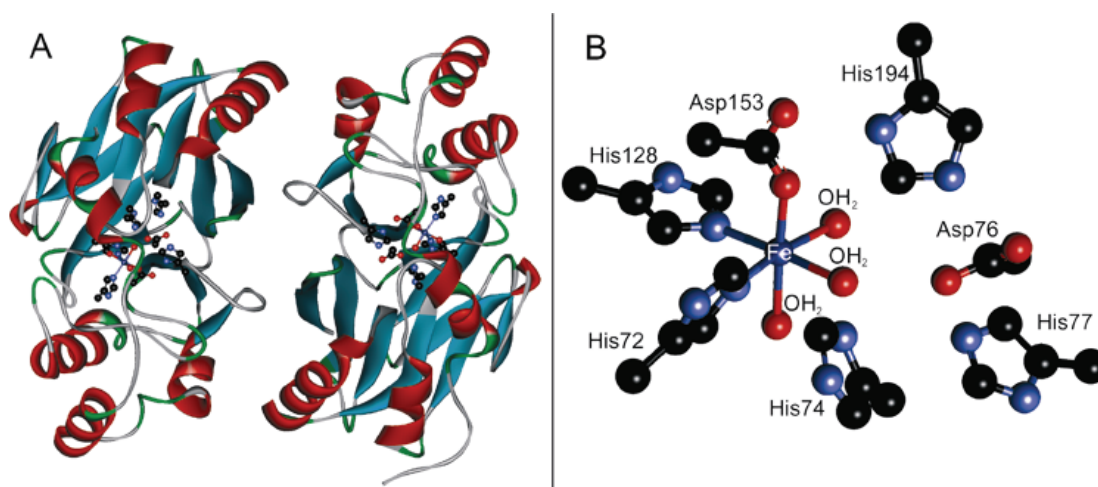


Fig. 2: *AtETHE1* structure and metal binding site.

A) Three dimensional structure of homodimeric ETHE1 from *Arabidopsis thaliana* represented in cartoon style: red, α -helices; ocean-green, β -sheets; green, loops; grey, linkers between secondary structures. In scaled ball and stick the metal binding site of each subunit is represented: black, the carbons; red, the oxygens; light sky-blue, the nitrogens; sky-blue, the iron. B) Zoom in the metal binding site. Scaled ball and stick representation: black, the carbons; red, the oxygens; light violet-blue, the nitrogens; violet-blue, the iron. The figure shows the iron coordination sphere and the potential second binding site aminoacids.

identity of 54% and a similarity of 66%, which is surprising for protein so evolutionarily distant. A three dimensional molecular model of *HsETHE1* has been build using the SWISS-MODEL server (web page: <http://swissmodel.expasy.org/>).[19] It is worthy to notice that the *HsETHE1* structural model shows the presence of the conserved metal binding aminoacids (His 59, 61, 64, 175, Asp 32, 63, 134; add 21 to get the full length protein aminoacid number) packed in proximity (3-5 Å from each other). The model shows a conserved Tyrosine (177/198) pointing towards the active site at about 7 Å from the iron ion and the characteristics c-terminal part arching over above the active site (Fig. 3).

Here, the aminoacid sequence alignment of *AtETHE1* (PDB sequence) with respect to *HsETHE1* is presented:

■: aa potentially important for metal binding
 ■: b-sheet
 ■: helix
 ■: Mutation in EE
 _: Same aa

Introduction

(12)

```
AtETHE1: -----KLLFRQLFENESSTFTYLLADVSHPKPALLIDPWDKTVDRDLKLIDELGLKLIYAMNTVVAADHVTGTGLLKTLPGVK
HsETHE1: MAEAVLRVARRQLSQRGGSGAPILLRQMFEPVSCFTFTLLGDRES--REAVLIDPVLETAPRDAQLIKELGLRLLYAVNTVCAADHITGSGLLRSLLPGCQ

          90      100      110      120      130      140      150      160      170      180
AtETHE1: SVISKASGSKADLFLEPGDKVSI GDIYLEVRATPGTAGCVTYVTGEGADQPQPRMAFTGSAVLIRGCGRTFQEGSDQLYESVHSQIFTPKDTLIYP
HsETHE1: SVISRLSQAQADLHIEDGDSIRFGRFALETRASFGITPGCVTFVLNDHS-----MAFTGSAALLIRGCGRTFQQQCAKTLYHSVHEKIIFTPGDCLIYP

          190      200      210      220      230      240
AtETHE1: AHTYKGFVSTVGEEMQHNPRLTKDKETFKTIMSNLNSYPKMI DVAVPANMVCGLQDVPSQAN 244
HsETHE1: AHTYHGFTVSTVVEERTLNPRLTLSCEEFVKIMGNLNLPKQQIDFAVPANMRCVQTPTA--- 254
```

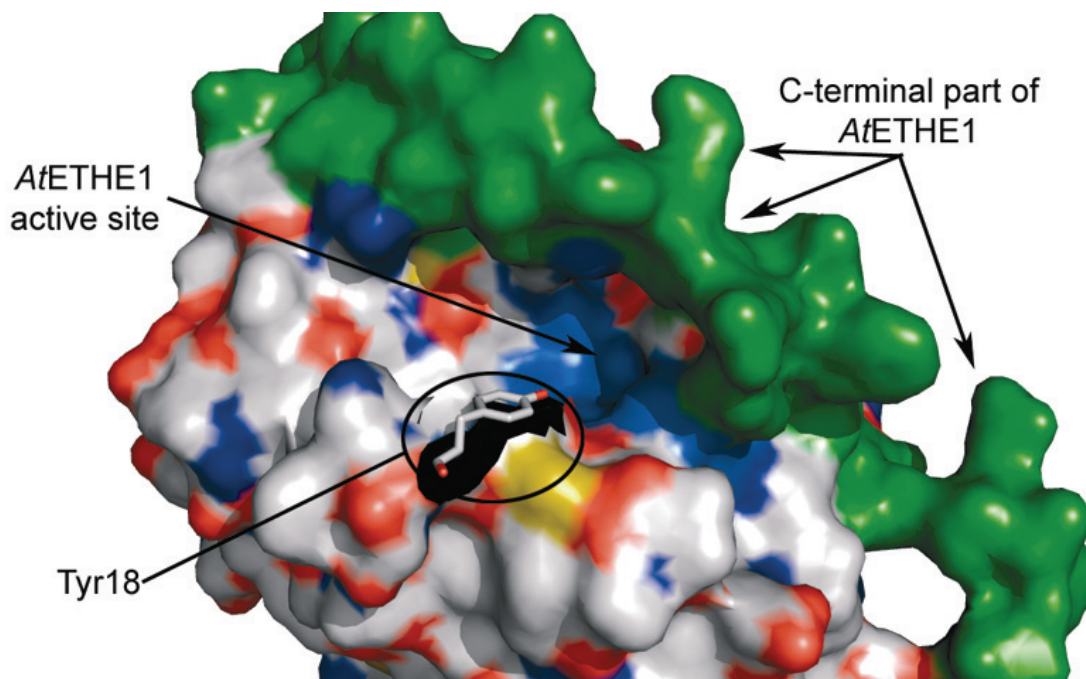


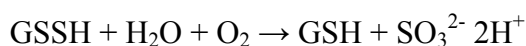
Fig. 3: *AtETHE1* active site.

Electrostatic surface representation of the molecular model of *HsETHE1*: red, the negatively charged regions; blue, the positively charged regions; grey, the neutral regions; green, the c-terminal part of the protein; blue-marine, the conserved metal-binding site aminoacids. The tyrosine 18 is represented as stick style: red, the oxygens; grey, the carbons. The image was created with PyMol: <http://pymol.sourceforge.net/>.

The alignment has been carried out using the server ClustalW2 at the European Bioinformatics Institute web site and successively manually refined.

1.1.5 *Hs*ETHE1 activity

Recently, Valeria Tiranti and her collaborators revealed that *Hs*ETHE1 is a sulfur dioxygenase[11] involved in a pathway for detoxification from excess of sulfide (H₂S), which accumulates to toxic levels in ethylmalonic encephalopathy. The sulfide detoxification system is fundamental for metazoa. In fact, H₂S is a gastro transmitter acting as a signaling molecule, but at supraphysiological concentration it is a powerful inhibitor of COX (Cytochrome c Oxidase)[6,20,21] and of SCAD (Short Chain Acyl-CoA Dehydrogenase) activity.[11,17] H₂S is released by bacteria in large amounts in the lumen of the large intestine, is vasoactive and at high concentrations is toxic to endothelial cells. Taken together, these considerations explain the biochemical marks found in patients affected by EE: COX deficiency, ethylmalonic aciduria in the urine, high levels of C4 and C5 acylcarnitine species in the blood, acrocyanosis, petechiae, chronic diarrhea, and neurodevelopmental delay and regression. H₂S disposal is carried out by a mitochondrial system[22] that uses sulfide as a respiratory substrate (Fig. 4).[23] The system comprises SQR (Sulfide:Quinone Oxidoreductase), SDO (Sulfur Dioxygenase), Rhodanase and SO (sulfite oxidase).[22] The final products are sulfate (SO₄²⁻, major sulfur metabolite in mammalian urine) and thiosulfate (metabolically inert). In this pathway, SQR produces at a cysteine residue a persulfide (R-SSH), which is transferred to a thiophilic acceptor such as glutathione, forming GSSH. The latter compound is the natural substrate of ETHE1. GSSH is unstable and highly reactive. Molecular oxygen (O₂) and water (H₂O) is then used by ETHE1 (the mitochondrial-matrix sulfur dioxygenase) to oxidize the sulfane sulfur persulfide (R-SSH) to sulfite (H₂SO₃) and restore the R-SH acceptor. Reaction:



The structurally and functionally closest enzymes known are the glyoxalases-II (GLX2). The comparison between the *Arabidopsis thaliana* structures of ETHE1 and GLX2s shows that they share the same highly conserved substrate and metallo binding aminoacids and that these are in different positions.[13] Interestingly, also the GLX2

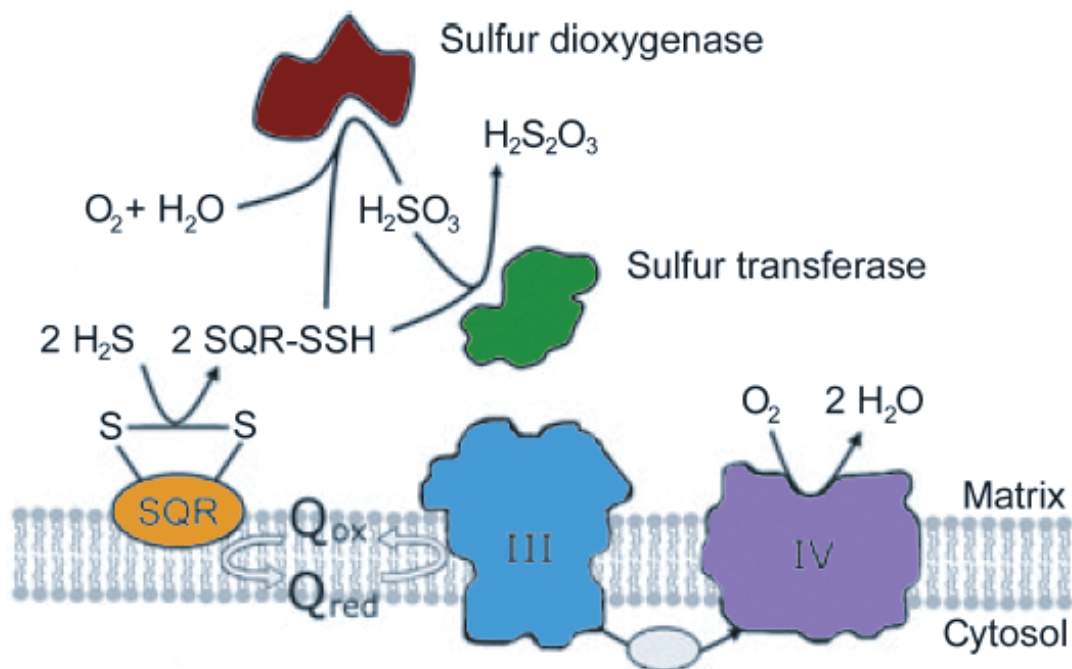


Fig. 4: Model of the mitochondrial sulfide-oxidation system.

Membrane-bound sulfide:quinone oxidoreductase (SQR) oxidizes sulfide (H_2S) to the level of elemental sulfur, simultaneously reducing a cysteine disulfide bond so that a persulfide group is formed at one of the cysteine residues (SQR-SSH).[6] The electrons are fed into the respiratory chain via the quinone pool (Qox/Qred), and finally transferred to oxygen by cytochrome oxidase (complex IV). A sulfur dioxygenase in the mitochondrial matrix oxidizes persulfides to sulfite (H_2SO_3), consuming molecular oxygen and water. The final reaction is catalyzed by a sulfur transferase, which produces thiosulfate ($\text{H}_2\text{S}_2\text{O}_3$) by transferring a second persulfide from the SQR to sulfite.

enzymes are active against a derivative of glutathione, hydrolyzing S-(2-hydroxyacyl)glutathione to glutathione and a 2-hydroxy carboxylate. It is then worth to notice that the conserved aminoacids of *HsETHE1* comprise motifs present in the ZiPD/tRNaseZ M β L-fold protein.[24]

1.1.6 *HsETHE1* metal binding site(s)

ETHE1 is a protein with Metallo- β -Lactamase (M β L) superfamily fold (Fig. 1 A). These proteins are enzymes bearing one or two metals in their active sites.[25,26] Following the revised Ambler structural classification,[27] M β L are divided in B1, B2, B3 and β -CASP families. The B1 family shares sequence and structural homology with the B2, while the B3 is only structurally related to B1 and B2. B1 and B3 usually contain 2

metal ions and they show a broad substrate spectrum. Instead, B2 enzymes are full active with one metal ion and possess a narrower substrate spectrum. The metal ions exploited by MβL for their activity are commonly Zn^{2+} and/or Fe^{2+} , but they are usually able to bind also other metals such $Mn^{2+/3+}$ and Ni^{2+} . The β-CASP family is involved in DNA and RNA metabolism and repair. Enzymes with MβL fold can have sundry activities, ranging from hydrolysis of β-lactams to glyoxalase II activity, as well as arylsulfatase, CMP-NeuAc hydrolase, cAMP phosphodiesterase, DNase and RNase activity. The metal binding residues are commonly histidines, aspartates, glutamate, waters, but some have sulfur affinity and need a cysteine residue as ligand to be active.[28,29] Sulfur-based molecules are commonly used as MβL inhibitors.[30,31] Bridging ligands are also common, as in the tRNase Z family proteins, where an aspartate is bridging two zinc ions.[32-34] The structure from *Arabidopsis thaliana* reveals a mononuclear iron binding site that classifies ETHE1 as a B1 MβL according to the Ambler classification.[13,27] In the structural model the iron has an octahedral coordination comprising histidine and oxygen ligands. A similar coordination is found in a number of mononuclear iron dioxygenases such as the lipoxygenase, the α-keto acid-dependent enzymes, the isopenicillin-N synthetase, the ethylene forming enzymes and pterin-dependent hydroxylases[35-37] This fits very well the recent discovery that ETHE1 is a sulfur dioxygenase.[11] The mononuclear-iron dioxygenases show a wide variety of mononuclear iron binding sites.[35-37] The iron ions can be ferric or ferrous, with five or six ligands bound to the metal. It can possess different geometries, such as trigonal bipyramidal or square pyramidal in case of penta-coordinated iron centers, and octahedral, for exa-coordinated iron centers. The iron site in *At*ETHE1's structure is defined by two histidines, one aspartate and three solvent-oxygens. This coordination possesses the 2-his-1-carboxylate facial triad motif in common with the iron(II) high spin oxygen-activating dioxygenases (α-keto acid dependent enzymes, isopenicilline-N synthetase, ethylene-forming enzyme, pterin dependent hydroxylase, naphthalene dioxygenase).[35-37] In particular, considering the activity and the metal coordination sphere modeled in the structure from *Arabidopsis thaliana*, *Hs*ETHE1's iron binding site should be considered highly similar to the isopenicilline-N synthetase one, which

catalyzes the formation of isopenicilline-N from α -(L-R-aminoadipoyl)-L-cysteinyl-D-valine (ACV). ACV binds the iron with its sulfur atom during catalysis. Besides, beyond *Hs*ETHE1, another mononuclear iron sulfur dioxygenase is known in human and its structure is reported.[38,39] This enzyme is a cysteine dioxygenase (CDO), converting cysteine residues in cysteine sulfinates and thereby carrying out a reaction very similar to the persulfide dioxygenase activity of ETHE1. Nevertheless, the cysteine dioxygenase has substantial differences respect ETHE1. CDO has a cupin superfamily fold as the α -keto acid-dependent dioxygenases and the iron ion in the active form of the enzyme has an unusual tetrahedrally coordinated iron with three histidine and a solvent oxygen as ligands.[39] On the other hand, the enzyme has been found also in different non-active states with nickel or zinc bound and in octahedral geometry comprising the three histidines and three solvent molecules.[38]

The understanding at molecular level of *Hs*ETHE1 has important implications because it sheds light on:

- The basis for an action against ethylmalonic encephalopathy and hepatocellular carcinoma.
- The molecular reasons for the variety of reactions that ETHE1-like enzymes are able to perform.
- The sulfur detoxification system in humans and likely in all metazoa and superior plants.
- The general requirement for substrate dioxygenation.
- The physical-chemical properties that nature chose for sulfur oxidation.
- Improve our understanding of apoptosis.

1.2 X-ray Absorption Spectroscopy (XAS)

X-ray Adsorption Spectroscopy (XAS) is a powerful spectroscopic method based on synchrotron radiation.[40] In a homodisperse phase, XAS is able to determine the local environment of a given element with high resolution. XAS is very effective for studying the architecture, disorder and electronic structure of (in principle) any site of a given element up to about 5 angstrom (\AA) radius from the absorber. During my doctorate, I

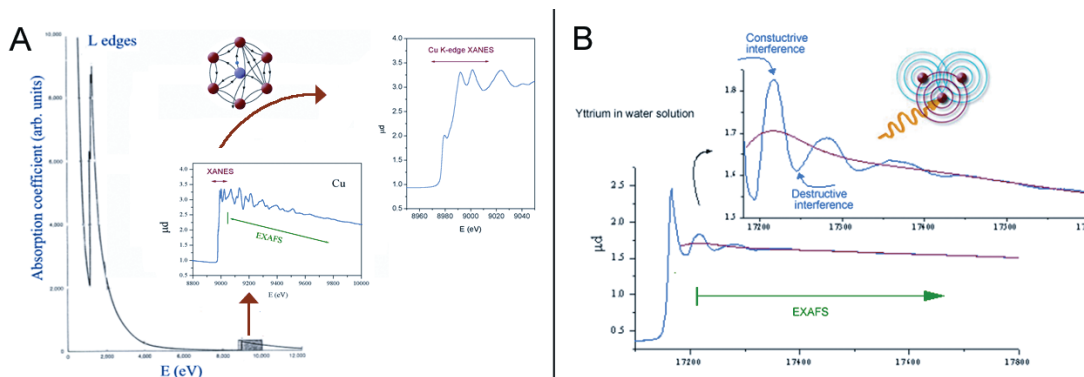


Fig. 5: XAS principles.

A) Example of X-ray Absorption Spectroscopy spectrum. Here the copper L and K edges are considered. For the K-edge a zoom in of the spectrum is present. The division in the XANES and EXAFS parts is also shown. In the upper right part there is a zoom in of the XANES part. B) Example of a K-edge XAS spectrum of Yttrium. In the upper part, the EXAFS region of the spectrum and the interference path between the outgoing photoelectron and the incoming scattered waves originating the characteristic undulatory behavior of the EXAFS are presented.

worked on BioXAS, which focuses on the metal sites of proteins. Synchrotron radiation is applied to excite deep electrons by scanning an energy range from about one hundred and fifty electron volts before the adsorption edge characteristic for the metal under study, up to several hundreds of electron volts (eV) after the main adsorption edge. In the dominant adsorption process, an electron is ejected from the core and a photoelectron is emitted in the form of a spherical wave (for our purposes, its description as wave is more convenient than its description as particle). The adsorption energy value varies, depending on the nature of the metal (the binding energies of the core electrons grow monotonically with the atomic number), as well as on the edge we want to excite. In different words, we can choose which metal to excite and if involving electrons in the most deep shell or higher shell electrons (electrons in higher energy orbitals). The characteristic resulting spectra can be divided in two parts: X-ray Absorption Near Edge Structure (XANES) (Fig. 5 A) and Extended X-ray Absorption Fine Structure (EXAFS) spectra (Fig. 5 A, B). The XANES spectrum comprises energies from about -20 eV below up to 50 eV above the adsorption edge. It allows study the electronic structure of metal centers. The shape and position of the X-ray absorption edge serve as fingerprints of a specific binding motif and, if good reference systems are available, allow the determination of oxidation states, number of ligands and symmetry of the coordination

sphere. In fact, both edge position and electronic structure of a system depend on the nature of the donor groups. It is worth to notice that XANES is mainly a qualitative approach, since there is no “XANES equation” due to the difficulties to interpret quantum mechanical events correlated to many-body multiple scattering events dominating the XANES. The EXAFS spectrum comprises the energy range from 5 eV up to 400/1650 eV above the absorption edge. It is characterized by an undulatory behaviour caused by the interference effects between the outgoing photoelectron wave and its component backscattered by the surrounding atoms (Fig. 5 B). The interference pattern modifies the probability of the photoeffect (the adsorption coefficient is changing):

$$\chi \equiv \frac{\mu - \mu_0}{\mu_0}$$

χ is the fractional change in the absorption coefficient function (oscillatory part); μ is the absorption coefficient of an element in a particular environment at a particular energy and μ_0 in the theoretical absorption coefficient of the absorber alone. Thereby, while the adsorption spectrum is scanned by changing the photon energy, the energy of the photoelectron changes and its wavelength varies. Consequently, the interference with the scattered photons changes from constructive to destructive and back again. This creates the characteristic spectra (Fig. 5 B). EXAFS can give us information about the nature of the metal-ligands, about the thermal and structural disorder of individual components and highly precise information about the coordination distances. Commonly, the working environment for analysis is not in the energy space, but in the more convenient photoelectron wavevector space, which is dependent from the wavenumber (number of wavelengths per unit distance). The wavevector is an independent variable that is proportional to momentum rather than energy. Since energy is conserved, excess energy given by $E - E_0$ is conserved by being converted in the kinetic energy of the photoelectron wave. Since wavelengths are dependent of kinetic energies, the

photoelectron wave (de Broglie wavelength) propagates through the EXAFS region with a velocity v when the wavelength of the photoelectron is scanned.

This is the equation for the conversion of the energies to wavenumbers:

$$k = \frac{2\pi m_e v}{h} = \frac{2\pi}{\lambda} = \left[\frac{8\pi^2 m_e v}{h^2} (E - E_{edge}) \right]^{1/2} = \frac{\sqrt{2m_e (E - E_{edge})}}{\hbar} = \sqrt{0.262449(E - E_{edge})}$$

Where, m_e is the resting mass of the electron, v is the electron speed ($m_e v =$ photoelectron momentum), h is the Planck constant, E is the energy and \hbar is $h/2\pi$.

The fundamental basic equation governing the EXAFS as a function of the photoelectron wavenumber for a given j shell is the following:

$$\chi(k) = \sum_j \frac{N_j S_0^2 f_j(k) e^{-R_j/\lambda(k)} e^{-2k \sigma_j^2}}{k R_j^2} \sin[2kR_j + \delta_j(k)]$$

S^2 is the amplitude reduction factor. If we know the scattering amplitude $f_j(k)$ and the phase shift $\sigma_j(k)$ of the neighbouring atoms, which depend on the atomic number (Z) of the scattering atom, and we know the mean free path $\lambda(k)$, we can determine:

- R : distance to neighbouring atom
- N : coordination number of the atoms in a shell
- σ^2 : mean square disorder of neighbour distance

This equation takes in account also the inelastic scattering through the term: $e^{-2R_j/\lambda(k)}$. Successively, the Fourier transform (FT) allow us to switch from the k space to the radial distribution function space (R space, or space of the distances). The FT of $\chi(k)$ is:

$$FT(R) = \frac{1}{\sqrt{2\pi}} \int_{k_{\min}}^{k_{\max}} k^n \chi(k) e^{i2kR} dk$$

Where k' is the k weighting. The Fourier transform can have different k weightings. This is used to distinguish between high and low Z scatterers around the absorber atom. An element with low mass (like oxygen) will scatter mainly at lower k -values, while an element with high mass (like zinc) will scatter significantly at higher k -values. Therefore, the weighting of the Fourier transformation will emphasize the important scatterer in a specific region. The distances found in the Fourier transformation is about 0.2–0.5 Å shorter than the actual distances due to the energy dependence of the phase factors in the sine function. I focused on X-ray Absorption Spectroscopy (XAS) of highly important metallo-proteins. The project involves the opportunity to explore and develop a powerful spectroscopic technique and to widen my knowledge on metallo-proteins by collaborating with experts on the individual systems. Moreover, XAS has been applied on HsETHE1 and can be performed on ETHE1-like metallo-proteins.

EXAFS data reduction and normalization was carried out using the program KEMP[41] or the program KEMP2, which is under development by Dr. Gerd Wellenreuther.[42] XANES and EXAFS analysis were performed with the programs WinXAS[43], Excurve98[44] and ATHENA.[45] XANES simulation were made with the program FEFF.[46]

1.2.1 Mononuclear [Fe]-hydrogenases

I performed EXAFS and XANES analysis of the protein Hmd from *Methanocaldococcus jannaschii* (jHmd). Hmd are mononuclear-iron hydrogenases ([Fe]-hydrogenases). They represent one of three classes of hydrogenases, not phylogenetically related to each other, but sharing striking similarities.[2,47] The name Hmd stands for H₂-forming methylene-tetrahydromethanopterin (methylene-H₄MPT) dehydrogenase, because its function is the reduction of methenyl-H₄MPT⁺ (acceptor) to methylene-H₄MPT through the transfer of an hydride (Fig. 6 A).[4,48]

In contrast to other hydrogenases, Hmd lacks iron-sulfur clusters and exploits only one metal-ion, which is incorporated in an iron guanylyl pyridone cofactor (FeGP) (Fig. 6 B).[3,49] The cofactor can be extracted, purified and studied separately from the apoprotein, and the active enzyme can be reconstructed by incubation of the isolated

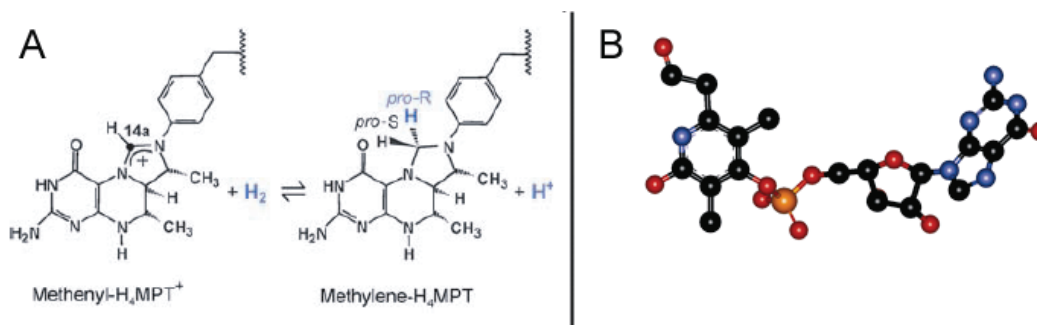


Fig. 6: Hmd hydride acceptor and cofactor.

A) Hydride acceptor: Hmd reversibly reduces methenyl-H₄MPT⁺ (acceptor) to methylene-H₄MPT. B) Guanylyl pyridone cofactor. This cofactor can be extracted from Hmd and studied separately.[3]

cofactor with the apo-form of the enzyme.[3] Due to the presence of a single metal-ion, this enzyme is an ideal target for studying the relationship between electronic structure and hydrogen activation. Our understanding of [Fe]-hydrogenases is still at the beginning. The first biophysical studies on [Fe]-hydrogenases were carried out only recently.[50-53] Infra Red (IR) spectroscopy studies showed that Hmd's iron binds 2 carbon monoxide (CO) molecules and that the enzyme can be inhibited upon binding of an additional CO or a cyanide (CN), while incubated in, respectively CO or CN atmosphere at room temperature.[52] The inhibition by CN is a peculiar characteristic, not common with the other hydrogenases, which are inhibited only by CO. Mössbauer and EPR spectroscopy revealed the presence of a low spin iron with an unclear oxidation state that can be assigned as 0 or 2+ with equal probability.[53] The iron within the extracted cofactor has the same oxidation state. The enzyme is light and oxygen sensitive (UV-A/blue) and the FeGP cofactor is even temperature sensitive.[51] Upon UV-A/blue-light illumination, both CO molecules are irreversibly flashed off from the active site, which results in the loss of the enzyme activity. EXAFS on Hmd from *Methanothermobacter marburgensis* (mHmd) and Hmd from *Methanocaldococcus jannaschii* (jHmd) clearly showed the presence of two COs and sulfur chelating the iron. Besides, the iron site has been modeled with one additional O/N, in case of mHmd, or two additional O/Ns, in case of jHmd and its isolated cofactor. Additional light ligands such as oxygens and nitrogens might have been present as iron chelator, but the strong contribution of the COs (multiple scatterers) and the sulfur (strong scatterer) limited further assumptions and modeling. A XANES study revealed the extraordinary intensity

of Hmd's pre-edge peak, which is unique among iron binding proteins.[50] The structure of the cofactor[49] and the x-ray diffraction structure of apo-Hmd[54] have been available, respectively since 2004 and 2006. Further developments of our scientific knowledge on Hmd are presented in the results chapter dedicated to the mononuclear [Fe]-hydrogenase.

Gain knowledge on the active site of Hmd may lead towards biomimetic methods for efficient generation and utilization of H₂. [55] Therefore, I consider of high interest to shed light on the [Fe]-hydrogenases requirements for H₂ activation and thus on the characteristics of the iron core.

1.2.2 [Cu₂L₂(μ-O)₂]I₂

I collaborate to the characterization of the optically excited state of a bis (μ-oxo)-dicopper(III) species mimicking the potential di-oxo to μ-oxo transition in the tyrosinase (monophenol monooxygenase) active site (Fig. 7 A). Tyrosinase is a wide spread copper-containing enzyme present in plant and animal tissues that catalyzes the production of melanin and other pigments from tyrosine by oxidation.

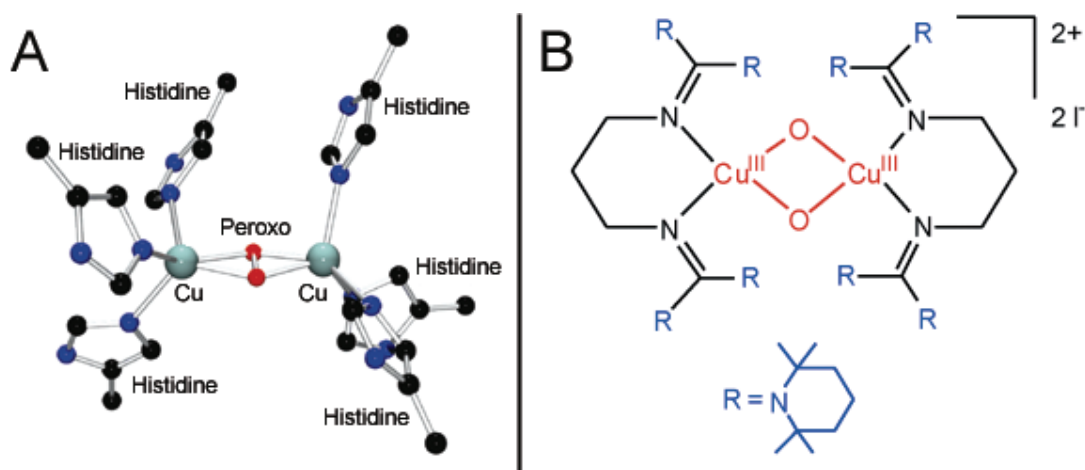


Fig. 7: Tyrosinase metal binding site and Cu-based model complex.

A) Ball and stick representation of the tyrosinase metal binding site: sea green, coppers atoms; red, the oxygens; blue, the nitrogens; black, the carbons. B) First bis(-oxo)dicopper(III) complex mimicking the tyrosinase metal binding site stable at room temperature. [5]

Specific mutations in the tyrosinase active site resulting in impaired tyrosinase

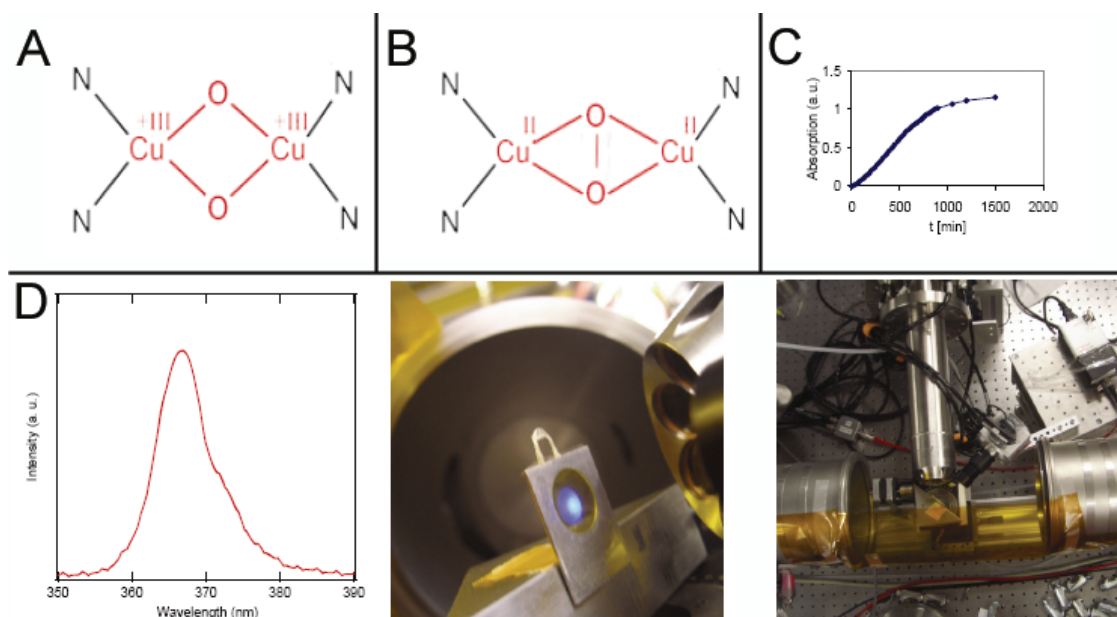


Fig. 8: $[\text{Cu}_2\text{L}_2(\mu\text{-O})_2]\text{I}_2$ formation and pumped-XAS experimental set up.

A) Potential Oxo-form (O-state) and B) Peroxo-form (P-state) of complexes modeling hemocyanin and tyrosinase metal binding sites. C) Formation of $[\text{Cu}_2\text{L}_2(\mu\text{-O})_2]\text{I}_2$ (right) upon oxidation of $[\text{Cu}(\text{L})\text{I}]$ with dioxygen at 25 °C monitored by the absorption intensity for λ_{max} (366 nm). D) Left: spectral distribution of the light emitted by our UV source. Centre: UV-excitation of the sample. Right: setup for the pumped-XAS experiment. The $[\text{Cu}_2\text{L}_2(\mu\text{-O})_2]\text{I}_2$ solution is excited with optics of the UV-source (black). The multi-element fluorescence detector and the safety shield (Kapton, orange) are also shown.

production leads to type I oculocutaneous albinism. This is a hereditary disease that affects one in every 17,000 person.[56] Understanding the requirements of this enzyme for its activity is strictly connected to the understanding of the chemical basis of oculocutaneous albinism, which are related with hematologic-storage disease, susceptibility to skin cancer, and optic neuronal defects, as well. The use of model complexes mimicking the tyrosinase's active metal binding site it can surely be a fruitful bottom-up approach to the problem.

Here, we compare two approaches aimed to structurally characterize such states: we exploited an innovative combination of pumped-XAS and resonant Raman scattering, which allows to efficiently studying the charge-transfer within complexes in their ground and excited state. My contribution consists in the set up and collection of the pumped-XAS data.

The relaxation of excited states into the ground state provides new insights in the dynamics of the systems under study. The dynamics of metal-donor interactions is particularly interesting for the molecular biology and bioinorganic chemistry communities. We focused on a system mimicking the Cu_2O_2 -core in hemocyanin and tyrosinase. These proteins share the binuclear copper binding site, as well as most of the structural features.[57]

In both metallo-proteins, molecular oxygen binds to two copper ions in the side-on peroxo mode (P-state).[58] Complexes modeling these features have the potential to serve as highly specific oxidation catalysts.[59] Typically, these systems are stable at cryogenic temperatures only.[60]

Recently, the first system stabilizing the O-state at room temperature has been presented (Fig. 7 B).[5] It is formed within several hours by the reaction of molecular oxygen with the Cu(I)-complex, Cu(L)I with $\text{L} = \text{Bis}(\text{guanidin}) \text{ } N^1, N^3 \text{-Bis}[\text{bis}(2,2,6,6\text{-tetramethylpiperidin-1-yl)methylen}] \text{propan-1,3-diamin} = (\text{B}(\text{TMPip})\text{G}_2\text{p})$, as visualized by the increasing absorption at 366 nm (Fig. 8 A-C). Here, we compare strategies to characterize this excited state, either by optical-pumping (Fig. 8 D; optical source with λ_{max} at 365nm, in line with the Raman active transition), or by resonance Raman spectroscopy.

1.2.3 The ATP binding cassette protein ABCE1

ABCE1 (ATP-binding cassette, sub-family E (OABP), member) is one of the most conserved proteins in the evolution of eukaryotes. Initially, the protein was identified as the RNase L inhibitor in the innate immune response and called RL11.[61] It was subsequently shown that the assembly of the HIV-1 capsids requires ABCE1 in a strictly ATP-dependent manner.[62] Recently, an even more fundamental and general role was proposed in the process of translation initiation and ribosome biosynthesis.[63-66] ABCE1 was found to interact with translation initiation factors, such as eIF2, eIF3, eIF5, the 40S ribosomal subunit and several ribosomal RNAs. Depletion of the protein causes defects in the assembly of the pre-initiation complex, in rRNA processing, and in the accumulation of ribosomal subunits inside the nucleus. Thus, ABCE1 has a fundamental

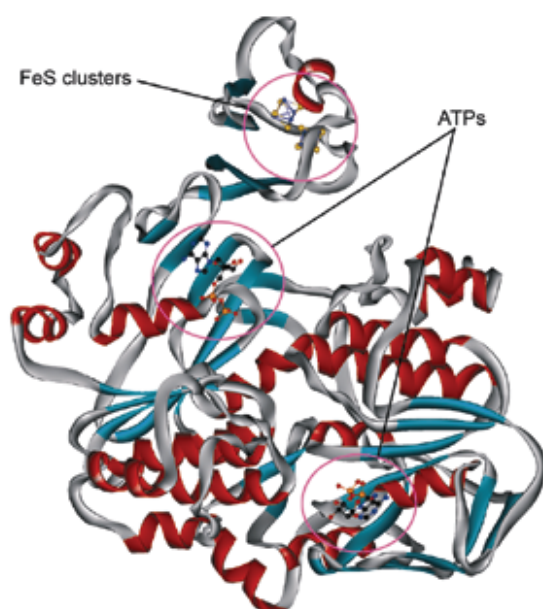


Fig. 9: X-ray diffraction structure of the protein ABCE1 from *Pyrococcus abyssi* (PDB: BK7).

The protein is represented as cartoon: red, α -helices; marine-green, β -sheets; grey, loops and linker regions. In the figure, the iron-sulfur clusters and the ATP molecules bound to the protein are highlighted in scaled ball and sticks representation: black, carbons; red, oxygens; blue, nitrogens; violet, iron; yellow, sulfur; orange, phosphorus.

cluster was not available. Thus, ABCE1 is an extremely interesting target and I collaborate to its characterization by XAS analysis. Within this thesis I present the XAS work I carried on ABCE1 from *Sulfolobus solfataricus*.^[67] Recently, the X-ray structure of the complete ABCE1 protein from *Pyrococcus abyssi* at the nominal resolution of 2.8 Å has been reported (Protein Data Bank (PDB): 3BK7) (Fig. 9)

1.3 Aim of the projects

The projects aim to characterize biochemically and biophysically highly interesting metalloproteins. A wide spectrum of techniques has been applied on the protein ETHE1, while XAS analysis has been applied on all the other studied samples (proteins and bioinorganic complexes).

role in translation initiation, ribosome biosynthesis and in HIV-1 capsid assembly. ABCE1 is a unique ATP Binding Cassette (ABC) protein because it bears an N-terminal consensus sequence for the binding of an iron-sulfur cluster, which is an uncommon feature for ABC proteins. This N-terminal region includes eight conserved cysteine residues with the CX4CX3CX3CPX_nCX2CX2CX3P consensus sequence.

A specific incorporation of iron and the interaction with members of the Fe-S cluster assembly machinery have been demonstrated.^[63] However, information regarding the type and structural organization of the Fe-S

1.3.1 ETHE1 project

*Hs*ETHE1 is a non-heme mononuclear-iron sulfur dioxygenase fundamental for proper sulfur detoxification in metazoan. It has been found overexpressed in a vast percentage of patients affected by HCC and it is able to inhibit p53 dependent apoptosis by two ways. Moreover, it is strictly involved in EE, a severe recessive metabolic disease. For the above reasons it is an extremely interesting target. The project aims to characterize biochemically and biophysically ETHE1 from *Homo sapiens*. Gain knowledge about this enzyme may lead to understand how to keep ETHE1-related HCCs under control and to find a specific therapy for EE. In order to gain knowledge about the physicochemical properties of *Hs*ETHE1, with particular focus on its active metallo binding site, the protein has been investigated by several techniques, such as: X-ray Absorption Spectroscopy (XAS), Small Angle X-ray Scattering (SAX), Total X-ray Reflection Fluorescence (TXRF), Mass Spectrometry (MS), Isothermal Titration Calorimetry (ITC), substrate screening, enzyme kinetics, crosslinking, Circular Dichroism (CD), Light Scattering techniques (DLS, SLS), Electron Paramagnetic Resonance (EPR), Mössbauer spectroscopy, site directed mutagenesis, surface entropy reduction.

1.3.2 XAS project

The XAS projects aim to the characterization of highly interesting metalloproteins and bioinorganic complexes. The architecture and the electronic structure of the metal centers have been investigated by X-ray Absorption Spectroscopy. The proteins were probed at synchrotron XAS beamlines and the collected data were primarily processed for background subtraction, data reduction and normalization. Successively, EXAFS and/or XANES analysis were applied. XAS gave us information on the metal-center geometry, oxidation state, type, number and distances of the metal ligands and disorder level of individual components of the system. The acquired knowledge may be fruitfully applied to clean energy technology development (hydrogenases; low cost H₂ production), understand the nature of reactions involving charge transfer processes (tyrosinase model systems) and inhibit HIV capsid assembly (ABCE1).

2 Materials and methods

The materials and methods section has been divided in:

- Cloning
- Protein expression
- Protein purification
- Protein characterization

Herein, I present separately the material used and the methods applied, except for the protein characterization chapter, where the exploited apparatus and the modality of their usage are treated together. Moreover, on the behalf of the text fluency I created an appendix (Appendix A) containing a list of the used material with the relative suppliers.

2.1 Cloning

The cloning procedure covers the steps from the amplification of the source DNA till the preparation of the expression clones. The general practice has been the following: the source gene is amplified by Polymerase Chain Reaction (PCR) using specific primers bearing sequences designed for subsequent insertion in specific plasmid vectors. The destination vector is amplified with high copy number *E. coli* strains and purified. The PCR products are then purified from solution or from agarose gel. The purified PCR products (pPCRp) and the destination vectors are cut with opportune restriction enzymes. At this point, in case of standard cloning, the digested pPCRp and the plasmids are purified from restriction enzymes and they are legated together using a ligase enzyme. In the case of Ligase Independent Cloning (LIC), the pPCRp and the vectors are treated before with T4-polymerase and after with a phosphatase in specific reaction mixtures, and then mixed. In each case, the ligation products are used to transform *E. coli* strains. Usually, the first transformation is done using strains able to propagate plasmids in high copy number. The transformed cells are let growth and the cultures are plated on agar and incubated over night. Once obtained the transformants, some colonies are picked

and checked for the presence of the insert with different techniques such colony PCR, or with alternative restriction enzyme digestion followed by Agarose Gel Electrophoresis (AGE). The integrity of the cloned gene sequence is then checked by sequencing. The final vectors are amplified and purified again and the DNA is used to transform *E. coli* strains optimized for expression. The very same procedure is applied to find the final expressing clones bearing the vector with the expected sequence in the right position and orientation. All the desired clones are used to grow minicultures from which glycerol stocks are prepared and kept at -80°C.

2.1.1 Material for cloning

The material for cloning derived from internal sources or from the following companies: ImaGenes, New England BioLabs, Finnzyme, Fermentas, BioRad, Sigma Aldrich, Stratagene, Macherey Nagel, and Qiagen (see Appendix A for details).

The sequence of HsETHE1 cDNA:

Homo sapiens ETHE1 ; Entrez Nucleotide NM_014297;

```
atggcggaggctgtactgagggctgccccggcggcagctgagccagcgcggcgggctctggagccccatcct
cctgcggcagatgttcgagcctgtgagctgcaccttcacgtacctgctgggtgacagagaggtcccgggagg
ccgttctgatcgaccagtcctggaaacagcgcctcgggatgccagctgatcaaggagctggggctgcgg
ctgctctatgctgtgaatacccactgccacgggaccacattacaggctcggggctgctccgttccctcct
ccctggctgccagctctgtcatctcccgccttagtggggcccaggctgacttacacattgaggatggagact
ccatccgcttcgggcgcttcgcggttgagaccagggccagccctggccacaccccaggctgtgtcaccttc
gtcctgaatgaccacagcatggccttcactggagatgcctgttgatccgtgggtgtgggcggacagactt
ccagcaaggctgtgccaagaccttgtaccactcgggtccatgaaaagatcttcacacttccaggagactgtc
tgatctaccctgctcacgattaccatgggttcacagtgtccaccgtggaggaggagaggactctgaacctt
cggctcacctcagctgtgaggagtttgtcaaaatcatgggcaacctgaacttgctaaacctcagcagat
agactttgctgttccagccaacatgcgctgtgggggtgcagacacccactgctga
```

2.1.1.1 Primers

The primers were chosen in order to clone the wild type form of *HsETHE1* and a number of truncated forms: *In vivo*, the enzyme is directed to the mitochondrion through an N-terminal tag and then a short peptide at the terminus is cleaved.[10] This cleavage is predicted to create the active for of the enzyme. The site where the cut takes place was

not clear when most of the clones were made, but estimated to be within the first 20 aminoacids. For example the TargetP (<http://www.cbs.dtu.dk/services/TargetP/>) server predicted the truncation of the first 11 aa, while MITOPROT(<http://ihg.gsf.de/ihg/mitoprot.html>) predicted the truncation after the first 21 aa. Moreover, exploiting predictors available on the web (such as PONDR, DisEMBL, RONN, DISOPRED2, GlobProt and DRIP-PRED), I have found that the protein is potentially disordered at the N-terminal part till aa 24 and at the C-terminal part in correspondence of the last 4 aa.

Primers for ligase dependent cloning

Primers for wt-HsETHE1 cloning

Forward primer used for the insertion of wild type *HsETHE1* (wt-*HsETHE1*) in the pETM-11 or pETM-13 vectors:

5' -ctgacagta|catgtcg^{gcg}gaggctgtactgagg-3'

- = restriction site (***PciI***); *PciI* produces the same sticky ends as *NcoI*, which is the only restriction site available for ligation of the 5' end of the DNA to the 3' available end at the multiple cloning site of the vector. *NcoI* cuts in the *ETHE1* gene)

^{gcg} = first original protein codon: the previous atg and tcg codons are respectively the starting codon and a codon codifying for a serine. The latter was not present in the original sequence and is an obliged construct artifact. In fact, a codon starting with a "t" is necessary because of the specific restriction site used.

Reverse primer for the insertion of wt- *HsETHE1* in the pETM-11 or pETM-13 vectors:

Stop
| |

5' -ctgacagtc|tcgag^{ctatcaggc}agtgggtgtctgcac-3'

- = restriction site (***XhoI***)

^{ctatcaggc} = original protein termination codon

Reverse primer without stop codon for the insertion of wt- *HsETHE1* in pETM-13 vector and fuse the gene with a C-terminal histidine tag:

5' -ctgacagt**c** | **tcgagggc** agtggggtgtctgcacccc-3'

- = restriction site (*Xho*1)

█ = original protein codon

Primers for Δ14-HsETHE1 cloning:

Forward primer used for the insertion of *HsETHE1* lacking the first 14 aminoacids (Δ14-*HsETHE1*) in the pETM-11 or pETM-13 vectors:

5' -ctgccatga | **catgtctcag** cgcgggcggtctgga-3'

- = restriction site (*Pci*I);

█ = first original protein codon: the previous atg and tct codons are respectively the starting codon and a codon codifying for a serine. The latter was not present in the original sequence and is a construct artifact.

The reverse primer is the same as for wt-*HsETHE1*.

Primers for Δ24-HsETHE1 cloning:

Forward primer used for the insertion of *HsETHE1* lacking the first 24 aminoacids (Δ24-*HsETHE1*) in the pETM-11 or pETM-13 vectors:

5' -ctgccatga | **catgttgctg** cggcagatgttcgagcct-3'

- = restriction site (*Pci*I);

■ = original protein codon: the previous atg and ttg codons are respectively the starting codon and a codon codifying for a leucine. The latter is the same aminoacid present in the original sequence. Therefore the real shortening is of 23 aa.

The reverse primer is the same as for wt-*HsETHE1*.

Primers for ligase independent cloning

LIC primers should be like the following:

Forward primer: 5'-cagggcgccatg-3' -gene of interest

Reverse primer: 5'-gacccgacgcggtta-3' -gene of interest (rev. comp.)

The complementary overhangs are shown in red. The start codon (forward primer) and the stop codon (reverse primer) are underlined.

Primers for $\Delta 14$ -*HsETHE1*- $\Delta 4$ (14E4) cloning

N.B.: the resulting PCR products don't need to be digested by restriction enzymes, according to the protocol for LIC.

Forward primer used for the insertion of *HsETHE1* lacking the first 14 aminoacids and the last 4 aa ($\Delta 14$ -*HsETHE1*- $\Delta 4$; 14E4) in the pETM-11_LIC vector:

5' -cagggcgccatgcagcgcggcgggtctgga-3'

Reverse primer used for the insertion of *HsETHE1* lacking the first 14 aminoacids and the last 4 aa ($\Delta 14$ -*HsETHE1*- $\Delta 4$; 14E4) in the pETM-11_LIC vector:

5' -gacccgacgcggttattactgcacccacagcgcattggt-3'

Primers for $\Delta 19$ -*HsETHE1*- $\Delta 4$ (19E4) cloning

Materials and methods

Forward primer used for the insertion of *HsETHE1* lacking the first 19 aminoacids and the last 4 aa ($\Delta 19$ -*HsETHE1*- $\Delta 4$; 19E4) in the pETM-11_LIC and pETM-20 vectors:

5' -cagggcgccatgggagcccccatcctcctgcgg-3'

The reverse primer is the same as for $\Delta 14$ -*HsETHE1*- $\Delta 4$.

*Primers for $\Delta 7$ -*HsETHE1*- $\Delta 4$ (7E4) cloning*

Forward primer used for the insertion of *HsETHE1* lacking the first 7 aminoacids and the last 4 aa ($\Delta 7$ -*HsETHE1*- $\Delta 4$; 7E4) in the pETM-11_LIC vector:

5' -cagggcgccatgggtcgcccggcggcagctg-3'

The reverse primer is the same as for $\Delta 14$ -*HsETHE1*- $\Delta 4$.

Site directed mutagenesis (sdm)

Three primers were designed for the creation of four mutants (MutA, B, C).

Below the *HsETHE1* cDNA and aminoacid sequences are respectively shown. The bases target of mutation are highlighted in red:

```
1      10      20      30      40      50      60      70      80
|      |      |      |      |      |      |      |      |
atggcggaggctgtactgagggtcgccccggcggcagctgagccagcgcggcggtctggagcccccatcctcctgcggca

81     90     100    110    120    130    140    150    160
|      |      |      |      |      |      |      |      |
gatgttcgagcctgtgagctgcaccttcacgtacctgctgggtgacagagaggtcccgggagggccgttctgatcgaccag

161    170    180    190    200    210    220    230    240
|      |      |      |      |      |      |      |      |
tcctggaaacagcgcctcggggatgccagctgatcaaggagctggggctgcggctgctctatgctgtgaataccactgc

241    250    260    270    280    290    300    310    320
|      |      |      |      |      |      |      |      |
cacgcgaccacattacaggtcggggctgctccgttccctcctcctggctgccagtctgtcatctccgccttagtgg
```

321 330 340 350 360 370 380 390 400
 | | | | | | | | |
 ggcccaggctgacttacacattgaggatggagactccatccgcttcggcgcttcgcggttgagaccaggccagccctg

401 410 420 430 440 450 460 470 480
 | | | | | | | | |
 gccacaccccaggctgtgtcaccttcgtcctgaatgaccacagcatggccttcactggagatgcctgttgatccgtggg

481 490 500 510 520 530 540 550 560
 | | | | | | | | |
 tgtggggggacagacttcagcaaggctgtgccaagacctgtaccactcggccatgaaaagatcttcacactccagg

561 570 580 590 600 610 620 630 640
 | | | | | | | | |
 agactgtctgatctaccctgctcacgattaccatgggttcacagtgtccaccgtggaggaggaggactctgaaccctc

641 650 660 670 680 690 700 710 720
 | | | | | | | | |
 ggctcaccctcagctgtgaggagtttgtcaaaatcatgggcaacctgaacttgccctaacctcagcagatagactttgct

721 730 740 750 760 765
 | | | | | |
 gttccagccaacatgcgctgtgggggtgcagacacccactgcctga

1 10 20 30 40 50 60
 | | | | | | |
 MAEAVLRVARRQLSQRGGSGAPIILLRQMFEPVSCFTFYLLGDR**E**SREAVLIDPVLETAPR

61 70 80 90 100 110 120
 | | | | | | |
 DAQLI**KE**LGLRLLYAVNTHCHADHITGSGLLRSLLPQCQSVISRLSGAQADLHIEDGDSI

121 130 140 150 160 170 180
 | | | | | | |
 RFGRFALETRASPGHTPGCVTFVLNDHSMFAFTGDALLIRGCGRTDFQQGCAKTLYHSVHE

181 190 200 210 220 230 240
 | | | | | | |
 KIFTLPGDCLIYPADHYHGFTVSTV**EE**ERTLNPRLTLSCEEFVKIMGNLNLPKPQQIDFA

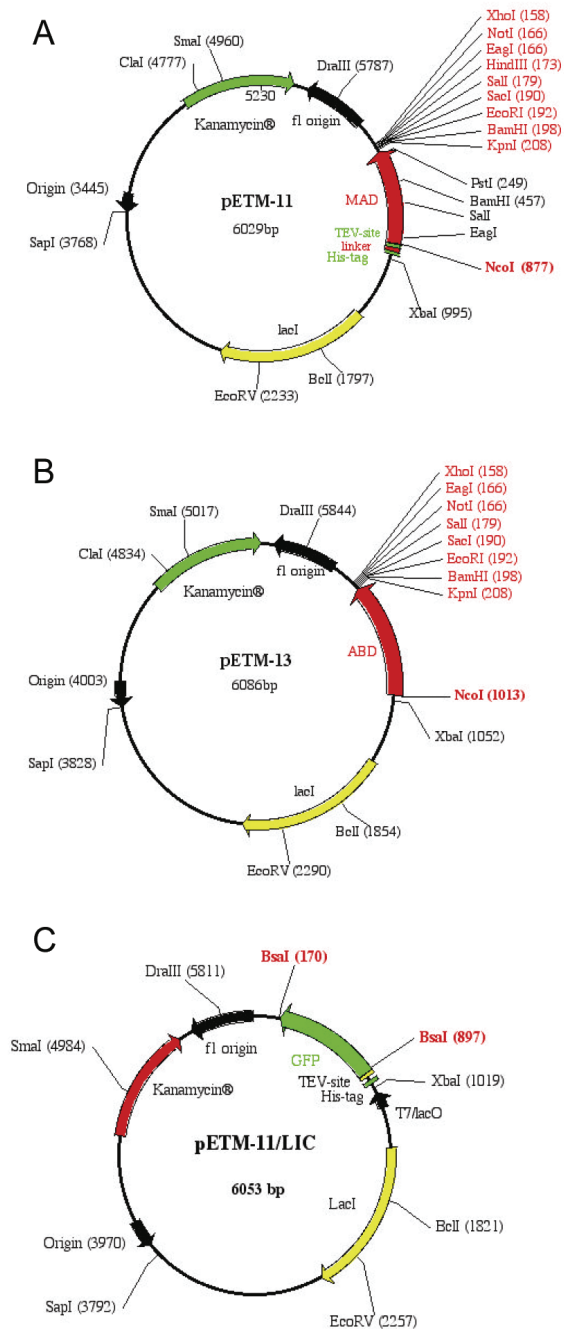


Fig. 10: HsETHE1 cloning vectors.

Maps of the three plasmid-vectors used for cloning and expression of the HsETHE1 constructs. A) pETM11. B) pETM13. C) pETM11_LIC.

2.1.1.2 Kits used for cloning

During cloning commercially available kits were used for DNA amplification, purification and mutagenesis. The kits were purchased from Nagel, Qiagen or Stratagene (see Appendix A for details).

2.1.1.3 Plasmid vectors

All the plasmid vectors were provided by Arie Geerlof from an internal library. The vectors are the following: pETM-11 (can fuse a 6-histidine tag and a Tobacco Etch Virus (TEV) protease cleavage site at the N-terminal or at the C-terminal), pETM-13 (can fuse a 6-histidine tag at the C-terminal), pETM-11_LIC (can fuse a 6-histidine tag and a TEV protease cleavage site at the N-terminal or at the C-terminal), pETM-20_LIC (Fig. 10).

2.1.1.4 Bacterial Strains

The bacterial strains used were mainly prepared internally by lab members. The cells were initially propagated and then made competent through a chemical procedure. The

purchased cells are the Top10 (Invitrogen) and the Solopack (Invitrogen). The strains used are: DH5 α , Top10, Solopack, Nova Blue, BL21(DE3), BL21(DE3)-pLys, BL21(DE3)-Star, BL21(DE3)-Rosetta, BL21(DE3)-RIL, Origami.

2.1.1.5 Agarose Gel Electrophoresis (AGE) apparatus

The AGE devices used were or the BioRad Power PAC 300 or the Consort EV243.

2.1.1.6 Polymerase Chain Reaction (PCR) apparatus

The PCR apparatus used were or the Mastercycle gradient or the Mastercycle personal purchased from Eppendorf AG.

2.1.2 Methods for cloning

This section treats the protocols used during cloning. The preparation of all the reactions is ideally performed under sterile conditions. The water used for cloning was sterilized milliQ water. All the media were sterilized before usage.

2.1.2.1 Gene amplification

*Hs*ETHE1 gene was amplified by growing cultures of the bacterial clones transformed with a vector containing the cDNA sequence of the protein and/or by PCR.

2.1.2.1.1 Amplification by cell culture

At the very beginning, the DH10B TonA *E. coli* cells, containing the pCMV-SPORT6 vector with the *Homo sapiens* ETHE1 cDNA insertion, were grown over night (o/n) at 37°C, in 5 ml LB cultures in presence of Ampicillin (100mg/mL: 1000X), at 200 rpm.

After each transformation, some randomly picked colonies were grown, amplifying the inner plasmid (o/n at 37°C, in 5 ml LB cultures in presence of the proper antibiotic, at 200 rpm). The extracted DNA was needed to check the presence of the insert by restriction enzyme digestion test, for sequencing, to have positive vector ready for new transformations, and for storage.

2.1.2.1.2 Amplification by PCR

Every time the insertion of *HsETHE1* cDNA in a vector was necessary, the DNA has been amplified exploiting specific primers.

The protocol used for PCR amplification can vary in dependence of the annealing and melting temperatures of the primers and of the level of stringency I wanted to reach. In general the protocol has been the following:

Mix:

- Polymerase buffer-10X
- dNTPs 50/200 μ M final concentration
- Primers 1 μ M final concentration
- Template: 1/20 ng/ μ L
- Polymerase 0.5/1 μ L
- Autoclaved milliQ water

PCR program:

1. 94°C 5'
 2. 94°C 30''
 3. 50/65°C 30/45'' (dependent on the specific annealing temperature of the primers)
 4. 72°C 30''/1' per Kb (it is dependent on the polymerase)
- 30 x steps 2-4
5. 72°C 7'
 6. 4°C ∞

At this stage the DNA may be purified directly from the solution or from gel after AGE. Store at -20°C.

Le positive controls are made using a known DNA template and primers known to be working.

For the negative controls no DNA template is added to the PCR reaction mixture.

2.1.2.2 Agarose Gel Electrophoresis (AGE)

AGE standard procedure:

1. Mix AGE commercial buffer (10x) with agarose 0.5/2% (long plasmids/PCRp).
2. Boil the solution till complete solubilization of the agarose.
3. Pour the hot mixture in the gel chamber.
4. Add ethidium bromide (1:25000/50000) and mixed.
5. Once polymerized I add AGE buffer till all the gel is covered.
6. Load samples (1-20 μ L) and one or more DNA ladders (5 μ L).
7. Run the gel applying a constant voltage chosen within the range of 80/120 milli volts.
8. Let run for 30'/1h.

2.1.2.3 DNA purification

The DNA was purified with commercially available kits and kept at -20°C: plasmid extraction, PCR and gel extraction purification kits. As protocol, I followed the manufacturer instructions.

2.1.2.4 DNA digestion

The digestion of the DNA with restriction endonucleases has been done in the following cases:

- To create complementary ends for ligation. The standard ligation plasmids (within the MCS (Multiple Cloning Site)) and the PCRp have been digested (*PciI*, *XhoI* enzymes).
- To cut the plasmid used for LIC (*BsaI* enzyme). During LIC only the plasmids needs to be cleaved with restriction enzymes.
- To check for the presence of the insert after cloning (*PciI*, *XhoI*, *NcoI*, *XbaI*). The construct DNA has been digested in order to create fragments with expected length. On the basis of the obtained fragments it is possible to sort out if whether an insert of proper length is present or not.

- To cut away the host derived DNA strand after amplification for site directed mutagenesis (*DpnI*). During SDM, the entire vector is amplified by PCR, creating a construct with one strand bearing the specific mutations and one coming from the host, used as template and not bearing the mutations. The host strand possesses methylations on specific adenine nucleotides and it is recognized and cleaved by the restriction endonuclease *DpnI*.

Restriction enzyme digestion protocol

Mix:

- Reaction buffer-10X
- Restriction enzymes-20X
- DNA material (up to μgs)

Procedure:

- 4h at 37°C
- Heat inactivation: 20' at 70°C

At this stage the DNA may be purified with PCR purification kit.

Storage at -20°C.

2.1.2.5 DNA ligation

The ligation of DNA has been achieved by two different procedures. One technique is based on the use of the ligase enzyme. The other system takes advantage of the creation of special complementary overhangs in the vector and insert. These overhanging sticky ends are long enough for the very specific, enzyme-free annealing of the two DNA.

2.1.2.5.1 Ligase dependent cloning

During ligase dependent cloning the acceptor linearized and successively purified (from gel or solution) vector is linked to the digested and purified (from gel or solution) gene of interest through the joining of complementary blunt or sticky ends present on both the

vector and the gene. The ligase is able to create a new covalent bond between the phosphate group present on a 5' terminus of one DNA molecule and the 3' carbon of the sugar ring of the 3' terminus. During this work I used two different types of ligases. One is the standard T4 DNA ligase and the other enzyme is called "quick" ligase and is an engineered enzyme able to ligate DNA with faster catalysis than the standard T4 DNA ligase.

The protocol used for standard ligation is the following:

Mix:

- Ligase buffer-10X (T4 DNA ligase) /-2X (quick ligase)
- Ligase 1 μ L
- Linearized vector ~50ng
- Insert: ng insert = ng vector x bp insert/ bp vector (usually, insert:vector = 2/3:1)

Procedure:

- 4h to o/n at 16°C (T4 DNA ligase) / 5' 25°C (quick ligase)
- Heat inactivation: 15' at 70°C (T4 DNA ligase) / 15' at 65°C (quick ligase)

At this stage the DNA may be purified with PCR purification kit.

Storage at -20°C.

2.1.2.5.2 Ligase Independent Cloning (LIC)

During LIC no enzyme is needed for ligation. The vector is treated with the restriction enzyme BsaI. The vector is then dephosphorilated in order to avoid self annealing. Afterwards, or the vector is purified from gel, avoiding the presence of not digested DNA, or is directly treated with T4 DNA polymerase in the presence of dTTP. Because of the 3'--> 5' activity of the polymerase, the bases are removed from both 3' ends until the first thymidine (T) residue is reached. This leads to two specific overhangs in the LIC vector of 10 and 12 bases, respectively, which allow the specific, ligase-independent annealing reaction. In the mean time the pure insert PCR product is treated with T4 DNA polymerase in the presence of dATP. Finally, the T4 polymerase treated

insert and vector are mixed in an annealing reaction and incubated for some minutes. The mixture is then directly used for transformation.

Vector digestion with BsaI

Mix:

- *BsaI* buffer-10X
- LIC vector DNA 5 µg (for more than 20 reactions)
- *BsaI* (10 units/µL) 20X
- Add sterile water up to the final volume

Procedure:

- 1h at 50°C
- Heat inactivation: for 20' at 70°C

Vector dephosphorilation

Mix:

- Vector BsaI-digested reaction mix 50 µL
- Phoshatase buffer-10X
- Antarctic phosphatase (5 units/µL) 30X
- Add sterile water up to the final volume

Procedure:

- 1h at 42°C
- Heat inactivation: for 5' at 70°C

At this step the vector may be purified from agarose gel.

Storage at -20°C.

T4 DNA polymerase treatment of the vector

Mix:

- T4 DNA polymerase buffer-10X
- *Bsa*I-digested LIC vector 600 ng (for ~20 annealing reactions)
- dTTP (100 mM) 40X
- DTT (100 mM) 20X
- BSA-100X
- T4 DNA polymerase (3 units/ μ l) 50X
- Add sterile water up to the final volume

Procedure:

- 30' at 22°C/room temperature
- Heat inactivation: for 20' at 75°C

The LIC prepared vector solution obtained in this way can be used directly in the annealing reaction or purified with a PCR purification kit. Take care that the final vector concentration is 10-20 ng/ μ L.

Storage at -20°C.

T4 DNA polymerase treatment of the insert

Mix:

- T4 DNA polymerase buffer-10X
- PCR product 0.2 pmol (for ~10 annealing reactions)

The DNA concentration can be determined using the absorbance at 260 nm (assuming $A_{260} = 1$ is 50 ng/ μ l). To calculate the DNA concentration in pmol/ μ l the following equation has been applied:

number of base pairs x 0.65 = ng/pmol

- dATP (100 mM) 0.5 μ L
- DTT (100 mM) 20X
- BSA 100X
- T4 DNA polymerase (3 units/ μ l) 50X
- Add sterile water up to the final volume

Procedure:

- 30' at 22°C/room temperature
- Heat inactivation: 20' at 75°C

At this step the insert DNA may be purified from gel or from solution with a PCR purification kit.

Storage at -20°C.

Annealing of the insert and LIC-vector

Mix:

- Insert DNA 0.02 pmol
- LIC prepared vector DNA 25-50 ng

The control ligation is carried out with sterile water instead of the insert.

The amount of LIC prepared vector DNA needed depends on the size of the vector and the molar ration of vector to insert (normally 1:2 or 1:3 is used).

Procedure:

- 5' at 22°C/room temperature
- EDTA (25 mM) 1 μ L
- Mix gently by stirring the solution with the tip

- 5 at 22°C/or room temperature

2.1.2.6 Transformation of *Escherichia coli* strains

The transformations have been carried out using a standard protocol:

- Thaw the appropriate amount (~50/200 µL reaction) of competent cells on ice.
- Transfer 5-100 ngs of the vector DNA to a 1.5-ml microfuge tube and incubate on ice for at least 5'.
- Add 50/100 µL aliquots of competent cells.
- Incubate the tubes for 30' on ice.
- Heat shock the cells for 45'' at 42°C.
- Place the tubes immediately on ice and incubate for at least 2'.
- Add 200/1000 µL SOC or LB media to each tube and incubate for 1 hour at 37°C at 200 rpm in a shaker/incubator.
- Spin for 1 min at 5,000 rpm in a microfuge centrifuge.
- Remove 3/4 of the supernatant and resuspend the cells in the remaining medium.
- Plate out the cell suspension on a LB agar plate containing the proper antibiotics.
- Incubate the plates overnight at 37°C.

The positive control is the transformation of an aliquot of competent cells with a known vector bearing the same resistance.

The negative control is an LB-agar plate with not transformed competent cells, which followed the same transformation procedure without the addition of the vector DNA.

2.1.2.7 Clones selection

After successful transformation of a host with a new prepared construct, we can be sure that those cells have our vector inside, but the colonies needs to be checked for the presence of the wanted insert into the internalized plasmid. Two methods have been applied for checking the presence of the insert. One method exploits restriction enzyme digestion, the other is a technique called colony PCR.

Colony test by restriction endonucleases

1. Pick some colonies and plate them on an opportunely gridded agar dish containing the appropriate antibiotic. Each colony must be placed in its own slot. The plate is incubated o/n at 37°C. This ensures to possess not only the vectors of potential positive colonies, but also the clones them self.
2. At the same time, some cells of each colony are used for inoculating a 10ml LB culture. The cultures are grown o/n at 37°C, at 200 rpm, in the presence of the proper antibiotics. Before the cultures reach an Optical Density at 600 nm (OD₆₀₀) of 1 an aliquot can be used for preparing a glycerol stock that may be kept in case of positivity of the tested colony.
3. The day after, the plasmids of each clone culture are extracted with a plasmid extraction kit.
4. Part of the extracted DNA is digested with opportunely chosen restriction enzymes.
5. The resulting DNA is then checked by AGE for presence of DNA fragments of the expected size.
6. Keep the extracted DNA of the positive colonies.

Colony test by colony PCR

1. Prepare a PCR reaction mixture of opportune volume without polymerase. The primers used for the colony PCR are a primer used for amplify the gene of interest and a standard primer which is flanking the cloning site of the vector. Usually these primers are the forward primer of the insert and the reverse T7 primer. In this way we can be confident that if we detect a DNA fragment corresponding to our insert, this comes from the vector. This is particularly useful in the case one treats genes coming from common species like human. In fact, there can always be some DNA contamination from external sources.
2. Divide the master mix in as many aliquots as the number of colony to test, plus 2 aliquots for positive and negative controls.
3. Pick some colonies and plate them on an opportunely gridded agar dish containing the appropriate antibiotic. Each colony must be placed in its own slot.

The plate is incubated o/n at 37°C. This ensures to possess not only the vectors of potential positive colonies, but also the clones them self.

4. At the same time, some cells of each colony are used for inoculating a PCR reaction mixture.
5. The polymerase is added. The Taq polymerase is used because in this phase we don't care much about the fidelity of the enzyme (proofreading activity) and the Taq polymerase doesn't have proofreading activity and it is cheap.
6. The amplified DNA is then checked by AGE for the presence of the insert.
7. Use the positive colonies previously plated on a grated LB-agar dish to produce small LB cultures (~5/10mL). The cultures are grown o/n at 37°C in the presence of the proper antibiotics, at 200 rpm. Before the cultures reach an Optical Density at 600 nm (OD₆₀₀) of 1 an aliquot can be used for preparing a glycerol stock that may be kept in case of positivity of the tested colony.
8. The day after, the constructs of each clone culture are extracted with a plasmid extraction kit.
9. Keep the extracted DNA of the positive colonies.

2.1.2.8 Sequencing

The sequencings have been carried out by the company Eurofins MWG Operon. For sequencing 1µg of dried out DNA has been used for each sequencing (1 direction, using 1 primer). In order to cover all the sequence of the gene, both the forward and reverse standard T7 primers were exploited. The clones bearing the construct with the expected sequence are kept. The others are discarded together with the relative extracted DNA and glycerol stocks.

2.1.2.9 Clones storage

The clones were stored in glycerol stocks, which are used to preserve a ready to use clone. The stocks are stored at -80°C.

Procedure:

- Prepare an autoclaved 70% glycerol solution

Add 300 μ L of a growing culture to 700 μ L of the 70% glycerol solution

- Mix and keep at -80°C

2.2 Protein expression

Protein expression is the key step for protein production. During this work the proteins were expressed in *E. coli* strains (BL21 (DE3)-like strains). The procedure I used for the expression of HsETHE1 consist in inoculate a small amount of LB medium (20-100 mL) with the *E.coli* clone expressing the protein of interest and let it grow over night at 37°C . The obtained procedure is used to set up a large scale culture (1-6 liters). The cells are grown at 37°C for 3-5 hours and then the expression of the protein is induced. The induction can be done upon chemical addition (IPTG) or it is self-induced in the medium by chemical depletion (glucose). The protein is expressed for about 20 hours before cell harvesting.

2.2.1 Materials for Protein expression

The material for protein expression has been bought from the following companies: Carl-ROTH, NALGENE, BRAND, Sigma Aldrich, Schott Duran, Eppendorf, Infors, Riedel Haën (see Appendix A for details).

2.2.2 Methods for protein expression

This section treats the protocols used during protein expression. The preparation of all the cell cultures is ideally carried on under sterile conditions. The water used was sterilized milliQ water. All the media were sterilized before usage.

2.2.2.1 Protein expression in Luria-Bertani medium

LB medium has been exploited for:

- Cell cultures (20/100 mL) used to inoculate large scale expression cultures (1/6 L): pre-cultures.
- Protein expression and solubility tests (10/50 mL): to check the protein expression levels and confinement in the host. The cells are disrupted, the

soluble fraction is separated from the insoluble fraction and the two components are checked by PAGE to evaluate expression level and solubility. The overexpressed protein can be found or in the cytoplasm, or in the inclusion bodies, or in a combination of both. The inclusion bodies are biological-membrane based confinement compartments where the overexpressed protein accumulates when poorly soluble or toxic for the host. The expression levels and solubility may be varied by:

- changing expression vector
- changing the gene of interest construct
- varying the temperature at which the protein is expressed
- varying the IPTG concentration

Mix:

- 20 g/L LB
- Antibiotics: *e.g.* ampicillin (100 mg/mL: 1000X); kanamycin (100 mg/mL: 2000X); chloramphenicol (34 mg/mL:1000X).
- Expressing clone cells: from glycerol stock (5/10 μ L) (pre-cultures) or directly from cells picked up from a colony grown on agar-plate solid medium (expression test cultures).

Procedure:

- Grow the culture o/n at 37°C, 200 rpm
- In the case of the expression test cultures, IPTG (0.1/1 mM final concentration) is added at an OD₆₀₀ of ~0.6 in order to induce the T7-promoter-dependent expression of the heterologue protein. The culture is then left o/n at 37°C, 200 rpm

2.2.2.2 Protein expression in ultra rich Auto-Inducing Medium (AIM)

AIM has been exploited for large scale expressing cultures. The ultra rich AIM used during this work is called ZYP.

Mix:

- ZY (for 1L ZYP) (autoclaved)
 - Tryptone 10 g
 - Yeast extract 5 g
 - H₂O 925 mL
- NPS 20X (autoclaved; pH 6.75)
 - (NH₄)SO₄ 0,5 M
 - KH₂PO₄ 1 M
 - Na₂HPO₄ 1 M
- 5052 50X (autoclaved)
 - Glycerol 10%
 - Glucose 1%
 - Lactose 4%
 - H₂O
- MgSO₄ 1000X (autoclaved)
 - MgSO₄ 1 M
- antibiotics (filtered)
 - Ampicillin (100 mg/mL) 1000X
 - Kanamicin (100 mg/mL) 500X
 - Chloramphenicol (34 mg/mL) 1000X
- ammonium iron(II) sulfate 1000X
 - Fe(II)(NH₄)₂(SO₄)₂ 200 mM
- pre-culture
 - 50X final volume

Procedure:

- Grow at 37°C, 200 rpm till the OD₆₀₀ reaches a value of 2/5.
- Switch to the desired temperature for expression (25°C has been found to be the optimal temperature for *HsETHE1* overexpression).

- Incubate o/n at 200 rpm.
- Harvest the cells.

i.e.: the expression of the protein is induced in the culture by the lactose as soon as the glucose source is consumed.

The final OD₆₀₀ reached by the culture should be between 10 and 15.

2.2.2.3 Protein expression in minimal medium

The minimal medium is exploited in the case it is desirable to avoid contaminants and impurities deriving from rich media, or when it is needed to have total control on the components of the medium. In this work minimal medium culture has been used to control the availability of specific microelements, such as iron, zinc, nickel and manganese.

The minimal medium used during this work is called M9.

Mix:

- M9 5X (1 L, pH7.5):
 - KH₂PO₄ 15 g/L
 - (NH₄)SO₄ 6.25 g/L
 - Na₂HPO₄ 30 g/L
 - NaCl 2.5 g/L
 - H₂O 895 mL
- MgSO₄ 1000X
 - MgSO₄ 1 M
- Glucose (filtered with a 0.2 μm cut-off membrane) 50X
 - Glucose 0.2 g/mL
- Antibiotics (filtered)
 - kanamycin (100 mg/mL) 500X
- Metal solution 1000X
 - Fe(II)(NH₄)₂(SO₄)₂ 200 mM or

- Zn₂SO₄ 200 mM or
- Mn₂SO₄ 200 mM or
- Ni₂(SO₄) 200 mM or
- Pre-culture
 - 50X final volume

Procedure:

- Grow the culture at 37°C, 200 rpm, till the OD₆₀₀ reaches a value of 0.6.
- Add IPTG (0.1/1 mM final concentration) to induce the expression.
- Grow o/n at 25°C, 200 rpm.
- Harvest the cells.

2.3 Protein purification

The protein purification is a necessary step to obtain a significant amount of protein suitable for research. Initially, the cultured cells containing the protein of interest are disrupted and the protein is withdrawn to the soluble fraction (supernatant). The supernatant is divided from the insoluble fraction containing all the lipophilic material. Successively, multiple chromatographic purification steps follow. The first step is a metal affinity chromatography, with which most of the impurities are discarded. During this step the protein binds to the resin of the column thanks to the N-terminal histidine tag, which possesses high affinity for the metal ions bound to the resin of the column. Typically, the exploited metal is Ni(II), but also Co(II), Zn(II), Cu(II), Fe(III) or other metal ions.. I personally always took advantage of Ni(II). At this stage, the tag is removed through proteolytic cleavage by the TEV protease. TEV, which bears a histidine tag itself, the uncut protein and the cleaved tags are then removed exploiting another step of metal affinity chromatography. Afterwards, the protein undergoes to size exclusion chromatography. If the holo-form of *HsETHE1* is needed, the above mentioned are the essential purification steps. Otherwise, the apo-form (metal-free protein) can be produced from the holo-form. In order to purify apo-*HsETHE1*, the as isolated form is incubated in a partially denaturing solution in presence of deferoxamine (specific iron

chelator). The stripped iron ion is removed by extensive dialysis against metal-free buffer.

2.3.1 Materials for protein purification

The material for protein expression has been bought from the following companies: Carl-ROTH, Soltec Ventures, Sigma Aldrich, Invitrogen, New England BioLabs (NEB), Fluka, Merck, Omni Life Science, Eppendorf, Sorvall, Bandelin, Avanti, Amersham Bioscience, BioRad, Pharmacia, Sartorium Stedim, Millex GP, MILLIPORE, NALGENE, Ikamag RCT, Heidolph, Thermo Scientific (see Appendix A for details).

2.3.2 Methods for protein purification

A robust and reproducible protocol for the production of pure *HsETHE1* and its metal-free (apo) form has been established.

The production of as isolated protein takes four days.

- Day 1: a small culture in LB is set up (see par. Deicated to protein expression).
- Day 2: a large scale culture in AIM is set up and the protein is expressed o/n.
- Day 3: the protein is extracted from the cells and undergoes to the first purification step (IMAC). The protein is incubated with TEV protease o/n.
- Day 4: the protein is purified from TEV, uncleaved protein and free histidine tags present in solution. The protein is then purified by SEC.

2.3.2.1 Sample preparation

- The cells overexpressing *HsETHE1* are harvested in 1 liter centrifuge tubes.
- The cells are centrifuged for 1h at 4°C, at 6000 rpm.
- The surnatant is discarded.
- The cell pellet is resuspended in buffer A.
- The resuspension is promptly sonicated on ice in 20' cycles, comprising a sonication period of 0.1 s followed by a resting period of 0.9 s.
- The cell lysate is ultracentrifuged at 4°C, at 20000 rpm for 30'.
- The surnatant is collected and ultracentrifuged again for 30'.

- The supernatant is collected and filtered with a 0.45 μm cut-off filter.
- The supernatant is filtered with a 0.22 μm cut-off filter.

The solution is now ready to be loaded onto a chromatographic column, and should be kept at 4°C for a short period (no more than some hours), otherwise TCEP and protease inhibitors must be added to the solution.

The insoluble and soluble fractions can be analyzed by PAGE to check expression performance.

2.3.2.2 Immobilized Metal Affinity Chromatography (IMAC)

The IMAC purification has been carried out using both a peristaltic pump (sample loading and column preparation and cleaning) and the AKTA purifier apparatus (sample elution). The columns used are the 5 mL HiTrap IMAC HP from Amersham Bioscience. Preferably, the elution should be performed at 4°C to enhance protein stability.

Peristaltic pump

- Column washing with 5 column volumes (CV) H₂O
- Column metal-recharging with 3.5 mL filtered 0.1 M NiSO₄ solution
- Column washing 10 CV H₂O
- Column equilibration with 10 CV buffer A
- Sample loading (the flow through is collected)
- Sample washing with 5 CV buffer A (the flow through is collected)

AKTA purifier

- Sample washing with 5 CV buffer A
- Sample elution with a gradient of 0 to 80% buffer B (100 to 20% buffer A) in 10 CV. The protein starts to be eluted at 32 % buffer A (180 mM). The buffer B percentage is held at 40% (220 mM) till the protein UV₂₈₀ peak begins to decrease. This procedure has been found to be the more efficient in terms of protein purity. The eluate is collected in 1.5 mL fractions.

- The fractions with an UV₂₈₀ signal greater than 100 mAU can be checked by PAGE and/or mixed
- Column washing of bound remains with 5 CV buffer B (the flow through is collected)

PAGE can be used to check for the presence and purity of the protein in every fraction, comprising also the washing eluates and the flow through.

Peristaltic pump

- Metal stripping with 5 CV 0.1 M EDTA pH 8.0
- Column cleaning with 5 CV 1 M NaOH
- Column washing with 10 CV H₂O

The column is kept at 4°C. For long term storage the column is loaded with a 70% ethanol solution.

2.3.2.3 Estimation of the protein concentration

The protein concentration has been estimated applying the calculated absorbance at 280 nm and the extinction coefficient of the protein (calculated with ProtParam web server tool, which is available on the ExPASy web site, the Expert of Protein Analysis System) to the Lambert-Beer equation:

$$A = -\log(I/I_0)$$

$$A = \epsilon dc$$

A: the absorbance

I: intensity of the transmitted light

I₀: intensity of the incident light

ε: extinction coefficient

d: optical path (constant for a determined apparatus: usually 0.1 or 1 cm)

c: concentration

2.3.2.4 Digestion with TEV protease

- The IMAC purified protein solution (15/30 mL) is concentrated until about 10 mL. Small volumes allow a greater yield of digested protein.
- The protein concentration is then estimated and the TEV protease is added to the solution to a 1:100 ratio with the protein
- The protein is incubated with TEV o/n at ambient temperature T_A

2.3.2.5 Purification from the TEV and uncleaved protein

HsETHE1 is purified from the TEV, from the uncleaved protein and the delivered free tags, through IMAC step purification. In this case, we are interested in the unbound fraction, containing the digested protein. The TEV, which is fused with a histidine tag itself, the uncleaved protein and the free tags, bind to the resin. A peristaltic pump and a dedicated HiTrap IMAC HP column have been used during this purification step.

Peristaltic pump

- Column washing with 5 column volumes (CV) H_2O
- Column metal-recharging with 3.5 mL filtered 0.1 M $NiSO_4$ solution
- Column washing 10 CV H_2O
- Column equilibration with 10 CV buffer C (high salt concentration inhibits the TEV and improve the binding to the resin)
- The sample is diluted 5/10 times with buffer C in order that the Imidazole concentration goes from ~200 mM down to ~ 20/40 mM.
- The sample is filtered through a 0.22 μm cut-off membrane
- Sample loading
- The flow through with the digested protein is collected and kept at 4°C.
- Column washing of bound remains with 5 CV buffer B (the flow through is collected)

- Metal stripping with 5 CV 0.1 M EDTA pH 8.0
- Column cleaning with 5 CV 1 M NaOH
- Column washing with 10 CV H₂O

PAGE can be used to check for the presence and purity of the protein in every fraction, comprising also the washing eluates and the flow through.

The column is kept at 4°C. For long term storage the column is loaded with a 70% ethanol solution.

2.3.2.6 Size Exclusion (SE)/ Gel Filtration (GF) chromatography

Size Exclusion Chromatography (SEC) has been performed using or a Superdex 75, or a Superdex 200 column. In each case, the column volume is about 120 mL.

- The column is equilibrated with 1.5 CV buffer S/H
- The TEV digested protein is concentrated until a maximum value of 20 mg/mL or to a volume ~ 5 mL
- The sample is filtered through a 0.22 µm cut-off membrane
- The sample is loaded into a proper loop attached to the column and injected onto the column during a personally designed running program
- The protein elutes between 57 and 70 mL using the Superdex 75 column and between 73 and 90 mL using the Superdex 200 column
- The fractions with an UV₂₈₀ signal greater than 100 mAU can be checked by PAGE and/or mixed
- Column washing with 1.5 CV H₂O

PAGE can be used to check for the presence and purity of the protein in every fraction.

At this stage the protein is usually of high purity, metal contamination free, at a concentration of 8-10 mg/mL. The protein yield at this step is about 100 mg/L of AIM culture.

2.3.2.7 Production of metal-free *Hs*ETHE1

The production of the metal-free form of *Hs*ETHE1 (apo-*Hs*ETHE1) is a necessary step in order to carry on metal titration with isothermal Calorimetry (ITC). The following is the final optimal protocol established for the purification of the apo-protein.

- Pure *Hs*ETHE1 solution it is mixed with the buffer Apo in a ratio 1:1
- The protein is incubated o/n at 4°C
- The protein is then extensively dialyzed (dialysis membrane cut-off of 8 kDa) 3 times against 5 L of metal-free buffer H, at 4°C under stirring. The dialysis can be extended for half a day, or for an entire day, as soon as the protein is kept at 4°C.
- The protein is collected and filtered before usage or storage

2.3.2.8 Protein storage

The protein has been stored at 4°C for very short periods (up to few days) or at -80°C for long periods. Glycerol can be added to the protein before conservation to enhance stability. A concentration from 5 to 30 % of glycerol can be used without problems.

2.4 Protein characterization

The characterization of *Hs*ETHE1 is the main goal of this project. *Hs*ETHE1 has been characterized by a number of biophysical and biochemical techniques to gain innovative knowledge on this enzyme. Within this chapter, each technique have been described independently.

2.4.1 Poly Acrylamide Gel Electrophoresis (PAGE)

PAGE is a great technique in order to verify the purity of a preparation, and to evaluate the molecular weight of the protein species present in solution.

PAGE can be performed in native or in denaturing conditions, using SDS in the preparation buffers and DTT in the protein dye. During this work I used the Sodium Dodecyl Sulfate - Poly Acrylamide Gel Electrophoresis (SDS-PAGE). SDS is able to

unfold the proteins (denaturation) through the hydrophobic moiety and supply negative charges through the hydrophilic part. In this way, the proteins can run drifted by the applied electric potential at a speed dependent exclusively on the particles size, which is proportional to their molecular weight.

The PAGE apparatus used was purchased from Invitrogen. Sometime, also the gels were bought from Invitrogen, but usually they were self-made exploiting a caster designed by Dr. Young-Hwa Song and constructed by the EMBL workshop. The gels can be of different type. I have been using glycine, tricine and bis-tris type gels. The gels can be divided in two parts: the stacking gel part, where the proteins are loaded into wells and they run through the lane irrespectively of their size (the polymeric net forming the gel is very wide), and the separating gel part, where the particles are separated in respect of their size.

During the run the gels are soaked in a running buffer that must be compatible with the gel type in use.

Chemicals used for Poly Acrylamide Gel Electrophoresis

See Appendix A for details.

Buffers and solutions for Poly Acrylamide Gel Electrophoresis

The following buffers and solution were used for PAGE:

- Tricine running buffer
- Tricine gradient gels
- Glycine separating gel buffer
- Glycine stacking gel buffer
- Bis-tris gel running buffer
- Bis-tris separating gel buffer
- Bis-tris stacking gel buffer
- Gel staining solution
- Gel destaining solution

See Appendix A for details.

Procedure

- The samples are mixed with the protein loading dye and they are heated up to 90°C to stimulate denaturation.
- The PAGE device is prepared with the ready to use gel soaked in running buffer.
- The samples are loaded into the gel wells. Commonly, at least one lane of the gel is dedicated to the protein markers, which supply a mixture of protein of known molecular weight for comparison.
- A constant potential of 120/200 eV is applied and the gel is left run for about 60/40'.
- When the run is complete, the gels are stained and destained leaving the dye in complex with the proteins. In this way, the protein bands on each lane can be optically distinguishable.

2.4.2 Dynamic Light Scattering (DLS)

The DLS supplies information about the polydispersity and the hydrodynamic radius of the protein in solution.[68]

Material

See Appendix A for details.

Procedure

- The protein solution is filtered through a 0.22 µm membrane or centrifuged at 14000 rmp for 15'.
- The cuvette is carefully cleaned to prevent the presence of dust.
- 20 µL of the protein solution is introduced into the UV cuvette.
- The solution is tested for the intensity and stability of the signal. The intensity of the scattering signal should be lower than 10 million count rates per second and the fluctuation should be less than 1000 count rates up and down. If the conditions are not satisfied there are multiple possibilities: the protein is too

concentrated (intensity too high); in the protein solution are present aggregates; there is still dust in the solution. The best condition for monodispersity should be sought, for example changing buffer, salts concentration, reducing agent type and concentration.

- Run the experiment with an acquisition time of 10s per data point collecting from 20 to 30 measurements.

In general, the resulting hydrodynamic radius should be between 2 and 5 nm and the polydispersity less than 20%.

2.4.3 Protein stability

The stability of the protein has been checked in different conditions. The effect of DTT on the protein has been investigated. Different reducing agents in various concentrations have been tested. Different storage temperatures have been tried to find the best way to preserve the protein for long time. The stability in different buffers at different pHs has been tested with a ThermoFluor device to find the solution in which the protein results more stable. In this technique, the protein is incubated with a reagent (Sypro Orange) that binds to the hydrophobic moieties of the proteins emitting light at a 470/570 nm wavelength after excitation at 300 nm.

Material for protein stability investigation

See appendix A for details.

DTT influence test

- 50 mM DTT are added to a 5 mg/mL *HsETHE1* solution under N₂ flux.
- The mixture is incubated for 5'.
- A UV-Vis spectrum of the mixture is taken and compared with the spectra of the DTT-free protein.
- Check the protein conditions after a night.

Reducing agent sensitivity test

- 21 samples are prepared (20 conditions plus 1 negative control with no reducing agent inside. The protein concentration has been 5 mg/mL each sample):
 - 5 sample β -mercaptoethanol at the concentrations of: 2, 5, 10, 20, 50 mM.
 - 5 sample with DTT at the concentrations of: 1, 2, 5, 10, 20 mM.
 - 5 sample with TCEP at the concentration of: 0.2, 0.5, 1, 2, 5 mM.
 - 5 sample with dithionite at the concentrations of: 0.2, 0.5, 1, 2, 5 mM.
- The solutions are incubated for 1 h at T_A .
- The samples are centrifuged at 14000 rpm for 15'.
- Check for protein precipitation by eye and with an optical microscope.
- Analyze the samples with the DLS and check the polydispersity and hydrodynamic radius of the species in solution.

The used concentrations are related to the reducing capacity of each individual compound and to the maxima concentrations at which these compounds are commonly used in protein science.

Low temperatures stability test

Protein samples of 10 mg/mL have been subjected to different temperatures (T_A , 4, -20, -80 °C) . The protein solutions have been incubated for one month and the protein degradation has been checked optically after centrifugation and by SDS-PAGE at fixed intervals of time (after 1 day, 2 days, 1 week, 2 weeks, 3 weeks and 1 month).

Differential buffers stability screening

- 1 μ L of Sypro Orange is added to 1 mL of protein at a concentration of 1 mg/mL.
- 5 μ L of the solution are added to 95 out of the 96 wells of the screening plate. Each well contains a final volume of 50 μ L.
- The solutions obtained are screened with the cyler for increasing of absorbance at 470 nm during a temperature gradient going from 16 up to 90 degrees.

- The solutions where the signal intensity rises up at the higher temperature represent the best conditions.

2.4.4 Static Light Scattering (SLS)

SLS it is used to gain information about the oligomeric state and molecular weight of the species present in solution.[69]

Material

See appendix A for details.

Procedure

- Connect the SLS machine to an AKTA purifier, following the manufacturer instruction.
- Load 500 μ L of a 1 mg/mL protein sample into a proper loop connected to the purifier.
- Start the purifier and be sure to start the acquisition by the SLS at the same moment the sample is injected into the column.
- At the end of the run check with the ASTRA software that the SLS scattering signal is aligned with the AKTA UV₂₈₀ signal. In case, the program allows you to make the proper alignment.
- Check that the scattering signal corresponding to the protein peak is flat. If this is not the case, probably multiple oligomeric/aggregation states are present in solution. The best condition for monodispersity should be sought, for example changing buffer, salts concentration, reducing agent type and concentration.
- Select only the homogeneous scattering signal corresponding to the UV peak of interest and analyze the data with the ASTRA software.

The software, on the basis of a standard measurement and relative parameters (usually BSA is used) and on the basis of the elution volume and extinction coefficient of the protein, calculates the molecular weight of the species of interest.

2.4.5 Crosslinking

The crosslinking it has been used as alternative method to check the oligomeric state of a protein in solution.[70] The crosslink has been achieved by two different techniques: the chemical and the physical crosslink. The first exploits chemical reagents in order to introduce covalent bonds between ϵ -amino groups of lysine residues present on the surface of the protein (if any!). If the protein is oligomeric, then the monomers should crosslink through the lysines present on the interaction interface. The second method is a UV-A driven unspecific crosslink. Covalent bonds are introduced between interacting molecules upon ionizing irradiation.

The resulting sample can be checked by SDS-PAGE.

Material

See Appendix A for details.

Procedure

Chemical crosslinking:

- Prepare 7 sample (50 μ L final volume) for each protein:
 - Protein + 0.1% glutaraldehyde
 - Protein + 0.2% glutaraldehyde
 - Protein + 0.3% glutaraldehyde
 - Protein + 0.4% glutaraldehyde
 - Protein + 0.5% glutaraldehyde
 - Protein alone (negative control)
 - Protein + 2.5% glutaraldehyde + BSA (100 μ L final volume, 1 mg/ml concentration of BSA and *HsETHE1*)
- Incubation for 1h
- Stop the reaction by addition of 10 μ l of 1 M Tris-HCl, pH 8.0.

UV crosslinking:

- Prepare 7 samples for each protein and mix one with BSA (100 μ L final volume, 1 mg/ml concentration of BSA and *HsETHE1*)

- Take 5 samples with the protein and the sample with the protein plus BSA and expose the samples to the radiation of a UV transilluminator: expose individual samples for a dedicated time 30'', 1', 2', 3', 4', 5'. The Protein + BSA sample is exposed for 5' and represent the negative-interaction control. The remaining sample is used as negative control.

Check all the results by SDS-PAGE.

2.4.6 Total X-ray Reflection Fluorescence (TXRF)

TXRF spectrometry is a powerful x-ray based technique that allows quantitative investigation of a number of elements present in a sample.[71] Recent development improved considerably its application for biological purposes.[72] The target is hit with an x-ray beam at ideally 180 degrees respect a surface where the specimen is placed, and the fluorescence emissions at 90°C is acquired. Potentially, TXRF can discriminate the elements from silicon to uranium (depending on the standards used) with a detection limit in the lower pg, ppb and ppm-regions (pico/micro molar in solution). Herein, the considered elements have an atomic number ranging within the scandium and gallium ones, which were used as standards. In this case, TXRF gives very precise metal quantification for first row transition metals.

TXRF has been useful for testing:

- metal-protein correlation
- metal contamination

This technique requires little volumes (~20µL) and low concentrations of protein (20-50µM) and the collected data are quick to analyze for standard measurements. Moreover, no cooling is needed. The disadvantages are limited to the high precision requested for the used volumes and the time needed for each measurement. In fact, for each sample, three specimens are probed for statistical purposes and usually, more than one sample needs to be probed in order to perform comparisons. Every data collection of a specimen takes about 1 hour. TXRF experiments and data analysis were carried out by myself. Access to the instrumentation (PicoTAX) was kindly provided by Peter Freimann of the "Institute Bundesamt fuer Seeschiffahrt und Hydrographie" in Hamburg).

TXRF was applied on all the purified protein batches and buffers for quality control. Moreover, TXRF was used on each ITC experiment sample: apo-protein, buffers, and metal solutions. This procedure was essential for quality check and for the determination of the precise metal concentration in the solutions titrated during ITC experiments.

Material

See Appendix A for details.

Procedure

For the preparation of 5 μ L drop specimens:

- Prepare an intermediate standard solution (use a balance with one hundred of milligram sensitivity):
 - 20 mg/L gallium
 - 200 mg/L scandium
- Mix 20 μ L of each sample with 2 μ L of standard solution. (final concentrations: 2 mg/mL gallium, 28.68 μ M; 20 mg/mL scandium, 420 μ M)
- Place 5 μ L of each resulting solutions at the center 3 individual plexies: you should have 5 μ L triplicates for every sample.
- Leave dry out at 37°C.
- Measure the fluorescence for 5000 seconds each specimen.
- Convert the “spx” output files of the PicoTAX program in “mca” files.
- Analyze the data with PyMCA.
- Create a table resuming all the PyMCA output values of the measurements.

i.e.: when the specimens are dried out we assume that the standards were already present in solution and thus, that their concentration in the solution was 1:10 the intermediate solution and not 1:11 (we add 2 μ L to 20 μ L!).

2.4.7 Isothermal Titration Calorimetry (ITC)

ITC is a powerful method to study the thermodynamics of chemical interactions such as protein-protein, protein-molecule, or even protein-ion interactions.[73]

ITC is a quantitative technique that can directly measure the binding affinity (K_a), enthalpy changes (ΔH), and binding stoichiometry (n) of the interaction between two or more molecules in solution. From these initial measurements Gibbs energy changes (ΔG), and entropy changes (ΔS), can be determined using the relationship:

$$\Delta G = -RT\ln K = \Delta H - T\Delta S$$

The enthalpy changes during time are calculated respect a reference cell. ITC systems use a cell feedback network to differentially measure and compensate for heat produced or absorbed between the sample and reference cell.

2.4.7.1 The ITC experiment

Materials

See Appendix A for details.

Procedure

- Dialyze the protein o/n against a metal free buffer. Concentrate/dilute the protein to a concentration of 20/50 μM .
- Use the dialysis buffer to prepare a metal solution ($\sim 450 \mu\text{L}$ per experiments, but a bigger volume is needed for comfortable loading): the concentration depends on the binding affinity for the protein and on the protein concentration. Usually the concentration ranges between 0.1 and 1 mM.
- Set the sample chamber jacket temperature to the constant temperature of 25°C .
- Select a proper computer path where to save the results.
- Wash with water and equilibrate with buffer the ITC sample chamber.
- Wash with water and equilibrate with buffer the ITC injections syringe.

- Degass the sample and the binding partner solution using the proper device, which is part of the ITC system.
- Load the sample into the sample chamber avoiding bubbles.
- Open the syringe and load the partner solution avoiding bubbles. Pour the liquid up and down till no bubbles are present.
- Close the syringe.
- Purge two times the liquid into the syringe.
- Introduce the syringe into the apparatus.
- Set the parameters on the main control window: 30 injections; reference power at 20; delay at 60; stirring speed at 307; feedback mode to high; ITC eq. to fast and auto; 1st injection of 3 μL with 6 s injection; 29 injection of 10 μL with 20 s injections; spacing time between injection of 240 s; filter period of 2.
- Set the concentrations used on the main control window (this is fundamental for the correct interpretation of the results).
- Run the experiment: the machine with equilibrate the temperatures of the sample cell with the reference cell after addition of the solution. After the machine starts the stirring of the syringe (in order to mix properly the solution during injections). At this point the machine needs to equilibrate the sample and reference chamber taking in account the stirring if the syringe. Afterward the experiment starts.
- Analyze the data with the Origin software.

2.4.7.2 Solutions used in the ITC experiments

Materials

See Appendix A for details.

Solutions

All the solution were prepared using the apo-*HSETHE1* dialysis buffer and filtered with a 0.22 μm cut-off membrane. The metal concentrations were calculated by TXRF and refer to representative experiments.

The following metal solutions have been prepared:

- $\text{Fe(II)(NH}_4\text{)(SO}_4\text{)}_2$ 100 μM + dithionite 5 mM
- $\text{Fe(III)-citrate-NTA}_{(n)}$ (iron concentration of 90 μM in the presented results)
- Prepare a solution 10 mM iron citrate and 20 mM NTA.
- Dissolve the compounds in the apo-protein dialysis buffer.
- Vortex extensively.
- Quick filter the solution.
- This procedure should give an iron(III) stock solution at a concentration of about 1 mM.
- Ni(II)SO_4 235 mM
- Zn(II)Cl 135 mM
- Mn(II)Cl 300 mM
- GSH 1 mM

The metal concentrations used depended on the protein concentrations and on single preparations. It is important to notice that often the metal concentrations supposed during preparation were not the real ones. TXRF was carried out after each experiment to determine the exact metal concentrations. Only then, the results were analyzed and interpreted. The results of TXRF have been also used to determine standard protocol to obtain defined concentrations prior to the experiments.

2.4.8 Optical absorption spectrophotometry

Spectrophotometry is a technique able to quantify the incident light absorption of a solution respect to another.[74] The absorption values are then used to:

- Fingerprint the characteristic absorption spectrum of a solution within a selected range of wavelengths (220-750 nm).
- Calculate the concentration of the species in solution (280 nm)
- Evaluate a cell culture density (600 nm).

The commonly used bench-top spectrophotometers have the possibility to span wavelengths from 190 to 900 nm. Typically, I used the spectrophotometer or to carry on UV-Vis experiments, or for measuring the protein concentration, which can be

calculated through the Lambert-Beer equation knowing the extinction coefficient of the target molecule, its absorbance at 280 nm and assuming that is the only species in solution (pure protein solution in this case).

Lambert-Beer equation:

$$A = -\log(I/I_0)$$

$$A = \epsilon dc$$

A: the absorbance

I: intensity of the transmitted light

I_0 : intensity of the incident light

ϵ : extinction coefficient

d: optical path (constant for a determined apparatus: usually 0.1 or 1 cm)

c: concentration

Material

See Appendix A for details.

Method

- Using the Eppendorf spectrophotometer:
 - A volume of 200-1000 μ Ls of a blank solution (same composition of the sample solution, but without the species you want to measure the absorbance of) is placed into a 1 mL cuvette.
 - Set its absorbance as the zero point.
 - A volume of 200-1000 μ Ls of the sample solution are placed into a 1 mL cuvette.
 - The absorbance respect the blank is measured.
- Using the Nanodrop:

- 2 μL of a blank solution are directly placed on the “sample surface” (the beam path is passing through the centre of the “sample surface”).
- Set the zero point.
- Clean the surface and place on it 2 μL of the sample solution
- Measure the absorbance.

2.4.9 Mass Spectrometry (MS)

Mass spectrometry has been used to check the integrity of the protein in solution and to get information about the molecular weight of the *HsETHE1*- dimer in solution.[75]

Materials

See Appendix A for details.

Procedure

- Prepare the matrix solution:
 - SAPA 10 mg/mL
 - Acetonitril 30%
 - TFA 0.1%
- Put 1 μL of the matrix and 1 μL of the protein solution on a spot of a sample grid-plate
- Leave the drop to dry out
- Take shots at different spots

2.4.10 Circular Dichroism (CD) spectroscopy

CD spectroscopy measures differences in the absorption of left-handed polarized light versus right-handed polarized light which arise due to structural asymmetry.[76] The absence of regular structure results in zero CD intensity, while an ordered structure results in a spectrum which can contain both positive and negative signals. In general, this phenomenon will be exhibited in absorption bands of any optically active molecule. Thereby, circular dichroism is exhibited by biological molecules because of their

dextrorotary and levorotary components. Even more important is that alpha helix of proteins and the double helix of nucleic acids have CD spectral signatures representative of their structures. Many compounds can absorb differently left/right polarized light so that the composition of the used buffers must be chosen carefully. Any compound which absorbs in the region of interest (250 - 190 nm) should be avoided. A buffer or detergent or other chemical should not be used unless it can be shown that the compound in question will not mask the protein signal. For instance imidazole cannot be used below 220 nm and chlorine must be avoided. In general, any chemical that is unnecessary for protein stability/solubility should be left out. Obviously, the protein purity is also very important for the results. Filtering of the solutions (0.02 um syringe filters) may improve signal to noise ratio.

Circular dichroism spectroscopy is particularly good for:

- Determining whether a protein is folded or not.
- Characterizing the secondary or tertiary structure of a protein.
- Comparing structures
- Studying the conformational stability of a protein under variable conditions.
- CD is excellent for finding solvent conditions that increase the melting temperature.
- Studying conformational changes.

Determination of Protein Secondary Structure by Circular Dichroism

Secondary structure can be determined by CD spectroscopy in the "far-UV" spectral region (190-250 nm). At these wavelengths the chromophore is the peptide bond, and the signal arises when it is located in a regular, folded environment.

Alpha-helix, beta-sheet, and random coil structures each give rise to a characteristic shape and magnitude of CD spectrum.

Information About Protein Tertiary Structure from Circular Dichroism

The CD spectrum of a protein in the "near-UV" spectral region (250-350 nm) can be sensitive to certain aspects of tertiary structure. At these wavelengths the chromophores are the aromatic amino acids and disulfide bonds, and the CD signals they produce are sensitive to the overall tertiary structure of the protein.

Signals in the region from 250-270 nm are attributable to phenylalanine residues, signals from 270-290 nm are attributable to tyrosine, and those from 280-300 nm are attributable to tryptophan. Disulfide bonds give rise to broad weak signals throughout the near-UV spectrum. The presence of significant near-UV signals is a good indication that the protein is folded in a well-defined structure.

Material

See Appendix A for details.

Procedure

- Prepare protein solution samples in phosphate buffer salt free at the concentrations of 0.5, 1.0, 1.5 mg/mL.
- Centrifuge the samples at 14000 rpm 4°C for 15'.
- Filter the sample by a 0.22 µm cut-off membrane.
- Switch on the nitrogen flux (the sample should be in oxygen free atmosphere because of the absorption of the oxygen in the UV range).
- Open the pumps for temperature control.
- Measure protein-free buffers and protein samples following the manufacturer instructions.
- Analyze the data with the JASCO software.

2.4.11 Crystallization

Crystallization is the necessary step to carry on an x-ray diffraction experiment aiming to solve the three dimensional structure of a target molecule or supramolecular structure. Protein crystallization occurs when the concentration of protein in solution is greater than its limit of solubility in a given solvent and so the protein solution is in a

superstaturated state. Crystals start growing by a process called "nucleation". Nucleation can either start with the molecules themselves (we'll call this unassisted nucleation), or with the help of some solid matter already in the solution (assisted nucleation). Once a solution is saturated, or a melt nears the solidification point, solid material starts to form. If the molecules come together in a random arrangement, they do not occupy the closest packed space. However, if the molecules come together in an ordered array, they pack together in a much smaller space such that the packing uses less space and is also of lowest energy. This ordered array pattern repeats itself regularly in 3 dimensions, and the crystal is the macroscopic object we see as a result.

Crystallization has been tried exploiting the facility[77] available at EMBL-Hamburg and by manual crystallization set up for conditions optimization and spherulites seeding.

Material

See Appendix A for details.

Procedure

I tested for crystallization different protein constructs ($\Delta 14$ -*HsETHE1*, $\Delta 14$ -*HsETHE1*- $\Delta 4$, $\Delta 19$ -*HsETHE1*- $\Delta 4$, Apo- $\Delta 14$ -*HsETHE1*- $\Delta 4$, $\Delta 7$ -*HsETHE1*- $\Delta 4$, *HsETHE1*-MutA, *HsETHE1*-MutB, *HsETHE1*-MutC), at different concentrations (8, 10, 20 mg/mL, 1 mM, 2mM), different temperatures (19, 4 °C), different reducing conditions. I exploited the bio-robot available at the high throughput crystallization facility of EMBL-Hamburg, or I set up the crystallization plates manually for optimizations, pre crystallization tests (Hampton-PCT) and seeding. The biorobot prepared 96 conditions per screen on a Greiner Low Profile plate, using the sitting drop technique. The crystallization drops had a volume from 1 to 2 μ L with a protein:reservoir ratio of 1:1. Hundreds of conditions have been tested, using standard crystallization screening plates, *e.g.* Hampton_Index, Hampton_Crystal, Hampton_Grid, Jena (1-10), Quiagen_ClassicI, Quiagen_ClassicII, Quiagen_PEGI, Quiagen_PEGII, Quiagen_Pact. Manual screenings were carried out on 24 well plates with the hanging drop method. The drops were about 2 μ L in volume. Besides, I applied the reductive methylation on *HsETHE1* in order to add methyl-groups to the lysines exposed on the protein surface. In this way, I aimed to enhance the protein

monodispersity by lowering of the surface entropy and thereby boosting the probability of crystallization.

Reductive methylation protocol

The reductive methylation was optimized for proteins. To avoid side reaction, the protein should be put in a non-reducing buffer. The protein was used at a concentration of 5 mg/mL.

Material

See Appendix A for details.

Procedure

1. Add 20 μ L of 1 M dimethyl-borane complex every mL of protein solution.
2. Add 40 μ L of 1 M formaldehyde every mL of protein solution.
3. Incubate on ice for 2h.
4. Repeat steps 1 to 3.
5. Add 10 μ L of 1 M dimethyl-borane complex every mL of protein solution.
6. Incubate 24h on ice.
7. Exchange the buffer by dialysis, or repeated concentration-dilution steps.
8. Perform a SEC on the reductively methylated protein.

Crystallization trials

EMBL-Hamburg facility crystallization screens: the protein solutions are supplied directly to the technician responsible of the facility. See Appendix A for details about the construct used and the conditions tested.

2.4.12 Substrate screening

Substrate screenings have been performed to check whether *HsETHE1* is able to perform any of the more common M β L-like activities: lactamase, phosphatase, aryl-sulfatase and esterase.

Material

See Appendix A for details.

Procedure

The experiments were carried out at the pH values of 7.2 and 8.5, corresponding to the mean values found in the human cytoplasm[78] and mitochondrial matrix,[79] respectively. The reason behind the choice is that the protein has been found in the cytoplasm, in the nucleus and in the mitochondrial matrix. An exception is the esterase activity test, where the experiment was carried in a pH of 8.0.

The experiments were performed using UV-96-well-plates and 200 μ L reaction solutions per well. The substrates working concentration it has been of 10 mM (2 μ mol), but for Nitrocefin, where it was 100 μ M, and nitrophenyl acetate, where it was 350 μ M. The enzymes concentrations are calculated in order that at least 2 μ mol of substrate are processed in less than 1 hour.

Prepare: (in TrisHCL and phosphate buffers)

- As isolated *Hs*ETHE1 160 μ M (>700 μ L), 50 μ L/well, final concentration of 40 μ M
- Apo-*Hs*ETHE1 160 μ M. (>1400 μ L), 50 μ L/well, final concentration of 40 μ M
- Ammonium iron sulfate solution 1 mM; final target concentration: 80 μ M.
- EDTA solution: 0.1 mM. final target concentration: 10 mM.
- ZiPD stock solution: 100 μ M; 25 μ M final concentration.
- Penicillinase type III solution: 32 U/mL; 0.4 U/well.
- Antarctic phosphatase: 5000 U/mL; 500 U/well.
- Aryl-sulfatase type VIII: 800 U/mL; 40 U/well.
- Esterase: 8 U/mL; 0.1 U/well.
- Nitrocefin (final concentration of 100 μ M):
 - Add 2 mg Nitrocefin to 200 μ L DMSO
 - Take 100 μ L and add 1.9 mL buffer pH 7.2
 - Take the remaining 100 μ L and add 1.9 mL buffer pH 8.5

- bis-p-nitrophenyl phosphate: dissolve in buffer 10% DMSO to get a solution 20mM; final concentration of 10 mM.
- p-nitrophenyl phosphate: 100 mM; final concentration of 10 mM.
- p-nitrochatecol sulfate: 100 mM; final concentration of 10 mM.
- p-nitrophenyl sulfate: 100 mM; final concentration of 10 mM.
- Glucose-3-sulfate: 100 mM; final concentration of 10 mM.
- p-nitrophenyl acetate: 3.5 mM; final concentration of 350 μ M.
 - Dissolve in methanol at a volume of 10% the desired one. Fill up with water. The final concentration we want in the well is 350 μ M.
- Final set up of the plates in a dark room.

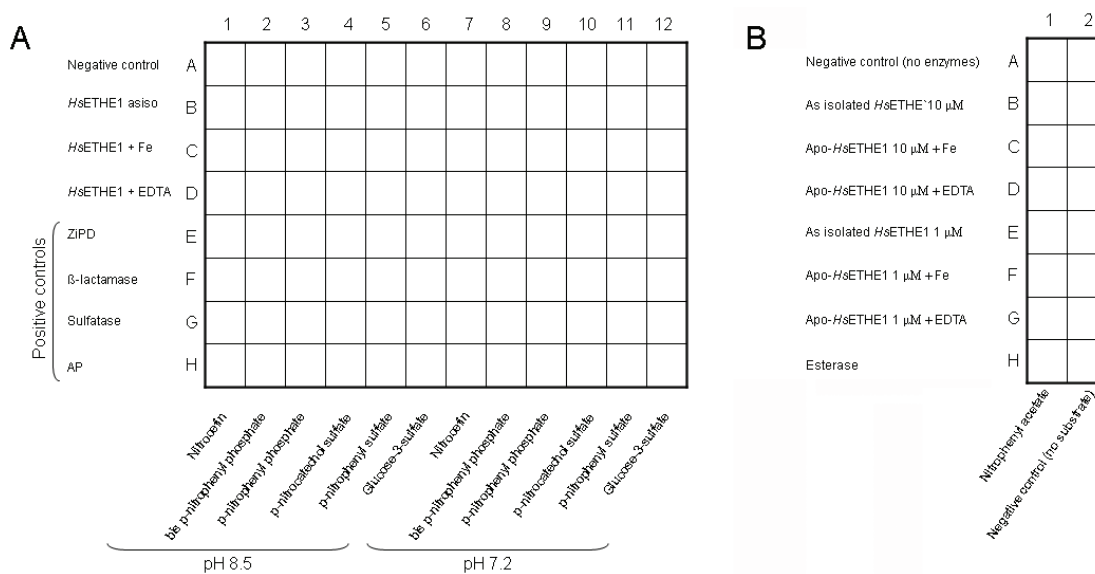


Fig. 11: Substrate screenings.

A) The lactamase, phosphatase and aryl-sulfatase activity are tested at 2 different pHs. B) The esterase activity is tested (pH 8.0).

During these experiments 2 plates were set up. One plate was set to cover the lactamase, phosphatase and aryl-sulfatase activity and another testing the esterase activity (Fig. 11). N.B.: Glyoxalases II are the ETHE1 structurally closest enzymes known so far. The glyoxalases II reaction produces D-lactate and reduced glutathione (GSH) from S-D-lactoyl-glutathione. The glyoxalase II reaction was not tested, because it was reported that ETHE1 doesn't have such activity.[9]

2.4.13 Small Angle X-ray Scattering

SAXS can supply structural information of macromolecules between 5 and 25 nm, or up to 150 nm for highly ordered repetitive systems.[80] SAXS is used for the determination of the microscale or nanoscale structure of particle systems in terms of averaged particle sizes, shapes, distribution, and surface-to-volume ratio. SAXS is a small-angle scattering (SAS) technique. The elastic scattering of X-rays (with a wavelength of about 0.1-0.2 nm) is collected at low angles ($\sim 0.1-10^\circ$). This angular range contains information about the shape and size of macromolecules, characteristic distances and more. The materials can be solid or liquid. The method is accurate and in principle non-destructive, but radiation damage can always occur and affect the sample under measurement.

Material

The data were collected at the EMBL beamline X33 of the storage ring DORIS III (DESY, Hamburg, Germany). See Appendix A for details.

Procedure

- Prepare protein samples at different concentrations:
 - *E.g.*: 1, 2, 3, 5 mg/mL
 - I carried out experiments on olo-*Hs*ETHE1 and apo-*Hs*ETHE1 in the presence and absence of the reducing agent TCEP.
- Collect the data at 10°C.
- The data are normalized to the intensity of the transmitted beam and radially averaged; the scattering of the buffer is subtracted and the curves are scaled for protein concentration. The low angle data measured at lower protein concentrations were extrapolated to infinite dilution and merged with the higher concentration data to yield the final composite scattering curves.
- Data processing: using the program package PRIMUS.[81]
- The forward scattering $I(0)$ and the radius of gyration R_g are evaluated using the Guinier approximation and assuming that at very small angle ($s < 1.3/R_g$) the intensity is represented as $I(s) = I(0) \exp(-(sR_g)^{2/3})$.

- The molecular mass (MM) of the solute is evaluated by comparison of the forward scattering with that from reference solution of bovine serum albumin (MM = 66 kDa). The excluded volume of the hydrated particle was computed from the small angle portion of the data ($s < 0.25 \text{ \AA}^{-1}$) using the equation:[1]

$$V = 2\pi^2 I(0) / \int_0^{\infty} s^2 I_{\text{exp}}(s) ds$$

- Distance distribution function $p(r)$: the distance distribution function $p(r)$ gives the relative number of distances of two points inside the particle as a function of the distance r . It is obtained from the intensity $I(q)$ as:

$$p(r) = \frac{r^2}{2\pi} \int_0^{\infty} I(q) \frac{\sin qr}{qr} q^2 dq$$

The limits of integration are from 0 to ∞ , which means that in practice the experimental intensity has to be extrapolated to $q=0$.

***Ab initio* shape determination**

The “shape scattering” curve was further used to generate the low resolution *ab initio* shapes of *HsETHE1* by the programs DAMMIN[82] and DAMMIF.[83] Both programs represent the particle shape by an assembly of densely packed beads and employ simulated annealing to construct a compact interconnected model fitting the experimental data $I_{\text{exp}}(s)$ by minimizing the discrepancy between experimental and simulated spectra:

$$\chi^2 = \frac{1}{N-1} \sum_j \left[\frac{I_{\text{exp}}(s_j) - cI_{\text{calc}}(s_j)}{\sigma(s_j)} \right]^2$$

N is the number of experimental points, c is a scaling factor and $I_{\text{calc}}(s)$ and $\sigma(s_j)$ are the calculated intensity and the experimental error at the momentum transfer s_j , respectively. A dozen DAMMIN and DAMMIF runs were performed to check the stability of solution. These models were averaged to determine common structural features using the

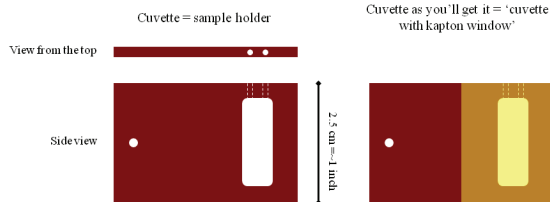


Fig. 12: EXAFS sample holder design.

programs DAMAVER[84] and SUPCOMB[85]. The latter program aligns two arbitrary low or high resolution models represented by ensembles of points by minimizing a dissimilarity measure called normalized

spatial discrepancy (NSD). The program DAMAVER generates the average model of the set of superimposed structures and also specifies the most typical model.

2.4.14 X-ray Absorption Spectroscopy (XAS)

The general aspects of XAS are discussed in paragraph 1.2.

2.4.14.1 Synchrotron beamlines

XAS experiments were carried out at the following beamlines:

- E4 (DORIS III, EMBL, DESY, Hamburg, Germany)
- C1 (DORIS III, EMBL, DESY, Hamburg, Germany)
- D2 (DORIS III, EMBL, DESY, Hamburg, Germany)
- SuperXAS (SLS, Villigen, Swiss)
- ID26 (ESRF, Grenoble, France)
- BM 7-3 (SSRL, SLAC National Accelerator Laboratory, California, U.S.A)

See Appendix A for details about the beamlines.

2.4.14.2 XAS measurements

Experiments were carried out in absorption or in fluorescence mode. When measuring in fluorescence the sample holder has been kept typically at 45°C respect the source and the detector. The samples were kept constantly at liquid nitrogen (LN) temperature (77°K) in the proper sample holders (Fig. 12). They had biological (proteins) or synthetic (bioinorganic metallo-complexes) origin. The proteins had a concentration ranging from 0.5 to 3 mM and often the protein solution contained glycerol in a percentage within 0 and 30%. Glycerol has been used as cryoprotectant and to increase

homodispersity. The bioinorganic compounds were or lyophilized or in solution with a concentration always higher than 1 mM. Every sample underwent to multiple scans. The number of scans depended on the obtained signal to noise ratio, which depends on the sample concentration. The number of scans ranges typically from 2 to 15. The duration of each scan varied from 20' to 2 h. The scans start from about 150 eV before the absorption edge to energies about 400 eV ($k = 10 \text{ \AA}^{-1}$) to 1650 eV ($K = 20 \text{ \AA}^{-1}$) above the edge.

2.4.14.3 Data processing (background removal, data reduction, normalization)

Data reduction and normalization was carried out using the program KEMP[41] or the program KEMP2,[86] under constant development by Dr. Gerd Wellenreuther.

The spectra were evaluated for radiation damage.

The general procedure has been the following:

- Evaluation of the quality of the spectra and of potential radiation damage.
- Select good spectra.
- Average spectra.
- Background subtraction.
- Deglitching.
- Spline determination.
- Normalization.
- K space determination (wave number against EXAFS amplitude).

2.4.14.4 EXAFS analysis

The EXAFS data analysis has been performed with the programs Excurve98[44] and occasionally ATHENA for spectra analysis and smoothing.[45]

The data were analyzed in the K^3 weighted space and the relative FT space. Excurve98 has been used to minimize the R-factor and Fit-Index (FI) functions.

The R-factor gives a quality of the fit of the EXAFS data in K-space:

$$R_{EXAFS} = \sum_i^N \frac{1}{\sigma_i} \left(\chi_i^{\text{exp}} - \chi_i^{\text{th}}(k) \right) \times 100\%$$

The Fit-Index is an absolute index of goodness of fit:

$$FI_{EXAFS} = \sum_i \left(\frac{1}{\sigma_i} \right) [Exp_i - Theory_i]^2$$

The minimization of these functions provides theoretical spectra fitting the experimental ones. These models are calculated starting from a number of variable parameters given to the program as input for the minimization calculation. When the best, meaningful model has been obtained the refined parameters represent our analysis results. The parameters are:

- Number of ligands
- Type of ligand
- Distance from the absorber
- Debye-Waller factors (disorder factors)
- Geometric parameters

Another important information can be extracted from the EXAFS parameters obtained from analysis: the Bond Valence Sum (BVS).[87-90] The BVS is an empirical approach developed by I. D. Brown for analysis of the crystal structures of solids.[91,92]. The assumption is that the BVS surrounding an atom or ion is equal to its oxidation state.

$$z_j = \sum_i s_{ij}$$

Z_j is the oxidation state of the target ion and s_{ij} is the BVS.

The valences of the individual bonds can be calculated from the observed bond lengths.

$$s_{ij} = \exp\left[\frac{R_0 - r_{ij}}{b}\right]$$

$$s_{ij} = (r_{ij} / R_0)^{-N}$$

r_{ij} is the observed bond length, R_0 and N are constants that are dependent upon the nature of the ij pair, and b is usually taken to be 0.37. The R_0 value can be viewed as a bond length of unit valence. The usual procedure was to assume an oxidation state and to use a previously determined R_0 value appropriate to the bond being considered.

2.4.14.5 XANES analysis

XANES analysis were carried out with the program XInXAS[43]. The program has been used for pre-edge peak area calculation and qualitative *ab initio* XANES spectra evaluation. The exact edge position and derivatives were calculated with the program KaleidaGraph 4.0 (Synergy Software).

2.4.14.6 XANES simulations

The XANES simulations were performed exploiting the FEFF software.[93]. FEFF is supplied with an input file containing the geometrical coordinates of all atoms considered in the ligands shells. The coordinates came from the available PDB structures or from the EXAFS parameter files derived from 3D-structure-based EXAFS refinements. The program was used to calculate the theoretical spectra and the Local Density Of States (LDOS: describes the space-resolved number of states at each energy level that are available to be occupied. A high DOS at a specific energy level means that there are many states available for occupation. A DOS of zero means that no states can be occupied at that energy level). Outputs evaluation were carried out with the programs KaleidaGraph 4.0 (Synergy Software) and ATHENA.[45]

2.4.15 Electron Paramagnetic Resonance (EPR) spectroscopy

Electron paramagnetic resonance (EPR) spectroscopy is a technique for studying chemical species with one or more unpaired electrons.[94] In biology is frequently used to investigate paramagnetic transition-metals in proteins. The basic physical concepts of EPR are based on electron-spin excitations. Because most stable molecules have all their

electrons paired, the EPR technique restricted to paramagnetic species. However, this limitation also means that the EPR technique possesses great specificity, since ordinary chemical solvents and matrices do not give rise to EPR spectra.

The degeneracy of the electron spin states is lifted when an unpaired electron is placed in a magnetic field, creating two spin states, $m_s = \pm \frac{1}{2}$, where $m_s = -\frac{1}{2}$, the lower energy state, is aligned with the magnetic field. The spin state on the electron can flip when electromagnetic radiation is applied. In the case of electron spin transitions, this corresponds to radiation in the microwave range.

The energy difference between the two spin states is given by the equation

$$\Delta E = E^+ - E^- = h\nu = g\beta B$$

where h is Planck's constant ($6.626 \times 10^{-34} \text{ J s}^{-1}$), ν is the frequency of radiation, β is the Bohr magneton ($9.274 \times 10^{-24} \text{ J T}^{-1}$), B is the strength of the magnetic field in Tesla, and g is known as the g -factor. The g -factor is a unitless measurement of the intrinsic magnetic moment of the electron, and its value for a free electron is 2.0023. The value of g can vary, however, and can be calculated by rearrangement of the above equation, i.e.,

$$g = \frac{h\nu}{\beta B}$$

using the magnetic field and the frequency of the spectrometer. Since h , ν , and β should not change during an experiment, g values decrease as B increases. The concept of g can be roughly equated to that of chemical shift in NMR.

Materials and methods for EPR

HsETHE1 has been dialyzed o/n against 5 L of HEPES 50 mM, NaCl 100 mM, TCEP 1mM, pH 8.0. The protein solution used was 50 μL 1mM.

X-Band EPR spectra were recorded on a Bruker ELEXSYS E500 spectrometer equipped with the Bruker standard cavity (ER4102ST) and a helium flow cryostat (Oxford Instruments ESR 910). Microwave frequencies were calibrated with a Hewlett-Packard frequency counter (HP5352B), and the field control was calibrated with a Bruker NMR field probe (ER035M). Spin quantification was accomplished by double integration of the experimental derivative spectra and comparison with an iron standard. Only linear corrections were invoked for adjustments of the experimental baseline.

2.4.16 Mössbauer spectroscopy

In 1957 Rudolf Mossbauer achieved the first experimental observation of the resonant absorption and recoil-free emission of nuclear γ -rays in solids during his graduate work at the Institute for Physics of the Max Planck Institute for Medical Research in Heidelberg Germany.[95] The Mossbauer effect can be described very simply by looking at the energy involved in the absorption or emission of a γ -ray from a nucleus. When a free nucleus absorbs or emits a γ -ray to conserve momentum the nucleus must recoil, so in terms of energy:

$$E_{\gamma\text{-ray}} = E_{\text{nucleartransition}} - E_{\text{recoil}}$$

When in a solid matrix the recoil energy goes to zero because the effective mass of the nucleus is very large, the momentum can be conserved with negligible movement of the nucleus. So, for nuclei in a solid matrix:

$$E_{\gamma\text{-ray}} = E_{\text{nucleartransition}}$$

This is the Mossbauer effect, which results in the resonant absorption/emission of γ -rays and gives us a means to probe the hyperfine interactions of an atoms nucleus and its surroundings. A Mossbauer spectrometer system consists of a γ -ray source that is oscillated toward and away from the sample by a “Mossbauer drive”, a collimator to filter the γ -rays, the sample, and a detector. The primary characteristics looked at in

Mossbauer spectra are isomer shift (IS), quadrupole splitting (QS), and magnetic splitting (MS or hyperfine splitting). These characteristics are effects caused by interactions of the absorbing nucleus with its environment. Isomer shift is due to slightly different nuclear energy levels in the source and absorber due to differences in the s-electron environment of the source and absorber. The oxidation state of an absorber nucleus is one characteristic that can be determined by the IS of a spectra. For example due to greater d electron screening Fe²⁺ has less s-electron density than Fe³⁺ at its nucleus which results in a greater positive IS for Fe²⁺. For absorbers with nuclear angular momentum quantum number $I > \frac{1}{2}$ the non-spherical charge distribution results in quadrupole splitting of the energy states. For example Fe with a transition from $I=1/2$ to $3/2$ will exhibit doublets of individual peaks in the Mossbauer spectra due to quadrupole splitting of the nuclear states. In the presence of a magnetic field the interaction between the nuclear spin moments with the magnetic field removes all the degeneracy of the energy levels resulting in the splitting of energy levels with nuclear spin I in $2I + 1$ sublevels.

Materials and methods for Mössbauer spectroscopy

For preparation of the Mössbauer sample, metallic ⁵⁷Fe (Chemotrade, 96% enrichment) was dissolved in 75% (v/v) HCl and 25% methanol (used as proton exchanger) at 75°C o/n under shaking.. The obtained ⁵⁷FeCl₃ solution concentration was determined from the difference in weight of the metal bar before and after treatment. The obtained solution was diluted till a concentration of 100 mM. The solution was directly added to the cell culture medium to a final concentration of 100 μM. ⁵⁷Fe-*Hs*ETHE1 has been dialyzed o/n against 5 L of HEPES 50 mM, NaCl 100 mM, TCEP 1mM, pH 8.0. The protein solution used was 500 μL 1mM.

Mössbauer spectra were recorded with alternating constant acceleration. The minimum experimental line width of the spectrometer was 0.24 mm s⁻¹ (full width at half-height). The sample temperature was kept constant either in an Oxford Instruments Variox or in an Oxford Instruments Mössbauer-Spectromag cryostat. The latter is a split-pair superconducting magnet system for applied fields of up to 8 T, where the temperature of the sample can be varied in the range of 1.5-250 K. The field at the sample is

perpendicular to the γ -beam. The $^{57}\text{Co}/\text{Rh}$ source (1.8 GBq) was positioned at room temperature inside the gap of the magnet system at a zero-field position. Isomer shifts are quoted relative to iron metal at 300 K.

2.4.17 Molecular visualization tools

The following programs have been used for molecular visualization, structural analysis and molecular building: PyMol (v. 2.r1; <http://www.pymol.org/>), DS Visualizer (v. 2.5; <http://accelrys.com>), RasMol (v. 2.7; <http://rasmol.org>), Spdbv (v. 4.0; <http://spdbv.vital-it.ch>), UCSF Chimera[96] (v. 1.4; <http://www.cgl.ucsf.edu/chimera/>), VMD (v. 1.8; <http://www.ks.uiuc.edu/Research/vmd>).

3 Results

This chapter is devoted to the results obtained about the biochemical and biophysical characterization of *Hs*ETHE1 and about the XAS characterization of highly interesting bioinorganic compounds and metallo-proteins, such as $[\text{Cu}_2\text{L}_2(\mu\text{-O})_2]\text{I}_2$, the mononuclear [Fe]-hydrogenases Hmd and the [Fe-S]-cluster dependent ATP binding cassette protein ABCE1.

3.1 Biochemical and biophysical characterization of *Homo sapiens* ETHE1

Broaden our knowledge about *Hs*ETHE1 could lead to defeat the devastating, infantile, metabolic disorder known as ethylmalonic encephalopathy and to fight a common form of liver cancer (HCC).

3.1.1 Cloning

Several construct have been created starting from the wild type full length sequence of *Hs*ETHE1. Different cloning techniques have been used (see par. 2.1.2.5) and the LIC protocol was the more efficient method. In Fig. 13 there is an example of an agarose gel showing the run of two pETM vectors and *Hs*ETHE1 pPCRps.

The following constructs have been created as discussed in par. 2.1:

wt-*Hs*ETHE1_pETM11; Δ 14-*Hs*ETHE1_pETM11; Δ 24-*Hs*ETHE1_pETM11;

wt-*Hs*ETHE1_pETM13; Δ 14-*Hs*ETHE1_pETM13; Δ 24-*Hs*ETHE1_pETM13;

Δ 14-*Hs*ETHE1- Δ 4_pETM-11_LIC; Δ 19-*Hs*ETHE1- Δ 4_pETM-11_LIC;

Δ 19-*Hs*ETHE1- Δ 4_pETM-20_LIC;

Δ 7-*Hs*ETHE1- Δ 4_pETM-11_LIC;

MutA-*Hs*ETHE1_pETM-11_LIC;

MutB-*Hs*ETHE1_pETM-11_LIC;

MutC-*Hs*ETHE1_pETM-11_LIC;

MutD-*Hs*ETHE1_pETM-11_LIC.

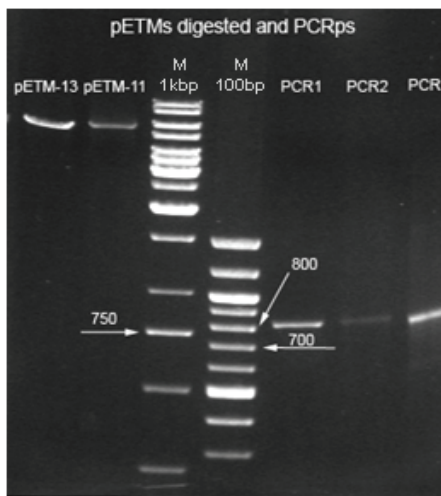


Fig. 13: Agarose gel of *HsETHE1* and plasmid vectors DNA.

Agarose gel showing the DNA of the vectors pETM-13 (first lane), pETM-11 (second lane), and PCR reaction products from the amplification of *HsETHE1* (lanes 5-7).

The constructs have been used to transform the following cell lines:

Plasmid propagation cell lines

DH5 α , Top10, Solopack, Nova Blue.

Protein expression cell lines

BL21(DE3), BL21(DE3)-pLys, BL21(DE3)-Star, BL21(DE3)-Rosetta, BL21(DE3)-RIL, Origami.

The BL21(DE3) cell line is the used for most of the constructs overexpression.

3.1.2 Expression and purification

- Tests were carried to check for the protein expression level and its localization, favoring the constructs resulting in the expression of the protein within the soluble fraction (Tab. 1). The addition of Fe(II)(NH₄)₂SO₄ to the cultures increased significantly the quantity of cells and protein without affecting its ratio in the soluble fraction.

Eventually, the constructs:

- Δ 14-*HsETHE1*_pETM11
- Δ 14-*HsETHE1*- Δ 4_pETM-11_LI
- Δ 7-*HsETHE1*- Δ 4_pETM-11_LIC
- MutA-*HsETHE1*_pETM-11_LIC
- MutB-*HsETHE1*_pETM-11_LIC
- MutC-*HsETHE1*_pETM-11_LIC

were used to follow up with the purification.

As isolate *HsETHE1*-constructs purification

	Expression	Soluble frac.	1 st Pur. IMAC	2 nd Pur. TEV	3 rd Pur SEC
wtE-his ₆	✓	×			
Δ14E-his ₆	✓	1/2	✓	✓	✓
Δ24E-his ₆	✓	1/4			
wtE	✓	×			
Δ14E	✓	1/2			
Δ24E	✓	×			✓
Δ14EΔ4-his ₆	✓	3/4	✓	✓	
Δ19EΔ4-his ₆	✓	1/4			
Δ19EΔ4-trx-his ₆	✓	1/4			
Δ7EΔ4-his ₆	✓	1/2	✓	✓	✓
MutA: [E206A,E207A, E208A]_Δ7EΔ4-his ₆	✓	1/2	✓	✓	✓
MutB: [E206A,E207A, E208A,E44A]_Δ7EΔ4-his ₆	✓	1/2	✓	✓	✓
MutC [E206A,E207A, E208A,K66A,E67A]_Δ7 EΔ4-his ₆	✓	1/2	✓	✓	✓
MutD [E24A,K66A,E67A]_Δ7Hs EΔ4-his ₆	✓	1/2	✓	✓	✓

Tab. 1: HsETHE1 constructs.

All proteins were expressed in the selected cell lines. The protein fraction that has been found in the soluble fraction, and which steps of purification were performed (1st Pur.: immobilized metal affinity chromatography; 2nd Pur.: purification from TEV, uncleaved protein and cleaved tags; 3rd Pur.: size exclusion chromatography).

The protein constructs have been expressed in ultra rich auto-inducing media for ~23h at 25°C, until an OD₆₀₀ greater than 10. The harvested cells were centrifuged and the obtained pellet has been resuspended in TrisHCl 50 mM, NaCl 200 mM, imidazole 20 mM, pH 8.0, and sonicated for the cell lysis. The lysate was immediately ultracentrifuged and the supernatant (soluble fraction) collected and filtered through a 0.22 μm cut-off membrane. SDS-PAGE showed the protein levels before induction, after

Results

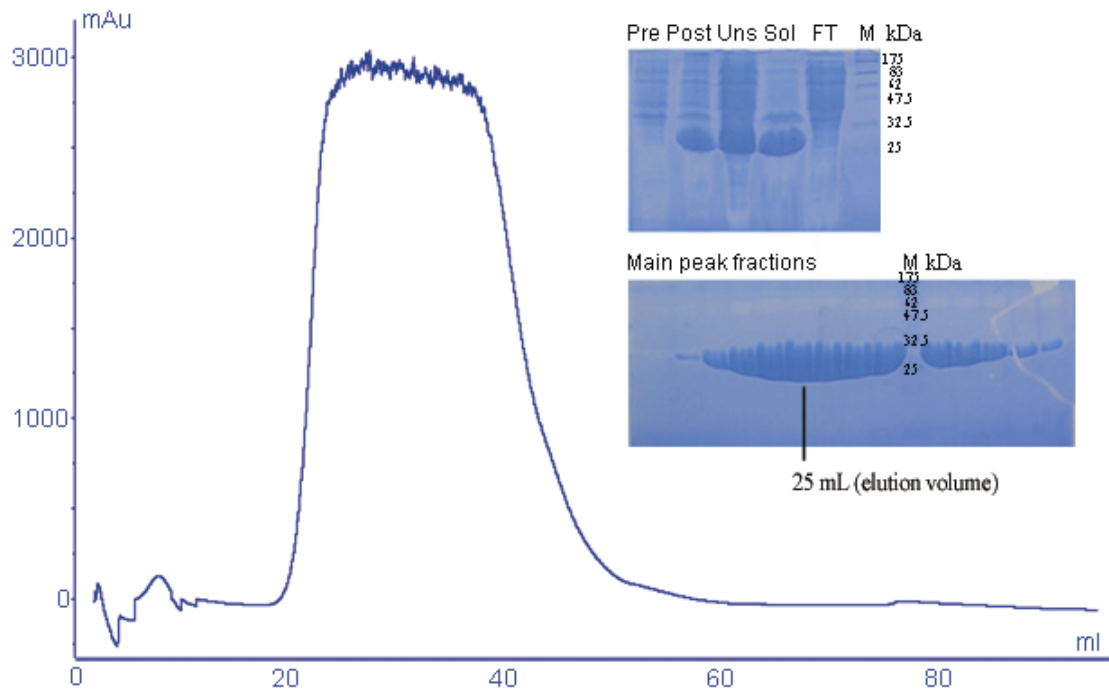


Fig. 14: *HsETHE1* IMAC

First step of purification: IMAC chromatogram and SDS-PAGEs. In the chromatogram, the main peak shows the oversaturation of the UV₂₈₀ signal due to the abundance of the protein. The upper gel picture shows the cell lysate fraction before induction (Pre), the cell fraction after expression (Post), the insoluble (Uns) and the soluble (Sol) fractions after sonication and ultracentrifugation, and the flow through (FT) of the soluble fraction loaded into the IMAC column. The gel in the bottom shows the IMAC main peak fractions.

induction, in the insoluble fraction, in the soluble fraction and in the flow through (FT) of the supernatant loaded onto the IMAC column (Fig. 14). Successively, the supernatant underwent through an IMAC purification step and the main absorption (A_{280}) peak was tested by SDS-PAGE as well (Fig. 14). Usually, the protein yield was > 100 mg/L culture and the column got saturated. This resulted in the oversaturation of the UV₂₈₀ signal of the purifier internal spectrophotometer. Under saturating conditions the protein eluted from the column typically had higher purity. Afterwards, the protein fractions corresponding to the main peak were pulled together and the *HsETHE1*-construct was incubated o/n with TEV protease at T_a for the cleavage of the his₆-tag (Fig. 15). The day after, the protein solution has been diluted 10 times and loaded on another IMAC column to separate the *HsETHE1* construct from the TEV (endowed with a his₆-tag itself) and from the cleaved tags. The so obtained protein solution was concentrated to

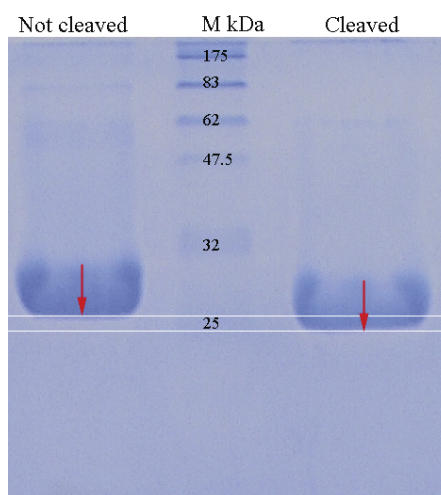


Fig. 15: *HsETHE1* TEV cleavage.

Second step of purification: SDS-PAGE of *HsETHE1*+his₆-tag prior and after TEV protease cleavage of the tag. The white lines show the different running fronts of the not cleaved (left) and cleaved forms (right).

~10 mg/mL and loaded onto a SEC column for the separation from remaining impurities and for buffer exchange. The protein elutes between 57 and 70 mL using the Superdex 75 column and between 73 and 90 mL using the Superdex 200 column. The protein fractions were checked by SDS-PAGE and the pure ones (purity > 98%) have been collected giving pure *HsETHE1*-constructs (Fig. 16) in TrisHCl or HEPES 20 or 50 mM, NaCl 100 mM, TCEP 1 mM pH8.0.

Metal-free *HsETHE1* purification

I developed a reproducible and robust protocol to obtain high quality apo-protein. This was a fundamental requirement for metal titration experiments by ITC. I initially tried the metal stripping with different concentration of EDTA (bivalent cations chelator), phenanthroline (chromogenic iron chelator, which appears red if the bound to Fe²⁺ and blue if bound to Fe³⁺) and deferoxamine mesylate (specific iron-ion chelator). These compounds alone were not capable to withdraw the metal from the protein. I tried the same procedure in the presence of different concentration of urea. Eventually, an o/n incubation of the protein in 2M urea and 50mM of deferoxamine and subsequent extensive multiple dialysis with metal free buffer yielded metal-free *HsETHE1*, as shown by TXRF (see par. 3.1.7).

3.1.3 Protein stability

For protein stability we can refer both to the tendency to form aggregates, precipitates or degradation products. *HsETHE1* had never shown degradation products. Within this paragraph, each time I refer to the stability of the protein, I refer to its tendency to form large aggregates inclined to precipitation.

HsETHE1 possesses 9 cysteine residues and none is thought to be involved in inter-molecule or intra-molecules disulfide bridges. Therefore, the addition of a reducing

Results

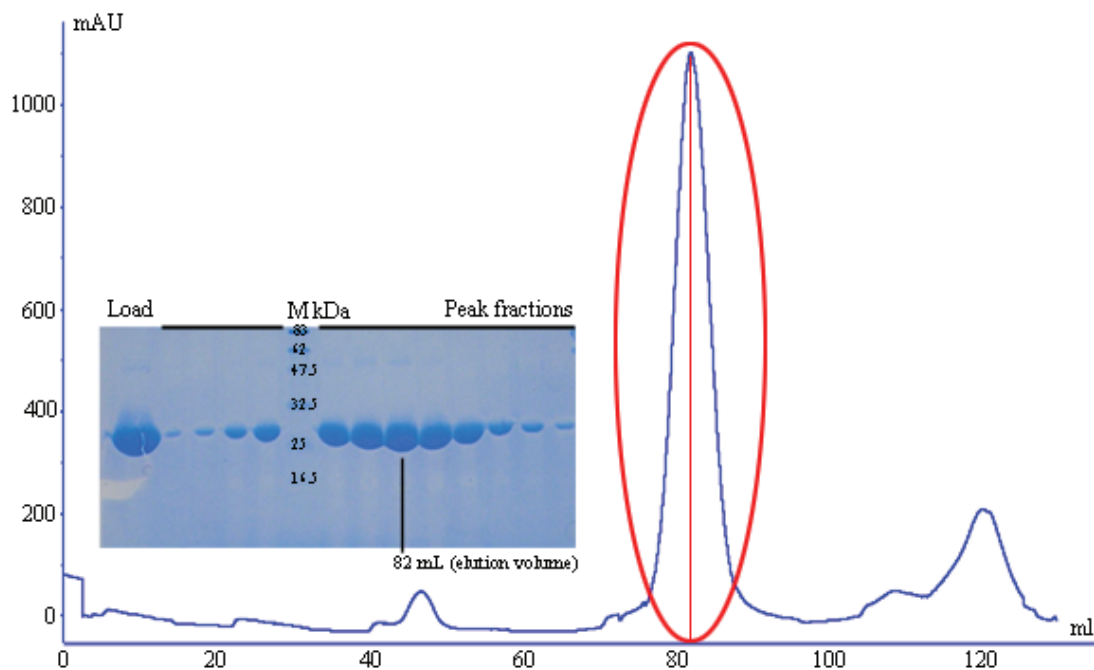


Fig. 16: HsETHE1 SEC.

Third step of purification: the picture shows a SEC chromatogram of HsETHE1 obtained with a Superdex200 1660 column and the SDS-PAGE of the eluted fractions. The main peak corresponds to the protein elution peak and is highlighted by a red oval. A red line is marking the protein elution volume (centered at 82 mL). The SDS-PAGE shows a sample of the protein solution before loading onto the column (Load) and the eluted fraction corresponding to the protein peak.

agent keeping the protein sulfurs in reduced state is mandatory in order to obtain stable protein solution. When DTT was added to a HsETHE1 solution the protein partially precipitated. I repeated the experiment adding DTT under N₂ flux and this time the protein solution, initially turned darkish and after some hours lost its color and the protein precipitated (Fig. 17 A, B). This suggested that the mercapto-based reducing compounds (R-SH) could have an effect on the iron-bound active site of the protein and that oxygen may be involved. The UV-Vis spectra of the protein in the absence and in the presence of DTT revealed that the absorption profile is changing in the whole region from 250 to 550 nm, especially at 300 and 450 nm, which can be an indication of metal-sulfur charge transfer (Fig. 17 D).[97,98]

Besides, I tested a variety of reducing agents, including β -mercaptoethanol, DTT, dithionite (not mercapto-based compound) and TCEP. The solutions were analyzed for aggregation by an optical microscope. The results showed clearly that β -mercaptoethanol and in particular DTT have a deleterious effect on the stability of the

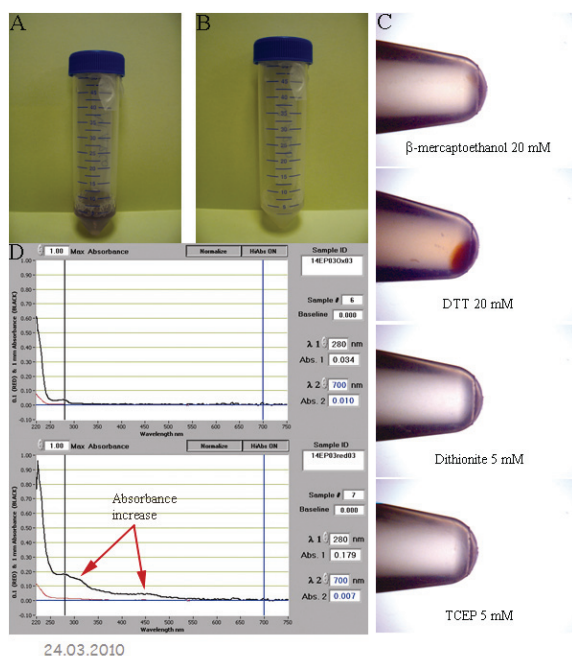


Fig. 17: reducing agents test.

Influence of reducing agents on *HsETHE1*. A) Addition of DTT 50 mM to a 5 mg/mL *HsETHE1* solution under N_2 flux. The solution turns darkish. B) The same protein solution of A after o/n incubation. The color is lost and the protein is fully precipitated. C) Protein solution after incubation with different reducing agents. Protein precipitation is visible for the solutions enriched with β -mercaptoethanol and particularly with DTT. D) UV-Vis spectra of a *HsETHE1* solution without reducing agents (upper) and with 20 mM DTT (lower).

- -20°C: totally unstable. The protein precipitates immediately if frozen at -20°C and quickly thawed.
- -80°C: The protein is quite stable. Little precipitation (5%) is found after thawing, independently from the time spent at this temperature.

To optimize the storage at -80°C, glycerol had been added to the protein solution, which was quickly frozen in LN and stored at -80°C. This procedure prevented any kind of precipitation. Glycerol in a concentration of about 5/10% is enough for the protein stabilization. Thereby, the optimal condition for *HsETHE1* storage is at -80°C, after a quick freeze in LN in the presence of 10% glycerol.

I looked also for the best buffer able to enhance the stability of *HsETHE1* in solution.

protein, which started to aggregate and form a precipitate after centrifugation (Fig. 17 C). Such effect was not detectable when dithionite or TCEP were used. Considering the efficiency and stability of TCEP, this compound has been selected as standard reducing agent for this work on *HsETHE1*.

In order to look for an optimal condition for protein storage, the stability of *HsETHE1* at different temperatures had been checked: T_a , 4, -20 and -80°C. Samples of protein were left for one month at different temperatures and the protein was checked for precipitation at defined intervals of time: after 1 day, 2 days, a week, 2 weeks, 3 weeks and 1 month.

- T_a : stable for 2 days-1 week.
- 4°C: stable for 1-2 weeks.

Results

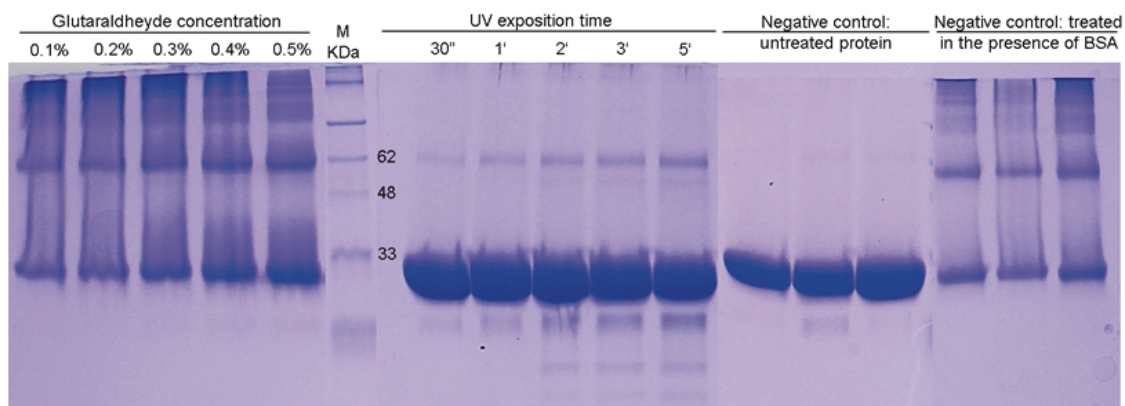


Fig. 18: SDS-PAGE of the cross-linking experiment samples.

For this purpose, a thermofluor machine has been used, testing 96 conditions. The experiment showed that TrisHCL and HEPES based buffers were optimal for the stability of the protein. The pH effect is more consistent. The protein prefers pHs from 4 to 5 and from 7 to 9, which is consistent with the isoelectric point of most of the used protein constructs that is about 6.0. During all preparations and experiments, HEPES or TrisHCl based buffers at the pH of 8.0, with the addition of NaCl 100/200 mM and TCEP 1mM, have been used.

3.1.4 Oligomeric state and exact mass determination

The oligomeric state and the exact Molecular Mass (MM) of *HsETHE1* have been determined by SLS, crosslinking and MS.

3.1.4.1 Crosslinking experiment

Crosslinking experiments carried out with UV-A light and with a chemical crosslinker showed clearly that *HsETHE1* is present in solution as a dimer (otherwise, would have been unlikely to detect the dimer formation in denaturing conditions). In fact, the protein ran mainly as monomer and dimer during SDS-PAGE (Fig. 18).

3.1.4.2 Static Light Scattering (SLS)

SLS showed us that the protein is prompt to aggregate if not kept under optimal conditions. In fact, to carry out a successful SLS experiment the protein must be freshly

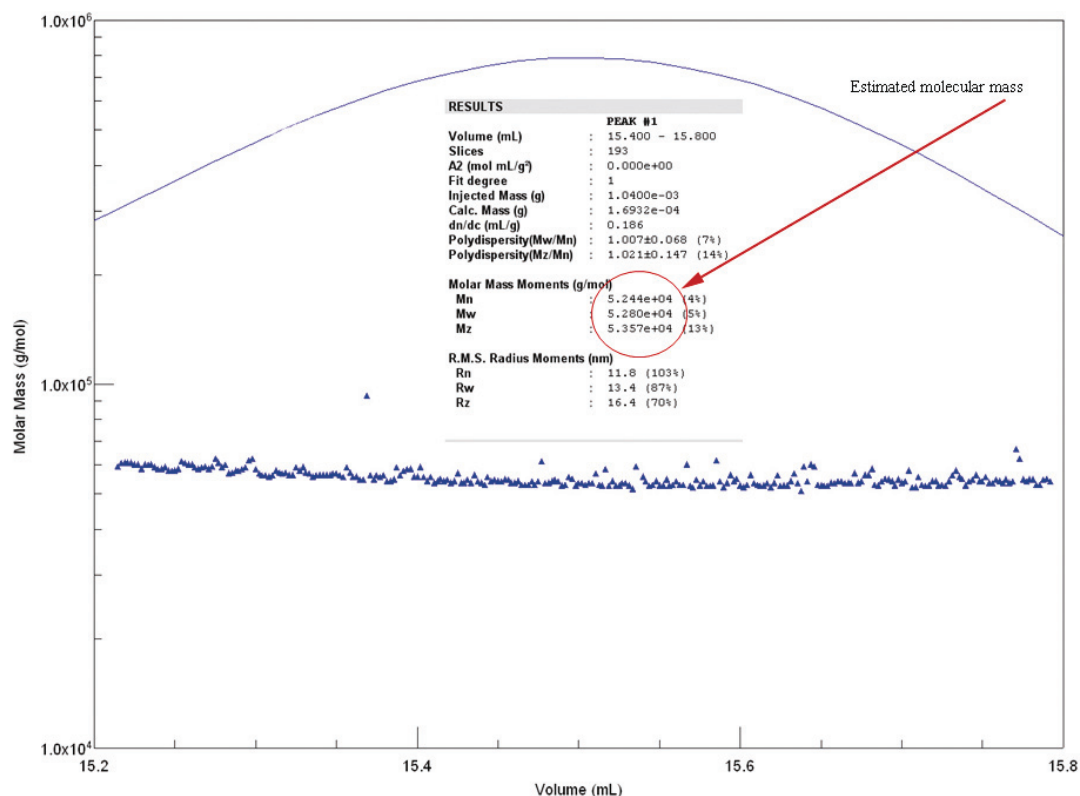


Fig. 19: SLS spectrum of HsETHE1.

The blue line represents the UV₂₈₀ signal corresponding to the chromatographic protein peak. The blue spots represent the scattering signal deriving from the protein. Between the line and the spots, a table shows the parameter values resulting from the data analysis. The red circle is highlighting the molecular mass found for HsETHE1 in solution: 52.8 kDa, corresponding to a dimer.

prepared or optimally conserved and fresh TCEP must be present in the buffer. SLS revealed that the protein in solution is a homodimer, in similarity with AtETHE1.[13] Moreover, SLS estimated the molecular mass of the dimer to be 52.8 kDa (Fig. 19).

3.1.4.3 Mass Spectrometry (MS)

MS performed on the native protein provided interesting quantitative information about the monomer and dimer molecular mass and qualitative information about the strength of the homodimeric interaction. MS determined a molecular mass for the monomer of 26.7 kDa and it was also able to detect and determine the mass of the dimer of 53.4 kDa (Fig. 20). The detection of the ETHE1 dimer under MS conditions suggests that the interaction between the subunits is strong.

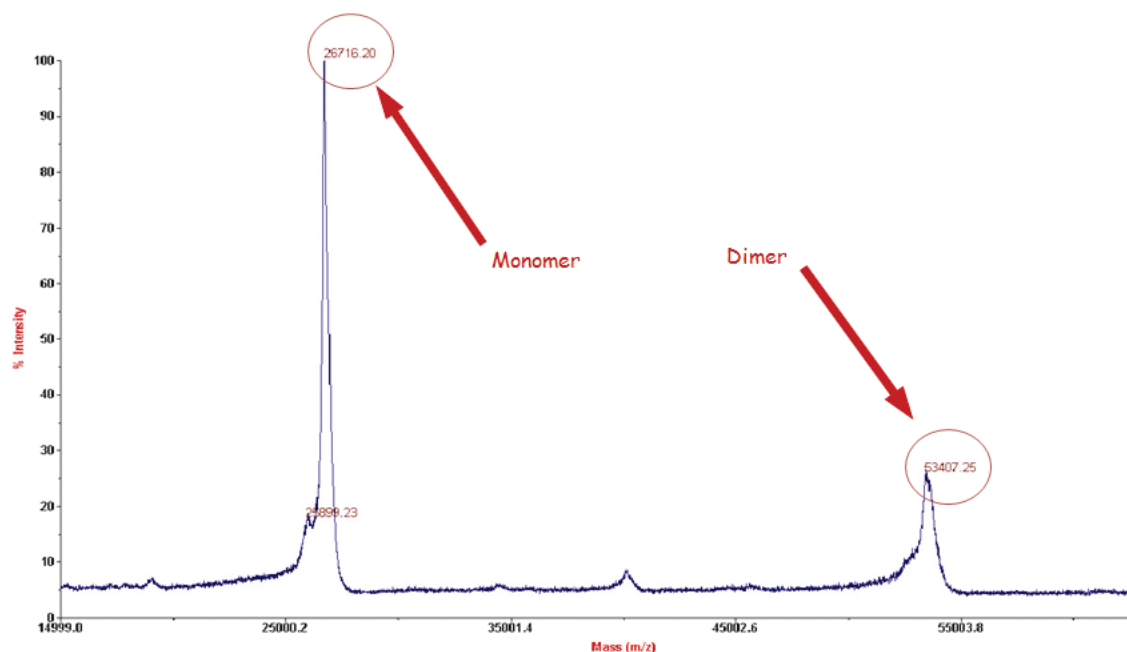


Fig. 20: Mass spectrometry spectrum of *HsETHE1* as isolated.

The spectrum shows the peaks corresponding to the monomer (26.7 kDa) and the dimer (53.4 kDa) of *HsETHE1*.

The overall results of the SLS, crosslinking and MS experiments demonstrated that *HsETHE1* is a homodimer in solution with a molecular mass of 53.1 kDa (average between the MM calculated with SLS and MS). The expected MM predicted by ProtParam (www.expasy.org) was of 53 kDa.

3.1.5 Substrate screening

The β -lactamase, phosphatase, and arylsulfatase activities were tested in one experiment using the following potential substrates: nitrocefin (β -lactam), bis(p-nitrophenyl)phosphate, p-nitrocatechol sulfate and p-nitrophenyl sulfate. Nitrocefin turns from yellow to red/dark red (max absorption at 486 nm) upon hydrolysis. Anyhow, under standard conditions, due to its sensitivity to light and different pHs, it can turn orange over time because of spontaneous hydrolysis (Fig. 21, column 1). The other compound solutions turn from colorless to yellow/orange or from light-yellow to yellow/orange (p-nitrocatechol sulfate), with maximum of absorption at 405 nm upon hydrolysis. The protein used was *HsETHE1* as isolated, the apo-form with addition of iron and the apo-form in presence of EDTA. The negative controls were carried out

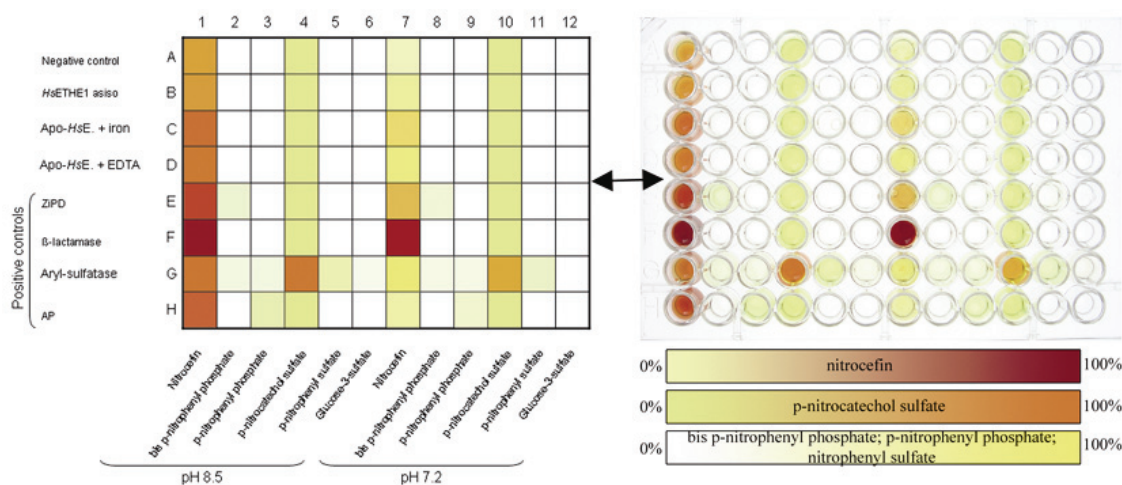


Fig. 21: Results of a substrate screening test.

Substrate screening carried out to test the lactamase, phosphatase and aryl-sulfatase activity of *HsETHE1*. On the left there is a schematic representation of the experiment shown on the right. On the bottom right, a legend for the interpretation of the results is given (from 0 to 100% activity). The experiment has been carried at two pHs. The results for the two different pHs are complementary, except for Nitrocefin (columns 1 and 7), where the pH-sensitivity is reflected in the spontaneous hydrolysis observed at pH 8.5. The results show a mild activity for apo-*HsETHE1* in the presence of 2 molar excess of ammonium iron sulfate.

using the substrates with no enzymes and glucose-3-sulfate, which is not a substrate of any used enzyme. For the positive controls I used: penicillinase type III, alkaline phosphatase and sulfatase type VIII, all commercially available. Also the zinc phosphodiesterase ZiPD was used. ZiPD is a MβL-like protein, thereby it is structurally related to *ETHE1*. ZiPD is able to hydrolyze bis(p-nitrophenyl)phosphate.[99] The activity was tested at pH 8.5 (tris buffer) and 7.2 (phosphate buffer), corresponding to the mean physiological values, respectively found in the mitochondrial matrix[79] and in the cytoplasm[78] of human cells. The results show a mild detectable β-lactamase activity for the apo-*HsETHE1*+iron, but not for the protein as isolated (Fig. 21). A similar β-lactamase activity is present for ZiPD. Further experiments showed that the hydrolysis of nitrocefin cannot be addressed to the protein (data not shown). Thus, no significant β-lactamase, phosphatase, arylsulfatase and sulfatase activities were detected. Besides, I probed the esterase activity using p-nitrophenyl acetate. The reaction can be followed by the change in color from colorless to yellow upon hydrolysis. As negative controls, I used the substrate with no enzyme and simple buffer with no substrate and no enzyme. The positive control consisted of substrate incubated with a commercially available esterase. The results show esterase activity for apo-*HsETHE1*+iron (Fig. 22).

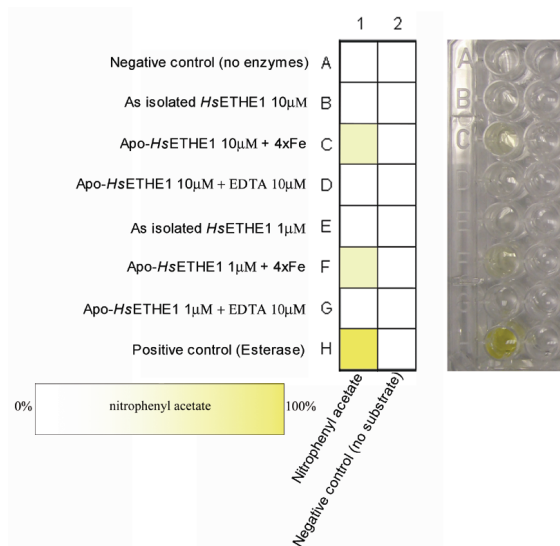


Fig. 22: Results of the esterase activity test.

On the left it is shown a schematic representation of the experiment presented on the right. On the bottom left, a legend for the interpretation of the results is given (from 0 to 100% activity). The results showed a mild esterase activity for apo-*HsETHE1* in the presence of 4 molar excess of ammonium iron sulfate. Further experiments (data not shown) proved that the hydrolysis is due to free-iron in solution.

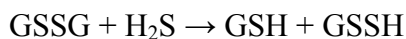
Further experiments proved that the hydrolysis was due to the presence of free iron-ions in solution, which acted as catalyst for the hydrolysis.

It is worth to notice that *HsETHE1* is structurally very similar to the glyoxalase II enzymes, which are able to hydrolyze S-(2-hydroxyacyl)-glutathione to glutathione and 2-hydroxy-carboxylate. The glyoxalase II activity was not probed because it was already tested with negative results.[9]

3.1.6 UV-Vis and the interaction with reduced glutathione

The UV-Vis spectrum of *HsETHE1* has been recorded looking for signature features. No particular feature characterizes the *HsETHE1* UV-Vis spectrum (Fig. 23 A).

During experiments aimed to test spectrophotometrically the sulfur dioxygenase activity of *HsETHE1* independently from oxygen consumption measurements, I found an unexpected color change. The protein became blue upon addition of the following reaction mixture:



The products are GSSH and GSH, which correspond to the substrate of *HsETHE1* and to one of the products of the protein reaction, respectively. Batch experiments with individual components of reaction 2 revealed that the responsible for the color gaining was reduced glutathione (GSH). This is highly interesting because GSH may have a regulatory activity on the enzyme. *HsETHE1* activity experiments indicate that GSH is

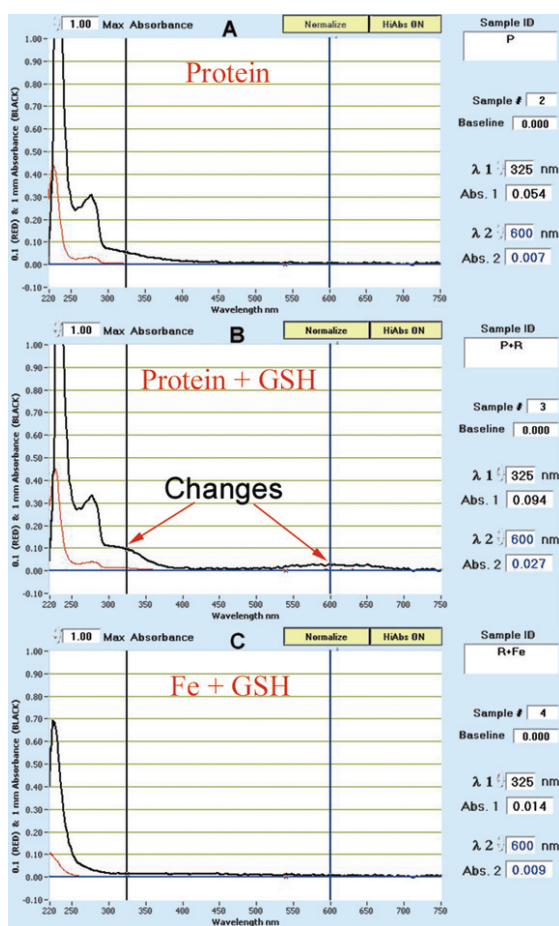


Fig. 23: *HsETHE1* UV-Vis.

This picture shows the UV-Vis spectra of *HsETHE1* in solution. A) The same sample with the addition of reduced glutathione. B) An iron(II) solution with the addition of reduced glutathione. The solvent used is the protein buffer (C). Spectra A and B revealed that reduced glutathione has an effect on the protein UV-Vis spectra. This is particularly evident around 325 and 600 nm. Spectrum C is used as control and confirmed that the effect is not due to the only presence of glutathione or the interaction of glutathione with iron.

Fluorescence (TXRF)

TXRF has been applied to

unlikely to have inhibitory effect on the enzyme.[11] In fact, excess of GSH is used in these experiments in order to produce the substrate GSSH.

To further investigate the interaction between the protein and GSH, I performed UV-Vis and ITC experiments. The UV-Vis spectra showed an increase of the absorbance at 325 and 600 nm for the sample protein+GSH that can be addressed only to an interaction between the two molecules (Fig. 23). Intriguingly, these absorption peaks are more intense and at higher wave-length than those observed for *HsETHE1* in presence of DTT (see par. 3.1.3; Fig. 17) Similar absorption spectra are reported for oxy-hemocyanin (350 and 580nm), a binuclear-copper oxygen-carrying protein, that appears blue in the presence of oxygen[100] and for the Co^{2+} -substituted β -lactamase from *A. hydrophila*. [28]

3.1.7 Total X-ray Reflection

Results

A	Sc conc. [µM] corr. SB	Sc error [%]	Cr conc. [µM] corr. SB	Cr error [%]	Mn conc. [µM] corr. SB	Mn error [%]	Fe conc. [µM] corr. SB	Fe error [%]	Co conc. [µM] corr. SB	Co error [%]	Ni conc. [µM] corr. SB	Ni error [%]	Cu conc. [µM] corr. SB	Cu error [%]	Zn conc. [µM] corr. SB	Zn error [%]	Ga conc. [µM] corr. SB	Ga error [%]
P30_B	445.05	0	1.08	13	0.38	27	2.74	5	0.30	21	0.54	10	0.34	12	0.09	40	28.69	0
P30_B	445.05	0	0.81	14	0.39	22	3.03	4	0.19	28	0.37	12	0.23	15	0.05	66	28.69	0
P30_B	445.05	0	1.15	15	0.70	19	3.41	4	0.38	20	0.46	13	0.32	15	0.22	19	28.69	0
P30	445.05	0	0.85	15	0.68	15	58.60	0	0.47	14	2.31	2	0.29	14	0.47	7	28.69	0
P30	445.05	0	0.44	26	0.77	12	56.05	0	0.35	17	2.27	2	0.28	12	0.40	8	28.69	0
P30	445.05	0	0.88	20	0.59	23	58.10	0	0.44	20	2.30	3	0.34	15	0.49	9	28.69	0

B	Sc conc. [µM] corr. SB	Sc error [%]	Cr conc. [µM] corr. SB	Cr error [%]	Mn conc. [µM] corr. SB	Mn error [%]	Fe conc. [µM] corr. SB	Fe error [%]	Co conc. [µM] corr. SB	Co error [%]	Ni conc. [µM] corr. SB	Ni error [%]	Cu conc. [µM] corr. SB	Cu error [%]	Zn conc. [µM] corr. SB	Zn error [%]	Ga conc. [µM] corr. SB	Ga error [%]
P15_B	444.89	2	1.51	44	0.78	63	1.67	23	1.10	25	0.73	29	0.73	25	0.73	23	28.68	
P15_B	444.89	1	1.58	26	1.34	24	1.72	15	0.99	18	0.44	33	0.51	26	0.01	757	28.68	
P15_B	444.89	2	1.11	56	0.91	51	2.73	15	1.05	27	1.10	21	0.75	24	0.23	74	28.68	

C	Sc conc. [µM] corr. SB	Sc error [%]	Cr conc. [µM] corr. SB	Cr error [%]	Mn conc. [µM] corr. SB	Mn error [%]	Fe conc. [µM] corr. SB	Fe error [%]	Co conc. [µM] corr. SB	Co error [%]	Ni conc. [µM] corr. SB	Ni error [%]	Cu conc. [µM] corr. SB	Cu error [%]	Zn conc. [µM] corr. SB	Zn error [%]	Ga conc. [µM] corr. SB	Ga error [%]
P15	444.8900	1	2.0289	20	0.8467	38	25.4064	2	0.6734	31	2.0212	9	0.0165	679	0.0951	111	28.6800	1
P15	444.8900	1	1.4278	38	0.3346	126	28.9775	3	1.0411	28	2.8363	9	0.4111	40	0.4712	32	28.6800	1
P15	444.8900	1	3.0455	17	1.0925	34	27.0455	2	0.8915	28	2.8145	8	0.3620	42	0.3391	40	28.6800	1

D	Sc conc. [µM] corr. SB	Sc error [%]	Cr conc. [µM] corr. SB	Cr error [%]	Mn conc. [µM] corr. SB	Mn error [%]	Fe conc. [µM] corr. SB	Fe error [%]	Co conc. [µM] corr. SB	Co error [%]	Ni conc. [µM] corr. SB	Ni error [%]	Cu conc. [µM] corr. SB	Cu error [%]	Zn conc. [µM] corr. SB	Zn error [%]	Ga conc. [µM] corr. SB	Ga error [%]
Apo11F_B	445.05	0	0.97	20	0.65	22	2.49	5	0.37	22	0.75	9	0.48	11	0.29	16	28.69	0
Apo11F_B	445.05	0	0.97	22	0.57	27	2.54	5	0.70	13	0.92	8	0.45	13	0.25	20	28.69	0
Apo11F_B	445.05	0	0.72	24	0.53	24	2.37	5	0.35	21	0.56	11	0.44	12	5.33	1	28.69	0
Apo11F	445.05	0	0.74	17	1.25	8	1.82	4	0.41	14	2.22	2	0.17	22	2.97	2	28.69	0
Apo11F	445.05	0	0.70	19	1.35	8	1.61	5	0.31	19	2.68	2	0.21	18	4.00	1	28.69	0
Apo11F	445.05	0	0.49	28	1.02	11	1.35	6	0.30	20	2.72	2	0.29	14	3.94	1	28.69	0

E	Sc conc. [µM] corr. SB	Sc error [%]	V conc. [µM] corr. SB	V error [%]	Cr conc. [µM] corr. SB	Cr error [%]	Mn conc. [µM] corr. SB	Mn error [%]	Fe conc. [µM] corr. SB	Fe error [%]	Co conc. [µM] corr. SB	Co error [%]	Ni conc. [µM] corr. SB	Ni error [%]	Cu conc. [µM] corr. SB	Cu error [%]	Zn conc. [µM] corr. SB	Zn error [%]	Ga conc. [µM] corr. SB	Ga error [%]
Apo10_B	445.05	1	0.90	68	2.15	18	1.48	19	1.46	15	0.05	260	0.52	25	0.37	29	0.02	370	28.69	1
Apo10_B	445.05	2	0.24	300	1.16	39	0.56	54	2.01	14	0.74	25	1.08	15	0.71	18	0.32	35	28.69	1
Apo10_B	445.05	2	0.06	1255	0.76	62	0.88	40	1.77	16	1.03	20	0.67	24	0.40	30	0.40	29	28.69	1
Apo10	445.05	2	1.08	156	1.41	72	3.28	25	3.68	17	1.62	28	4.21	11	0.72	42	1.88	15	28.69	2
Apo10	445.05	1	1.30	52	1.83	27	1.65	24	0.93	30	0.40	50	1.94	12	0.30	49	1.25	13	28.69	1
Apo10	445.05	2	1.94	48	2.81	23	1.62	30	1.16	31	0.28	91	2.11	13	0.44	43	1.78	11	28.69	2

Tab. 2: TXRF results on the as isolated and metal-free *HsETHE1*.

A) Example of TXRF analysis results for *HsETHE1* as isolated (P30=protein; P30_B=buffer). B, C) Another example of TXRF analysis results for *HsETHE1* as isolated. The results for the buffer (P15_B) are shown in B. The results for the protein (P15) are shown in C. D) Example of TXRF analysis results for the metal-free protein (Apo11F_B= buffer; Apo11F=protein). E) Another example of TXRF analysis results for the metal-free protein (Apo11_B=buffer; Apo10=protein). The protein concentration used in the experiments was of about 57 µM for the protein as isolated and 40 µM for the metal-free protein. The results in A show that the iron: protein ratio is 1:1, respect the protein-free buffer where the iron concentration approaches basal levels. The results in D and E show that the iron concentration in the protein-free buffer and in the apo-protein preparation is comparable.

- Check for metal contamination of the buffers.
- Investigate the iron:protein ratio.
- Check the quality of the protein preparations for XAS.
- Check the quality of the apo-protein preparations.

TXRF showed that the buffers used were transition metals free, even when they were not treated with chelex. The iron:protein ratio has been always found to be of 1:1 (Tab. 2 A, B, C). Moreover, thanks to TXRF it has been possible to develop a robust and reproducible protocol for the apo-*Hs*ETHE1 production. This has been a necessary step in order to perform reliable ITC titration experiments (Tab. 2 D, E). Thereby, in terms of metal quantification, TXRF should be thought as powerful technique for standard quality check of protein preparations and solutions.

3.1.8 Isothermal Titration Calorimetry (ITC)

I carried out a large number of microcalorimetric experiments in order to determine the stoichiometry and the binding constants for different metals and reduced glutathione.

3.1.8.1 Metal titration

In these experiments *Hs*ETHE1 has been titrated with different metal solutions obtained using the very same protein buffer. The tested metals were Fe(II), Fe(III), Zn(II), Mn(II), Ni(II), Co(II). The ferrous solution consisted of ammonium iron sulfate in the presence of dithionite. The ferric solution was obtained mixing Fe(III)-citrate with NTA (Nitrilo Triacetic Acid) in a ratio 1:2, giving equilibrium to multiple species (Fe(III)-NTA_n). In this case, we can observe the interaction only if the affinity of Fe(III) for *Hs*ETHE1 is higher than the affinity for NTA and thus the dissociation constant we would observe is not a measure of the real affinity of the protein for the metal free in solution, but lower. We refer to this dissociation constant as “observed dissociation constant” (K_{obs}). The other metal-titrating solutions consisted of zinc chloride, manganese chloride, nickel sulfate and cobalt chloride. In each case, the metals were resuspended and solubilized using the apo-protein dialysis buffer, which contained 1mM of the reducing agent TCEP, which is thought to don't affect the oxidation state of the iron,[101] although this possibility cannot be excluded.[102]

Achieving the best conditions for the experiments has not been straightforward. The main issues were:

1. Difficulty to handle the metal solutions, especially Fe(II) and Fe(III).

2. Use the proper concentration of metal to avoid a dilution enthalpy affecting significantly the signal to noise ratio.
3. Find a protocol that allows obtaining always the same amount and proper concentration of metal in the titrating solution (this is particularly a problem for the ferric solutions, due to its poor solubility).
4. Get an optimized protein concentration on the basis of the metal one. The apo-protein concentration should be low enough to allow the titration to reach the saturation point and not too low so that the signal is not lost.

In order to solve these issues, I took advantage of a cooperative method coupling TXRF and ITC experiments. TXRF allowed the measurement of the metal amount in every solution used in the measurements. The experiments revealed that the protein interacts with the iron present in the Fe(III)-citrate-NTA_(n) solution in a 1:1 stoichiometry ($K_{\text{obs}} = 1.65 \mu\text{M}$) and with Ni(II) in a 1:0.65 stoichiometry ($K_{\text{d}} = 31.6 \mu\text{M}$) (Fig. 24 A, B). Thus, the affinity for Fe(III) is at least 20 times that for Ni(II). Moreover, no interaction is observed titrating with Fe²⁺, Zn²⁺, Mn²⁺ and Co²⁺ indicating a high specificity. The undetected interaction with Fe(II) was unexpected, because metal stripping experiments with phenanthroline, EPR and Mössbauer spectroscopy clearly detect the presence of iron(II). This can be explained from the fact that the iron(III) may turn to an iron(II) upon charge transfer from an anionic coordinating ligand such as aspartate and/or hydroxide (see par. 3.1.10.1). In this case, the metal reduction would be due to the high covalency of the metal/anionic-ligand bond. Commonly, the M β L proteins possess a comparable or lower metal affinity and lower specificity. For example the affinity of ETHE1 for iron is higher than the affinity that the ZiPD/tRNaseZ/ElaC1 phosphodiesterase M β L proteins have for both their zinc binding sites (dissociation constant between 2 and 30 μM).[103] These proteins are also able to bind other metals such as nickel and manganese.

3.1.8.2 Glutathione titration

ITC titration experiments have been carried out to investigate the interaction of HsETHE1 with reduced glutathione. The ITC experiment shows a mild interaction HsETHE1/GSH (Fig. 24 C). The data were fitted considering a different number of

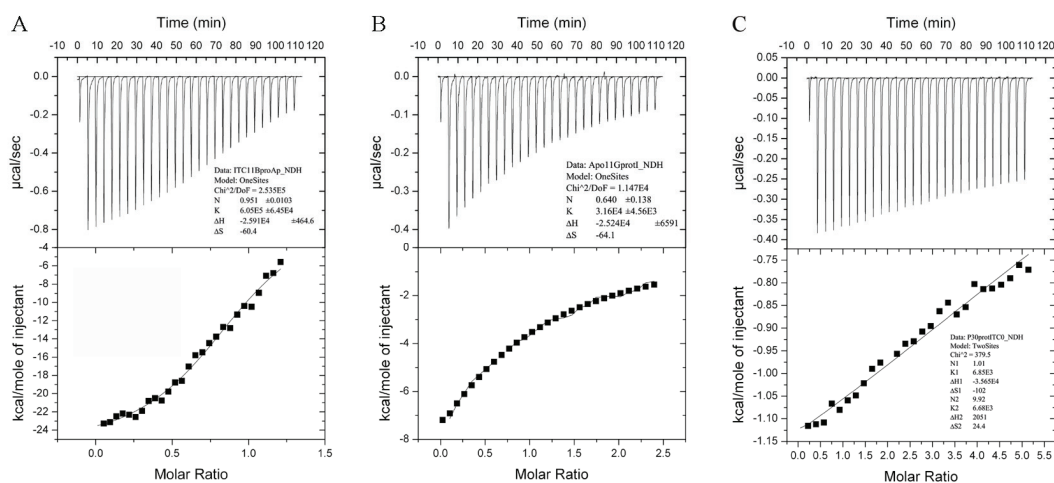


Fig. 24: Results of ITC experiments.

A) Titration with Fe(III)-citrate-NTA_(n). The iron:protein ratio is about 1:1 and the calculated K_{obs} from the K_d shown in the picture, is 1.65 μ M. B) Titration with Ni(II)sulfate. The nickel:protein ratio is 0.65:1 and the K_d is 31.6 μ M. C) Titration with reduced glutathione. The data were fitted with 1 and 2 sets of sites. Here is shown the more meaningful result with two set of sites. The GSH:protein ratio for the first site is about 1:1 and for the second is about 10:1. The dissociation constants are both of about 150 μ M. The results in C must be considered only indicative of an interaction. In fact, it is not possible to rely on the calculated parameters because the curve comprises only the central part of a typical interaction curve. This is the reason why in C the errors are not given. Every attempt to optimize the experiment led to inconsistencies.

potential sets of sites. Here, I present the most reasonable fitting obtained using two sets of sites. The ratio GSH:protein for the first site is 1:1 with a K_d of 146 μ M and 1:10 for the second set with a K_d . Unfortunately, these values must not be considered critical. The results indicate an interaction of the protein with GSH, but the data were not covering enough of the binding curve, thus preventing any precise quantification. Any further attempt to improve the data collection led to irreproducible and inconsistent results.

3.1.9 Small Angle X-ray Scattering (SAXS)

SAXS has been exploited to gain structural information about olo- and apo- *HsETHE1* in solution.

3.1.9.1 SAXS on olo-*HsETHE1*

SAXS have been applied to *HsETHE1* at different concentrations (2, 5 mg/mL) in the absence and presence of the reducing agent TCEP. SAXS experiments showed that olo-

Results

<i>Hs</i>ETHE1 concentrations; TCEP concentration	R_g, nm	Porod volume, nm³	MM(I_0), kDa	N° of monomers fitting the low resolution models
Olo 2 mg/mL; 1mM	2.5 ± 2%	73 ± 10%	29 ± 10%	2*
Olo 5 mg/mL; 1mM	2.5 ± 3%	72 ± 10%	27 ± 10%	2*
Apo 1 mg/mL; 1 mM	7.6 ± 26%	254 ± 10%	166 ± 10%	6± 1
Apo 2 mg/mL; 1mM	8.8 ± 11%	531 ± 10%	231 ± 10%	9± 1
Apo 3 mg/mL; 1mM	11.2 ± 8%	560 ± 10%	333 ± 10%	12± 1
Apo 5 mg/mL; 1 mM	12.0 ± 10%	625 ± 10%	400 ± 10%	15± 1
Apo 10 mg/mL; 1 mM	12.9 ± 10%	730 ± 10%	434 ± 10%	16± 1

Tab. 3: *Hs*ETHE1 SAXS parameters.

Parameters resulting from SAXS analysis on olo- and apo-*Hs*ETHE1 at various concentrations. In the first column, the concentrations of protein and TCEP used are given. The second column shows the radius of gyration found for the different species. The third column shows the Porod volume: excluded volume of the hydrated particle calculated from the Porod equation.[1] The fourth column shows molecular mass estimated from the I_0 . The fifth column shows how many monomers can fit each oligomeric low resolution model. *: here the radius of gyration, the scattering curve and the low resolution model fit perfectly the dimeric *Hs*ETHE1. The wrong estimation of the molecular mass is assigned to a miscalculation of the exact protein concentration at the beginning of the experiments. The concentration should have been roughly twice the estimated one.

*Hs*ETHE1 forms large aggregates (70-250 kDa) in oxidizing conditions. When TCEP is added (1 mM), the solution becomes homodisperse by DLS. SAXS revealed that *Hs*ETHE1 possesses a radius of gyration of 2.5 nm (Tab. 3). The experimental spectrum of *Hs*ETHE1 has been fitted to the theoretical SAX spectra of *At*ETHE1 as monomer and dimer (extracted from PDB: 2GCU) (Fig. 25 A). The fitting is very good for the dimeric form till a momentum transfer of 0.25, indicating that *Hs*ETHE1 in solution is a dimer closely resembling *At*ETHE1. A bad fitting has been achieved when using monomeric *At*ETHE1. Nevertheless the calculated molecular mass (Tab. 03) is closer to the monomer. The wrong estimation of the molecular mass is assigned to a miscalculation of the exact protein concentration at the beginning of the experiments. The concentration should have been roughly twice the estimated one. Successively, a low resolution model of dimeric *Hs*ETHE1 has been build from the experimental data (Fig. 25 C). The protein results globular and high ordered.

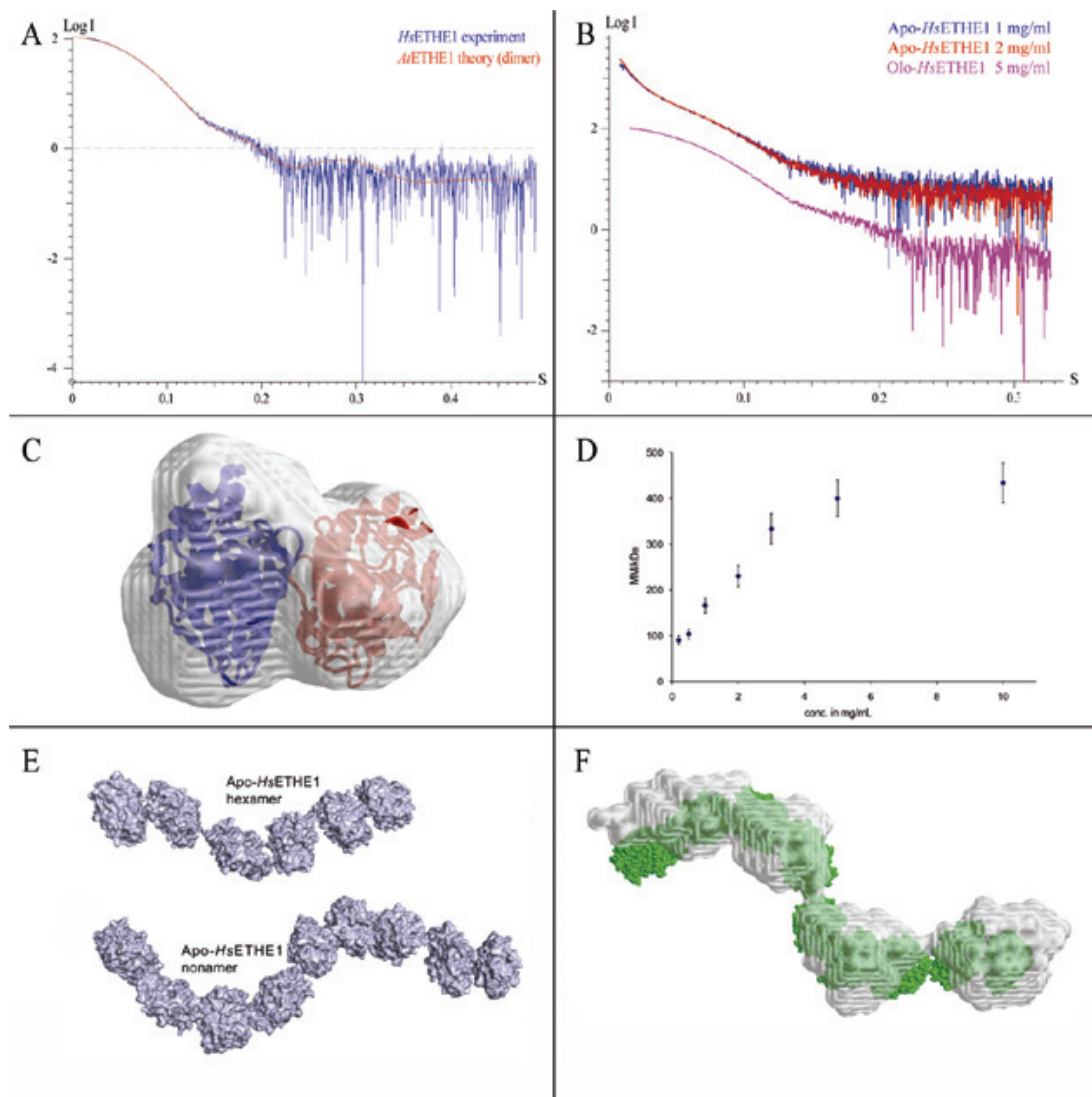


Fig. 25: Results of SAXS experiments.

A) SAXS experimental spectrum of *HsETHE1* (blue) compared to the theoretical spectrum of the *AtETHE1* dimer (red). S , the momentum transfer, is expressed in \AA^{-1} . I is the intensity of the signal. B) Comparison between the experimental spectrum of *HsETHE1* and the spectra of apo-*HsETHE1* at two different concentrations (1, 2 mg/ml). C) Low resolution model of *HsETHE1*. The dimeric structure of *AtETHE1* has been fitted inside. D) Plot of the molecular mass of the apo-species against the protein concentration. E) Comparison between hexameric (1 mg/ml) and nonameric (2 mg/ml) rigid body refinement models of apo-*HsETHE1*. F) Example of apo-*HsETHE1* low resolution model at 2 mg/ml. Inside, a rigid body refinement model of nonameric *AtETHE1* have been fitted.

Pilot experiments have been performed using various concentrations of apo-protein (1, 3, 5 mg/ml) and in the absence and presence of TCEP. SAXS reveals that apo-*HsETHE1* forms ~ 700 kDa aggregates under oxidizing conditions. When TCEP is added to the

solution, these aggregates broke down and the apo-protein results in a lower molecular weight homodisperse solution shown by DLS. Successively, a second round of experiments has been carried out on apo-*Hs*ETHE1 in the presence of TCEP at the protein concentrations of 0.2, 0.5, 1, 2, 3, 5, 10 mg/mL. SAXS showed that the metal-free protein forms supramolecular structures. The analysis revealed that globular structured units form these aggregates. The molecular masses (MMs) were calculated through the extrapolation of the I_0 and the volumes were calculated from the Porod equation.[1] (Tab. 3). The encountered masses resulted closed to integer numbers of monomeric ETHE1 units. We plotted the MMs against the protein concentration and we observed a crescent sigmoid-like distribution (Fig. 25 D). The SAXS expert collaborator (Alexey Kikhney) and me compared the SAXS curves resulting from the measurement of different protein concentration solutions, solved and compared the distance distribution functions for each sample. The SAXS curves show different intensities at low angles, which explain the different masses and exhibit small, but detectable differences at higher angles. This is an indication that the overall shape is similar, but not the same. Hence, the distance distribution function showed that the supramolecular structures probed were different. We can conclude that the observed increase in size towards higher concentrations is not due to intermolecular interaction artifacts, but is real. Unfortunately, due to the intrinsic averaging nature of SAXS we cannot state that at a given concentration we have a defined number of units forming these structures, but we can argue that the observed size of these particles in solution is proportional to the concentration of the protein. We proceeded building low resolution models of these supramolecular species. Strikingly, the low resolution models show that apo-*Hs*ETHE1 forms filaments (chain-like). Monomers and dimers of *At*ETHE1 have been fitted to the low resolution models. Only the monomers could be nicely fitted. Hence, rigid body refinement has been applied to build from the monomers chain-like structures able to fit the experimental data (Fig. 25 E). Finally, we superimposed the rigid body models to the relative low resolution models, obtaining nice fits (Fig 25 F).

These results taken together demonstrate that the metal-free form of ETHE1 is particularly sensitive to oxidizing conditions. In presence of TCEP, the apo-protein is

not able to dimerize properly and forms chain-like oligomers of a size proportional to the protein concentration.

Likely, *in vivo* cells must ensure that the protein is kept always charged with iron in order to avoid protein aggregation and deposition.

3.1.10 X-ray Absorption Spectroscopy (XAS)

Several XAS experiments have been carried out on *HsETHE1* in order to investigate its metal binding site. Pilot experiments were made at DESY (beamline D2, EMBL Hamburg, DESY). These were not successful due to the instability and aggregation tendency of *HsETHE1* in the used conditions. Thus the results were ambiguous and not trustworthy. Further experiments were carried out at ESRF (beamline BM26A-Double, ESRF, Grenoble; bending magnet source). The quality of the protein preparation improved, but we could exploit the EXAFS spectra only up to $k_{\max} = 10 \text{ \AA}^{-1}$, underlining that the quality of the collected data was still not satisfying. The results kept ambiguity about which of the two potential metal binding sites is occupied.

Eventually, *HsETHE1* 2.9 mM in HEPES 50 mM, NaCl 100 mM, TCEP 1 mM, glycerol 30 %, pH 8.0 has been measured at the iron K-edge at the BioXAS beamline 7-3 (wiggler source), SSRL, Stanford, California, in the presence and absence of GSH. We know that *HsETHE1* is very sensitive to mercaptans (see par. 3.1.3), that the substrate is glutathione persulfide (GSSH) and one of the products is GSH. This means that the iron in the active site should possess some affinity for thio-groups and thereby the enzyme might bind to some mercapto-component present in the buffer or dragged out from the purification. The possibility of a sulfur ligand was already taken into account before the experiments; in fact, the protein in the presence of GSH has been measured and analyzed as well. GSH is not only one of the products of *HsETHE1* reaction, but is also able to turn the protein solution to light blue modifying its UV-Vis spectra (see par. 3.1.6).

The outputs of these experiments represent our best data set and the result of their analysis is presented. The EXAFS can be exploited till $k_{\max} = 14 \text{ \AA}^{-1}$, which is a great improvement in terms of data quality.

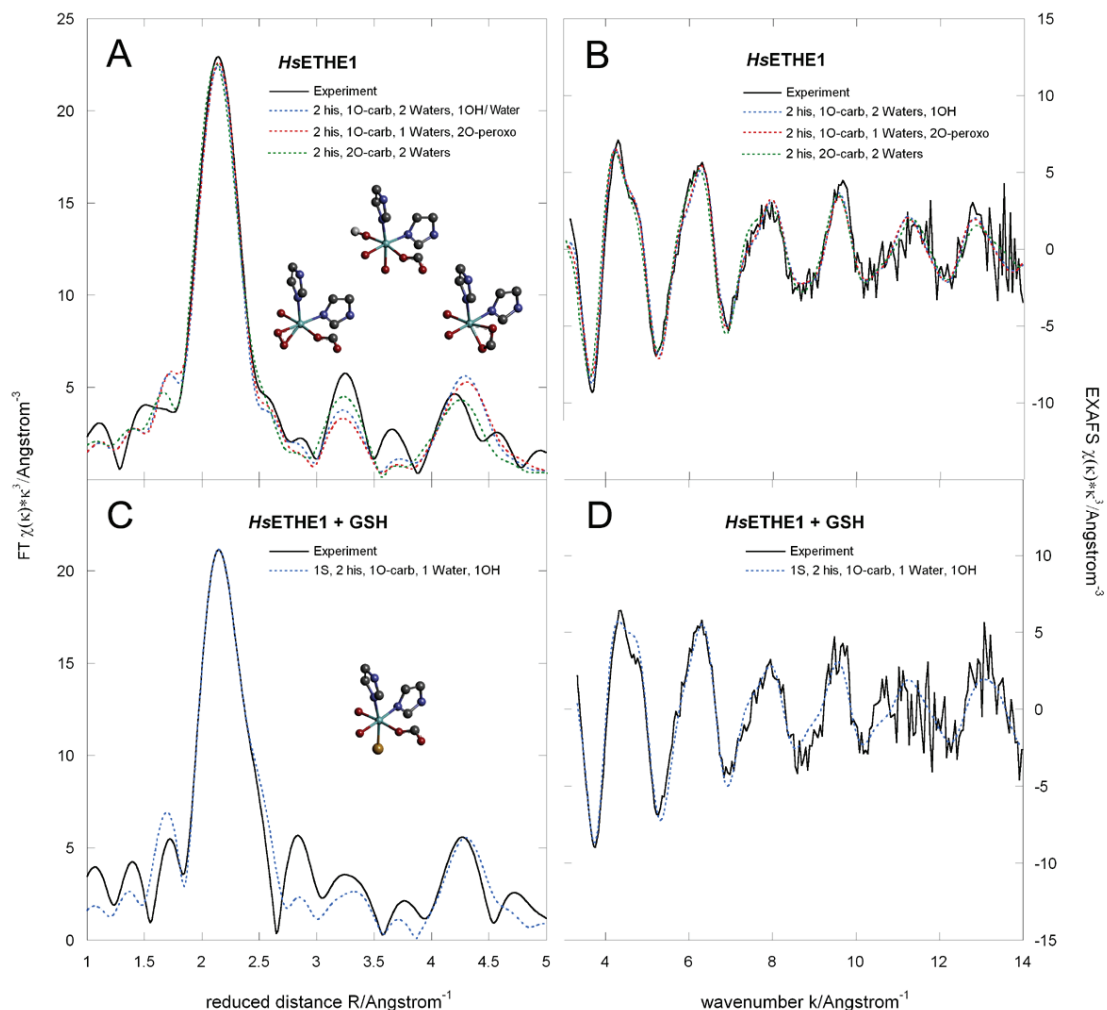


Fig. 26: *HsETHE1* EXAFS.

Example of EXAFS fittings of *HsETHE1* as isolated and in the presence of GSH. On the left column (A, C), the EXAFS Fourier transforms (FTs) spectra are shown, while on the right (B, D) the relative k^3 -weighted EXAFS spectra are presented. The black lines represent the experimental data. The broken lines represent the theoretical curves. A, B) FT and EXAFS spectra of as isolated *HsETHE1*. Here, the potential iron coordination spheres are schematically shown within the picture. C, D) FT and EXAFS spectra of *HsETHE1* in the presence of GSH. The iron coordination sphere scheme is presented within the picture.

The iron K-edge EXAFS spectra of $\Delta 14$ -*HsETHE1*- $\Delta 4$ and $\Delta 14$ -*HsETHE1*- $\Delta 4$ in the presence of two molar excess of GSH have been analyzed.

The experimental k^3 -weighted EXAFS spectra of the two samples are characterized by the typical imidazole ligands signature at $k = 4.5 \text{ \AA}^{-1}$ (Fig. 26). Comparing the experimental Fourier Transform (FT) of the two samples we can immediately observe

that the two spectra show many similarities and some important differences. Firstly, the main peaks have a slightly different intensity, which is higher for the as isolated protein. *HsETHE1* in the presence of GSH possesses a more intense shoulder on the same peak at about 2.4 Å. Its peak at 2.85 Å is more intense than the corresponding one in the as isolated form. The peaks at 3.25 and at 4.25 Å characterizing the contributions of the non-bonding imidazole multiple scattering atoms have different intensities as well. In the case of the as isolated form, the peak at 3.25 Å has higher intensity, while the one at 4.25 has lower intensity, indicating that the Debye-Waller factors are not the leading responsible of these differences or a change in the angle of the imidazoles rings. Moreover, the peak at 3.8 Å is shifted to 3.6 Å in the as isolated form. This a priori information tell us that in both cases the iron it is bound to imidazole ligands and that *HsETHE1* in the presence of GSH might have a sulfur ligand coordinating the iron. In addition, the different intensities and the peak shifts suggest some geometrical rearrangements in presence of GSH.

The experiments were simulated using the exact curved wave theory.[104] The spectra were k^3 -weighted for best modeling (see par. 1.2). The considered energy range spanned from a wavenumber (k) of 3 till 14 Å⁻¹. Imidazole, carbonyl, oxygen, peroxo-groups and sulfur were assumed as potential ligands. All atoms within a ligand were considered as part of the same unit. This allowed considering multiple scattering events within a unit, or among all atoms. The units have been used in the refinements rigid bodies (constrained refinement).[44] The disorder parameters (Debye-Waller factors; $2\sigma^2$) were restrained to a range from 0.002 to 0.025 Å². The Debye-Waller factors of the not coordinating imidazole-atoms were constrained on the basis of empirical data (experience) taking into account their distance from the absorber. In general, it is a good assumption/approximation to consider the Debye-Waller factors of the second (C₂, C₄) and third (N₁, C₅) imidazole shells, respectively 1.6 and 2.1 times the Debye-Waller factor of the donor atom (N₃/N_e). The imidazole and the carbonyl coordination were refined by iterating the distances and the Debye-Waller factors of the pivotal (directly coordinating) atoms. The rotational, twist and tilt angles of the imidazole and carbonyl units were also refined. Two hundred iterations were made each round of refinement. The analysis has been initially carried out using an ideal geometry. Successively, the

coordinates and thus the geometry of the iron binding sites of two PDB structures have been applied as starting parameters:

The *Hs*ETHE1 conserved metal binding residues (by homology with *At*ETHE1, glyoxalase 2 and ZiPD/RNaseZ, data not shown) create two potential metal binding sites closed to each other. Thanks to the available ETHE1 structure from *Arabidopsis thaliana*, we can assume that one site (site 1) could form an octahedral 6-fold-coordination site with two histidines, one carbonyl and up to three oxygens (hydroxides/waters). The other (site 2) could form a tetragonal pyramidal 5-fold-coordination site comprising three histidines, one carbonyl and up to one oxygen. Also the possibility of the presence of dioxygen (molecular oxygen) has been taken into account as linear or bidentate peroxy-form. The structural coordinates of an octahedral and of a tetragonal pyramidal iron binding sites have been extracted to build specific PDB files, which were then used for refinement: 2GCU (*At*ETHE1, 1.48 Å nominal resolution; site 1) 1AR5 (cambialistic SOD, 1.6 Å nominal resolution; site 2). Only the iron and the coordinating groups were considered in the calculations. In the case of histidines, the imidazole moieties were kept for refinement. In the case of aspartate, only the carbonyl group was used. As needed, oxygens have been substituted by a sulfur atom or by a dioxygen-group for refinement.

When the ideal geometry has been applied to the refinements, the analysis couldn't distinguish between the two potential metal binding sites. Instead, when the analysis was carried out starting from structural coordinates, the results strongly favored the octahedral binding site. A large number of different scenarios have been taken into account, considering the information we possess about the active site of other non-heme mononuclear iron dioxygenases.[35-37,105] Eventually, the analysis of as isolated *Hs*ETHE1 in the as isolated form reveals an iron coordinated by 2 N_{εIm} (nitrogen *epsilon* of the Imidazole ring) at 2.16 Å, 1O_{carbonyl} (oxygen of the carbonyl group) and 2 O_{water} (oxygen of a solvent molecule referred as water on the basis of its distance from the iron ion) at 2.10 Å and an Oxygen at 1.93 Å. This model is supported by the Mössbauer spectrum (see par. 3.1.12). Imidazol and carboxylate distances are typical for high spin 2-his 1-carb facial triad mononuclear iron dioxygenases.[35-37,106] Instead, a short Fe(II)-oxygen bonds at such distance have been found exclusively in two different cases:

- In the extradiol dioxygenase upon extradiol bidentate binding.[37] Here, EXAFS analysis found one oxygen is bound at 2.10 and one at 1.93 Å.
- In the naphthalene 1,2 dioxygenase (NDO) (a Rieske dioxygenase), where, in the presence of a substrate analogue (indol) and O₂, a peroxy group binds in a bidentate manner the iron-ion.[36] In this case, a crystallographic study found one oxygen at about 1.8 and one at 2.0, which is in good agreement with Fe-O_{peroxy} bond lengths obtained from the EXAFS analysis of the model compound [Fe(N4Py)(η^2 -O₂)]⁺ (1.93 Å; N4Py = *N*-(bis(2-pyridyl)-methyl)-*N,N*-bis(2-pyridylmethyl)-amine), and from the crystal structure of a heme/copper complex with a μ - η^1 : η^2 -peroxy bridge (1.89 and 2.03 Å).

Hydroxide can also bind iron(III) at about 1.9 Å. For example, EXAFS studies of yellow soybean lipoxygenase-1 (SLO-1) show the presence of a short (1.88 Å) bond, which has been assigned to a hydroxide. This model has been excluded because from XANES, EPR (see par. 3.1.12) and Mössbauer (see par. 3.1.11) we demonstrated the only presence of an Fe(II) species. On the other hand the possibility of an hydroxide-Fe(II) bond at 1.94 Å stabilized by hydrogen bonding network might exist.

From the results of the analysis three potential scenarios are emerging (Tab. 4):

1. 6-ligand (6C) octahedral geometry with 2 N_{elm}, 1O_{carbonyl} and 2 O_{water} and an Oxygen at 1.94 Å.
2. 6-ligand (6C) octahedral geometry with 2 N_{elm}, 1O_{carbonyl} and 1 O_{water} and a peroxy anion bound with both oxygens, one at 2.10 and one 1.94 Å.
3. 6-ligand (6C) octahedral geometry with 2 N_{elm}, 1O_{carbonyl} bidentate with one oxygen at 2.07 and one at 1.92 Å, and 2 O_{water}.

The EXAFS models for these three cases are very similar and led to the best scored refinements (Tab. 4, Fig. 26 A, B). The first scenario would be unique, in fact, Fe(II) hydroxide-bound has never been detected. The second scenario cannot be excluded because the non-heme iron(II-high spin) enzymes are described as oxygen activating enzymes, On the other hand, the conformation with a peroxy-group bound should be

Results

<i>Hs</i> ETHE1 EXAFS analysis							
<i>N</i>	Fe	L	R	$2\sigma^2$	<i>EF</i>	Φ	R
			\AA	\AA^2	<i>eV</i>	$\times 10^3$	
<i>Hs</i>ETHE1 as isolated (2 Im, 3 O_{carb/w}, 1 O_{OH})							
2	Fe	Nε	2.16(3)	0.006(7)	-2(1)	0.6357	27.1
3	Fe	O _{carb/w}	2.09(1)	0.007(3)			
1	Fe	O _{OH}	1.92(2)	0.007(3)			
<i>Hs</i>ETHE1 as isolated (2 Im, 3 O_{carb/w/peroxo}, 1 O_{peroxo})							
2	Fe	Nε	2.16(5)	0.007(7)	-2(1)	0.6587	27.3
3	Fe	O _{carb/w/peroxo}	2.10(2)	0.007(7)			
1	Fe	O _{peroxo}	1.94(3)	0.007(7)			
<i>Hs</i>ETHE1 as isolated (2 Im, 3 O_{carb/w}, 1 O_{carb})							
2	Fe	Nε	2.17(1)	0.005(2)	-3(1)	0.5912	25.7
3	Fe	O _{carb/w}	2.07(1)	0.002(3)			
1	Fe	O _{carb}	1.92(6)	0.011(7)			
<i>Hs</i>ETHE1 + GSH (1S, 2 Im, 2 O_{carb/w}, 1 O_{OH})							
1	Fe	S	2.36(3)	0.01(1)	0(1)	0.8687	32.8
2	Fe	Nε	2.15(6)	0.008(9)			
3	Fe	O _{carb/w/peroxo}	2.06(3)	0.002(7)			
1	Fe	O _{peroxo}	1.89(3)	0.002(7)			
<i>Hs</i>ETHE1 + GSH (2 Im, 3 O_{carb/w}, 1 O_{OH})							
2	Fe	Nε	2.19(4)	0.007(4)	-11(1)	0.9526	37.7
3	Fe	O _{carb/w}	2.08(2)	0.004(6)			
1	Fe	O _{OH}	1.90(4)	0.004(6)			

Tab. 4: *Hs*ETHE1 EXAFS parameters.

Parameters of the best models obtained for the EXAFS analysis of *Hs*ETHE1. The numbers (*n*) of ligand atoms (L) to the iron ion, their distance to the iron ion (*R*), the respective Debye-Waller factor ($2\sigma^2$), the C–O, the Fermi energy for all shells (*EF*), and the fit index (Φ) and the R_{EXAFS} (R) indicating the quality of the fit are shown. The geometry has been modeled as well in octahedral and tetragonal pyramidal conformations. As starting points for the modelization, the structures of *A*ETHE1 (PDB: 2GCU; octahedral) and of the cambialistic SOD (PDB: 1AR5; tetragonal pyramidal) have been used. The results presented in the table refers to an octahedral 6-fold coordination geometry.

rather unstable and its presence as stable ligand would be not less surprising. The third

possibility has been found in the rieske dioxygenase, where an aspartate residue is chelating in a bidentate manner the iron ion. In principle, this would be the favored scenario, but would also require a displacement of the aspartate residue that is hard to imagine grounding on the *At*ETHE1 structure. Thereby, I consider the short-bound oxygen as part of a water-solvent molecule, which is stabilized at about 1.9 Å by the electronic structure at the iron ion.

For *Hs*ETHE1 in the presence of GSH (*Hs*ETHE1-GSH) the scenario is slightly different. In this case the best model is achieved assuming a coordination sphere comprising 1 S at 2.26 Å, 2 N_{elm} at 2.15 Å, 1O_{carbonyl} and 1 O_{water} at 2.07 Å and an Oxygen at 1.89 Å (Tab. 4, Fig. 26 C, D). Interestingly, even in this case the modeling requires the presence of an oxygen donor at about 1.9 Å. This suggests that the GSH binds to the iron ion, explaining the color and UV-Vis changes observed upon addition of this product of the physiological reaction (see par. 3.1.6) and that the protein might be inhibited or kept bound by its own product. Unfortunately, ITC experiments could not strongly support the interaction, giving inconsistent and not reproducible results (see par. 3.1.8.2). Reasonable EXAFS fits with slightly worst r-factor and fit-index have been obtained using the two imidazoles, 1 carboxylate, 2 waters and 1 shortly bound oxygen configuration. This result underlines the possibility of a mixture of sulfur bound and unbound forms in the protein preparation measured.

It is of interest that the estimated Fe-L (Fe-Ligand) distances were found to be higher than the Fe-L distances in case of a low spin iron(II). These are compatible with a high spin iron(II). In fact, in the latter case the energy levels of the different molecular orbitals in the iron electronic structure have similar energy. As a consequence, many electrons occupy quantum states at similar energies. According to the Pauli's exclusion principle, the electrons with similar quantum states need greater physical distance from each other. This causes the boundary of the electron density of the iron to increase, which makes the electron density become less dense. As a result, the ionic radius of the iron augments (from 0.61 Å of a low spin to 0.78 Å of a high spin iron(II)).[107] Consequently, the bond length established between the donor groups and the metal increases. To gain further information from the EXAFS, another important parameter can be taken in consideration: the Bond Valence Sum (BVS) (see par.

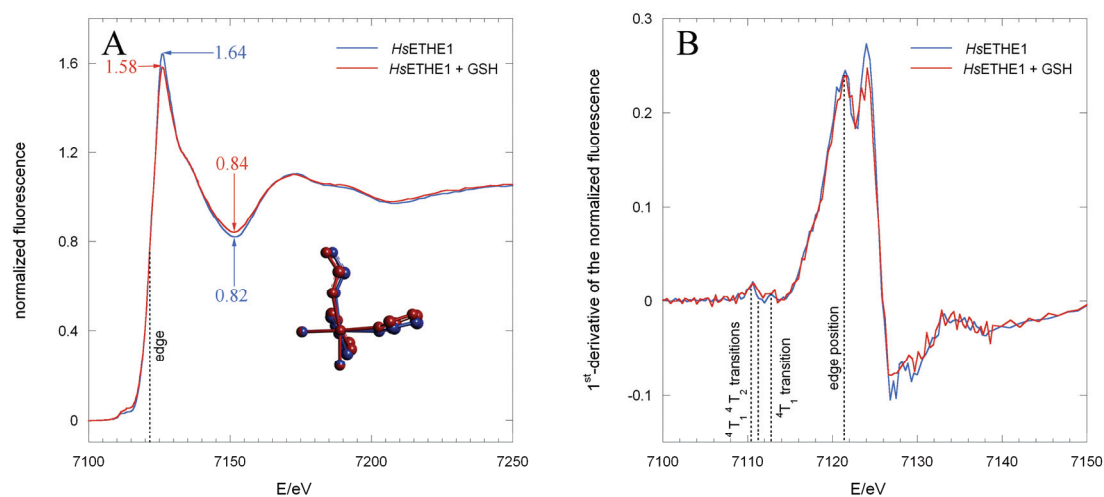


Fig. 27: *HsETHE1* XANES spectra.

Experimental normalized-XANES spectra of *HsETHE1* as isolated (blue lines) and in presence of GSH (red lines). A) The picture shows the comparison of the XANES of as isolated *HsETHE1* and *HsETHE1* + GSH. The projection of the edge position is shown. The overall curves shape is very similar, but not identical. Differences between peak intensities are noticeable for the pre-edge, 1st maximum and 1st minimum peaks. These differences are assigned to geometry distortion rather than to different coordination number in agreement to the EXAFS results. The picture in picture shows a comparison of the metal binding sites of *HsETHE1* and *HsETHE1* + GSH according to the coordinates extracted from the EXAFS refinements. The perpendicular front ligands have been removed for clarity of the picture. It is noticeable that the *HsETHE1* + GSH (red) has a higher geometry distortion than the as isolated from. B) 1st derivative of the same spectra within 7100 and 7150 eV. In the pictures, the 1s→3d transition states and the estimated absorption edge positions are marked by black broken lines.

2.4.14.4).[87-92] BVS it is an empirical approach that allows to postulate the metal oxidation state from the M-L bond lengths, knowing the oxidation-state-independent bond distances (R_0). R_0 can be viewed as a bond length of unit valence. The assumption is that the BVS of a j^{th} atom or ion is close to the oxidation state z_j . In the case of the iron ion, we can refer to the R_0 estimated for iron-O/N bonds.[89] The BVS for *HsETHE1* iron ion has been calculated assuming a R_0 of 1.745, in between the R_0 of an iron(II, low spin)-L (1.734) and iron(III, low spin)-L (1.759).[89] The BVS resulted of about 2.4, which suggests the presence of an iron(II).

In conclusion, *HsETHE1* iron ion has an octahedral geometry and binds to the 2his, 1carb facial triad, which is typical for high-spin non-heme iron(II) oxygenases. The iron-triad ligands bond lengths suggest the high-spin nature of the iron ion. The other three positions resulted fully occupied by oxygen ligands, one of which has been modeled at about 1.9 Å and features the *HsETHE1* iron-binding site. Moreover, exploiting EXAFS refinements based on structural 3D-coordinates we can have geometrical information

suggesting a significant distortion of the iron site from ideal centrosymmetry, particularly for *HsETHE1* in presence of GSH, which EXAFS detected to be bound to the iron ion. Eventually, the similarities with non-heme mononuclear high-spin iron(II) dioxygenases and the BVS suggests the presence of a ferrous iron centre. The presented results fully agree with the Mössbauer analysis carried on *HsETHE1* (see par. 3.1.11-12).

3.1.10.2 XANES on *HsETHE1*

The experimental normalized XANES spectra of *HsETHE1* as isolated and in the presence of GSH have been analyzed. A general comparison of the XANES spectra shows that their overall shape is very similar, but not identical. In fact, the intensities of the pre-edge peak and first maximum and first minimum within the white-line range of energy are slightly different (Fig. 27 A). This has been assigned to the different geometric distortion of the metal binding site. In particular, the first white-line maxima in *HsETHE1* as isolated and in the presence of GSH are found at 1.64 and 1.58, respectively, while the first minima reside at 0.82 and 0.84 (Fig. 27 A). Thereby, the as isolated form presents a more intense first maximum and a less intense first minimum, which are characteristics of a change in the coordination sphere and/or in the centrosymmetry distortion. Very similar XANES spectra were reported for different forms of the tyrosine hydroxylase.[108]

The first and second derivatives of the spectra were calculated in order to more efficiently follow the pre-edge $1s \rightarrow 3d$ transition on the spectra (Fig. 27 B; 28). From the first derivatives of the spectra I calculated the edge position to be at 7122.5 eV for both, assuming an E_0 (from Fe-reference foil) of 7111.2 eV.[108] The first derivatives highlight a 2-fold splitting of the white-line centered at 7123 eV (Fig. 27 B). This characteristic is assigned to two different transitions to highly energetic unoccupied orbitals. Within the pre-edge peak range (7110-7116 eV) we can distinguish the splitting of the pre-edge peak in two smooth sub-peaks. This characteristic has been here assigned to high-spin octahedral (Oh) iron sites.[40,108,109]

Sample		Number of peaks fitted	Pre-edge peaks energy position eV	Pre-edge peak energy intensity 10^{-2}eV^2	Total pre-edge peak intensity 10^{-2}eV^2
<i>Hs</i>ETHE1	as	2	7111.3	8.5(9)	10(1)
isolated			7113.6	2(2)	
<i>Hs</i>ETHE1	as	3	7109.3	1.9(9)	11(3)
isolated			7111.5	7.3(9)	
			7113.7	1.7(9)	
<i>Hs</i>ETHE1	+	2	7111.5	2.5(1)	16.6(5)
GSH			7113.5	14.1(3)	
<i>Hs</i>ETHE1	+	3	7106.3	0.1(9)	18(3)
GSH			7111.4	3.2(9)	
			7113.5	15.2(9)	

Tab. 5: *Hs*ETHE1 pre-edge peak analysis.

Pre-edge peaks analysis. The pre-edge peak features has been fitted using 2 or 3 pseudo-Voigt peaks. The total areas reveal that the iron geometry is distorted, in particular for the protein in the presence of GSH. Interestingly, the *Hs*ETHE1 as isolated pre-edge peaks can be nicely fitted assuming two peaks, one bigger at lower energy and one smaller at higher energy. This scenario is inverted for *Hs*ETHE1 + GSH. This characteristic can be directly observed into the 2nd derivatives of the experimental XANES spectra.

In case of iron(II) complexes, this two peaks originate from the $(t_{2g})^2(e_g)^2 \rightarrow (t_{2g})^2(e_g)$ and $(t_{2g})^2(e_g)^2 \rightarrow (t_{2g})(e_g)^2$ transitions, corresponding to the ${}^4T_{1g}$, ${}^4T_{2g}$ and ${}^4T_{1g}$ states. Usually, these transitions are pointed at about 7111.3(2), 7112.2(4) and 7113.4(3) eV and the first two typically overlay and form a unique peak. As a consequence, two pre-edge peaks are visible at about 7111.5 and 7113.5 eV, respectively. In case of iron(III) complexes the peaks originate from the $(t_{2g})^3(e_g)^2 \rightarrow (t_{2g})^2(e_g)^2$ and $(t_{2g})^3(e_g)^2 \rightarrow (t_{2g})^3(e_g)^1$ transitions, corresponding to the 5T_2 and 5E states. These two transitions are usually found at 7112.9(5) and 7114.3(5) eV and split by no more than 1.5 eV. Focusing on the two visible peaks, for both forms their position is at about 7111.4(2) and 7113.5 (2) eV. These positions fits very well the pre-edge peak positions found for a number of octahedral high spin iron(II) model complexes[109,110] and enzymatic sites, such as in the tyrosine hydroxylase[108] and in the soybean lipoxygenases.[111]

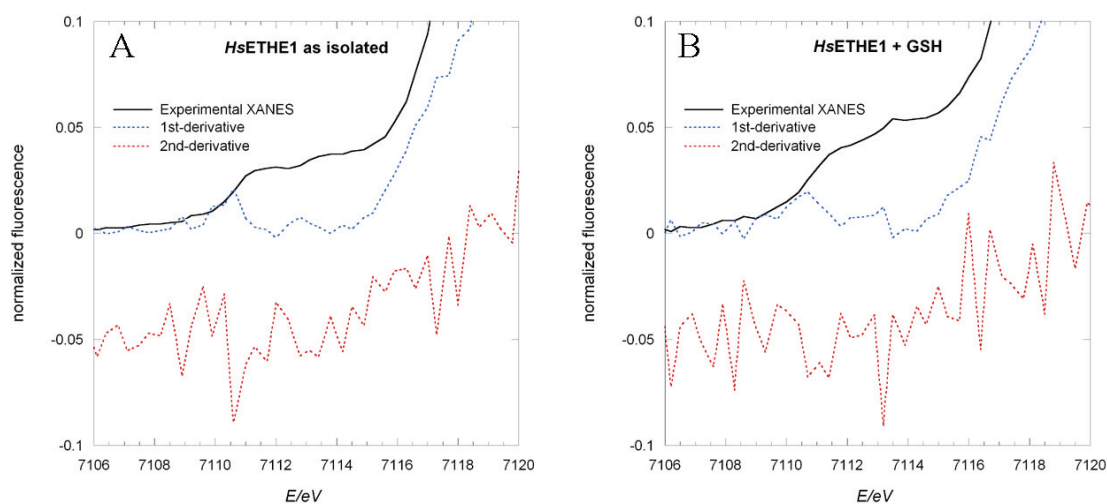


Fig. 28: HsETHE1 XANES pre-edge peak analysis.

A) Zoom-in of the as isolated HsETHE1 XANES spectra (full black line). The 1st (broken blue line) and 2nd (broken red line) derivatives are also presented. B) As A, but the spectra refers to HsETHE1 + GSH.

Moreover, as mentioned above, these peaks are typically distant 2 eV from each other. Instead, the pre-edge peaks of octahedral high spin iron(III) complexes are commonly distant 1.5 eV from each other and shifted about 1.5 eV towards higher energies. I calculated the pre-edge peak areas using either two or three pseudo-Voigt peaks. The results using three peaks sounded artificial, considering the intrinsic energy resolution of the Si[220] monochromator at the Fe K-edge of 0.4 eV, but for comparison, the obtained values are presented (Tab. 5). The areas under the pre-edge peaks were determined to be 8.5 and 2 eV², respectively for the lower and higher energy peaks of the as isolated form, and 2.5 and 14.1 eV², respectively for the lower and higher energy pre-edge peaks of HsETHE1 + GSH (Tab. 5). Thus, their intensities are swapped. This can be nicely observed if we zoom in the second derivatives between 7110 and 7115 eV, where the two pre-edge peaks of the two forms look mirrored. (Fig 28 A, B). This means that for HsETHE1 as isolated, the probability of the configuration $(t_{2g})^2(e_g)$ (${}^4T_{1g}$, ${}^4T_{2g}$ transitions at about 7111 eV) is higher than the probability of the configuration $(t_{2g})(e_g)^2$ (${}^4T_{1g}$ transition at about 7113.5 eV). The reasons for this reside in the electronic structure of the iron site and they are still unclear.

The total areas under the pre-edge peaks are 10 and 16.6 eV² for HsETHE1 as isolated and in presence of GSH, respectively. These peaks are very intense and they

indicate, or a lower coordination number (about 4), or that the geometry is highly distorted from ideality.

In conclusion, the pre-edge peak analysis revealed that *Hs*ETHE1 bears a high spin iron(II). This is in perfect accordance with EPR and Mössbauer analysis results (see par. 3.1.11-12). The theoretical three pre-edge peak transitions forming the double pre-edge peak are highlighted in Fig. 27 B. Moreover, according to the EXAFS results (see par. 3.1.10.1; Fig. 27 A, picture in picture), which favors a hexa-coordination, the total pre-edge peak area indicates a significant centrosymmetric distortion from ideality. The diversities between the XANES of the as isolated and GSH enriched forms are assigned to geometric distortion of the metal binding site rather than to a different coordination number, particularly for the GSH enriched protein that possesses a significantly higher total pre-edge peak area (Tab. 5). This geometrical rearrangement has been assigned to the interaction of *Hs*ETHE1 with GSH, which binds the iron ion as presented in the EXAFS analysis.

3.1.11 Electron Paramagnetic Resonance (EPR)

EPR has been applied on *Hs*ETHE1 in the as isolated state deriving from the same batch used for XAS analysis. The results revealed that the protein is EPR silent. Ruling out the possibility of an iron(IV), which has been observed only as intermediate during oxidoreductive enzymatic reactions,[112] this result suggests the unique presence of iron(II) in high or low spin configuration.

3.1.12 Mössbauer spectroscopy

The electronic structure of *Hs*ETHE1 has been investigated by Mössbauer spectroscopy to further investigate the protein iron oxidation state, its coordination number and the nature of the ligands.

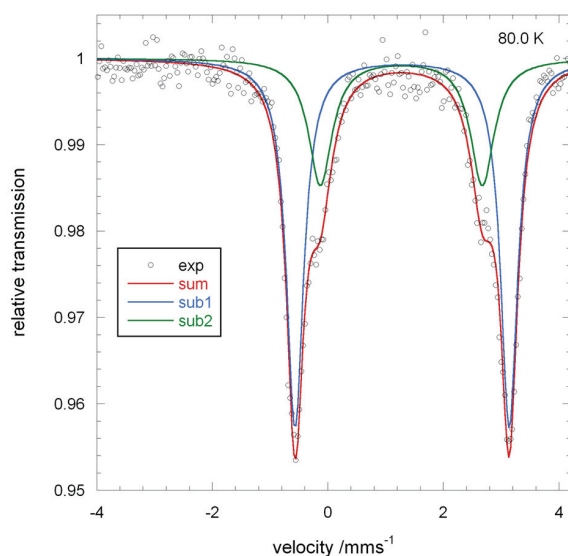


Fig. 29: Mössbauer spectrum of HsETHE1.

The analysis revealed two subspectra corresponding to two iron site states in a ratio 2:1. Both subspectra show high isomer shift, typical of hexacoordinated iron centers, with weak field ligands only. The two configurations differ exclusively by quadrupole splitting, *i.e.* in the (a)symmetry of coordination.

Mössbauer analysis detected the presence of two sub-spectra representing two iron(II) sites in 2:1 ratio (Fig. 29, Tab. 6). Each sub-spectrum is formed by two doublets. One doublet represents about two thirds (68%) of the iron and shows an Isomer Shift (I.S./ δ ; mm/s) of 1.28 mm/s. The second doublet has a $\delta = 1.27$ mm/s. Thereby, both sub-spectra show very high isomer shift, as it is typically found for 6-ligand coordination spheres with weak field ligands only. This result rules out sulfur coordination. The large isomer shift is compatible with only ferrous

high spin iron. This scenario is similar to the one presented for the benzoate dioxygenase (BZDO), where the enzyme in the resting state exhibits two doublets, but with lower splitting.[113] In BZDO, one doublet represents about the 75% of the iron and has ΔE_Q of 3.1 mm/s and δ of 1.26 mm/s while the other doublet exhibits ΔE_Q of 2.0 mm/s and a δ 1.27 mm/s. These data indicate that also BZDO high spin iron in two different electronic environments.

The doublets differ significantly by Quadrupole Splitting (Q.S./ ΔE_Q ; mm/s), *i.e.* in the (a)symmetry of coordination. They have very high quadrupole splittings giving rise to important geometrical considerations. The majority species showed a $\Delta E_Q = 3.71$ mm/s, which indicates a large splitting of the t_{2g} orbitals. This is the result of a considerable geometrical distortion from ideality in terms of angles and bond lengths. This is in perfect agreement with the EXAFS results (see par. 3.1.10.1) that revealed the presence of an oxygen ligand at about 1.9 Å from the iron and a consistent distortion from an ideal octahedral geometry. The minority species, which differs substantially from the other state only in the quadrupole splitting, possesses a $\Delta E_Q = 2.80$ mm/s. This scenario

I.S. (δ)	Q.S. (ΔE_Q)	FWHM	Rel. I. [%]
1.28	3.71	0.36	67.95
1.27	2.80	0.50	32.05

Tab. 6: *HsETHE1* Mössbauer parameters.

Parameters obtained from Mössbauer spectroscopy analysis of *HsEthe1*. I.S.: Isomer Shift (δ). Q.S.: Quadrupole Splitting (ΔE_Q). FWHM.: Full Width at Half Maximum. Rel. I.: Relative Intensity of the two subspectra.

not only indicates that the minority species has a less distorted geometry, but also suggests a flexibility of the iron binding site that can be crucial for *HsETHE1* functionality. Notably, the minority species exhibits Mössbauer parameters very similar to those of another mononuclear iron dioxygenases, the phenylalanine and tyrosine hydroxylases.[114]

In conclusion, the Mossbauer results of *HsETHE1* are consistent with a non-heme mononuclear iron(II) high spin dioxygenases.

The next step would be to carry out further Mössbauer spectroscopy experiments for characterizing the iron spectral changes upon addition of GSH and upon triggering the enzymatic reaction through the addition of a reaction mixture where the unstable substrate is freshly formed. In fact, even if the turnover would be at low rate ($\sim 10\%$), Mössbauer spectroscopy is able to detect small traces of such species. In this way, we should gain insight to the geometrical and electronic changes featuring the reaction cycle.

3.1.13 Crystallization

So far, the crystallization of *HsETHE1* has not been successful. Hundreds of crystallization conditions have been screened exploiting different construct (see par. 2.4.11). Nevertheless, the protein gave no crystals suitable for X-ray diffraction studies. The construct $\Delta 14$ -*HsETHE1* supplied spherulites-like pseudo-crystalline formations at the following conditions: Mg formate 0.1M, PEG 3350 15%; ammonium sulfate 1.4 M, MES 0.1 M pH 6.0, PEG 3350 (Fig. 30). The spherulites were growing slowly within 2/3 months. These conditions were optimized manually by varying the concentration of salt and PEG and they were used for seeding. Up to now, only the spherulites were reproduced and no protein crystal formed. The construct $\Delta 7$ -*HsETHE1*- $\Delta 4$ yielded

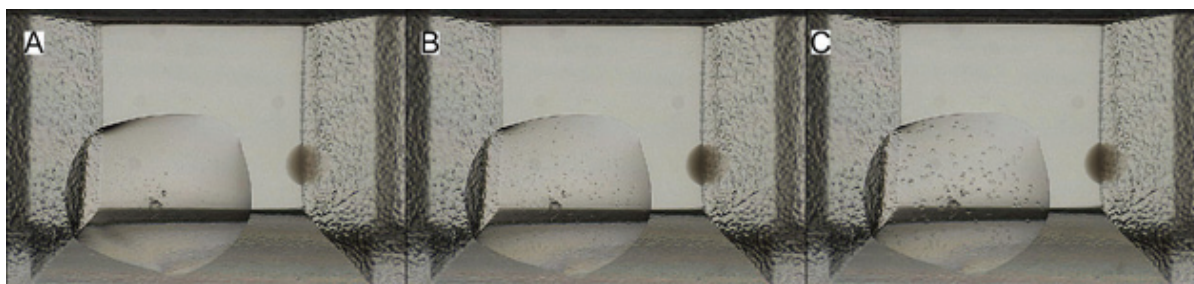


Fig. 30: *HsETHE1* crystallization spherulites.

Spherulite-like formations obtained from *oHsETHE1* crystallization trials. From A to C is presented an example of spherulites formed after 10 days (A), 1 month (B) and 2 months (C) in Ammonium Sulfate 1.4 M; MES 0.1 M pH 6.0; PEG 3350 and reducing conditions given by TCEP.

reproducible crystals in different conditions, *i.e.* ammonium acetate 0.2 M, bis-tris 0.1 M pH 6.5, PEG 3350 25%; HEPES pH 7.5, PEG 6000 10%, MPD 5%;; Zn acetate 0.2 M, PEG 3350 20%. Unfortunately, synchrotron based crystal tests revealed that the crystals were formed exclusively by salt.

3.1.14 Hypothetic *HsETHE1*'s reaction mechanism

The working hypothesis for *HsETHE1*'s reaction mechanism is summarized in Fig. 31. The mechanism has been proposed on the basis of our results and considering the reaction mechanism proposed for other non-heme mononuclear high spin iron(II) dioxygenases, such as the biosynthetic oxidases.[35] The cycle starts with the resting state of the ferrous metal binding site (A). Here, the iron ion is coordinated by the 1-carboxylate 2-imidazole triad and by three water's oxygens. The substrate (GSSH) enters the active site, displaces two water molecules and binds to the iron (B), which is now penta-coordinated and bound to a sulfur ligand. The iron ion is now ready to accept and activate an oxygen molecule. The O₂ binding displaces the last water molecule and forms a Fe(III)-superoxo complex (C). The superoxo has a radical character and triggers the attack to the sulfur affording the creation of a peroxo-iron-sulfur circular form species (D). The sulfur donor starts its oxidation process (S¹⁺). At this point, two possibilities are presented: *a*) Formation of a sulfoxycation radical and of an metal-bound activated oxygen radical atom (E1). The sulfur is now S³⁺. From E1, the

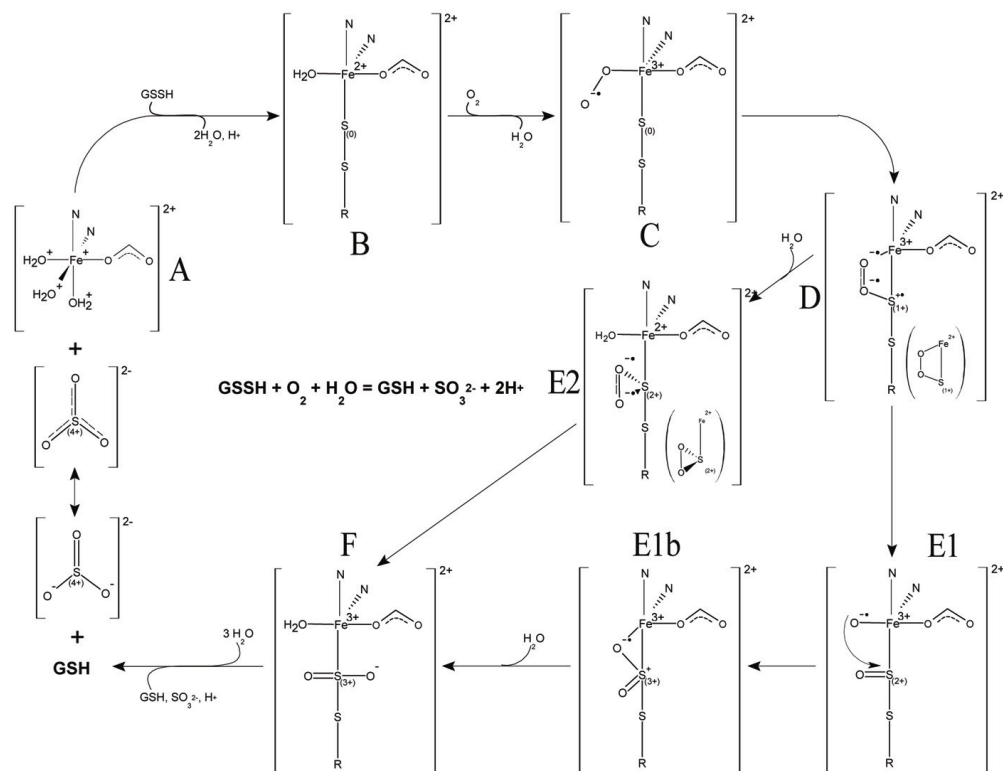


Fig. 31: Proposed catalytic mechanism for *HsETHE1*.

The overall reaction equation is presented in the centre of the picture. A) Resting state. B) Substrate (GSSH) binding and two waters displacement. The iron is now pentacoordinated with a sulfur ligand. C) O_2 binding, displacement of a water molecule and formation of a Fe(III)-superoxo complex. The superoxo has a radical character that triggers the attack to the sulfur. D) Formation of a peroxo-iron-sulfur ring. Here the sulfur donor starts the oxidation process. E1) Formation of a sulfoxy-cation radical and of metal-bound activated oxygen radical atom. The sulfur is now in the 2+ oxidation state. E1b) The metal-bound activated oxygen radical atom attacks the sulfur donor. The sulfur is further oxidized to 3+. E2) Possibility of a sulfur-peroxo intermediate and reintroduction of a water molecule. The sulfur would be in the 2+ oxidation state. F) Formation of a Fe-S-sulfonate intermediate. The sulfur is in a 3+ oxidation state. Then, the nucleophilic attack of a water molecule to the iron triggers the S-S and Fe-S bond breaking and the final oxidation of the sulfur donor to a 4+ oxidation state. Other two water molecules can re-establish the resting state. The picture has been produced with the ChemSketch software ACD/Labs® (Advanced Chemistry Development®).

metal-bound activated oxygen radical atom attacks the sulfur donor (E1b). *b*) Formation of a sulfur-peroxo intermediate and reintroduction of a water molecule (E2). Then, from E2 or E1b the formation of a Fe-S sulfonate intermediate takes place (F). The sulfur is now in the oxidation state 3+. Then, the nucleophilic attack of a water molecule to the iron triggers the S-S and Fe-S bond breaking, affording the products: During Fe-S bond lysis the sulfur leaves the last electron to the iron ion, concluding the oxidation

process (S^{4+}). Other two water molecules can re-establish the resting state. It is worth to consider that herein the iron ion passes through the oxidation state III (C, D, E1, E1b, F). However, in step E1 the iron ion might be at oxidation state IV as oxo-Fe(IV).[35-37]

3.2 X-ray Absorption Spectroscopy applications and methods development

This chapter is dedicated to the results obtained by XAS studies on the mononuclear [Fe]-hydrogenase Hmd from *Methanocaldococcus jannaschii*, on the optical excited state of a bis(μ -oxo)-dicopper(III) species and on the ATP binding cassette protein ABCE1.

3.2.1 XAS study of the mononuclear [Fe]-hydrogenases Hmd

The mononuclear [Fe]-hydrogenase Hmd from *Methanocaldococcus jannaschii* (jHmd) has been investigated by a synergic combination of EXAFS and XANES analysis.

3.2.1.1 jHmd: EXAFS analysis

EXAFS analysis was performed on jHmd wild type reconstituted (the iron-coordinating cofactor has been isolated and the apo-protein was then reconstituted), under the conditions used for crystallization[2], on two forms inhibited by carbon monoxide (CO) or cyanide (CN) and on the mutants C176A and C176S.[4] Initially, the analysis of jHmd was carried out taking into account the available information on the [FeFe]- and [NiFe]-hydrogenases,[47] on a previous work about jHmd and Hmd from *Methanothermobacter marburgensis* (mHmd)[50] and on the jHmd X-ray diffraction model supplied by our collaborators.[2] Successively, the 3D structure of the mutant C176A has been available from our collaborators, opening the doors for a remodeling of jHmd iron-site.[4]

The experiments were simulated with Excurve9.3, using the exact curved wave theory.[104] The spectra were k^3 -weighted for best modeling. The considered energy range spanned from a wavenumber (k) of 3 till 14 \AA^{-1} . All atoms of a same ligand group were considered as part of the same unit. This allowed considering multiple scattering events within a unit, or among all atoms, which is extremely important in the presence of intense multiple scatterers such as CO and CN ligands.

<i>n</i>	Fe	L	R	$2\sigma^2$	$R_{C_x}(\text{\AA})$	<i>EF</i>	Φ
A			\AA	\AA^2	\AA	<i>eV</i>	$\times 10^3$
mHmd as isolated							
2	Fe	C ^a	1.801 (4)	0.0084 (8)	1.121 (8)	-9.0 (4)	0.1196
1	Fe	O	2.034 (6)	0.007 (1)			
1	Fe	S	2.308 (3)	0.0051 (6)			
2	Fe	O ^a	2.922 (4)	0.0083 (5)			
<hr/>							
B 3							
mHmd + KCN							
2	Fe	C ^a	1.789 (4)	0.0061 (6)	1.137 (9)	-9.7 (4)	0.1710
1	Fe	C ^b	1.971 (8)	0.005 (1)	1.180 (15)		
1	Fe	O	1.997 (9)	0.016 (1)			
1	Fe	S	2.343 (9)	0.016 (1)			
2	Fe	O ^a	2.926 (5)	0.010 (6)			
1	Fe	N ^b	3.151 (7)	0.005 (1)			
<hr/>							
C 3							
jHmd rec. wt (1)							
2	Fe	C ^a	1.813 (5)	0.007 (1)	1.100 (13)	-7.3 (4)	0.4825
2	Fe	O	2.004 (5)	0.007 (1)			
2	Fe	S	2.34 (1)	0.008 (1)			
1	Fe	O ^a	2.923 (8)	0.013 (1)			
2							
<hr/>							
D 3							
jHmd rec. wt (2)							
2	Fe	C ^a	1.792 (4)	0.0077 (9)	1.142 (8)	-8.9 (4)	0.2005
1	Fe	O	2.040 (9)	0.013 (2)			
1	Fe	S	2.321 (4)	0.0071 (8)			
2	Fe	O ^a	2.934 (4)	0.0081 (5)			

Results

E			3				
jHmd cry							
2	Fe	C ^a	1.795 (5)	0.007 (1)	1.12 (1)	-8.3 (7)	0.3643
1	Fe	O	2.03 (1)	0.008 (2)			
1	Fe	S	2.351 (6)	0.007 (1)			
2	Fe	O ^a	2.921 (7)	0.0098 (9)			
F							
jHmd (CO-i)							
2.5(4)	Fe	C ^a	1.80(1)	0.003(2)	1.16(2)	-10.2(6)	0.2676
1	Fe	O	1.93(2)	0.001(1)			
1	Fe	S	2.332(9)	0.014(2)			
2.5(4)	Fe	O ^a	2.968(8)	0.007(1)			
G							
jHmd (CN-i)							
2	Fe	C ^a	1.76(1)	0.005(1)	1.16(2)	-5(1)	0.4754
1	Fe	C ^b	2.10(2)	0.0246(1)	1.04(3)		
1	Fe	O	1.88(1)	0.004(2)			
1	Fe	S	2.33(2)	0.019(2)			
2	Fe	O ^a	2.920(9)	0.009(1)			
1	Fe	N ^b	3.14(1)	0.003(1)			
H							
jHmd rec. wt (2-new)							
2	Fe	C ^a	1.769(5)	0.0050(7)	1.170 (8)	-10.6(5)	0.1664
1	Fe	C ^c	1.88(1)	0.0020(1)			
1	Fe	O	2.052(9)	0.014(2)			
1	Fe	N	2.052(9)	0.014(2)			
1	Fe	S	2.335(4)	0.0064(7)			
2	Fe	O ^a	2.939(3)	0.0025(4)			

I							
jHmd C176A							
1.5	Fe	C ^a	1.76(1)	0.010(3)	1.16 (2)	-12(1)	0.2758
1	Fe	C ^c	1.87(7)	0.0038(3)			
1	Fe	O	2.01(1)	0.005(1)			
1	Fe	N	2.01(1)	0.005(1)			
1	Fe	S	2.303(7)	0.005(1)			
1.5	Fe	O ^a	2.922(7)	0.004(1)			
L							
jHmd C176S							
1.75	Fe	C ^a	1.75(1)	0.017(8)	1.16 (2)	-10.4(8)	0.3685
1	Fe	C ^c	1.83(2)	0.0029(2)			
1	Fe	O	1.997(8)	0.005(1)			
1	Fe	N	1.997(8)	0.005(1)			
1	Fe	S	2.295(7)	0.0048(9)			
1.75	Fe	O ^a	2.91(1)	0.003(2)			
M							
mHmd wt (new)							
2	Fe	C ^a	1.77 (1)	0.009 (3)	1.155 (13)	-9.6 (4)	0.1179
1	Fe	C	1.85 (2)	0.004 (4)			
1	Fe	O	2.043 (8)	0.012 (1)			
1	Fe	N	2.043 (8)	0.012 (1)			
1	Fe	S	2.314 (3)	0.0047 (6)			
2	Fe	O ^a	2.925 (3)	0.0075 (4)			

Tab. 7: jFHmd EXAFS parameters.

EXAFS parameters resulting from the analysis of several mononuclear [Fe]-hydrogenase samples. The numbers (n) of ligand atoms (L) to the iron ion (Fe), their distance to the iron ion (R), the respective Debye-Waller factor ($2\sigma^2$), the C–O/C–N distance, the Fermi energy for all shells (EF), and the fit index (Φ), indicating the quality of the fit, are shown. A) As isolated *Methanothermobacter marburgensis* Hmd (mHmd).[50] B) Cyanide inhibited mHmd.[50] C) Reconstituted *Methanocaldococcus jannaschii* Hmd (jHmd).[50] D) Reconstituted jHmd sample with higher quality and metal concentration.[2] E) jHmd in the crystallization conditions.[2] F) Carbon monoxide inhibited jHmd.[2] G) Cyanide inhibited jHmd.[2] H) Reinterpretation of the reconstituted jHmd model presented in D.[4] I) jHmd C176A mutant.[4] L) jHmd C176S mutant.[4] M) Reinterpretation of the mHmd wild type model presented in A.[115]

The so defined units have been used as rigid bodies. The disorder parameters (Debye-Waller factors; $2\sigma^2$) were restrained from 0.002 to 0.025 \AA^2 . The rotational, twist and tilt

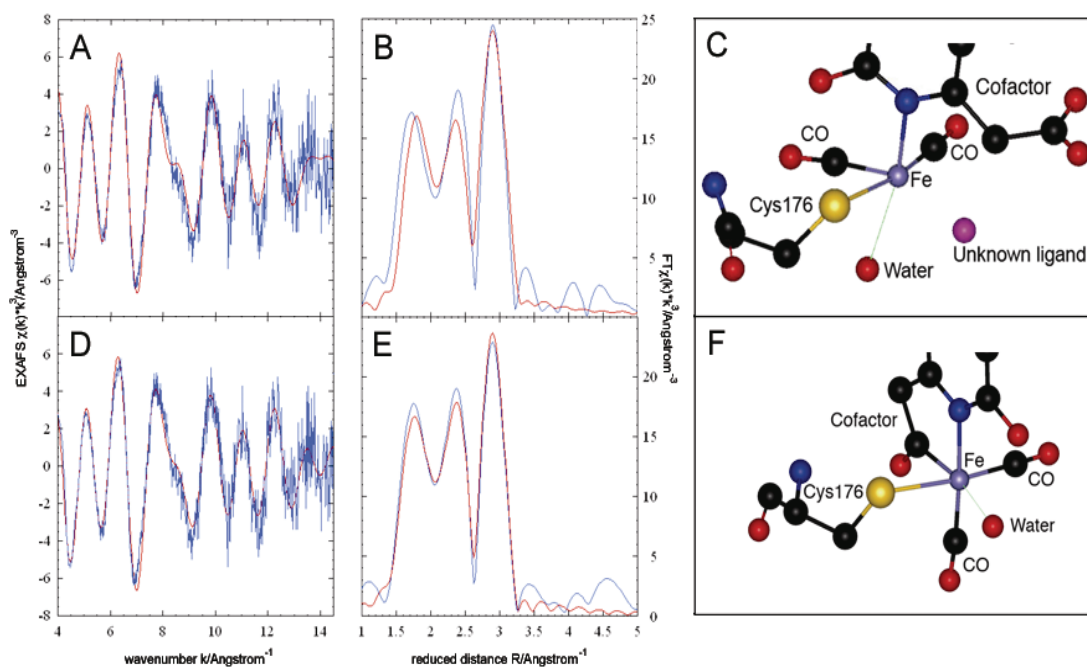


Fig. 32: Hmd EXAFS analysis.

A, B, C) Respectively, the EXAFS, FT and 3D model of jHmd wild type iron binding site as firstly published.[2]. D, E, F) Respectively, the EXAFS, FT and 3D model of jHmd wild type iron binding site as lately published.[4]. It is clear from the spectra that the new model fits much better the data. In C and F the atoms are represented in scaled ball and stick: violet, the iron; black, the carbon; red, the oxygens; blue, the nitrogens; yellow, the sulfur.

angles of the CO/CN units were also refined, considering the carbons as pivotal atoms. Up to two hundred iterations were made each round of refinement. The overall results are summarized in table 7 (Tab. 7).

3.2.1.1.1 jHmd EXAFS-model[2]

The jHmd XAS data were analyzed up to 800 eV above the edge, corresponding to a wavenumber $k = 14 \text{ \AA}^{-1}$. jHmd iron ion was known to bind CO, sulfur and the FeGP cofactor (Fe-Guanidyl-Pyridone cofactor) through a nitrogen atom of the heterocyclic ring bound to the guanidyl moiety.[50] The known ligands can be clearly addressed in the 3D structure. The remaining electron donors were not well understood. In the 3D model our collaborators observed an electron density at about 2 Å from the iron, which was assigned to a solvent molecule. Another electron density was found at the site where the molecular hydrogen is supposed to bind, at about 2.5 Å from the iron ion. The chemical nature of this ligand is unknown, and its electron density cannot definitely be

assigned as a monatomic or diatomic ligand, although it is clearly connected with that of the iron.[2]

Looking at the k^3 -weighted wave vector experimental spectra we could observe a phase shift at about $k = 9 \text{ \AA}^{-1}$, which can be due to multiple scattering effects (Fig. 32 A, D). Besides, looking at the relative FT, it was evident the presence of three main peaks at about 1.75, 2.35 and 2.9 \AA . These peaks fitted very well the assumption of CO ligands, represented by the peaks at 1.75 and 2.9 \AA , and sulfur ligands, represented by the peak at 2.35. The analysis confirmed that jHmd wild type (jHmd-wt) EXAFS is dominated by the contributions of two COs at 1.792 \AA and a sulfur at 2.321 \AA . In fact, these are strong scatterers, in particular the COs, which give multiple scattering contributions. The presence of a soft ligand (O/N) could also be nicely fitted at 2.04 \AA . On the basis of mutational studies, the sulfur is assigned to cysteine 176 of jHmd and the soft ligand to the nitrogen electron donor of the FeGP cofactor. Notably, another O/N contribution could be introduced in the model at 2.03 \AA with no worsening of the fit quality (Fig. 32 B, E).

Successively, based on the results obtained for the reconstituted wild type form, the EXAFS of jHmd in the crystallization conditions and inhibited by CO or CN has been analyzed as well. The results revealed that, within the error margins, jHmd-iron coordination sphere in the crystallization conditions is analogue to the reconstituted jHmd (protein separate from the cofactor and reassembled back). CO inhibited jHmd showed the presence of another carbon monoxide as iron ligand in partial occupancy (0.5). The EXAFS analysis of the CN inhibited form revealed the presence of a CN molecule with full occupancy at 2.10 \AA from the iron. Interestingly, the Fe-O/N distance in the CO inhibited form (1.93 \AA) is sensibly shorter than in jHmd-wt. In the CN inhibited form something similar could be observed, but in this case the O/N ligand exhibited an even shorter distance (1.88 \AA). Besides, the CN inhibited form exhibits also the COs molecules at a shorter distance respect all the other forms (1.76 \AA). CO and CN are strong back bonding electron donors due to their nature of σ -donor/ π -accepting ligands.[116] Thus, they strongly contribute to the electron delocalization at the iron ion. This means that they affect markedly the electronic structure of the iron and their influence is detected by EXAFS as differences in the Fe-L distances.

3.2.1.1.2 Revisited jHmd EXAFS-model[4,115]

In 2008, the structure of the jHmd mutant C176A has been solved, revealing a unique and unexpected scenario. In fact, it became evident that the FeGP cofactor was not bound to the iron only by the pyridinol nitrogen, but also by an acyl-carbon of a carbonyl arm branching off from the pyridinol moiety. This kind of coordination has never been observed within an enzyme. In the crystal structure, the iron ion is in octahedral geometry. The mutant C176A possesses an alanine instead of the cysteine responsible for the binding of the iron. The cysteine is here substituted by a thiol group from a DTT molecule present in the buffer, which also supplies an oxygen atom. Carbon monoxide molecules occupy the other two positions.

Under the light of this new iron ion coordination sphere model, I carried out the EXAFS analysis on the jHmd mutants C176A and C176S and the reinterpretation of the results on jHmd wild type reconstituted[2] and mHmd wild type as isolated[50]. The outcome of the analysis is an outstanding fit (Tab. 7 H-M): For all the four samples the results revealed not only the presence of a carbon ligand at an intermediate distance from the O/N and the CO-carbon donors (at about 1.87 Å), but was able to distinguish between the contributions of the nitrogen and an oxygen electron donors. As the nitrogen ligand is substituted by an oxygen atom the quality of the model worsen and *vice versa*. This is uncommon and not expected, in fact, the scattering contributions of oxygen and nitrogen are typically undistinguishable. The whole coordination sphere is then comprised by 2 COs (environmental), 1S (from protein or DTT), 1C and 1N (cofactor) and a potential oxygen (solvent) (Fig. 32 D-F). It is also important to notice that models lacking the oxygen ligand give comparable fit quality, indicating the uncertainty on the sixth binding site. Anyhow, the presence of alternative donor atoms (*e.g.* sulfur, chlorine, phosphorus, beryllium, lithium, hydrogen) have been taken into account, but led to inconsistencies with the EXAFS data. The comparison between the previous and the revisited model of jHmd iron binding site clearly show the improvement of the model quality (Fig. 32).

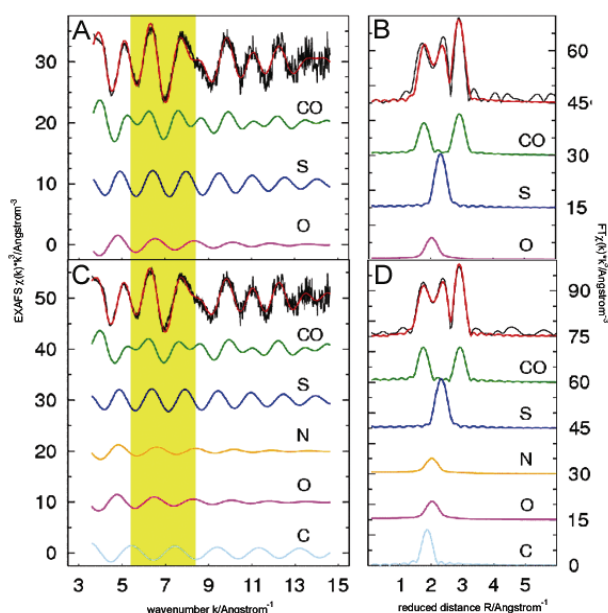


Fig. 33: Single scatterer contributions to Hmd EXAFS.

A, B) Individual EXAFS contributions of jHmd wild type iron binding site as firstly modeled.[2] C, D) Individual EXAFS contributions of jHmd wild type iron binding site as lately modeled. In C we can observe that the contributions of the nitrogen, the oxygen and the carbon are in opposite phase, thus partially canceling each other in the region highlighted in yellow. This explains why it has been so hard to hypothesize *a priori* the whole coordination sphere.

This scenario is unique and was hard to predict based on the raw EXAFS data. In fact, it would have been rejected in the absence of additional information because of the large number of refined parameters. Indeed, the contributions of C and N/O can hardly be detected, because they partially cancel out each other over a wide k -range (from $k = 4.5$ to $k = 8.5 \text{ \AA}^{-1}$) (Fig. 33). The simulation of these contributions requires individual Fe-L distances, which have been excluded deliberately in the initial refinements.

3.2.1.2 jHmd: XANES analysis[117]

The XANES spectra of the reconstituted wild type mononuclear [Fe]-hydrogenase jHmd (jHmd-wt), its cyanide inhibited form (jHmd-CN) and five model complexes have been extracted from the XAS spectra and investigated, in order to shed light on the electronic structure of jHmd iron ion. The analysis supplied information about the oxidation state of the metal ion, about the strong influence of the ligand type on the edge position and spectrum shape, about the impact that the coordination geometry has on the XANES and about the fundamental contribution of the cofactor's electron donors to fine tune the electronic structure of the iron ion.

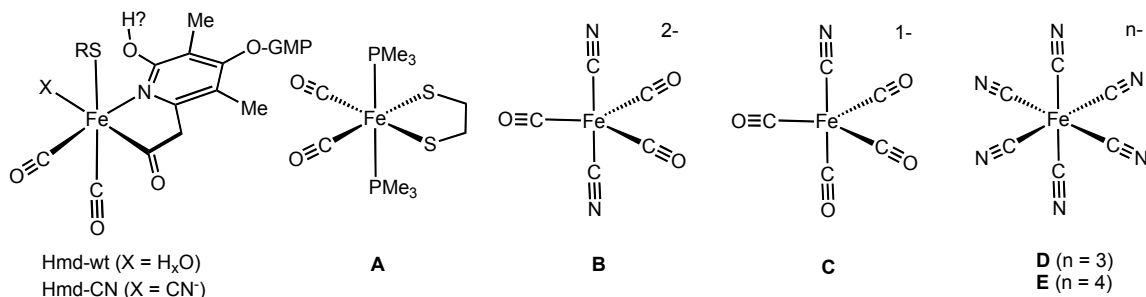


Fig. 34: Structural sketches of Hmd model complexes.

On the left: structure of the [Fe]-hydrogenase octahedral metal binding site. The iron is coordinated to: S-Cys176, two CO and the pyridinol- sp^2 -hybridized nitrogen and the acyl-carbon of the cofactor. An “unknown” donor, here represented as X, is associated to the iron trans to the acyl carbon. This is considered the vacant position ready for H₂ binding. The position of CO trans to pyridinol-nitrogen could not unambiguously be determined by X-ray crystallography, but it is estimated from the X-ray crystal structure of the mutant C176.[4] The model complexes are represented in A – E: A) Fe(II)(edt)(CO)₂(PMe₃)₂; B) [K(18-crown-6)]₂[Fe(0)(CN)₂(CO)₃]; C) K[Fe(0)(CN)(CO)₄]; D) K₃[Fe(III)(CN)₆]; E) K₄[Fe(II)(CN)₆]. For B – E, only the anions are shown.

Since the iron coordination in Hmd is unique, its XANES cannot be compared with spectra of known systems. Thus, we selected model compounds as anchor points for assessing the influence of iron oxidation state and its coordination sphere on the spectroscopic features. These model compounds are octahedral or five-coordinated low spin iron centers with electron donors groups similar to the ligands in the enzyme. The data from Fe(II)(edt)(CO)₂(PMe₃)₂ (**A**, edt = 1,2-ethanedithiolate), [K(18-crown-6)]₂[Fe(0)(CN)₂(CO)₃] (**B**), K[Fe(0)(CN)(CO)₄] (**C**), K₃[Fe(III)(CN)₆] (**D**) and K₄[Fe(II)(CN)₆] (**E**) are presented (Fig. 34). The two iron hexacyanides, **D** and **E**, were selected to enlighten the influence of the metal oxidation state on the absorption edge profiles. Both formal Fe(0)-compounds highlight the differences between CN and CO groups on the electronic structure of the metal ion: CO is a good σ donor and a strong π acceptor, while CN⁻ is a good σ donor and π acceptor. This affects Δ_0 (octahedral ligand field splitting energy: is the splitting between the nonbonding t_{2g} orbitals and the mildly anti-bonding e_g^* orbitals). It is interesting to notice that the presence of either of these ligand makes the iron ion in the low spin configuration increasing sufficiently Δ_0 . Compound **A** shows the influence of P/S donors.

The XANES spectra of all samples reveal strong differences in rising edge position and shape (Fig. 35). The hexacyanides **D** and **E** are highly symmetrical and only differ in the

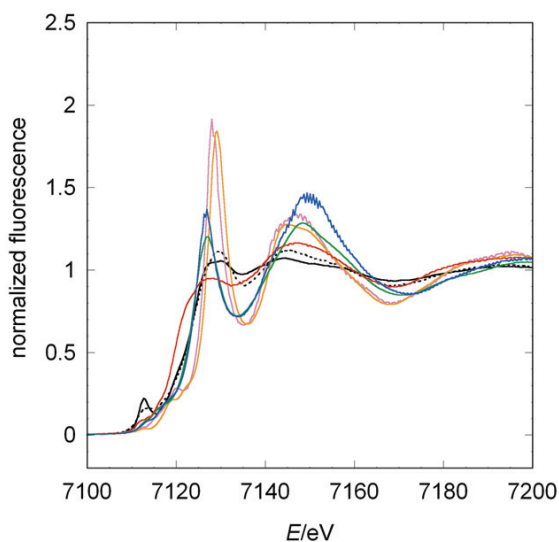


Fig. 35: Hmd and model complexes XANES.

Comparison among the experimental XANES of the model complexes and jHmd-wt. Black line: jHmd-wt; black broken line: jHmd-CN; red line: Fe(II)(edt)(CO)₂(PMe₃)₂ (A); blue line: [K(18-crown-6)]₂[Fe(0)(CN)₂(CO)₃] (B); green line: K[Fe(0)(CN)(CO)₄] (C); orange line: K₃[Fe(III)(CN)₆] (D); purple line: K₄[Fe(II)(CN)₆] (E).

formal oxidation state of the iron, which results in highly similar XANES spectra. The small shift in their absorption edges reflects the slightly different effective charges at the iron ion. In compounds **B** and **C**, the iron is in the formal oxidation state 0. These penta-coordinated complexes are structurally similar, differing only in the relative ratio of CO/CN⁻ donors. This similarity is reflected by their XANES (green and blue lines in Fig. 35). The differences observed in the peak intensities are ascribed to the exchange of one CO by CN⁻, which here influences in this case only the matrix element for the unoccupied orbitals, but not their energy

levels.[116] In compound **A**, the Fe(II) ion is bound to two CO ligands, two sulfur and two phosphine donors. The S and P donor ligands mimic to some extent the sulfur and nitrogen ligands bound to Fe in Hmd and they strongly affect the spectrum. jHmd-CN shares with the wild type the position of the pre-edge peak as well as the maxima and minima above the edge, but not the relative intensities, which indicate a higher symmetry for jHmd-CN (Fig. 36).

White lines (main peak formed by the rising edge and the following minimum):

D and **E** white-lines are very sharp, in line with the high symmetry of these iron centers. The penta-coordinated complexes **B** and **C** differ in the relative ratio of CO/CN⁻ donors. Their white-lines are less sharp, indicating a lower level of symmetry and the observed diversities between each other are due to the effect of the different backbonding properties of CO and CN⁻. In compound **A**, the low-symmetry of the iron coordination results in a broadened white-line. jHmd-wt XANES revealed characteristics very similar to compound **A**. The higher white-line intensity in jHmd-CN is indicative of a higher

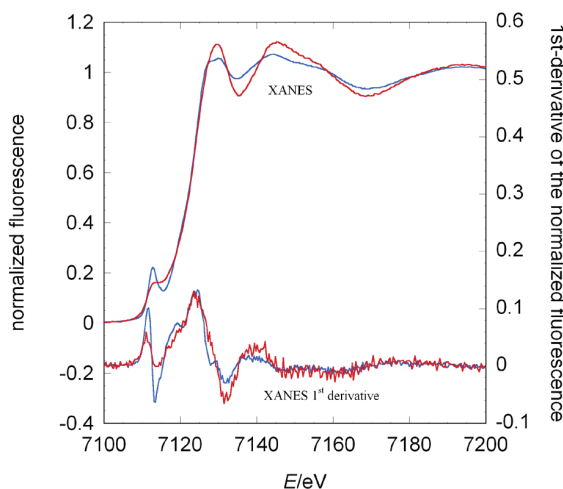


Fig. 36: Hmd-wt and Hmd-CN XANES comparison.

Comparison between the jHmd-wt and jHmd-CN XANES and their first derivatives. Blue lines, jHmd-wt; red lines, jHmd-CN.

symmetry. This is in line with the pre-edge peak area that is much smaller for jHmd-CN than for jHmd-wt (see below, Tab. 8). Moreover, The first derivative of the XANES spectra helps identifying fine features. The jHmd-wt derivative is characterized by the splitting of the second peak into three peaks representing unoccupied orbitals (white-line range: from 7115 to 7130 eV). This feature is absent in the inhibited form (Fig. 36). The presence

of the characteristic can be considered as an indicator of the active form of jHmd.

Absorption edges:

The absorption edges reflect the influence of both the formal oxidation state of the iron and of its ligands. The exact absorption edge positions were calculated from the first derivatives of the XANES spectra, following the definition: the exact edge position corresponds to the first maximum of the XANES first derivative within the white line rising edge energy window (Fig. 37, Tab. 8).

In accordance with its formal charge, the ferrocyanide compound (**E**) has an edge position at lower energies than the ferricyanide **D**, 7127 eV and 7127.5 eV, respectively (orange and purple lines in Fig. 37). As expected, both edge positions are at lower energies with respect to **D** and **E**. Interestingly, the edges of **B** and **C** differ by 1 eV from each other (B-edge = 7125 eV; C-edge = 7124 eV), although they are both Fe(0). This difference indicates the sensitivity of the effective charges at the metal ion. **A** shows a profound influence of the ligand type. Here, the donors P and S strongly affect the edge position, which is shifted towards lower energies by 7.5 eV from the other ferrous compound **E** (7126.6 eV). In accordance, the edge positions of jHmd-wt and jHmd-CN are similar to that of **A**, revealing a comparable effective charge at the iron ion and suggesting an analogue formal oxidation state.

Pre-edge peak areas:

Sample	edge position	pre-edge peak position	1s→3d pre-edge peak area
	<i>eV</i>	<i>eV</i>	10^{-2} <i>eV</i>
jHmd-wt	7119.2(2)	7112.7(2)	60(1)
jHmd-CN	7117.0(2)	7112.7(2)	28(2)
A	7116.0(2)	7112.0(2)	9(2)
B	7124.6(2)	7112.9(2)	8(1)
C	7123.8(2)	7112.6(2)	18(2)
D	7127.4(2)	7112.3(2)	2(1)
E	7126.6(2)	7111.9(2)	1(1)

Tab. 8: Edge and pre-edge peak parameters of Hmd and model complexes.

Edge positions, pre-edge peak positions and pre-edge peak areas for jHmd-wt, jHmd-CN and the model complexes. In parentheses the error margins on the last digit are given.

which reflects the heterogeneity of its octahedral ligand set. Complexes **B** and **C** are square pyramidal (penta-coordinated) and as a consequence, the areas are higher. An interesting case is complex **B** with an area of only 9×10^{-2} eV. This indicates higher symmetry potentially caused by the compensation of π -accepting and π -donating ligands. For jHmd-wt and jHmd-CN the largest pre-edge peak intensities are observed, indicating a highly distorted geometry at the iron site. jHmd-wt pre-edge peak is extraordinarily intense (60×10^{-2} eV) and is twice of that of the inhibited form (28×10^{-2} eV). These differences point towards a correlation between distortions of the active site geometry and catalytic activity of Hmd. In fact, in contrast to complex **A**, the octahedral symmetry is much more distorted in the enzyme, pointing to a specific tuning of the electronic structure (and thus most likely of the reactivity) by the protein environment, namely by the pockets harboring the CO groups. This hypothesis is supported by the much smaller pre-edge peak intensity observed for the isolated FeGP-cofactor.[50] Interestingly, such

This feature is frequently used as a measure of the symmetry and homogeneity of the iron coordination and is usually a good indication of the coordination number.[109,110,118,119]

Deviation from an ideal octahedral coordination increases the 1s to 3d/4p transition probability and thus the pre-edge peak intensity. In line with their octahedral iron-coordination and their homogenous ligand sphere, the hexacyanides **D** and **E** possess the smallest pre-edge peak intensity (1 and 2×10^{-2} eV) (Tab. 8). Complex **A** exhibits a pre-edge peak intensity of about 9×10^{-2} eV,

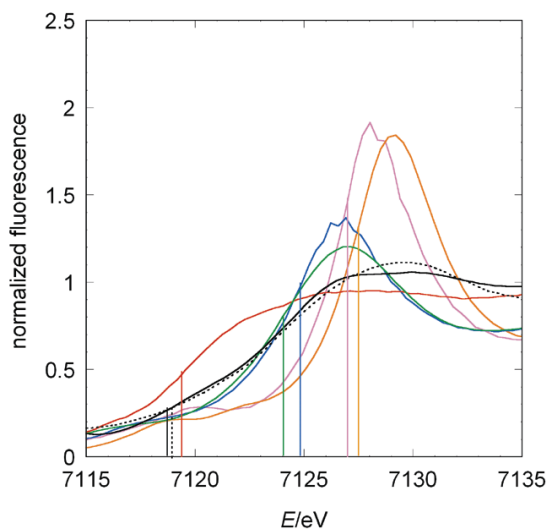


Fig. 37: Hmd and model complexes edge positions.

Comparison between the edge positions of the model compounds, jHmd-wt and jHmd-CN. Black line, jHmd-wt; black broken line, jHmd-CN; red line, Fe(II)(edt)(CO)₂(PMe₃)₂ (A); blue line: [K(18-crown-6)]₂[Fe(0)(CN)₂(CO)₃] (B); green line: K[Fe(0)(CN)(CO)₄] (C); orange line: K₃[Fe(III)(CN)₆] (D); purple line: K₄[Fe(II)(CN)₆] (E). For each sample, the edge position (first maximum of the first derivative in the rising edge) is indicated (straight lines).

big pre-edge peak intensities have never been reported for any other protein-bound iron ion.

Another consideration is worth to be mentioned. The model compounds were chosen to illustrate the two competing effects determining the edge position and the metal-ligand distances: metal oxidation state and ligand type. An additional effect becomes apparent: the overall shape of the XANES depends on the homogeneity of electron donors, which reflects in the geometry. Besides, the more cyanide molecules are bound to the iron, the sharper is the white-line. A confirmation of the trend comes from compound A. Its coordination is

heterogeneous and with no cyanides and the white line is small and broadened.

3.2.1.2.2 XANES simulations: model complexes and jHmd

To gain further insights in the electronic structure of the iron ion in [Fe]-hydrogenases, *in silico* simulations of the XANES spectra of the model systems and jHmd-wt were carried out with the program FEFF8.2 (see par. 2.4.14.6). Simulations of the model systems XANES served as a proof of principles and defined the required cluster size in this study. I analyzed both the XANES and their first derivatives highlighting homologies and differences among spectra. It is worth to remember that no “XANES equation” is available due to the difficulties to interpret quantum mechanical events correlated to many-body multiple scattering events dominating the XANES. Hence, our approach is purely qualitative.

n	Fe	L	R	$2\sigma^2$	$R_{CX}(\text{\AA})$	EF	Φ
			\AA	\AA^2	\AA	eV	$\times 10^3$
jHmd-wt							
2	Fe	C ^a	1.776(3)	0.0053(8)	1.16(1)	-1.9(7)	0.1691
1	Fe	C	1.91(1)	0.0053(8)			
1	Fe	O	2.49(7)	0.004(4)			
1	Fe	N	2.05(1)	0.0053(8)			
1	Fe	S	2.304(7)	0.008(3)			
2	Fe	O ^a	2.936(8)	0.004(1)			
jHmd-CNi							
2	Fe	C ^a	1.76(1)	0.005(1)	1.16(2)	-5(1)	0.4754
1	Fe	C ^b	2.10(2)	0.0246(1)	1.04(3)		
1	Fe	O	1.88(6)	0.004(2)			
1	Fe	S	2.33(2)	0.019(2)			
2	Fe	O ^a	2.920(9)	0.009(1)			
1	Fe	N ^b	3.14(1)	0.003(1)			
(A): Fe(II)(edt)(CO)₂(PMe₃)₂							
2	Fe	C ^a	1.781(6)	0.006(1)	1.16(1)	-5.3(5)	0.1902
2	Fe	S	2.31(3)	0.004(7)			
2	Fe	P	2.26(4)	0.004(7)			
2	Fe	O ^a	2.946(5)	0.007(1)			
(B): K₂[Fe(0)(CN)₂(CO)₃]							
3	Fe	C ^a	1.763(3)	0.0010(8)	1.163(9)	-1.8(4)	0.1578
2	Fe	C ^b	1.865(6)	0.0010(8)	1.18(1)		
3	Fe	O ^a	2.926(3)	0.0010(4)			
2	Fe	N ^b	3.048(6)	0.0010(4)			
(C): K[Fe(0)(CN)(CO)₄]							
4	Fe	C ^a	1.796(4)	0.0068(8)	1.156(9)	-1.2(5)	0.1830
1	Fe	C ^b	1.94(1)	0.0068(8)	1.16(3)		
4	Fe	O ^a	2.952(5)	0.0080(6)			
1	Fe	N ^b	3.10(2)	0.0080(6)			
(D): K₃[Fe(III)CN₆]							
6	Fe	C ^b	1.932(2)	0.0040(4)	1.163(5)	-4.6(3)	0.1535
6	Fe	N ^b	3.095(3)	0.0057(4)			
(E): K₄[Fe(II)CN₆]							
6	Fe	C ^b	1.911(3)	0.0045(5)	1.168(6)	-3.6(4)	0.1972
6	Fe	N ^b	3.079(3)	0.0047(4)			

Tab. 9: EXAFS parameters of jHmd and model complexes.

The table shows the parameter extracted after structure-based EXAFS refinement of jHmd-wt and the compounds A, B, C, D, E. The numbers (n) of ligand atoms (L), their distance to the iron ion (R), the respective Debye-Waller factor ($2\sigma^2$), the C–O or C–N bond length (R_{CX}), the Fermi energy for all shells (EF), and the fit index (Φ), indicating the quality of the model.

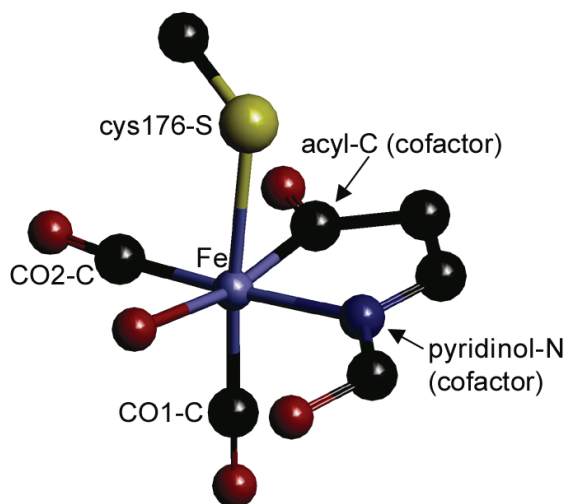


Fig. 38: Hmd metal binding site.

Ball and stick representation of the [Fe]-hydrogenase jHmd octahedral metal binding site as modeled by structure-based EXAFS analysis: violet, the iron; black, the carbons; blue, the nitrogen; red, the oxygens; yellow, the sulfur. The iron is coordinated to: the Cys176-sulphur, two CO and the pyridinol-*sp*²-hybridized nitrogen and the acyl-carbon of the cofactor. An “unknown” donor represented as an oxygen, is associated to the iron trans to the acyl carbon. This is considered the vacant position ready for H₂ binding.

In order to carry out the simulations, the atomic coordinates of the systems under study are necessary. Firstly we tried the simulations using the available x-ray diffraction coordinates either of the model complexes (kindly supplied by our collaborator Thomas B. Rauchfuss, Department of Chemistry, University of Illinois, USA) or of jHmd in the revisited model (kindly supplied by our collaborator Seigo Shima, Max-Planck-Institute für terrestrische Mikrobiologie, Marburg, Germany).

Successively, I performed EXAFS refinements exploiting the experimental data and the 3D structures of the samples (structure-

based EXAFS refinement). The atomic coordinates of the obtained EXAFS models have been extracted and used for the simulations (Tab. 9, Fig. 38). The outcome of the simulations clearly demonstrated that using the coordinates extracted from the structure-based EXAFS refinement the simulations were better representing the experimental data, in particular of jHmd.

The principal features of the model complexes XANES spectra have been reproduced: the curves trend, the sequence of the rising edge positions and the white-lines correlation with the symmetry and homogeneity of the coordination sphere (Fig. 39, coloured lines). Only the relative intensities and thus the magnitude of the transition matrix element are not adequately modeled. This result was the prerequisite to proceed on the analysis of jHmd XANES. Amazingly, the positions of maxima and minima and the general shape of the experimental data have been reproduced for the enzyme as well, suggesting the agreement between the electronic states in jHmd-wt and the simulation (Fig. 39 black

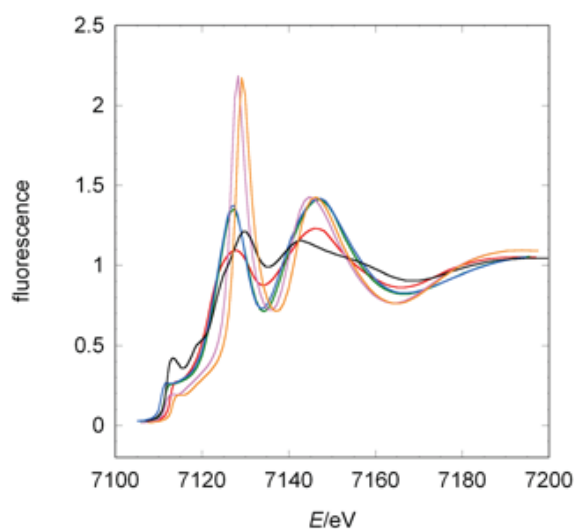


Fig. 39: Hmd XANES simulation.

Comparison among the simulated XANES of the model systems and jHmd-wt. Black line: jHmd-wt; red line Fe(II)(edt)(CO)₂(PMe₃)₂ (A); blue line: [K(18-crown-6)]₂[Fe(0)(CN)₂(CO)₃] (B); green line: K[Fe(0)(CN)(CO)₄] (C); orange line: K₃[Fe(III)(CN)₆] (D); purple line: K₄[Fe(II)(CN)₆] (E).

line, Fig. 40 A). Again, only the relative intensities and thus the magnitude of the transition matrix element are not adequately modeled. In the first derivative of the simulated spectrum, the distinctive 3-fold split white line peak is preserved, highlighting the existence of three narrow energy levels ascribed to three unoccupied orbitals (Fig. 40 B). As already mentioned in a previous paragraph, this electronic feature is disrupted upon inhibition by cyanide: CN⁻ binding alters significantly the electronic structure of the iron ion.

This change, as well as the saturation of the coordination sphere of the iron(II), is relevant to its inhibitory effect. Compared to the model systems, jHmd-wt simulations differ as much as the experimental data from compounds B – F, but for compound A the similarities are even higher than in the experimental data. The rather similar curves even share the edge position, pointing towards a ferrous ion.

In order to evaluate the impact of individual donors on the electronic structure of jHmd-wt, I successively omitted one of them at the time in the simulations and compared the resulting curves with the fully coordinated jHmd iron site spectrum. Here, I focused on first derivatives to highlight the impact on the electronic structure. Omitting one of the two CO ligands (CO1 and CO2) has a strong influence on the entire XANES spectrum, in the energy interval from 7120 to 7170 eV, in line with their intense multiple scattering contributions (Fig. 41 A, B). The differences between these simulations show the importance of the geometry. In the XANES simulations the geometry is taken into account by multiple scattering contributions (from the central iron ion to a donor, continuing via the central iron atom to the donor in trans position and back to the iron

ion); for CO1 this multiple scattering pathway includes the sulfur (2.3 Å away from the iron ion) and for CO2 the nitrogen atom opposite to CO2 (2.0 Å away from the metal ion) resulting in different phase and amplitude of these contributions. Interestingly, in both spectra the 3-fold white line split present in the first derivative of jHmd-wt experimental spectrum is conserved, indicating that these ligands cannot strongly contribute to the energy of the three unoccupied orbitals. Similarly, the sulfur contribution to this feature is milder than expected on this

region. Instead, the region from 7138 to 7155 eV is appreciably affected (peak following the white line in the XANES) (Fig. 41 E). The cofactor donors mainly influence the region from 7115 to 7150 eV (Fig. 41 C, D). In particular, the white line is affected. Pyridinol-N and acyl-C omissions markedly change the 3-fold split feature, indicating their function in fine tuning the electronic structure. The result reveals the essential contributions of the acyl-carbon and of the cofactor nitrogen to the electronic structure were visualized by changes in the three unoccupied orbitals of the rising edge. In the crystal structure, because of its planarity, the heterocyclic ring of the cofactor is present in a pyridinol and not in a pyridone tautomeric form, and therefore the nitrogen atom is in a π accepting sp^2 configuration. The pyridinol group in particular, if the hydroxyl group is in a deprotonated state, can have ligand back-bonding properties similar to those of cyanide, which acts as an iron ligand in the [NiFe]- and [FeFe]-hydrogenases.[120,121] Moreover, due to the aromaticity of the pyridinol group, the acyl-carbon, as the nitrogen, is in a π accepting sp^2 configuration leading to back-bonding properties likely more similar to carbon monoxide.

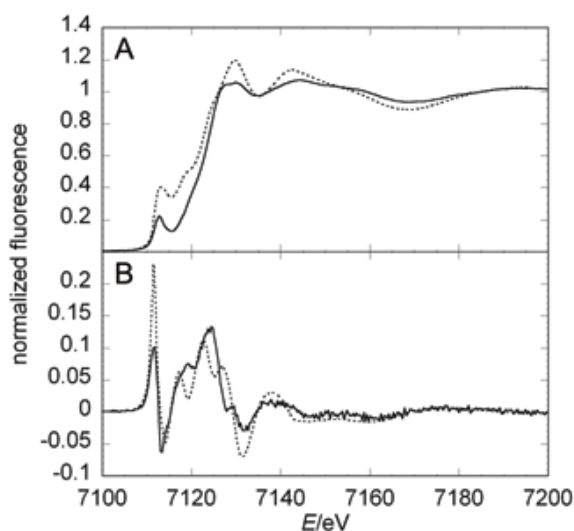


Fig. 40: Hmd simulated and experimental XANES.

Comparison between experimental and calculated spectra of jHmd-wt. The XANES (A) and its 1st derivative (B) is shown. The full lines represent the experimental data, while the broken lines represent the simulations.

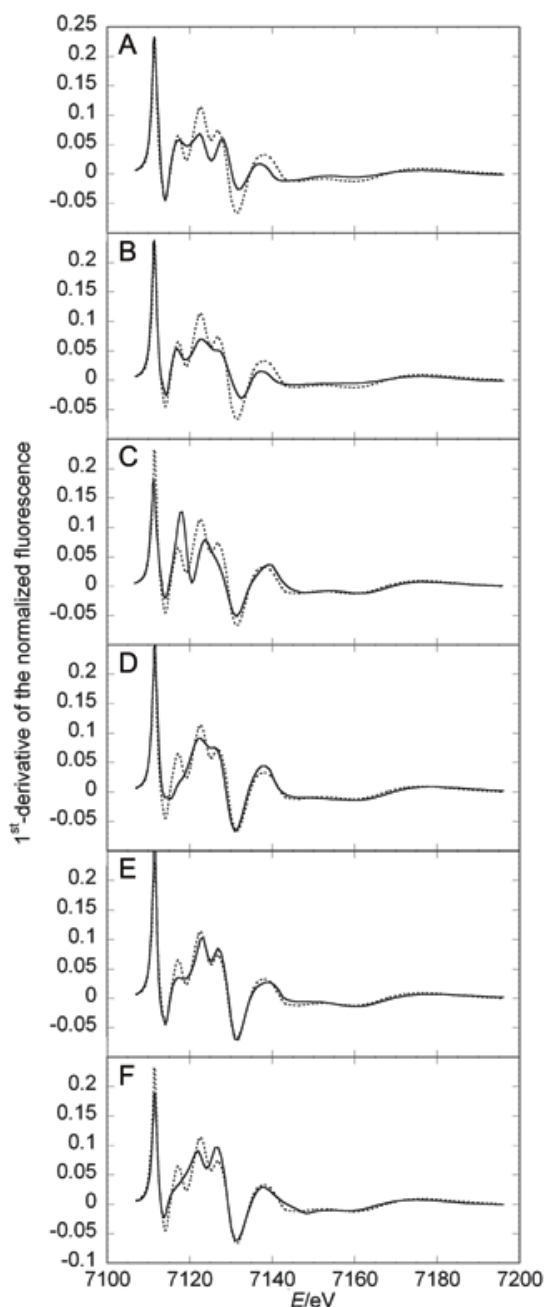


Fig. 41: Hmd-ligands contributions to the XANES.

Comparison between the first derivative of jHmd-wt XANES simulation in the full coordination (dotted lines) and in simulations where one donor at the time is omitted (full lines). A) CO1 knockout, B) CO2 knockout, C) acyl-C of the cofactor knockout, D) pyridinol-N of the cofactor knockout, E) Cys176-S knockout, F) oxygen knockout.

Thus, the electron density around the iron ion must be highly delocalized and the contributions of the COs and cofactor electron donors appears stronger than typical enzyme metal binding species, hence fading the influence of sulfur. When removing the “solvent-oxygen” from the simulation we obtained a small effect on the beginning of the rising edge (Fig. 41 F, from 7117 to 7132 eV). The triplet is conserved.

The above results highlight the distinctive contribution from each of the six ligands. The differing contributions of the two CO ligands suggest that they play a key electronic role, as expected because of their strong tendency to back-bond. They forced the iron in the low spin state and they promote the electron delocalization at the iron ion.

The comparison of the jHmd-wt XANES with the model complexes identified the ferrous complex **A** as a mimic for the enzyme’s electronic structure. Moreover, Hmd-wt and complex **A** share the CO and sulfur ligand types. Based on this similarity, the identical absorption edge positions allow concluding that the enzyme harbors a ferrous ion.

3.2.2 [Cu₂L₂(μ-O)₂]I₂ excited state characterization[122]

The ground state of [Cu₂L₂(μ-O)₂]I₂ (L = B(TMPip)G₂p) has been characterized by Cu-K edge XAS at 20 K (Fig. 42 A). Four light ligands (O / N) binding to each Cu ion have been identified. The Cu-Cu contribution is refined to a metal-metal distance of 2.84 Å. The absorption edge position points towards a change from Cu(I) to Cu(III) upon formation of the complex (Fig. 8). The transmission and fluorescence signals were monitored at 8990 eV upon optical excitation at room temperature to characterize the excited state of the complex. The collected spectra show that while the transmission increases immediately, the fluorescence follows with few seconds delay (Fig. 42 B). The reasons for this behavior are enigmatic: The UV-light might have heated up the sample causing lower absorption of X-rays in the 1 mm thick cuvette. Successively, a small percentage of the Cu-complex precipitated prior to the disruption of the experiment at elevated temperatures. Thus, after switching off the UV light the transmission decreases below the starting point. Other differences in the XANES with and without UV-light illumination could not be identified for a variety of concentrations, indicating a too low UV-photon intensity. This is in line with the lifetime of the excited state, which is estimated to $\Delta t \approx h/\Delta E \approx h/ 0.2 \text{ eV} \approx 20 \text{ fs}$ based on the width of the resonance Raman peaks. At the given UV intensity $\sim 10^{16}$ photons are generated per second; considering the absorption probability of $\sim 40\%$ in 1 mm solution only a small fraction of the 10^{15} Cu ions irradiated by the $1 \times 1 \text{ mm}^2$ X-ray beam are optically excited when the pulsed synchrotron beam hits the sample. Therefore, the characterization of optical excitation states by XAS might only be feasible with the help of a synchronized, pulsed UV-source. Although, even in this case the total power absorbed by the sample might cause similar artifacts. Hence, in order to elucidate the structural changes induced upon charge-transfer we exploited a more elegant and instrumentally less demanding approach. Resonance Raman spectroscopy does not require a full occupancy of the excited state, because only the excited molecules contribute. Thus, experiments can be performed at lower laser intensities. The Raman spectrum of [Cu₂L₂(μ-O)₂]I₂ exhibits strong vibrational excitations that can be assigned to the bending vibration of the copper-

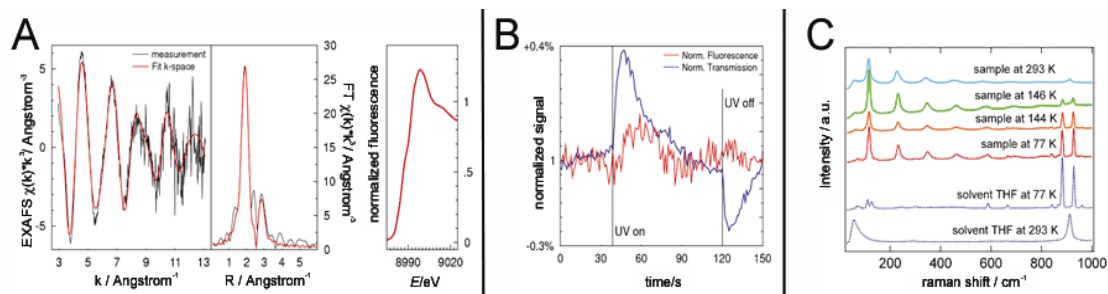


Fig. 42: Results of EXAFS, XANES and resonance Raman spectroscopy on $[\text{Cu}_2\text{L}_2(\mu\text{-O})_2]_2$.

A) EXAFS and corresponding FT plus XANES. B) Normalized transmission and fluorescence at 8990 eV. C) Raman spectra of $[\text{Cu}_2\text{L}_2(\mu\text{-O})_2]_2$ and THF at 350.7 nm. For data at 293 K and 77 K 10 minutes were given to reach stable temperature. Data around the melting point of THF (165 K) were taken while cooling down (144K/145K).

oxygen core at 114.3 cm^{-1} and its integer multiples. For a given local symmetry the structural change is calculated from the Huang-Rhys parameter given by the intensity decrease in the Raman spectra.[5,60] As previously reported,[5] the copper oxygen distance increases by 0.01 Å and the oxygen-oxygen distance decreases by 0.13 Å. So far, the limited stability of such complexes restricted the measurements to cryogenic temperatures. This experiment enabled a direct comparison of cryogenic and room temperature conditions. Below the freezing point of the solvent THF (165 K) additional contributions become apart (Fig. 42 C, green curve). These peaks can be assigned to THF (Fig. 42 C, dotted blue line). Due to the huge relative difference in intensity and similar energy transfers, no subtractive calculations were applied to the spectra in order to avoid artifacts. The induced structural changes show no temperature dependence.

3.2.3 ABCE1 protein: XAS characterization

The edge shape of the XANES spectra (Fig. 43 A) can be used as a fingerprint for the electronic structure of the metal ions. ABCE1 XANES resembles the one reported for oxidized hydrogenase II from *Clostridium pasteurianum*, which harbors $[\text{4Fe-4S}]^{2+}$ clusters.[123] Typical features are the resonance in the rising edge and the rather flat maximum followed by a sharp minimum. The pre-edge peak intensity of about $21 \times 10^{-2} \text{ eV}^2$ is consistent with a four ligands coordination sphere (4C) and with an oxidized iron-sulfur cluster. The extracted fine structure (EXAFS) is dominated by a

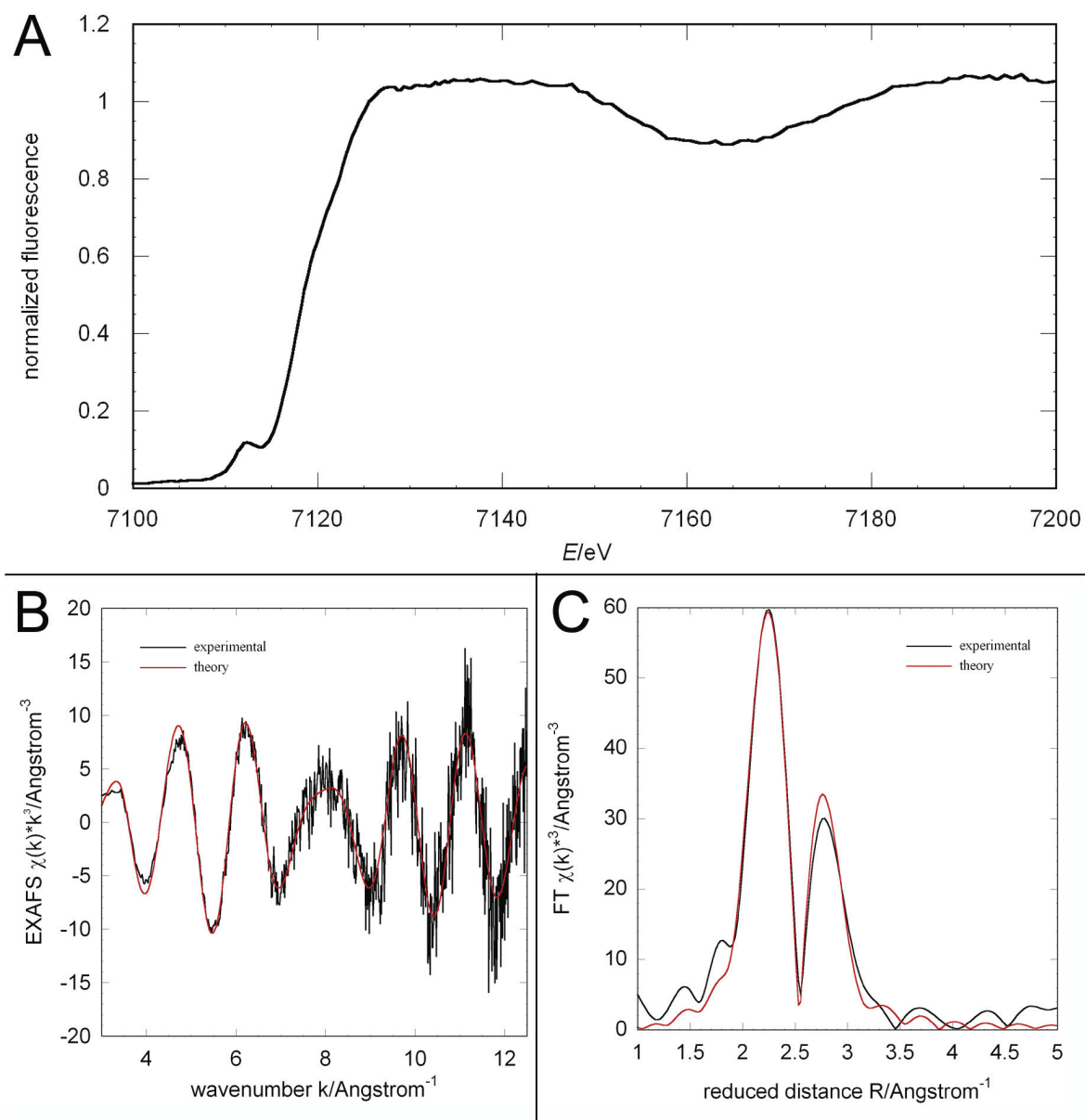


Fig. 43: XAS analysis of ABCE1.

A) Iron K-edge X-ray absorption spectrum of ABCE1 from *Sulfolobus solfataricus*. B) Iron K-edge, k^3 weighed, EXAFS spectrum and C) the corresponding Fourier transform. The EXAFS is dominated by two contributions, the Fe-4S signal at $2.29 \text{ \AA} \pm 0.01 \text{ \AA}$ and the Fe-3Fe signal at $2.74 \text{ \AA} \pm 0.01 \text{ \AA}$. The Debye-Waller factors ($2\sigma^2$) for these contributions were refined to $0.010 \pm 0.001 \text{ \AA}^2$ and $0.008 \pm 0.001 \text{ \AA}^2$, respectively. EF was $-3 \text{ eV} \pm 1 \text{ eV}$.

single frequency with a shift at about 8 \AA^{-1} (Fig. 43 B). The high intensity at wave numbers larger than 10 \AA^{-1} in biological samples indicates the presence of a multinuclear metal center. This is consistent with the peak at about 2.8 \AA in the corresponding Fourier

transformation (FT) (Fig. 43 C). The high intensity of the main peak at about 2.3 Å in the FT points towards a homogenous first coordination sphere formed by sulfur ligands. The FT is very similar to the one observed for the $[4\text{Fe-4S}]^{2+}$ clusters mentioned above.[123] Models based on the assumption of $[4\text{Fe-4S}]^{2+}$ clusters resemble the data very well. All attempts to replace one of the sulfur ligands in the fit by light atoms such as oxygen or nitrogen lead to artificially long Fe-O/N distances. Thus, recognizable contributions above 10% of the average ligand sphere are excluded. The Fe-S distance of 2.29 Å and the Fe-Fe distances of 2.74 Å match the literature values for oxidized $[4\text{Fe-4S}]$ clusters very well.[124]

4 Conclusions and discussion

This section summarizes and discusses the results presented so far about the biochemical and biophysical characterization of the human protein ETHE1 and about the XAS analysis of the mononuclear [Fe]-hydrogenase Hmd from *Methanocaldococcus jannaschii*, the (μ -oxo)-dicopper(III) species $[\text{Cu}_2\text{L}_2(\mu\text{-O})_2]\text{I}_2$ and the protein ABCE1 from *Sulfolobus solfataricus*.

4.1 *Homo sapiens* ETHE1 characterization

The non-heme mononuclear-iron sulfur dioxygenase ETHE1 from *Homo sapiens* has been cloned and expressed in *E. coli*. The protein has been purified (purity > 98%) and characterized biochemically and biophysically. Both a robust and reproducible protocol for the production of *Hs*ETHE1 and its metal-free form have been developed.

I demonstrate that the protein is sensitive to oxidizing conditions and requires non- thiol-based reducing agents such as TCEP to don't aggregate. With the help of this protocol, the protein can be stored for long periods at -80°C upon quick freezing in a buffer containing TCEP and glycerol. I proved by SLS, MS and crosslinking experiments (see par. 2.4.4, 5, 9) that *Hs*ETHE1 is a dimer in solution. No lactamase, phosphatase, aryl sulfatase and esterase activity has been detected for this enzyme. But, I discovered that *Hs*ETHE1 interacts with one of its supposed reaction products (GSH) gaining a light blue color. This change is detectable by UV-Vis. Apo-*Hs*ETHE1 has been titrated with metals. The experiments proved that the protein possesses high metal specificity. Under reducing conditions, it is able to bind with high affinity iron(III) in complex with NTA and with low affinity nickel ions. SAXS showed that *Hs*ETHE1 in solution is a dimer whose low resolution structure matches tightly the 3D structural model of *At*ETHE1. Moreover, SAXS showed that the metal-free protein is extremely sensitive to oxidizing conditions and that under reducing conditions it is no longer able to dimerize, forming chain like supramolecular structures from globular metal-free protein units. This means that, *in vivo*, cells must ensure that the protein is kept charged with iron, avoiding

protein aggregation and deposition. This might be achieved through a specific and still unknown metallo-chaperone.

EXAFS revealed an octahedral iron-binding geometry. The iron ion coordinates a 2-imidazole/1-carboxylate triad, which is typical of the non-heme mononuclear high spin iron(II) dioxygenases[35-37,105,114] and 3 oxygen atoms. Intriguingly, one of the coordinating oxygens is predicted to be at an atypically short distance, previously observed only in iron(III)-OH bonds, in the extradiol dioxygenase upon substrate binding, and in bidentate iron(II)-peroxo complexes.[36,37,105,114] XANES analysis showed an octahedral hexa-coordinated iron(II) high spin metal centre, which is consistent with the proposed EXAFS model. Mössbauer spectroscopy results exhibit the presence of two distinct states in which the protein seems to be in equilibrium. Both states correspond to octahedral high spin iron(II) ions coordinated by weak field ligands, which is in perfect agreement with the overall XAS analysis. The difference between the two states resides in the symmetry of the iron ion site. One state represents about the 68% of the population and is geometrically more distorted. I also presented the potential enzymatic reaction mechanism, in which molecular oxygen is reduced and highly reactive glutathione persulfide species are oxidized with formation of sulfite and reduced glutathione. In this mechanism, the iron is transiently oxidized to a ferric iron.

Thus, *Hs*ETHE1 is a homodimeric [Fe]-dioxygenase. Its iron binding site possesses characteristics in common with other oxygen activating high spin mononuclear iron dioxygenases[36], but also unique features (short Fe-O distance). The mononuclear non-heme high spin iron(II) enzymes bind and activate dioxygen to catalyze a variety of key biochemical transformations, including many of medical, pharmaceutical and environmental significance. These enzymes utilize high-spin iron(II) active sites and additional reducing equivalents from cofactors or substrates to couple the reduction of O₂ and the dioxygenation of a substrate.[114]

Besides, *Hs*ETHE1 in the presence of GSH has been studied by EXAFS. GSH is not only a product of ETHE1 reaction, but it is the major endogenous antioxidant produced by the cells of any organism.[125] The analysis showed the possibility that reduced glutathione directly binds to the iron ion by its sulfur atom in substitution of oxygen.

In conclusion, I elucidate the physical-chemical properties of a protein, which is a key element in the sulfur detoxification pathway and extremely important from the medical point of view due to its involvement in ethylmalonic encephalopathy, apoptosis and cancer. The gained knowledge on the ethylmalonic encephalopathy protein ETHE1 will be invaluable for attempts to further characterize this class of enzymes. In the future, it will be desirable to carry out further Mössbauer experiments aimed to investigate the ETHE1-GSH interaction and to study ETHE1 during its activity. Even if the turnover would be at low rate (~10%), Mössbauer spectroscopy is able to detect small traces of such species. Thereby, through spectral modifications we could understand the geometrical and electronic changes taking place during the reaction cycle. Moreover, obtaining the three dimensional structure of ETHE1 will allow describing in detail the reaction mechanism, the origin of the effects of the mutation found in ethylmalonic encephalopathy and the specifics of its interaction with protein partners.

4.2 X-ray Absorption Spectroscopy applications and methods development

The overall view of the results obtained about the biophysical characterization by XAS analysis of the [Fe]-hydrogenase jHmd, the tyrosinase-metal-binding-site mimicking compound $[\text{Cu}_2\text{L}_2(\mu\text{-O})_2]\text{I}_2$ and the protein ABCE1, are here presented and discussed.

4.2.1 Mononuclear [Fe]-hydrogenase

The XAS analysis carried out on the Hmd hydrogenase from *Methanocaldococcus jannaschii* revealed an unique coordination and electronic structure of the iron ion at the enzyme's active site. The coordination sphere is distorted octahedral and comprises two carbon monoxides, one sulfur ligand supplied by a cysteine residue in the protein, the FeGP cofactor, which binds the iron in a bidentate manner through a pyridinol nitrogen and an acyl carbon, and a solvent molecule at the site where the molecular hydrogen is supposed to bind. The cofactor coordination is unique. Unique because no biological system is known to exploit such iron-acyl interaction. Besides, the backbonding properties of the acyl monoxides together with the backbonding properties of the

cofactor (given by the acyl-pyridinol system) promote a strong electron delocalization at the iron ion, which is fundamental for the enzymatically active high spin state of the metal. In this scenario, while the two CO ligands ensure low-spin state, the arrangement of the other four donors tune the reactivity toward H₂, which is activated at the labile site trans to the acyl ligand. Interestingly, an acyl group coordinating an enzyme's metal has only been reported for the acetyl-CoA synthase/decarbonylase reaction as possible intermediate in the formation of acetyl-CoA from CO and a methyl group.[126,127] Here, the acyl group binds a nickel ion.

In addition, I demonstrate the importance of the geometry and of the cofactor's contributions to fine tune the sophisticated electronic structure of the iron ion. The geometrical distortion contributes to the molecular orbital fine energy splitting and the cofactor donors are essential to properly tune the orbitals energy levels.

jHmd iron ion formal oxidation state has been matter of debate.[50] Both Mössbauer and XAS couldn't supply a clear answer about the oxidation state of the iron because of the intrinsic ambiguity of the spectroscopic results. By XANES analysis, it has been possible to assign the oxidation state to 2+ that is also consistent with the iron's XANES of the hydrogen-sensing [NiFe]-hydrogenase HoxC subunit from *Ralstonia eutropha*, which is accepted as iron(II).[128]

The overall results supply novel and important knowledge about mononuclear hydrogenases iron sites and on molecular hydrogen activation in general. Hydrogenases have a reactivity at least comparable with that of platinum, which is used industrially to catalyze hydrogenation.[2,55] H₂ is considered a major fuel in future energy technology, but the amounts of catalyst required for large scale H₂ production and use will require alternatives to platinum, which is expensive and not abundant. One approach of current research is to learn from hydrogenases. The results of this work may provide a useful knowledge for designing new biomimetic catalysts aiming at cheaper and greener generation and utilization of H₂. [55] A lot of effort is presently put on the creation of such biomimetic compounds. Recently, thanks to our collaborator T.H. we analyzed a novel iron-acyl-thiolato complex: the cyanide derivative Et₄N[Fe(SPh)(Ph₂PC₆H₄CO)(¹³CN)(CO)₂] So far, this complex revealed striking similarities with the CN inhibited form of jHmd (data not shown). Moreover, several

model compounds mimicking the metal centers of hydrogenase and able to interact with protons and/or H₂ have recently been reported.[129-133]

4.2.2 [Cu₂L₂(μ-O)₂]I₂ excited state

Optical excited molecules play an increasingly important role in research at light sources. We exploited two synergic approaches: pumped-XAS and an innovative combination of EXAFS spectroscopy and resonant Raman scattering, to structurally characterize the ground and the excited states of a complex mimicking the active site of tyrosinases: [Cu₂L₂(μ-O)₂]I₂. So far, the limited stability of such complexes restricted measurements to cryogenic temperatures, but [Cu₂L₂(μ-O)₂]I₂ is the first μ-oxo dicopper complex stable at room temperature.

The pumped-XAS study shows that the X-ray transmission through the sample at the energy of 8990 eV increases immediately upon optical excitation, and the fluorescence signal follows with a few seconds delay. The reasons for these observations have been assigned to experimental artifacts, such as the increasing of the temperature due to UV light irradiation, protein precipitation and chemical reactivity of the compound solvent against the sample holder material or against the glue used to seal the cuvette. No other differences in the XANES could be detected upon irradiation because of a too low UV-photon intensity. Hence, XAS might only be feasible with the help of a synchronized, pulsed UV-source.

With resonance Raman scattering spectroscopy, the experiments can be performed at lower laser intensities because only the excited states contribute to the final signal. The Raman spectrum of [Cu₂L₂(μ-O)₂]I₂ exhibits strong vibrational excitations assigned to the bending vibration of the copper-oxygen core at 114.3 cm⁻¹ and its integer multiples. The analysis shows that the copper-oxygen distance increases by +0.01 Å and the oxygen-oxygen distance decreases by -0.13 Å. This behavior has no temperature dependence.

Whenever the local symmetry of the system allows such approach (in a centrosymmetric molecule, asymmetrical stretching and bending will be Raman inactive. In fact, only transitions where the polarizability of the molecule changes can be observed and a change in polarizability is compatible with preservation of the center of symmetry)[134],

resonant Raman spectroscopy is experimentally by far less demanding than pumped XAS experiments. Eventually, the combination of resonant Raman spectroscopy and X-ray absorption spectroscopy can give direct access to structural and electronic parameters of optical excited systems. In future, resonance Raman experiments at copper M-edges at free electron laser sources such as FLASH (DESY, Hamburg, Germany) may provide novel information to further characterize the optical excited state of $[\text{Cu}_2\text{L}_2(\mu\text{-O})_2]\text{I}_2$.

4.2.3 ABCE1

ABCE 1 is essential for the viability of all eukaryotes and archaea due to its involvement in translation initiation and/or ribosome biosynthesis. ABCE1 is a unique ATP binding cassette protein superfamily because of the presence of Fe-S clusters. In this study, I determined the type and coordination of the Fe-S clusters in ABCE1 from *Sulfolobus solfataricus*.

XAS demonstrates the presence of diamagnetic $[\text{4Fe-4S}]^{2+}$ clusters. XANES showed that the clusters were in their oxidized state from comparison with known systems.[123] EXAFS is consistent with this. The analysis revealed a homogeneous coordination sphere of the iron ions formed by four sulfurs and three iron ions. The calculated Fe-L distances are matching very well the literature.[124] Recently, the X-ray structure of the complete ABCE1 protein from *Pyrococcus abyssi* at the nominal resolution of 2.8 Å has been solved (Protein Data Bank (PDB): 3BK7) (Fig. 9).[135] The reported atomic structure is in total agreement with our results.

The fundamental role of ABCE1 in RNase L inhibition, HIV capsid maturation, translation initiation and ribosome biosynthesis,[61,62,64-66,136] suggests that the two essential diamagnetic $[\text{4Fe-4S}]^{2+}$ clusters identified in this study are involved in recognition and modification of RNA assemblies.

5 Outlook

1. Characterization of the [Fe]-dioxygenase ETHE1 from *Homo sapiens*

I performed a biochemical and biophysical characterization of the human protein ETHE1. Several techniques have been applied for studying this enzyme fundamental for human development and likely for all metazoa and superior plants. The knowledge on *Hs*ETHE1 I gained here will be a solid basis for attempts to further characterize this class of enzymes. In future, it will be desirable to carry out Mössbauer spectroscopy experiments to study *Hs*ETHE1's iron site while the protein performs its activity. This will help understanding changes in the oxidation state and coordination sphere of the iron ion during substrate oxidation, providing further insights into *Hs*ETHE1's reaction mechanism and biological sulfur dioxygenation. Besides, Mössbauer spectroscopy can be applied to determine changes in the electronic structure of the iron ion in presence of the reaction product GSH. Studying on the atomic level *Hs*ETHE1 and the interaction with protein partners by X-ray crystallography or NMR may allow to describe in detail the reaction mechanism, the origin of the loss of function observed in ethylmalonic encephalopathy, and its roles inside the cell. Ultimately, the acquired knowledge may lead to the development of a therapy against ethylmalonic encephalopathy and inhibition of the enzyme might improve chemotherapy of liver cancer.

2. X-ray Absorption Spectroscopy applications and method development

Taking advantage of X-ray Absorption Spectroscopy, I in addition shed light on the physical-chemical properties of other highly interesting metalloproteins and model complexes, such as the [Fe]-hydrogenase (Hmd), the tyrosinase model complex $[\text{Cu}_2\text{L}_2(\mu\text{-O})_2]\text{I}_2$ and the ATP binding cassette protein ABCE1. Comprehend in detail the metal binding sites of these enzymes is a crucial challenge towards clean energy technology development (hydrogenases; low cost H_2 production), understanding the nature of reactions involving charge transfer processes (tyrosinase model systems) and blocking HIV capsid assembly (ABCE1).

2a. XAS on [Fe]-hydrogenase jHmd's iron site

Hydrogenases are catalysts with efficiency comparable to platinum, which is used industrially to catalyze hydrogenation. However, platinum is expensive and not abundant. H₂ is considered a major fuel in future energy technology and the demand of catalyst for large scale H₂ production will require alternatives to platinum. Learning from hydrogenases may provide the knowledge for designing new biomimetic catalysts aiming at cheaper and greener generation and utilization of H₂. So far, three types of hydrogenases have been discovered. Despite they are not phylogenetically related and their different protein fold, the active sites reveal amazing similarities as result of convergent evolution presumably drift by special chemical requirements for H₂ activation. In all three types the iron (in [FeFe]- hydrogenase the iron proximal to the 4Fe–4S cluster) is redox inactive, low-spin, in the oxidation state II and bound to at least one sulfur and three p-accepting ligands such as CO, cyanide and/or a pyridinol that are arranged similarly in a square-pyramidal or octahedral geometry. Our results supply novel and important information about mononuclear hydrogenases iron sites and on molecular hydrogen activation in general. In the future, would be desirable to proceed on the characterization of the electronic structure of Hmd iron by creating new inhibitors and new model compounds. Their state, activity and interactions can be studied by complementary techniques ,as it has been done so far and even beyond, exploiting *in silico* methods such DFT (Density Functional Theory).

2b. Characterization of a tyrosinase model complex in its optical excited state

We exploited two synergic approaches, pumped- XAS and an innovative combination of EXAFS spectroscopy and resonant Raman scattering, to structurally characterize the ground and the excited states of a complex mimicking the active site of tyrosinases: [Cu₂L₂(μ-O)₂]₂I₂, the first μ-oxo complex stable at room temperature. We determined the geometrical changes characterizing the same kind of electron transfer described for tyrosinases. This information can be used to understand the oxygenation process performed by these enzymes. In future, the experimental artifacts encountered in our pumped-XAS experiments must be overcome. In fact, while in resonance Raman scattering the experiments can be performed at lower laser intensities (only the excited states contribute to the final signal), effective pumped-XAS might only be feasible with the help of a synchronized, pulsed UV-laser source. Being able to perform such

experiments is desirable, because understanding reactivity on an atomic or orbital level plays an increasingly important role in research at light sources. The combination of resonant Raman spectroscopy and pumped X-ray absorption spectroscopy would give direct access to structural and electronic parameters of optical excited systems. The acquired knowledge can be used in advanced technology. Sundry applications can benefit from this research. For example, nanobiomedicine could improve the rational design of carriers that can be functional at target locations upon specific irradiation. Photoactivable enzymes, protein transporters, or channels can be selectively regulated by lasers. Cosmetics can improve the development of molecules able to efficiently protect against UV radiation. In general, the rational design of sensors able to couple a photoresponse with a specific activity can have a broad spectrum of application in modern technology.

2c. X-ray Absorption Spectroscopy analysis of the unique ATP binding cassette protein ABCE1's iron-sulfur cluster:

The ATP binding cassette protein ABCE1 is essential for the viability of all eukaryotes and archaea. Studying the functionality of ABCE1 can shed light on its activity in translation initiation, ribosome biosynthesis, HIV-capsid assembling and RnaseL inhibition. Because of the presence of Fe-S clusters, ABCE1 is also a unique ATP binding cassette superfamily protein. Exploiting XAS we revealed which type of Fe-S clusters the protein carries and their oxidation state. This is fundamental to understand the essential role of the 2 diamagnetic $[4\text{Fe-4S}]^{2+}$ clusters identified in this study. Recently, the X-ray structure at 2.8 Å resolution of the complete ABCE1 protein from *Pyrococcus abyssi* has been solved (PDB: 3BK7). It starts to become evident that these clusters are involved in recognition and modification of RNA assemblies. Next step would be to characterize different electronic states for the protein by spectroscopical methods and demonstrate at molecular level the mechanism of action of this enzyme.

6 Appendix A: material

Chemicals for cloning

- Agarose: purchased from Carl-ROTH.
- AGE buffer: purchased from Carl-ROTH.
- Ampicillin: purchased from Sigma Aldrich.
- Antarctic phosphatase: purchased from NEB.
- BSA: the Bovine Serum Albumin derived from NEB or Fermentas.
- Chloramphenicol: purchased from Sigma Aldrich.
- Competent bacterial strains: supplied internally by the lab. The different strains were propagated and made competent by internal members of the lab. Protocols for competent cells production can be commonly found on the web.
- DNA ladders: 100bp and 1Kb ladders purchased from Fermentas and NEB.
- dNTPs mix, ATPs, TTPs: purchased from NEB.
- Ethidium bromide: purchased from Carl-ROTH.
- Glycerol: purchased from Carl-ROTH.
- Kanamicin: purchased from Sigma Aldrich.
- LB-Agar: purchased from Carl-ROTH.
- Luria-Bertani (LB) medium: purchased from Carl-ROTH.
- Petri dishes: purchased from Greiner BioOne.
- PfuTurbo-DNA polymerase: purchased from NEB.
- Phusion-DNA-polymerase: purchased from Finnenzyme.
- Plasmid vectors: supplied by the internal library managed by Dr. Arie Geerlof
 - pETM-11 (can fuse a tag at the N-terminal. The tag consists by a his₆-tag and a TEV cleavable linker region).
 - pETM-13 (can fuse a 6-histidine tag at the C-terminal).
 - pETM-20 (can fuse a tag at the N-terminal. The tag consists by a Trx (thioredoxin enhancing solubility tag) moiety, a his₆-tag and a TEV cleavable linker region).

- pETM-11_LIC (can fuse a tag at the N-terminal. The tag consists by a his₆-tag and a TEV cleavable linker region).
- Primers: purchased from Eurofins MWG Operon.
- QuikChange Multi Site Directed Mutagenesis Kit chemicals: purchased from.
- Restriction endonucleases type II: purchased from New England BioLabs (NEB) or Fermentas (*NcoI*, *XhoI*, *PciI*, *XbaI*, *DpnI*, *BsaI*).
- SOC medium: purchased from Invitrogen.
- Source clone: *Homo sapiens* ETHE1 full length cDNA clone was purchased from ImaGenes. The clone comes from a cDNA library of human eye retinoblastoma cell line. The gene has been supplied within DH10B TonA cells (*E. coli*) in a pCMV-SPORT6 vector. ID.: IRATp970H086D.
- T4 DNA ligase and quick ligase: purchased from NEB.
- T4-DNA-polymerase: purchased from NEB.
- Taq-DNA-polymerase: purchased from NEB.

Kits for cloning

- Plasmid purification kit: purchased from Macherey Nagel.
- Plasmid purification kit (mini prep): purchased from Qiagen.
- PCR purification kit: purchased from Qiagen.
- Gel extraction kit: purchased from Quiagen.
- QuickChange multi site directed mutagenesis kit: purchased from Stratagene.

Chemicals for protein expression

- Ammonium iron(II) sulfate 6-hydrate : purchased from Riedel-de Haën.
- Ammonium sulfate: purchased from Carl-ROTH.
- Ampicillin (sodium salt): purchased from Carl-ROTH.
- Chloramphenicol: purchased from Carl-ROTH.
- Glucose: purchased from Carl-ROTH.
- Glycerol: purchased from Carl-ROTH.
- Isopropyl β -D-1 thiogalactopyranoside (IPTG): purchased from Carl-ROTH.

- Kanamycin (sulfate): purchased from Carl-ROTH.
- Lactose: purchased from Carl-ROTH.
- Luria-Bertani (LB) medium: purchased from Carl-ROTH.
- Magnesium sulfate: purchased from Carl-ROTH.
- Potassium di-hydrogen phosphate: purchased from Carl-ROTH.
- Sodium chloride: purchased from Carl-ROTH.
- Sodium hydrogen phosphate: purchased from Sigma Aldrich.
- Terrific Broth (TB): purchased from Carl-ROTH.
- Tryptone: purchased from Carl-ROTH.
- Yeast extract: purchased from Carl-ROTH.

Equipment for protein expression

- Flasks: purchased from Schott/Duran (glass) or NALGENE (plastic).
- Shakers Multitron: purchased from Infors.
- Spectrophotometer cuvette: BRAND (Plastibrand).
- Spectrophotometer: purchased from Eppendorf.

Chemicals for protein purification

- 2-(*N*-morpholino)ethanesulfonic acid (MES): purchased from Carl-ROTH.
- 4-(2-hydroxyethyl)-1-piperazineethanesulfonic acid (HEPES): purchased from Carl-ROTH.
- Acetic acid (CH₃COOH): purchased from Carl-ROTH.
- Acrylamide: purchased from Carl-ROTH.
- Ammonium persulfate (APS): purchased from Carl-ROTH.
- BisTris: purchased from Carl-ROTH.
- Brilliant blue G (coomassie): purchased from Sigma Aldrich.
- Bromophenol blue: purchased from Merck.
- Chelex 200 (divalent cations unspecific chelator): purchased from BioRad. The chelex version with the bigger beads has been used in order to facilitate the filtration of the treated solution.

- Deferoxamine mesylate: purchased from Sigma Aldrich.
- Disodium hydrogen phosphate (Na_2HPO_4): purchased from Sigma Aldrich.
- Dithiotreitol (DTT): purchased from Carl-ROTH.
- Ethanol ($\text{CH}_4\text{CH}_3\text{OH}$): purchased from Carl-ROTH.
- Ethylenediaminetetraacetic acid (EDTA): purchased from Carl-ROTH.
- Glycerol: purchased from Carl-ROTH.
- Glycine: purchased from Carl-ROTH.
- Hydrogen Chloride (HCL): purchased from Carl-ROTH.
- Imidazole: purchased from Carl-ROTH.
- Methanol (CH_3OH) : purchased from Carl-ROTH.
- N,N,N',N'-tetramethylethylenediamine (TEMED): purchased from Carl-ROTH.
- NuPAGE protein dye: purchased Invitrogen.
- Phenanthroline: purchased from Fluka.
- Protein ladder: purchased from NEB.
- Sodium ascorbate: purchased from Sigma Aldrich.
- Sodium chloride (NaCl): purchased from Carl-ROTH.
- Sodium dihydrogen phosphate (NaH_2PO_4): purchased from Sigma Aldrich.
- Sodium dithionite: purchased from Fluka.
- Sodium dodecyl sulfate (SDS): purchased from Carl-ROTH.
- Sodium hydroxide (NaOH): purchased from Carl-ROTH.
- Tobacco Etch Virus protease (TEV): produced internally by Arie Geerolf or by single users. Protocols for TEV production can be commonly found on the web.
- Tricine: purchased from Omni Life Science.
- *tris*(2-carboxyethyl)phosphine (TCEP): purchased from Soltec Ventures.
- Trizma base (tris): purchased from Carl-ROTH.
- Urea: purchased from Carl-ROTH.
- B-mercaptoethanol: purchased from Sigma Aldrich.

Buffers for protein purification

All the buffers were filtered by a 0.22 μm cut-off membrane and degassed before usage. The following buffers have been applied during the purification steps (X 1 L):

- **Buffer A:**
 - 4.4 mL NaH_2PO_4 0.4 M
 - 78.9 mL Na_2HPO_4 0.4 M
 - NaCl 200 mM
 - Imidazole 20/50 mM
 - Fine adjust to pH 8.0 with HCl/NaOH
 - Add water up to 1 L

This is a PBS buffer with a final 50 mM concentration of phosphate. The pH is given by the ratio between monobasic and dibasic phosphate.

- **Buffer B:**
 - 4.4 mL NaH_2PO_4 0.4 M
 - 78.9 mL Na_2HPO_4 0.4 M
 - NaCl 200 mM
 - Imidazole 500 mM
 - Fine adjust to pH 8.0 with HCl/NaOH
- **Buffer C:**
 - NaH_2PO_4 4.4 mL 0.4 M
 - Na_2HPO_4 78.9 mL 0.4 M
 - NaCl 1M mM
 - Fine adjust to pH 8.0 with HCl/NaOH
- **Buffer S:**
 - Tris-HCL 20/50 mM
 - NaCl 100/150 mM

- TCEP 1/2 mM
- Adjust to pH 8.0 with HCl
- The buffer is incubated o/n with chelex at 4°C under stirring. This step avoids the presence of transition metal contaminants in the protein solution.

- **Buffer H:**
 - HEPES 50 mM
 - NaCl 100 mM
 - TCEP 1 mM
 - Adjust the pH to 8.0 (wild type) or 7.2 (mutants: this is due to the change in the isoelectric point with NaOH).
 - The buffer is incubated o/n with chelex at 4°C under stirring. This step avoids the presence of transition metal contaminants in the protein solution.

- **Buffer Apo:**
 - TrisHCL 100 mM
 - Urea 4M
 - NaCl 200mM
 - Deferoxamine mesylate 50 mM (solubilized freshly in the fraction to be used)

Equipment for protein purification

- AKTA purifiers (several distributions): purchased from Amersham Bioscience.
- Polyacrylamide gels caster: designed by Dr. Young-Hwa Song and produced by the EMBL-Hamburg workshop.
- Centrifuge (J-20 XP): purchased from Avanti.
- Chromatographic columns (HiTrap IMAC HP 5 mL; HiLoad 16/60 Superdex 75; HiLoad 16/60 Superdex 200): purchased from Amersham Bioscience.

-
- Concentrators (Amicon, Centricon): Sartorius Stedim and Millipore.
 - Disposable filtering units for solution filtering and degassing (Steritop): purchased from MILLIPORE.
 - Disposable filters for syringe (0.45 and 0.22 μm cut-off): purchased from Carl-ROTH, Sartorius Stedim and Millex GP.
 - Filtering unit for solution filtering and degassing: purchased from NALGENE.
 - Filters for filtering units (J-Cat): purchased from Sartorius Stedim.
 - Microfuges (5415 R and Minispin): purchased from Eppendorf.
 - Peristaltic pump: purchased from Pharmacia.
 - Poly-Acrylamide Gel Electrophoresis (PAGE) apparatus: purchased from Invitrogen.
 - Sonicator (Sonoplus): purchased from BANDELIN.
 - Spectrophotometer Nanodrop: purchased from Thermo Scientific.
 - Stirrers: purchased from IKMAG RCT, Heidelph and Thermo Scientific.
 - Syringes: purchased from Henke-Sass Wolf.
 - Ultracentrifuge (RC26 Plus): purchased from Sorvall.

Chemicals used for Poly Acrylamide Gel Electrophoresis (PAGE)

- 2-(*N*-morpholino)ethanesulfonic acid (MES): purchased from Carl-ROTH.
- 4-(2-hydroxyethyl)-1-piperazineethanesulfonic acid (HEPES): purchased from Carl-ROTH.
- Acetic acid (CH_3COOH): purchased from Carl-ROTH.
- Acrylamide: purchased from Carl-ROTH.
- Ammonium persulfate (APS): purchased from Carl-ROTH.
- BisTris: purchased from Carl-ROTH.
- Brilliant blue G (coomassie): purchased from Sigma Aldrich.
- Bromophenol blue: purchased from Merck.
- Dithiotreitol (DTT): purchased from Carl-ROTH.
- Ethylenediaminetetraacetic acid (EDTA): purchased from Carl-ROTH.
- Ethanol ($\text{CH}_4\text{CH}_3\text{OH}$): purchased from Carl-ROTH.

- Glycerol: purchased from Carl-ROTH.
- Glycine: purchased from Carl-ROTH.
- Methanol (CH₃OH) : purchased from Carl-ROTH.
- N,N,N',N'-tetramethylethylenediamine (TEMED): purchased from Carl-ROTH.
- NuPAGE protein dye: purchased Invitrogen.
- Protein ladder: purchased from NEB.
- Sodium dodecyl sulfate (SDS): purchased from Carl-ROTH.
- Tricine: purchased from Omni Life Science.
- Trizma base (tris): purchased from Carl-ROTH.

Buffers and solutions for PAGE

- Tricine running buffer (1 L 10X)
 - tris 121 g
 - Tricine 179 g
 - SDS 10 g
 - H₂O up to 1 L

- Tricine separating gel buffer (pH 8.5)
- Tris 3M
- SDS 0.3%

- Tricine gradient gels (X10 gels)
 - Solution L (8%)
 - Tricine gel buffer 13 mL
 - A₄₀ (Acrylamide 40%) 10 mL
 - H₂O 27 mL
 - TEMED 50 μL
 - APS 10% 510 μL
 - Solution H (20%)
 - Tricine gel buffer 13mL

- A₄₀ 25 mL
 - H₂O 8 mL
 - Glycerol 4 mL
 - TEMED 50 µL
 - APS 10% 510 µL

- Glycine gel running buffer (1 L, 10X, pH 8.3/8.6)
- Tris 30 g
- Glycine 144 g
- SDS 10 g
- H₂O up to 1 L

- Glycine separating gel buffer (15% X2 gels)
 - Lower buffer 2.2 mL. For the preparation of 200 mL of Lower buffer pH 8.8:
 - Tris 36g
 - SDS 0.8 g
 - H₂O up to 200 mL
 - A₄₀ 3.1 mL
 - H₂O 3.2 mL
 - TEMED 5 µL
 - APS 10% 50 µL

- Glycine stacking gel buffer (x2 gels)
 - Upper buffer 1.25 mL. For the preparation of 200 mL of Lower buffer:
 - Tris 12 g
 - SDS 0.8 g
 - pH 6.8
 - H₂O up to 200 mL
 - A₄₀ 0.5 mL
 - H₂O 3 mL

Appendix A: material

- TEMED 5 μ L
- APS 10% 25 μ L

- Bis-tris gel running buffer (1 L 20X)
 - MES 195 g
 - Tris 121 g
 - SDS 20 g
 - EDTA 6 g
 - H₂O up to 1 L

- Bis-tris separating gel buffer (15% X10 gels)
 - Bis-tris (1.6 M, pH 6.8) 25 ml
 - SDS 10% 1 mL
 - H₂O 36 mL
 - A₄₀ 37.5
 - TEMED 50 μ L
 - APS 500 μ L

- Bis-tri stacking gel buffer
 - Bis-tris (1 M, pH 6.3) 7.5 mL
 - SDS 10% 1 mL
 - H₂O 23.25 mL
 - A₄₀ 4.6 mL
 - TEMED 30 μ L
 - APS 300 μ L

- Gel staining solution (600 mL)
 - Ethanol 272 mL
 - Acetic acid 55 mL
 - Brilliant blue G (coomassie) 0.6 g

- H₂O 272 mL

- Gel destaining solution (1 L)
 - Acetic acid 75 mL
 - Methanol 50 mL
 - H₂O 875 mL

- Protein loading dye (20 mL FBS dye 5X, pH 6.8)
- Tris HCl 250 mM
- DTT 500 mM
- SDS 10%
- Bromophenol blue 0.5%
- Glycerol 50%

Alternatively the Invitrogen NuPAGE protein loading dye has been used.

Material for Dynamic Light Scattering (DLS)

- Apparatus: DynaPro99 purchased from PROTEIN SOLUTIONS, now available from Wyatt Technologies.
- UV sample cuvettes: purchased from PROTEIN SOLUTIONS.
- Dynamics 5.26: supplied with the apparatus by PROTEIN SOLUTIONS.
- Microfuges (5415 R and Minispin): purchased from Eppendorf.
- Disposable filters for syringe (0.45 and 0.22 μ m cut-off): purchased from Carl-ROTH, Sartorius Stedim and Millex GP.

Material for protein stability investigation

- Dithiotreitol (DTT): purchased from Carl-ROTH.
- B-mercaptoethanol: purchased from Sigma Aldrich.
- Sodium dithionite: purchased from Fluka.
- *tris*(2-carboxyethyl)phosphine (TCEP): purchased from Soltec Ventures.
- Sypro Orange protein stain: purchased from Invitrogen.

- Thermofluor device: MyiQ RT-PCR thermo cycler machine adapted to thermofluor functionality. Purchased from BioRad.
- Thermofluor 96 condition plate (96 well plate with a different buffer condition per well): prepared internally by lab technicians.
- Microfuges (5415 R and Minispin): purchased from Eppendorf.
- Apparatus: DynaPro99 purchased from PROTEIN SOLUTIONS, now available from Wyatt Technologies.
- UV sample cuvettes: purchased from PROTEIN SOLUTIONS.
- Dynamics 5.26: supplied with the apparatus by PROTEIN SOLUTIONS.
- Optical microscope Leica MZ 16: purchased from Leica.

Materials for Static Light Scattering (SLS)

- miniDAWN apparatus: purchased from Wyatt Technologies.
- Software ASTRA 5.3.4.11.
- Microfuges (5415 R and Minispin): purchased from Eppendorf.
- AKTA purifier (several distributions): purchased from Amersham Bioscience.
- Analytical gel filtration column: purchased from Amersham Bioscience.

Material used for crosslinking experiments

- 2 mg/mL protein samples: protein as isolated with and without TCEP, apo-protein. The buffers without free amines should be preferred (*e.g.* HEPES and PBS are ok, TrisHCl should be avoided).
- BSA 2 mg/mL sample as negative-interaction control: various sources (*e.g.* NEB)
- Glutaraldehyde stock solution (25%): purchased from Sigma Aldrich.
- UV transilluminator: purchased from Vilbert Lourmat.

Material for Total X-ray Reflection Fluorescence (TXRF)

- PicoTAX Automatic: purchased from Röntec, Berlin, Germany. The PicoTAX is a cooling-free portable bench-top device. It operates with an air-cooled Mo based tube working at 40 KeV, 1 mA. It contains a compact fine-focus x-ray tube

specially constructed in metal-ceramics. The x-ray beam is focused by a Ni/C-multi layer monochromator. The detector is a Peltier-cooled XFlash, 10 mm² with a resolution of 160 eV. Its power consumption is about only 180 Ws.

- PicoTAX software: modular software used for the device control, spectra collection, calibration.
- Python script for data conversion: written by Dr. Gerd Wellenreuther to convert files with spx extension (PicoTAX outputs) to files mca (readable by the PyMCA program).
- PyMCA program: python based program for data analysis and freely available on the web.[137]
- Python script for the tabulation of PyMCA output values: written by Dr. Gerd Wellenreuther to create a single table from the individual output values generate by PyMCA calculations for each specimen.
- Plexus: ultra-flat round-shaped plexyglass samples trays (1.5 mm Ø x 3 mm) manufactured by the EMBL-Heidelberg work shop.
- Standards: purchased from Bernd Kraft GmbH.
 - ICP-Standard Gallium 1.000 g/L
 - ICP-Standard Scandium 1.000 g/L

Material for Isothermal Titration Calorimetry (ITC)

- Microfuges (5415 R and Minispin): purchased from Eppendorf.
- Disposable filters for syringe (0.45 and 0.22 µm cut-off): purchased from Carl-ROTH, Sartorius Stedim and Millex GP.
- 2 mL of freshly dialyzed protein solution 20/50 µM.
- Metal solution 0.1/1 mM: use the protein dialysis buffer for preparation.
- ITC apparatus and relative accessories (VP-ITC MicroCalorimeter): purchased from Microcal.
- VPviewer software (to run the experiment): supplied with the ITC machine.
- Origin analysis software (for data analysis): supplied with the ITC machine.
- Ammonium iron(II) sulfate 6-hydrate : purchased from Riedel-de Haën.

- Dithionite sodium salt: purchased from Fluka.
- Iron(III) citrate: purchased from CarlROTH.
- Nitrilo Triacetic Acid (NTA): purchased from CarlROTH.
- Nickel(II) sulfate: purchased from CarlROTH.
- Zinc(II) chloride: purchased from CarlROTH.
- Manganese(II) chloride tetrahydrat: purchased from CarlROTH.
- Reduced glutathione: purchased from Sigma Aldrich.

Material for spectrophotometry

- Spectrophotometer cuvette: BRAND (Plastibrand).
- Spectrophotometer: purchased from Eppendorf.
- Spectrophotometer Nanodrop: purchased from Thermo Scientific.

Material for Mass Spectrometry (MS)

- Mass spectrometry experiments have been carried out at EMBL-Hamburg with a Voyager-DE STR apparatus purchased from Applied Biosystems. This is a MALDI-TOF (Matrix Assisted Laser Desorption and Ionization with Time Of Flight) type machine.
- The Voyager software has been used for data collection and analysis.
- Sample grid-plates: supplied by Applied Biosystem with the machine.
- Sinapic acid (SAPA): purchased from Fluka.
- Acetonitrile: purchased from Carl-ROTH.
- Tri-fluoroacetic acid (TFA): purchased from Merk.
- Protein sample in salt-free buffer at a concentration of 0.5-2 mg/mL.

Material for Circular Dichroism (CD)

- CD apparatus: JASCO-810 (JASCO corporation).
- Quartz UV-cuvettes : purchased from JASCO.
- Analysis software: JASCO software.

Materials for crystallization

- EMBL crystallization facility.[77]
- Bio-robot for solution preparation: Lissy 2002 purchased from Zinsser Analytic.
- Pipetting robot: HYDRAII+I purchased from MATRIX.
- Plates sealing robot: RoboSeal robot purchased from HJ-Bioanalytik.
- EMBL crystallization facility chemicals for crystallization reservoir solutions: purchased from Fluka. A list of the stock solutions is available at http://intranet.embl-hamburg.de/facilities/external_facilities/htpx/stocks_HTX.xls.
- Chemicals for manual crystallization trays preparation:
 - Magnesium chloride, magnesium formate, tris, bis-tris, Poly Ethylene Glycol (PEG 3350, PEG 6000, MME 5000, MME 2000, 8000), magnesium sulfate, zinc acetate, HEPES, MES, sodium, malonate, zinc sulfate, zinc acetate, ammonium sulfate, succinic acid, ammonium acetate, MPD, purchased from Carl-ROTH.

Material for reductive methylation

- Dimethylamine-borane complex: purchased from Fluka.
- Formaldehyde: purchased from Sigma Aldrich.

Construct and screens used for crystallization

- Every plate, except the manual ones, contains 96 conditions.
- The protein used was $\Delta 14HsETHE1$ unless specified.
- Incubation occurs at 19°C unless specified.
- 1mM = ~ 25mg/ml.
- Asiso = *HsETHE1* as isolated.
- Apo = apo-*HsETHE1*.
- Met = Reductively methylated protein.
- His-tagged = *HsETHE1* not processed with TEV protease and thus still bearing the histidine tag.

Appendix A: material

- 14E4 = Δ 14-*Hs*ETHE1- Δ 4.
- 19E4 = Δ 19-*Hs*ETHE1- Δ 4.

For each condition 0.5 μ L protein drops are mixed with 0.5 μ L of reservoir solution.

Screens:

- HR_Index
 - Asiso 2mM; 1mM; 10mg/ml; 1mM 4°C
 - Apo 1mM
 - Red 1mM
 - Met 20mg/ml; 10 mg/ml
 - His-tagged 1mM
 - 14E4 1mM; 10mg/ml
 - 19E4 1mM; 10mg/ml
- HR_Crystal
 - Asiso 2mM; 1mM; 10mg/ml; 1mM 4°C
 - Apo 1mM
 - Red 1mM
 - Met 20mg/ml; 10 mg/ml
 - His-tagged 1mM
 - 14E4 1mM; 10mg/ml
 - 19E4 1mM; 10mg/ml
- HR_Grid
 - Asiso 1mM; 1mM 4°C
 - Apo 1mM
 - Red 1mM
- Nx_Cryo
 - Asiso 1mM; 1mM 4°C
 - Jena 1-4
 - Asiso 1mM

- Jena 5-8
 - Asiso 1mM
- Jena 9-10
 - Asiso 1mM
- Optimizations plates
 - Asiso, 192 conditions 1mM; 10mg/ml
 - Asiso, 192 conditions 1mM
 - Asiso, 192 conditions 40mg/ml; 10mg/ml
- Manual optimization: For each condition 0.5 μ L protein drops are mixed with 0.5 μ L of reservoir solution.
 - Asiso, 144 conditions 1mM; 1mM 4°C

Material for substrate screening

- UV-96-well-plates: purchased from Greiner.
- Ammonium iron (II) sulfate (6-hydrate): purchased from Riedel-de Haën.
- Ethylenediaminetetraacetic acid (EDTA): purchased from Carl-ROTH.
- Enzymes:
 - ZiPD protein: M β L-like protein with phosphodiesterase activity. It has been obtained from an old stock of my group kept at -80°C.
 - Penicillinase type III: is a lactamase, purchased from Sigma Aldrich.
 - Antarctic phosphatase: purchased from Sigma Aldrich.
 - Aryl-sulfatase type VIII: purchased from Sigma Aldrich.
 - Esterase: purchased from Sigma Aldrich.
- Cromogenic substrates: for qualitative analysis you don't need a plate reader, the reaction can be followed optically.
 - Nitrocefin: substrate of any lactamase. It is light sensitive and should be handled in a dark place. It has been purchased from Sigma Aldrich. The compound turns from yellow to red upon hydrolysis and absorbs at 486 nm. The compound must be dissolved in di-methyl sulfoxide (DMSO).

- bis-p-nitrophenyl phosphate (bpNPP): substrate of phosphodiesterases, purchased from Sigma Aldrich. One of the products (p-nitrophenyl) absorbs at 405 nm.
- p-nitrophenyl phosphate (pNPP): substrate of the phosphatases, purchased from Sigma Aldrich. The product (p-nitrophenyl) absorbs at 405 nm.
- p-nitrochatecol sulfate: substrate of the aryl-sulfatase, purchased from Sigma Aldrich. The product (p-nitrophenyl) absorbs at 405 nm.
- p-nitrophenyl sulfate: substrate of the aryl-sulfatase, purchased from Sigma Aldrich. The product (p-nitrophenyl) absorbs at 405 nm.
- Glucose-3-sulfate: negative control. No color change should be detected.
- p-nitrophenyl acetate: substrate of the esterase, purchased from Sigma Aldrich. The product (p-nitrophenyl) absorbs at 405 nm.
- Buffers:
 - TrisHCL 50 mM, NaCl 100 mM, TCEP 1mM, pH 8.5.
 - PBS buffer (phosphate buffer), NaCl 100 mM, pH 7.2.

Materials for Small Angle X-ray Scattering (SAXS)

- The data were collected at the EMBL beamline X33 of the storage ring DORIS III (DESY, Hamburg, Germany). We used a photon counting Pilatus 1M detector placed at a distance of 2.7 m. The incoming x-ray had a wavelength of $\lambda = 1.5 \text{ \AA}$, the range of momentum transfer $0.01 < s < 0.6 \text{ \AA}^{-1}$ was covered ($s = 4\pi \sin\theta/\lambda$, where 2θ is the scattering angle).

X-ray Absorption Spectroscopy (XAS) beamlines

DESY (Deutsches Elektronen-Synchrotron): DORIS III accumulation ring:

Beamline E4

The EXAFS II beamline is designed to achieve a focused, high intensity photon beam in the energy range from ~2.8 keV to ~11 keV and is predominantly used for X-ray absorption spectroscopy. The layout of the beamline is schematically shown in the Fig. 2.

The beamline is equipped with two mirrors. The first mirror, which is situated half way between the source and the sample, collects ~30% of the bending magnet radiation vertically and 4 mrad horizontally and focuses it onto the sample with a magnification of ~1x. The second mirror (a plane mirror) is coated with three stripes (C, Ni, Au) to achieve the optimum higher order reduction at different energies.

Beamline parameters	
Source (4.5 GeV)	bending magnet, $E_c=16.6$ keV beam size 1.3 x 3.0 mm FWHM vert. electron beam divergence 0.06 mrad FWHM.
Mirrors	1. toroidal mirror with Au-coating, 1:1 focusing. 2. plane mirror with C-, Ni- or Au-coating (7 mrad incidence/exit angle for both mirrors).
Monochromator	Si(111) double crystal (+/-) (UHV) Digital-MOSTAB feedback system and water cooling on first crystal.
Detectors	Ionisation chambers in front of and behind experimental chamber and reference chamber.
Energy range	2.8 - 5 keV (C-mirror) 4.5 - 8.5 keV (Ni-mirror) 8 - 11.0 keV (Au-mirror).
Flux at sample	10^{10} photons/s/mm ² (4.5 GeV, 100mA).

Energy resolution	0.8 eV at 3.2 keV.
--------------------------	--------------------

Beamline C1

Beamline C is dedicated to bulk X-ray absorption spectroscopy experiments at energies between 5 and 43 keV. It is equipped with a fixed-exit double-crystal monochromator suitable for step-by step energy scans and quick continuous energy scanning (QEXAFS). Gas lines and a supervision system allow for in-situ experiments and the handling of toxic/reactive gases. In addition, the experimental station is equipped with a vertical diffractometer which can be used for DAFS (diffraction anomalous fine structure) and diffraction experiments. Besides monochromatic applications, the white beam may be used. The large hutch area enables the installation of specific user set-ups e.g. for X-ray standing-wave experiments.

Beamline parameters

Source	Bending magnet.
Monochromator	2.0×10^{-4} Si[111]
Energy range	2.4 - 43.4 keV.
Flux	10^9 ph/mm ² /10 ⁻⁴ BW at 9 keV.

Beamline D2

This is the former EMBL-Hamburg outstation XAS beamline. Presently, it is not operational anymore. The D2 beamline worked at energy from 5 to 40 GeV. It used a Si[111]- or Si[311]-monochromator, a toroidal segmented focusing Au-coated mirror with an angle of incidence of ~ 3.8 mrad and cut-off energy of 21.5 keV and a Canberra 13-elements germanium solid-state detector.

SLS (Swiss Light Source):*Beamline SuperXAS*

X10DA is a dedicated beamline to X-ray Absorption Spectroscopy (XAS) in the applied science.

Beamline parameters

Monochromator	Double Crystal Monochromator (DCM) for normal XAFS scanning mode . Quick scanning monochromator (QEXAFS) for time resolved scanning mode (few ms to sec).
Detector	13 element Ge detector with fast digital amplifiers.
Energy range	4.5 - 35 keV.
Flux	1×10^{12} ph/s/400 mA.
Energy resolution	2×10^{-4} for Si[111] 0.5×10^{-4} for Si[311]

ESRF (European Synchrotron Radiation Facility):

Beamline BM26A

BM26A is designed to perform high quality XAFS measurements in a broad range of elements and samples.. The high-brilliance X-ray beam allows for absorption studies on very dilute samples. X-ray emission spectroscopy is performed by means of a crystal spectrometer. By combining the tuneable incident energy with an emission spectrometer, advantage of resonance effects that can provide detailed information on the electronic structure is taken. BM26A is equipped for different sample environments to perform *in situ* studies and we can adapt to a variety of user experimental stations.

The local coordination and electronic structure of an X-ray absorbing atom are studied by Extended X-ray Absorption Fine Structure (EXAFS) and X-ray Absorption Near Edge Structure (XANES) spectroscopy.

Beamline parameters

Source	Bending magnet
Mirrors	Meridionally focusing mirror with either an Si or Pt coating
Monochromator	Double-crystal monochromator. Monochromator crystals: Si[111] and Si[311].
Detector	Three low noise ion chambers Oxford Instruments for transmission experiments at high concentrations. A 9-element monolithic Ge detector with a max. count rate per element ~150kHz and an energy resolution < 250 eV at 5.9 keV for fluorescence measurements at low concentrations. A position sensitive INEL CPS 590 detector for combined WAXS / XAFS measurements. A MarCCD 165 detector.
Energy range	4.9 - 32 keV.
Flux	1×10^{11} photons/sec.
Energy resolution	dE/E of 2×10^{-4}

SSRL (Stanford Synchrotron Radiation Lightsource):

This beamline is specifically dedicated to biological x-ray absorption spectroscopy.

Beamline BioXAS BM7-3

Beamline parameters	
Source	20-pole, 2-Tesla wiggler, 0.8 mrad beam, side station

Mirrors	M0 mirror: Flat, bent, vertically collimating, 1 m, Si, Rh-coated, LN2 cooled monochromator.
Monochromator	Si[220] $\phi=0^\circ$, Si[220] $\phi=90^\circ$ double-crystal, non-fixed exit slit.
Detector	30-element Ge detector array LHe cryostat (4-200 K) Ion chambers, PIPS detector.
Energy range	4.6 - 37 keV
Flux	10^{12} ph/sec @100 mA / 9 keV w 2x15 mm aperture.
Energy resolution	10^4 DE / E

Molecular visualization programs

PyMol 2r1 (<http://www.pymol.org/>): user-sponsored molecular visualization system on an open-source foundation. PyMol is a molecular viewer, render tool, and 3D molecular editor intended for visualization of 3D chemical structures including atomic resolution X-ray crystal structures of proteins, nucleic acids (DNA, RNA, & tRNA), and carbohydrates, as well as small molecule structures of drug leads, inhibitors, metabolites, sugars, nucleoside phosphates, and other ligands including inorganic salts and solvent molecules.

DS Visualizer 2.5 (<http://accelrys.com>): molecular visualization software.

The program features:

- Simultaneous data views (3D graphics, sequences, charts, graphics, data tables).
- Standard file-format support (3D structures, SMILES, sequences, graphics).
- Structure building, editing, and analysis functionality.
- Scripting capabilities (for automating molecular manipulation workflows).
- High-quality graphic rendering and visual adjustment functionality.
- Access to expert-level modeling and simulation functionality, as well as shared custom protocols.

RasMol 2.7 (<http://rasmol.org/>): RasMol is a molecular graphics program intended for the visualization of proteins, nucleic acids and small molecules. Supported input file formats include Protein Data Bank (PDB), Tripos Associates' Alchemy and Sybyl Mol2 formats, Molecular Design Limited's (MDL) Mol file format, Minnesota Supercomputer Center's (MSC) XYZ (XMol) format, CHARMM format, CIF format and mmCIF format files.

Spdbv 4.0 (<http://spdbv.vital-it.ch/>): Swiss-PdbViewer (aka DeepView) is an application that provides a user friendly interface, allowing the analysis of several proteins at the same time. The proteins can be superimposed in order to deduce structural alignments and compare their active sites or any other relevant parts. Amino acid mutations, H-bonds, angles and distances between atoms are easy to obtain thanks to the intuitive graphic and menu interface.

UCSF Chimera (<http://www.cgl.ucsf.edu/chimera/>): UCSF Chimera is a highly extensible program for interactive visualization and analysis of molecular structures and related data, including density maps, supramolecular assemblies, sequence alignments, docking results, trajectories, and conformational ensembles. High-quality images and animations can be generated.

VMD (<http://www.ks.uiuc.edu/Research/vmd/>): VMD is designed for modeling, visualization, and analysis of biological systems such as proteins, nucleic acids, lipid bilayer assemblies, etc. VMD can be used to animate and analyze the trajectory of a molecular dynamics (MD) simulation. In particular, VMD can act as a graphical front end for an external MD program by displaying and animating a molecule undergoing simulation on a remote computer.

7 Appendix B: abbreviations

Å: Angstrom

A₄₀: Acrylamide 40%

aa: aminoacids

ABC: ATP Binding Cassette

ABCE1: ATP-binding cassette, sub-family E (OABP), member

ACV: isopenicilline-N from α -(L-R-aminoadipoyl)-L-cysteinyl-D-valine

AGE: Agarose Gel Electrophoresis

AIM: Auto Inducing Media

APS: Ammonium PerSulfate

Asp: aspartate

AtETHE1: *Arabidopsis thaliana* ETHE1

BioXAS: Biological XAS

BVS: Bond Valence Sum

bpNPP: bis-p-nitrophenyl phosphate

CD: Circular Dichroism

CDO: Cysteine Dioxygenase

CN: CyaNide

CO: Carbon Monoxide

COX: Cytochrome c Oxidase

CV: Column Volume

dNTP: deoxy Nucleotide Three Phosphate

DTT: dithiotreithol

EDTA: ethylenediaminetetraacetic acid

EE: Ethylmalonic Encephalopathy

EMA: EthylMalonic Aciduria

EPR: Electron Paramagnetic Resonance

ETHE1: Ethylmalonic Encephalopathy protein 1

eV: electron volts

EXAFS: Extended X-ray Absorption Fine Structure

FeGP: iron-guanylyl pyridone cofactor

FI: Fit-Index

FT: Fourier Transform

GIFtS: gene card identifier

GSH: reduced glutathione

GSSH: glutathione perulfide

HEPES: 4-(2-hydroxyethyl)-1-piperazineethanesulfonic acid

His: histidine

HSCO1: Hepatoma Subtracted Clone One

HsETHE1: *Homo sapiens* ETHE1

IMAC: Immobilized Metal Affinity Chromatography

IPTG: Isopropyl β -D-1 thiogalactopyranoside

IR: Infra Red

IS: Isomeric Shift

ITC: Isothermal Titration Calorimetry

LB: Lauria Bertani culturing medium

LIC: Ligase Independent Cloning

LN: Liquid Nitrogen

MALDI-TOF: Matrix Assisted Laser Desorption and Ionization with Time Of Flight

MES: 2-(*N*-morpholino)ethanesulfonic acid

M-L: Metal-Ligand

MS: Magnetic Splitting or hyperfine splitting

MS: Mass Spectrometry

M β L: Metallo- β -Lactamase

NEB: New England BioLabs

NSD: Normalized Spatial Discrepancy

o/n: over-night

OD₆₀₀: Optical Density at 600 nm

PAGE: Poly-Acrylamide Gel Electrophoresis

par.: paragraph

PCR: Polymerase Chain Reaction
PDB: Protein Data Bank
pNPP: p-nitrophenyl phosphate
pPCRp(s): purified PCR product(s)
QS: ΔE_Q = Quadrupole Splitting
R_g: radius of gyration
SAPA: sinapic acid
SAS: Small-Angle Scattering
SAXS: Small Angle X-ray Scattering
SCAD: Short Chain Acyl-CoA Dehydrogenase
SCAD: Short Chain Acyl-CoA Dehydrogenase
SDM: Site Directed Mutagenesis
SDO: Sulfur Di-Oxygenase
SDS: Sodium Dodecyl Sulfate
SEC: Size Exclusion Chromatography
see par.: see paragraph
SO: sulfite oxidase
SQR: Sulfide:Quinone Oxidoreductase
T_a: Ambient Temperature
TB: Terrific Broth
TCEP: *tris*(2-carboxyethyl)phosphine
TEMED: N,N,N',N'-tetramethylethylenediamine
TEV: Tobacco Etch Virus protease
TFA: tri-fluoroacetic acid
TXRF: Total X-ray Reflection Fluorescence
UV-Vis: Ultra Violet - Visible
wt: wild type
XANES: X-ray Absorption Near Edge Structure
XAS: X-ray Absorption Spectroscopy

8 Acknowledgements

I would like to thank Wolfram Meyer-Klaucke for involving me in such exciting projects and sharing with me his wide scientific knowledge. Moreover, I thank him for the fruitful discussions and his continuing interest on my scientific development.

I thank the former member of Meyer-Klaucke's group Gerd Wellenreuther for being helpful solving XAS issues, particularly at the beginning of the doctorate. Thanks also for writing scripts for XAS raw data processing and for TXRF analysis. Besides, he taught me how to perform TXRF measurements and how to process and analyze the output data.

I thank all the wet-lab people for being so helpful.

I thank all my collaborators, notably: Alexey Kikhney (*Hs*ETHE1 SAXS measurements, data processing and evaluation); Seigo Shima, Rolf Thauer, Sonja Vogt, Thomas Rauchfuss, C. Matthew Whaley, Francesco Stellato ([Fe]-hydrogenases work); Stephan Binder, Sonja Herres-Pawlis (dicopper complex work); Robert Tampè and Dominik Barthelme (ABCE1 work)

I thank my parents and friends for the continue support, particularly in the more challenging periods.

At last, I thank the European Molecular Biology Laboratory for giving me the great opportunity to carry out a doctorate in such stimulating top level environment.

9 References

- [1] Porod, G. (1982) *Current Contents/Physical Chemical & Earth Sciences*, 22-22.
- [2] Shima, S. et al. (2008) *Science* 321, 572-575.
- [3] Buurman, G., Shima, S. and Thauer, R.K. (2000) *Febs Letters* 485, 200-204.
- [4] Hiromoto, T. et al. (2009) *FEBS Lett* 583, 585-90.
- [5] Herres-Pawlis, S. et al. (2009) *Chemistry-a European Journal* 15, 8678-8682.
- [6] Leschelle, X. et al. (2005) *Biochimica Et Biophysica Acta-General Subjects* 1725, 201-212.
- [7] Waldron, K.J., Rutherford, J.C., Ford, D. and Robinson, N.J. (2009) *Nature* 460, 823-830.
- [8] Higashitsuji, H., Higashitsuji, H., Nagao, T., Nonoguchi, K., Fujii, S., Itoh, K. and Fujita, J. (2002) *Cancer Cell* 2, 335-346.
- [9] Tiranti, V. et al. (2004) *American Journal of Human Genetics* 74, 239-252.
- [10] Tiranti, V. et al. (2006) *Journal of Medical Genetics* 43, 340-346.
- [11] Tiranti, V. et al. (2009) *Nature Medicine* 15, 200-205.
- [12] Higashitsuji, H., Higashitsuji, H., Masuda, T., Liu, Y., Itoh, K. and Fujita, J. (2007) *Journal of Biological Chemistry* 282, 13716-13725.
- [13] McCoy, J.G., Bingman, C.A., Bitto, E., Holdorf, M.M., Makaroff, C.A. and Phillips, G.N. (2006) *Acta Crystallographica Section D-Biological Crystallography* 62, 964-970.
- [14] Burlina, A.B. et al. (1991) *Lancet* 338, 1522-1523.
- [15] Mineri, R. et al. (2008) *Journal of Medical Genetics* 45, 473-478.
- [16] Tiranti, V., Mineri, R., Viscomi, C., Tiveron, C., Rimoldi, M. and Zeviani, M. (2008) *Neurology* 70, A484-A484.
- [17] Gregersen, N. et al. (1998) *Human Molecular Genetics* 7, 619-627.
- [18] Tiranti, V., Di Meo, I., Viscomi, C., Hildebrandt, T., Rimoldi, M., Prella, A. and Zeviani, M. (2009) *Febs Journal* 276, 35-35.
- [19] Arnold, K., Bordoli, L., Kopp, J. and Schwede, T. (2006) *Bioinformatics* 22, 195-201.

References

- [20] Szabo, C. (2007) *Nature Reviews Drug Discovery* 6, 917-935.
- [21] Dorman, D.C., Moulin, F.J.M., McManus, B.E., Mahle, K.C., James, R.A. and Struve, M.F. (2002) *Toxicological Sciences* 65, 18-25.
- [22] Hildebrandt, T.M. and Grieshaber, M.K. (2008) *Febs Journal* 275, 3352-3361.
- [23] Gubern, M., Andriamihaja, M., Nubel, T., Blachier, F. and Bouillaud, F. (2007) *Faseb Journal* 21, 1699-1706.
- [24] Schilling, O., Spath, B., Kostecky, B., Marchfelder, A., Meyer-Klaucke, W. and Vogel, A. (2005) *Journal of Biological Chemistry* 280, 17857-17862.
- [25] Callebaut, I., Moshous, D., Mornon, J.P. and de Villartay, J.P. (2002) *Nucleic Acids Res* 30, 3592-601.
- [26] Dal Peraro, M., Vila, A.J., Carloni, P. and Klein, M.L. (2007) *Journal of the American Chemical Society* 129, 2808-2816.
- [27] Hall, B.G. and Barlow, M. (2005) *Journal of Antimicrobial Chemotherapy* 55, 1050-1051.
- [28] Valladares, M.H. et al. (2000) *Febs Letters* 477, 285-285.
- [29] Concha, N.O., Rasmussen, B.A., Bush, K. and Herzberg, O. (1996) *Structure* 4, 823-836.
- [30] Heinz, U., Bauer, R., Wommer, S., Meyer-Klaucke, W., Papamicael, C., Bateson, J. and Adolph, H.W. (2003) *Journal of Biological Chemistry* 278, 39260-39260.
- [31] Pattanaik, P. et al. (2009) *Journal of Biological Chemistry* 284, 945-953.
- [32] Kostecky, B., Pohl, E., Vogel, A., Schilling, O. and Meyer-Klaucke, W. (2006) *Journal of Bacteriology* 188, 1607-1614.
- [33] Vogel, A., Schilling, O. and Meyer-Klaucke, W. (2004) *Biochemistry* 43, 10379-10386.
- [34] Vogel, A., Schilling, O., Spath, B. and Marchfelder, A. (2005) *Biological Chemistry* 386, 1253-1264.
- [35] Kovaleva, E.G. and Lipscomb, J.D. (2008) *Nature Chemical Biology* 4, 186-193.
- [36] Costas, M., Mehn, M.P., Jensen, M.P. and Que, L. (2004) *Chemical Reviews* 104, 939-986.
- [37] Que, L. and Ho, R.Y.N. (1996) *Chemical Reviews* 96, 2607-2624.

-
- [38] McCoy, J.G., Bailey, L.J., Bitto, E., Bingman, C.A., Aceti, D.J., Fox, B.G. and Phillips, G.N. (2006) *Proceedings of the National Academy of Sciences of the United States of America* 103, 3084-3089.
- [39] Simmons, C.R., Liu, Q., Huang, Q., Hao, Q., Begley, T.P., Karplus, P.A. and Stipanuk, M.H. (2006) *J Biol Chem* 281, 18723-33.
- [40] de Groot, F. (2001) *Chemical Reviews* 101, 1779-1808.
- [41] Korbass, M., Marsa, D.F. and Meyer-Klaucke, W. (2006) *Review of Scientific Instruments* 77, -.
- [42] Wellenreuther, G. (2009) *Journal of Physics: Conference Series* 190.
- [43] Ressler, T. (1998) *Journal of Synchrotron Radiation* 5, 118-122.
- [44] Binsted, N., Strange, R.W. and Hasnain, S.S. (1992) *Biochemistry* 31, 12117-12125.
- [45] Ravel, B. and Newville, M. (2005) *Journal of Synchrotron Radiation* 12, 537-541.
- [46] Lavrentyev, A.A., Nikiforov, I.Y., Dubeiko, V.A., Gabrelian, B.V. and Rehr, J.J. (2001) *Journal of Synchrotron Radiation* 8, 288-290.
- [47] Vignais, P.M., Billoud, B. and Meyer, J. (2001) *Fems Microbiology Reviews* 25, 455-501.
- [48] Zirngibl, C., Vandongen, W., Schworer, B., Vonbunau, R., Richter, M., Klein, A. and Thauer, R.K. (1992) *European Journal of Biochemistry* 208, 511-520.
- [49] Shima, S. et al. (2004) *Angewandte Chemie-International Edition* 43, 2547-2551.
- [50] Korbass, M., Vogt, S., Meyer-Klaucke, W., Bill, E., Lyon, E.J., Thauer, R.K. and Shima, S. (2006) *Journal of Biological Chemistry* 281, 30804-30813.
- [51] Lyon, E.J., Shima, S., Buurman, G., Chowdhuri, S., Batschauer, A., Steinbach, K. and Thauer, R.K. (2004) *European Journal of Biochemistry* 271, 195-204.
- [52] Lyon, E.J., Shima, S., Boecher, R., Thauer, R.K., Grevels, F.W., Bill, E., Roseboom, W. and Albracht, S.P.J. (2004) *Journal of the American Chemical Society* 126, 14239-14248.
- [53] Shima, S., Lyon, E.J., Thauer, R.K., Mienert, B. and Bill, E. (2005) *Journal of the American Chemical Society* 127, 10430-10435.
- [54] Pilak, O. et al. (2006) *Journal of Molecular Biology* 358, 798-809.
- [55] Armstrong, F.A. and Fontecilla-Camps, J.C. (2008) *Science* 321, 498-499.

References

- [56] Witkop, C.J. (1979) *Alabama Journal of Medical Sciences* 16, 327-330.
- [57] Decker, H., Schwelkardt, T., Nillius, D., Salzbrunn, U., Jaenicke, E. and Tuczec, F. (2007) *Gene* 398, 183-191.
- [58] Magnus, K.A., Hazes, B., Tonthat, H., Bonaventura, C., Bonaventura, J. and Hol, W.G.J. (1994) *Proteins-Structure Function and Genetics* 19, 302-309.
- [59] Eldik, R.v. and Reedijk, J. (2006) in: *Advances in inorganic chemistry*, Vol. 58 (Ellibs, Ed.) Elsevier.
- [60] Henson, M.J., Mukherjee, P., Root, D.E., Stack, T.D.P. and Solomon, E.I. (1999) *Journal of the American Chemical Society* 121, 10332-10345.
- [61] Bisbal, C., Martinand, C., Silhol, M., Lebleu, B. and Salehzada, T. (1995) *Journal of Biological Chemistry* 270, 13308-13317.
- [62] Zimmerman, C., Klein, K.C., Kiser, P.K., Singh, A.R., Firestein, B.L., Riba, S.C. and Lingappa, J.R. (2002) *Nature* 415, 88-92.
- [63] Kispal, G. et al. (2005) *Embo Journal* 24, 589-598.
- [64] Yarunin, A., Panse, V.G., Petfalski, E., Dez, C., Tollervey, D. and Hurt, E.C. (2005) *Embo Journal* 24, 580-588.
- [65] Chen, Z.Q., Dong, J.S., Ishimura, A., Daar, I., Hinnebusch, A.G. and Dean, M. (2006) *Journal of Biological Chemistry* 281, 7452-7457.
- [66] Dong, J.S., Lai, R., Nielsen, K., Fekete, C.A., Qiu, H.F. and Hinnebusch, A.G. (2004) *Journal of Biological Chemistry* 279, 42157-42168.
- [67] Barthelme, D. et al. (2007) *Journal of Biological Chemistry* 282, 14598-14607.
- [68] Bruce, J.B. and Robert, P. (2000), pp. 384 Dover Publications, New York.
- [69] Chu, B. (2007), pp. 368 Dover Publications, New York.
- [70] Fabrice, A., Fei, Y. and Véron, M. (2004) in: *Methods in Molecular Biology*, Vol. 261, part IV, pp. 427-442 Humana Press.
- [71] Strelis, C. (2006) in: *Applied Spectroscopy Reviews*, Vol. 5, pp. 473-489 Taylor & Francis.
- [72] Wellenreuther, G., Fittschen, U.E.A., Achard, M.E.S., Faust, A., Kreplin, X. and Meyer-Klaucke, W. (2008) *Spectrochimica Acta Part B-Atomic Spectroscopy* 63, 1461-1468.

-
- [73] O'Brien, R., Ladbury, J.E. and B.Z., C. (2000) (Ed. Harding, S.E.a.C., B.Z., Ed.) Oxford University Press.
- [74] Rendina, G. (1971) in: Saunders golden, pp. 333.
- [75] Sparkman, O.D. (2001) in: J.Chem. Educ. Pittsburgh: Global View.
- [76] Whitmore, L. and Wallace, B.A. (2008) *Biopolymers* 89, 392-400.
- [77] Mueller-Dieckmann, J. (2006) *Acta Crystallographica Section D-Biological Crystallography* 62, 1446-1452.
- [78] Alberts, B., Johnson, A., Lewis, J., Raff, M., Roberts, K. and Walter, P. (2007), Vol. IV-11 Garland Science Publishing.
- [79] Abad, M.F.C., Di Benedetto, G., Magalhaes, P.J., Filippin, L. and Pozzan, T. (2004) *Journal of Biological Chemistry* 279, 11521-11529.
- [80] Svergun, D.I. and Koch, M.H.J. (2003) *Reports on Progress in Physics* 66, 1735-1782.
- [81] Konarev, P.V., Volkov, V.V., Sokolova, A.V., Koch, M.H.J. and Svergun, D.I. (2003) *Journal of Applied Crystallography* 36, 1277-1282.
- [82] Svergun, D.I. (1999) *Biophysical Journal* 76, 2879-2886.
- [83] Franke, D. and Svergun, D.I. (2009) *Journal of Applied Crystallography* 42, 342-346.
- [84] Volkov, V.V. and Svergun, D.I. (2003) *Journal of Applied Crystallography* 36, 860-864.
- [85] Kozin, M.B. and Svergun, D.I. (2001) *Journal of Applied Crystallography* 34, 33-41.
- [86] Wellenreuther, G. and Meyer-Klaucke, W. (2009) *J. Phys.: Conf. Ser.* 190, 1-4.
- [87] Naskar, J.P., Hati, S. and Datta, D. (1997) *Acta Crystallographica Section B-Structural Science* 53, 885-894.
- [88] Scarrow, R.C. (1994) *Abstracts of Papers of the American Chemical Society* 207, 447-Inor.
- [89] Kanowitz, S.M. and Palenik, G.J. (1998) *Inorganic Chemistry* 37, 2086-+.
- [90] Thorp, H.H. (1998) *Inorganic Chemistry* 37, 5690-+.
- [91] Brown, I.D. (1989) *Journal of Solid State Chemistry* 82, 122-131.

-
- [92] Brown, I.D. and Altermatt, D. (1985) *Acta Crystallographica Section B-Structural Science* 41, 244-247.
- [93] Newville, M. (2001) *Journal of Synchrotron Radiation* 8, 96-100.
- [94] Weil, J.A., Bolton, J.R. and Wertz, J.E. (2001) Wiley-Interscience, New York.
- [95] Dickson, D.P.E. and Berry, F. (1986) Syndicate of the University of Cambridge, Cambridge.
- [96] Pettersen, E.F., Goddard, T.D., Huang, C.C., Couch, G.S., Greenblatt, D.M., Meng, E.C. and Ferrin, T.E. (2004) *Journal of Computational Chemistry* 25, 1605-1612.
- [97] Mirica, L.M., Rudd, D.J., Vance, M.A., Solomon, E.I., Hodgson, K.O., Hedman, B. and Stack, T.D.P. (2006) *Journal of the American Chemical Society* 128, 2654-2665.
- [98] Holt, B.T.O., Vance, M.A., Mirica, L.M., Heppner, D.E., Stack, T.D.P. and Solomon, E.I. (2009) *Journal of the American Chemical Society* 131, 6421-6438.
- [99] Vogel, A., Schilling, O., Niecke, M., Bettmer, J. and Meyer-Klaucke, W. (2002) *Journal of Biological Chemistry* 277, 29078-29085.
- [100] Kitajima, N. et al. (1992) *Journal of the American Chemical Society* 114, 1277-1291.
- [101] Getz, E.B., Xiao, M., Chakrabarty, T., Cooke, R. and Selvin, P.R. (1999) *Analytical Biochemistry* 273, 73-80.
- [102] Aitken, C.E., Marshall, R.A. and Pulglisi, J.D. (2008) *Biophysical Journal* 94, 1826-1835.
- [103] Schilling, O. et al. (2005) *Biochemical Journal* 385, 145-153.
- [104] Gurman, S.J., Binsted, N. and Ross, I. (1984) *Journal of Physics C-Solid State Physics* 17, 143-151.
- [105] Neidig, M.L. and Solomon, E.I. (2005) *Chemical Communications*, 5843-5863.
- [106] Meyer-Klaucke, W., Winkler, H., Schunemann, V., Trautwein, A.X., Nolting, H.F. and Haavik, J. (1996) *Eur J Biochem* 241, 432-9.
- [107] Kuppuraj, G., Dudev, M. and Lim, C. (2009) *Journal of Physical Chemistry B* 113, 2952-2960.

-
- [108] Chow, M.S., Eser, B.E., Wilson, S.A., Hodgson, K.O., Hedman, B., Fitzpatrick, P.F. and Solomon, E.I. (2009) *Journal of the American Chemical Society* 131, 7685-7698.
- [109] Westre, T.E., Kennepohl, P., DeWitt, J.G., Hedman, B., Hodgson, K.O. and Solomon, E.I. (1997) *Journal of the American Chemical Society* 119, 6297-6314.
- [110] Randall, C.R. et al. (1995) *Inorg Chem* 34, 1036-1039.
- [111] Scarrow, R.C., Buck, C.P., Grove, G., Cowling, R.A. and Nelson, M.J. (1994) *Abstracts of Papers of the American Chemical Society* 207, 369-Inor.
- [112] Rohde, J.U. et al. (2003) *Science* 299, 1037-1039.
- [113] Wolfe, M.D., Altier, D.J., Stubna, A., Popescu, C.V., Munck, E. and Lipscomb, J.D. (2002) *Biochemistry* 41, 9611-9626.
- [114] Solomon, E.I. et al. (2000) *Chemical Reviews* 100, 235-349.
- [115] Salomone-Stagni, M., Vogt, S., Shima, S. and Meyer-Klaucke, W. (2009) *Journal of Physics: Conference Series (JPCS)* 190.
- [116] Kubas, G.J. (2007) *Chemical Reviews* 107, 4152-4205.
- [117] Salomone-Stagni, M., Stellato, F., Whaley, C.M., Vogt, S., Morante, S., Shima, S., Rauchfuss, T.B. and Meyer-Klaucke, W. (2010) *Dalton Transactions* 39, 3057-3064.
- [118] Randall, C.R. et al. (1993) *Biochemistry* 32, 6664-6673.
- [119] Roe, A.L., Schneider, D.J., Mayer, R.J., Pyrz, J.W., Widom, J. and Que, L. (1984) *Journal of the American Chemical Society* 106, 1676-1681.
- [120] Wolfe, S., Weinberg, N. and Hsieh, Y. (2007) *Theoretical Chemistry Accounts* 118, 265-269.
- [121] Rawson, J.M. and Winpenny, R.E.P. (1995) *Coordination Chemistry Reviews* 139, 313-374.
- [122] Binder, S. et al. (2009) *Journal of Physics: Conference Series* 190.
- [123] George, G.N., Prince, R.C., Stockley, K.E. and Adams, M.W.W. (1989) *Biochemical Journal* 259, 597-600.
- [124] Carter, C.W., Jr., Kraut, J., Freer, S.T., Alden, R.A., Sieker, L.C., Adman, E. and Jensen, L.H. (1972) *Proc Natl Acad Sci U S A* 69, 3526-9.

References

- [125] Pompella, A., Visvikis, A., Paolicchi, A., De Tata, V. and Casini, A.F. (2003) *Biochemical Pharmacology* 66, 1499-1503.
- [126] Svetlitchnyi, V., Dobbek, H., Meyer-Klaucke, W., Meins, T., Thiele, B., Romer, P., Huber, R. and Meyer, O. (2004) *Proceedings of the National Academy of Sciences of the United States of America* 101, 446-451.
- [127] Ragsdale, S.W. (2007) *Journal of Inorganic Biochemistry* 101, 1657-1666.
- [128] Löscher, S., Zebger, I., Andersen, L.K., Hildebrandt, P., Meyer-Klaucke, W. and Haumann, M. (2005) *Febs Lett* 579, 4287-4291.
- [129] Tard, C. et al. (2005) *Nature* 433, 610-613.
- [130] Liu, T.B. and Darensbourg, M.Y. (2007) *Journal of the American Chemical Society* 129, 7008-+.
- [131] Justice, A.K., Zampella, G., De Gioia, L., Rauchfuss, T.B., van der Vlugt, J.I. and Wilson, S.R. (2007) *Inorganic Chemistry* 46, 1655-1664.
- [132] Ogo, S. et al. (2007) *Science* 316, 585-587.
- [133] Hu, X.L., Brunschwig, B.S. and Peters, J.C. (2007) *Journal of the American Chemical Society* 129, 8988-8998.
- [134] Que, L. (2000) (Que, L., Ed.) *University Science Books*.
- [135] Karcher, A., Schele, A. and Hopfner, K.P. (2008) *Journal of Biological Chemistry* 283, 7962-7971.
- [136] Kispal, G., Csere, P., Prohl, C. and Lill, R. (1999) *Embo Journal* 18, 3981-3989.
- [137] Sole, V.A., Papillon, E., Cotte, M., Walter, P. and Susini, J. (2007) *Spectrochimica Acta Part B-Atomic Spectroscopy* 62, 63-68.

Publications

Structural organization of essential iron-sulfur clusters in the evolutionarily highly conserved ATP-binding cassette protein ABCE1

Dominik Barthelme¹, Urte Scheele¹, Stephanie Dinkelaker¹, Adam Janoschka², Fraser MacMillan³, Sonja-Verena Albers⁴, Arnold J.M. Driessen⁴, Marco Salomone-Stagni⁵, Eckhard Bill⁶, Wolfram Meyer-Klaucke⁵, Volker Schünemann² and Robert Tampe^{1*}

¹Institute of Biochemistry, Biocenter, Johann Wolfgang Goethe-University Frankfurt, Max-von-Laue-Str. 9, D-60439 Frankfurt/M., Germany; ²Department of Physics, University of Kaiserslautern, Erwin-Schrödinger-Str. 56, D-67663 Kaiserslautern, Germany; ³Institute of Physical and Theoretical Chemistry, Johann Wolfgang Goethe-University Frankfurt, Max-von-Laue-Str. 9, D-60439 Frankfurt/M., Germany; ⁴Department of Molecular Microbiology, University of Groningen, Kerklaan 30, 9751 NN Haren, The Netherlands; ⁵European Molecular Biology Laboratory (EMBL), Outstation Hamburg at DESY, Notkestr. 85, D-22603 Hamburg, Germany; ⁶Max Planck Institute for Bioinorganic Chemistry, Stiftstr. 34-36, D-45470 Mülheim a.d. Ruhr, Germany

Running title: ABCE1 contains two essential [4Fe-4S]²⁺ clusters

*Correspondence to: Phone +49-(0)69-798 29475, Fax +49-(0)69-798 29495,
Email: tampe@em.uni-frankfurt.de

The ABC protein ABCE1, formerly named RNase L inhibitor RLI1, is one of the most conserved proteins in evolution, expressed in all organisms, except eubacteria. Due to its fundamental role in translation initiation and/or ribosome biosynthesis, ABCE1 is essential for life. Its molecular mechanism has however not been elucidated. In addition to two ABC ATPase domains, ABCE1 contains a unique N-terminal region with eight conserved cysteines, predicted to coordinate iron-sulfur clusters. Here, we present detailed information on the type and on the structural organization of the Fe-S clusters in ABCE1. Based on biophysical, biochemical and yeast genetic analyses, ABCE1 harbors two essential diamagnetic [4Fe-4S]²⁺ clusters with different electronic environments, one ferredoxin-like (CPX_nCX₂CX₂C; Cys-Pos. 4/5/6/7) and one unique ABCE1-type cluster (CXPX₂CX₃CX_nCP; Cys-Pos. 1/2/3/8). Strikingly, only seven of the eight conserved cysteines coordinating the Fe-S clusters are essential for cell viability. Mutagenesis of the cysteine at position 6 yielded a functional ABCE1 with the ferredoxin-like Fe-S cluster in a paramagnetic [3Fe-4S]¹⁺ state. Notably, a lethal mutation of the cysteine at position 4 can be rescued by ligand swapping with an adjacent, extra cysteine conserved among all eukaryotes.

Iron-sulfur (Fe-S)¹ clusters constitute an ancient prosthetic group, which can be found in proteins from all living organisms. They are only composed of the inorganic components, sulfur and iron. In the most common cluster variants, [2Fe-2S], [3Fe-4S] and [4Fe-4S], the metal ions are directly coordinated by the inorganic sulfur and the adjunct cysteinyl groups from the protein backbone (1). Nevertheless, amino acids like histidine can also contribute to the iron coordination, as known for [2Fe-2S] Rieske clusters. Additionally, much more complicated structural arrangements can be found. The complex FeMoco and P-cluster of nitrogenase are just one example of clusters with higher nuclearity, arising from smaller substructures and clusters containing additional metal atoms like molybdenum (2). Furthermore, interconversion of Fe-S cluster is a widely distributed phenomenon, reflecting the dynamic arrangement and behavior (3). Despite their relative simple composition of only iron and sulfur (in most cases), Fe-S clusters are often essential components for the enzymatic function and thereby involved in a vast variety of cellular processes. Beside their obvious role in electron transport, they operate as sensors for e.g. iron, modulate protein stability and play a role in nucleic acid binding and modification (1,4).

Although Fe-S clusters can be synthesized *in vitro* (5), their assembly and maturation *in vivo* requires a highly complex and regulated

machinery (6). Mitochondria are the central compartment in Fe-S cluster biogenesis, which is also the only essential function of this organelle to date (6,7). The underlying concept is not understood so far, since mitochondrial Fe-S cluster proteins are not essential for cell viability. The cytosolic Fe-S protein ABCE1 could explain this phenomenon, due to the fact that Fe-S clusters can be transported from mitochondria to the cytosol (8,9), where they are incorporated into the protein moiety.

ABCE1 is found evolutionary conserved in all archaea and eukaryota, where it is essential for life (9-13). ABCE1 belongs to the superfamily of ATP-binding cassette (ABC) proteins with twin ABC ATPase domains, which are arranged in a head-to-tail orientation via a flexible linker and hinge region (14). Most of these members constitute membrane proteins that mediate ATP-driven unidirectional transport of a variety of molecules across biological membranes. Because ABCE1 does not contain any transmembrane domain, its function cannot be related to a membrane transport process. The protein was originally identified as the RNase L inhibitor in the innate immune response and therefore called RL11 (15). It was subsequently shown that the assembly of the HIV-1 capsids requires ABCE1 in a strictly ATP-dependent manner (16). Very recently, an even more fundamental and general role was proposed in the process of translation initiation and ribosome biosynthesis (9,12,13,17). ABCE1 was found to interact with translation initiation factors, eIF2, eIF3, eIF5, the 40S ribosomal subunit and several ribosomal RNAs. Depletion of the protein causes defects in the assembly of the preinitiation complex, rRNA processing, and accumulation of ribosomal subunits in the nucleus. Nevertheless, the underlying molecular mechanism remains enigmatic.

ABCE1 harbors a unique N-terminal region including eight conserved cysteine residues with the CX₄CX₃CX₃CPX_nCX₂CX₂CX₃P consensus sequence. A specific incorporation of iron, the interaction with members of the Fe-S cluster assembly machinery, and the functional importance of two of these eight cysteine residues (Pos. 3 and 7) have been demonstrated (9). However, information regarding the type and structural organization of the Fe-S cluster has not been available until now.

By using homologously and heterologously expressed ABCE1 from the hyperthermophilic crenarchaeote *Sulfolobus solfataricus* (*S. solf.*), we provide detailed information on the Fe-S

clusters. Highlighted by functional studies in yeast, we show the pivotal role of conserved cysteines coordinating the prosthetic group. We finally present a model for the structural organization of the Fe-S clusters in this essential and evolutionary conserved protein.

EXPERIMENTAL PROCEDURES

Expression of ABCE1 in Sulfolobus solfataricus—For over-expression of affinity-tagged ABCE1, a stable and selectable shuttle vector based on the virus SSV1 of *Sulfolobus shibatae* was used (18). The open reading frame SSO0287 (*abce1*) was amplified by PCR using genomic DNA of *S. solf.* and the primers, P1f 5'-CCATATCCCATGGTGAGAGTTGC-3' and P4r 5'-GGGCCCTTAATGGTGATGGTGATGGTGATGGTGTTCATCAAATTGTGGATGTA CCAATTCTGGGTAGAAAGAA-3'. This resulted in the introduction of NcoI and ApaI restriction sites in the flanking regions of the gene and a tandem-affinity (His₈ and StrepII) tag at the C-terminus. The gene was cloned into pSVA5 (18), using the NcoI and ApaI sites yielding pSVA30. To transfer the *araS* promoter together with the gene to be expressed into the virus-based vector, the BlnI/EagI insert from pSVA30 was ligated into pMJ02 (19), resulting in the plasmid pSVA31. Electroporation of *S. solf. pyrEF* mutant PH1-16 with pSVA31 and the isolation of single transformants were carried out as described (20,21). Integration of the viral vector into the genome was confirmed by Southern blot analysis using standard procedures. *S. solf.* PH1-16 cells (21) harboring pSVA31 were inoculated in 50 ml Brock's medium containing 0.1% tryptone. After two days of growth ($A_{600} \sim 0.5$) at 80°C and pH 3.5, these cells (10 ml) were transferred to 400 ml medium containing 0.1% tryptone and 0.2% arabinose to induce expression of ABCE1. After two days of growth ($A_{600} \sim 0.8$), the cells were harvested and resuspended in 10 mM Tris/HCl, 100 mM NaCl, pH 7.4.

Expression of Sulfolobus solfataricus ABCE1 in E. coli—The ORF SSO0287 of *S. solf.* ABCE1 was amplified by PCR using genomic DNA of *S. solfataricus* and the primers, P1f 5'-CCATATCCCATGGTGAGAG TTGC-3' and P1r 5'-CCATATGGATCCCTGGGTAGAAAG AACCAAGGAG-3', and cloned into the NcoI and BamHI sites of the pSA4 expression vector (22). The resulting plasmid (pSD1) codes for wildtype ABCE1 of *S. solf.* with a C-terminal His₆-tag. The two conserved cysteines, C24 and

C54, were individually exchanged for serine residues (C24S and C54S) by QuikChange site-directed mutagenesis (Stratagene). PCR and mutagenesis products were confirmed by DNA sequencing. The *E. coli* strain BL21(DE3) (Novagen) was co-transformed with either of the ABCE1 constructs and the pRARE plasmid (Novagen) coding for rare tRNAs and grown in LB medium supplemented with 100 µg/ml ampicillin and 25 µg/ml chloramphenicol at 37°C. Expression was induced at an A_{600} of 0.6 for 3 h at 30°C by adding 0.2 mM isopropyl- β -D-thiogalactopyranoside.

Purification of ABCE1—All purification steps and experimental analysis were carried out under argon atmosphere or in an anaerobic chamber containing 95% N_2 /5% H_2 (Coy Laboratories). Before use, buffers were degassed and equilibrated inside the anaerobic chamber for several days. Cell pellets of *S. solf.* were resuspended in lysis buffer A (20 mM NaH_2PO_4 , 300 mM NaCl, 20 mM imidazole, pH 7.4), disrupted by using a Branson Sonifier 250 at 60% output in eight pulses of 30 s on ice and centrifuged for 30 min at 114,000 x g. Afterwards, ABCE1 was purified to homogeneity via metal affinity chromatography (HisSelect, Sigma) by washing/elution with 20 mM/300 mM imidazole. For purification of ABCE1 expressed in *E. coli*, frozen cells were thawed, resuspended in lysis buffer B (20 mM Tris-HCl, 100 mM NaCl, 1 mM DTT, 1 mM EDTA, pH 7.4) and disrupted by sonication as described before. After centrifugation at 114,000 x g for 30 min, the supernatant was heated at 70°C for 10 min and additionally centrifuged for 1 h at 114,000 x g. The solution was subsequently applied to metal affinity chromatography (HisTrap, GE Healthcare). ABCE1 was purified by washing/elution with 60 mM/200 mM of imidazole. Protein fractions were exchanged to buffer C (20 mM Tris-HCl, 100 mM NaCl, pH 7.4) using a Centricon device (Millipore). The protein concentration was determined by the Coomassie PlusTM Bradford Assay (Pierce) using bovine serum albumin as a standard.

Determination of Iron and Sulfur—Total reflection X-ray fluorescence (TXRF) as a trace multi-element analytical method was applied to quantify the iron and sulfur content of purified ABCE1. The measurement was carried out using an EXTRA IIA spectrometer (Atomica Instruments) with a sample volume of 4 µl in 50 mM Tris-acetate buffer (pH 7.5). 20 µl of

protein solution were placed onto siliconized quartz carrier plates and evaporated to dryness. By excitation with the $Mo(K\alpha)$ line for 1000 seconds, a multi-element fluorescence spectrum was obtained. The intensities of the sulfur and iron peaks were related to a rubidium peak as an internal standard. The iron content of ABCE1 was further determined colorimetrically by the method of Fish (23) and the inorganic sulfur was quantified according to Beinert (24).

UV/VIS Spectroscopy—Spectra of wildtype and ABCE1 mutants were recorded on a Cary 50 spectrophotometer (Varian) in buffer C. ABCE1 was titrated with sodium dithionite or freshly prepared potassium ferricyanide (both in buffer C). The spectra of the oxidant and reductant solutions alone were subtracted from the corresponding curves.

EPR Spectroscopy—ABCE1 was analyzed by continuous wave (cw) electron paramagnetic resonance (EPR), either untreated, reduced with sodium dithionite or ascorbate, or oxidized with potassium ferricyanide in buffer C. X-band EPR spectra were measured on a Bruker E-500 eleXsys spectrometer using a standard rectangular Bruker EPR cavity equipped with an ESR900 helium flow cryostat (Oxford Instruments). The spectra were recorded under following experimental conditions: microwave frequency, 9.424 GHz; microwave power, 8 mW, field modulation frequency, 100 kHz, field modulation depth, 5 Gauss (peak to peak); temperature 10 K.

To study the immediate environment around the Fe-S cluster pulsed EPR was performed on a Bruker E-580 spectrometer using a Bruker EPR cavity (MD5-W1) equipped with a helium flow cryostat (CF935, Oxford Instruments). The pulses were amplified using a 1 kW pulsed traveling wave tube amplifier. A conventional two-pulse ($\pi/2 - \tau - \pi$) sequence was used. A two-pulse, echo modulation experiment (ESEEM) was performed by integrating the area under the Hahn echo as a function of time between the two microwave pulses. The frequency domain spectrum was obtained by Fourier transformation of the time domain trace after subtraction of a mono-exponential decay function. This measurement was performed at 10 K at a microwave frequency of 9.745 GHz using a $\pi/2$ pulse length of 8 ns, a starting τ of 132 ns and a shot repetition rate of 1 ms.

Mössbauer Spectroscopy—For preparation of the Mössbauer sample, metallic ^{57}Fe (Chemotrade, 96% enrichment) was dissolved in

37% (v/v) HCl at 80°C for several days. The obtained $^{57}\text{FeCl}_3$ solution was directly added to the *S. solf.* medium (without FeCl_3) to a final concentration of 41 μM . Mössbauer spectra of purified ABCE1 were recorded in buffer C by using a conventional spectrometer in the constant acceleration mode. Isomer shifts are given relative to $\alpha\text{-Fe}$ at room temperature. Zero-field spectra were measured in bath cryostat (Oxford Instruments), whereas for the high field spectra ($4\text{ T} \perp \gamma$), a cryostat equipped with a superconducting magnet was used (Oxford Instruments). Magnetically split spectra were simulated within the spin Hamilton formalism (25), otherwise, spectra were analyzed by last-square fits using Lorentzian line shape.

X-ray Absorption Spectroscopy (XAS)–ABCE1 was concentrated to 1.2 mM in Fe. Afterwards, XAS sample was filled into the 25 μl plastic XAS cuvettes and stored at cryogenic temperatures. The K-edge iron X-ray absorption spectrum was recorded at the beam line D2 of the EMBL Outstation Hamburg at DESY (Germany). The DORIS storage ring operated at 4.5 GeV with the positron beam current ranging from 145 mA to 80 mA. An ^{111}Si double-crystal monochromator scanned X-ray energies around Fe K-edge (6.9–8.1 keV). Harmonic rejection was achieved by a focusing mirror (cut-off energy at 20.5 keV) and a monochromator detuning to 50% of its peak intensity. The sample cells were mounted in a two-stage Displex cryostat and kept at about 20 K. The X-ray absorption spectra were recorded as Fe K_{α} fluorescence spectra with a Canberra 13-element Ge solid-state detector. Data reduction, such as background removal, normalization and extraction of the fine structure, was performed with KEMP (26) assuming a threshold energy $E_{0,\text{Fe}} = 7120\text{ eV}$. Sample integrity during exposure to synchrotron radiation was checked by monitoring the position and shape of the absorption edge on sequential scans. No changes were detectable. The extracted Fe K-edge (25–860 eV) EXAFS data were analyzed as reported previously (27).

Functional Analysis of ABCE1 Mutants in Yeast–To investigate various cysteines mutants of ABCE1, we used a yeast strain, in which the endogenous promoter was replaced by a tetracycline-regulated one (28). The cells were transformed with the multi-copy plasmid pRS423 harboring the wildtype or ABCE1 mutants. A plasmid coding for *abce1* from *S. cerevisiae* was generated by PCR using the

primers P2f 5'-ATGGTCGACGCCCTCGTATCTGCAACG-3' and P2r 5'-ATACCCGGGAGTACGGATCACCGAAGAGG-3' with chromosomal DNA as a template. The amplified construct was inserted into the SalI and SmaI restriction sites of the vector pRS423. ABCE1 was expressed under the control of the endogenous promoter. The highly conserved N-terminal cysteine residues C16, C21, C25, C29, C55, C58, C61 and C65 as well as the cysteine C38 were exchanged to serines or to alanines by site-directed mutagenesis. Single, double and triple mutations were created and transformed into yeast cells. Following doxycycline treatment, the chromosomal expression of ABCE1 was repressed and the ABCE1 mutants substituted for the endogenous protein in the cells. The pRS423 vector containing the wildtype ABCE1 gene and the empty vector served as control plasmids.

RESULTS

Expression and Isolation of ABCE1–To analyze the structural organization and function of Fe-S clusters in ABCE1, we used a double tracked approach: (i) functional studies of each cysteine in Fe-S cluster assembly of ABCE1 were performed in yeast. (ii) For biophysical and biochemical analyses of the Fe-S cluster, we choose ABCE1 from the hyperthermophilic crenarchaeote *Sulfolobus solfataricus*. Notably, this thermostable protein contains only the eight conserved cysteines putatively coordinating Fe-S clusters. The yeast and archaeal protein are highly homologous (43% identity and 66% similarity, see also alignment of the N-terminal domain in Fig. 7B).

Based on a newly developed inducible expression system in *S. solf.* (18), ABCE1 was over-expressed and purified to homogeneity in quantities sufficient for biophysical studies (Fig. 1A). 0.5 mg of protein (68 kDa) was obtained from one liter culture. Because of the unexpected finding of viable ABCE1 cysteine mutants, we transferred the corresponding mutations into ABCE1 from *S. solf.* for further analysis. Genetic manipulations in archaea are still time-consuming and by far no routine method. Therefore, wildtype and the ABCE1 mutants were heterologously expressed in *E. coli* and purified to homogeneity as described above. In this case, 1–2 mg of protein was obtained from one liter *E. coli* culture. Interestingly, some degradation products were copurified with the C24S mutant (Fig. 1B). This behavior is typical

for Fe-S proteins, in which clusters are absent or not correctly assembled.

All ABCE1 preparations, except the C24S mutant, showed a brownish color, typical for Fe-S cluster proteins (Fig. 1C). After exposure to oxygen, the C54S mutant rapidly lost its color, whereas wt ABCE1 isolated either from *S. solf.* or *E. coli* remained brownish for at least several hours (data not shown).

Assembly of two Fe-S clusters in ABCE1—ABCE1 isolated from *S. solf.* exhibits a characteristic UV/VIS spectrum with a maximum at 280 nm, a shoulder at 320 nm and a broad peak around 410 nm (Fig. 2A), indicative for cuban [4Fe-4S] or cuboidal [3Fe-4S] type clusters (29). The molar extinction coefficient ϵ_{410} of 29,000 $M^{-1}\cdot cm^{-1}$ is in the range of proteins containing two of these clusters (30). The absorption spectrum of wt ABCE1 isolated from *E. coli* differed only by the extinction coefficient ϵ_{410} of 24,000 $M^{-1}\cdot cm^{-1}$ (17% reduction compared to ABCE1 isolated from *S. solf.*). Surprisingly, the C54S mutant showed an absorption spectrum very similar to wt ABCE1 purified from *E. coli* ($\epsilon_{410} = 22,500 M^{-1}\cdot cm^{-1}$), demonstrating that the assembly of the Fe-S clusters is comparable in both proteins. In contrast, the C24S mutant showed no specific absorption at 410 nm revealing a defect in Fe-S cluster assembly. As addressed below, the functional consequences of these mutations have been examined in yeast.

Titration of wt ABCE1 with the reductant sodium dithionite (Fig. 2B) or ascorbate (not shown) did not significantly change the UV/VIS spectra. This demonstrates the stability of the Fe-S cluster at low redox potential. In contrast, titration with the oxidant potassium ferricyanide resulted in loss of the 410-nm peak and the appearance of new absorption bands at 340 nm and 450 nm (Fig. 2C). Remarkably, the C54S mutant exhibited a greater sensitivity to oxidation by ferricyanide as compared to wt ABCE1, resulting in an immediate loss of the absorption at 410 nm (data not shown).

We next quantified the amount of incorporated iron and sulfur in the wt and ABCE1 mutants by total X-ray reflection fluorescence (TXRF) spectroscopy and colorimetric assays. Wt ABCE1 (1 nmol) isolated from *S. solf.* contains 7.0 nmol iron and 6.1 nmol acid-labile sulfur per nmol protein (Tab. 1). In comparison, wt ABCE1 purified from *E. coli* harbors 13% less iron (6.1 nmol) and 10% less acid labile sulfur (5.5 nmol).

Considering a small amount of impurities and the intrinsic error in protein quantification, it seems likely that the iron and sulfur content are slightly underestimated. Especially for the protein isolated from *E. coli* a small population of non-assembled Fe-S cluster can be found.

Together with the UV/VIS data, these findings clearly demonstrate the presence of two cuban or one cuban and one cuboidal Fe-S clusters in the ABCE1. The C54S mutant showed also incorporation of iron and acid-labile sulfur but with decreased values compared to wt ABCE1. It is worth mentioning that the Fe-S clusters in the C54S mutant were extremely labile, resulting in a loss of iron and sulfur during buffer exchange (e.g. dialysis). In the C24S mutant, no significant iron and acid-labile sulfur were detected, consistent with the colorless protein solution (Fig. 1C) and the UV/VIS spectra (Fig. 2A). Importantly, no other metal ions such as copper, nickel, zinc or molybdenum were found in all ABCE1 proteins by TXRF analysis.

ABCE1 Harbors Diamagnetic Fe-S Clusters—We next examined the Fe-S clusters in ABCE1 by electron paramagnetic resonance (EPR) spectroscopy. The two Fe-S clusters found in ABCE1 are EPR-silent and therefore in a diamagnetic state (Fig. 3A). It should be mentioned that ABCE1 isolated from *S. solf.* or *E. coli* showed identical spectroscopic behavior (data not shown). Interestingly, oxidation of the same sample with ferricyanide leads to an EPR signal (Fig. 3A), which, based on the relatively isotropic g-tensors, is characteristic for the formation of a $[3Fe-4S]^+$ cluster (31,32). Further addition of the oxidation reagent did not increase the EPR signal, which finally disappeared (data not shown). In agreement with the UV/VIS spectra, the two diamagnetic Fe-S clusters in ABCE1 could be reduced neither by ascorbate (not shown) nor by the strong reductant dithionite at pH 9.0 (Fig. 3B).

Notably, already without oxidation the C54S mutant showed an EPR signal (with regard to g-tensor and spin intensity) similar to oxidized wt ABCE1 (Fig. 3C). In contrast to wt ABCE1, oxidation of the C54S mutant leads to a decrease in the EPR signal even at low concentrations of ferricyanide (Fig. 3C). The slight difference in the overall line shape of the C54S mutant and the oxidized wildtype protein may result from a different electronic environment and the influence of the mutant on the g-tensor and/or some of the small proton hyperfine interactions, which determine this line shape. Indeed, two-

pulse ESEEM experiments of the C54S mutant did not reveal any other magnetic nuclei (e.g. ^{14}N) in the immediate environment of the cluster (data not shown). In conclusion, ABCE1 contains two diamagnetic $[\text{4Fe-4S}]^{2+}$ clusters, one being converted into a $[\text{3Fe-4S}]^+$ state upon oxidation or cysteine mutagenesis.

Two $[\text{4Fe-4S}]^{2+}$ Clusters of ABCE1 Exist in Different Electronic Environments—To finally confirm the type of the two diamagnetic Fe-S clusters, wt ABCE1 was analyzed by Mössbauer spectroscopy. ABCE1 was labeled with ^{57}Fe in *S. solf.* and purified as described in the Experimental Procedures. The Mössbauer spectrum of ABCE1 obtained at 77 K has been analyzed with three quadrupole doublets (Fig. 4A). Species 1 has an isomer shift of $\delta_1 = 0.43 \text{ mms}^{-1}$, a quadrupole splitting of $\Delta E_{Q1} = 1.32 \text{ mms}^{-1}$ and a relative contribution of 44%. Species 2 exhibits an isomer shift of $\delta_2 = 0.42 \text{ mms}^{-1}$, a quadrupole splitting of $\Delta E_{Q2} = -0.86 \text{ mms}^{-1}$ and also a relative contribution of 44%. The negative sign of ΔE_{Q2} has been determined by the analysis of the high-field Mössbauer spectra (see Fig. 4B). The isomer shifts of species 1 and 2 are characteristic for $\text{Fe}^{2.5+}$ -pairs of $[\text{4Fe-4S}]^{2+}$ clusters (25,33).

Figure 4B shows a Mössbauer spectrum of ABCE1 taken at 4.2 K in a field of 4 T perpendicular to the γ -beam. The observed magnetic splitting was successfully reproduced by the simulation shown in Figure 4B. The input parameters for the simulation are the hyperfine parameters of components 1 and 2 as obtained from the analysis of the spectrum taken at 77 K (Fig. 4A) and show diamagnetic ground states of both species. This spectroscopic signature is again indicative for $[\text{4Fe-4S}]^{2+}$ clusters (25,33). Species 3 with $\delta_3 = 0.26 \text{ mms}^{-1}$, $\Delta E_{Q3} = 0.63 \text{ mms}^{-1}$ and a relative contribution of 12% (Fig. 4A) does lead to a broad magnetic background in the high-field spectrum. Such a behavior is characteristic for an unspecific Fe^{3+} (33). Therefore, species 3 has been disregarded in the simulation. Considering the facts that iron quantification yields almost the amount of iron expected for two $[\text{4Fe-4S}]$ clusters and that species 1 and 2 are present at equal ratio, Mössbauer spectroscopy consistent with the model that ABCE1 has two $[\text{4Fe-4S}]^{2+}$ clusters in a slightly different electronic environment.

Coordination of Iron in the Clusters—The edge shape of the XANES spectra (Fig. 5A), which can be used as a fingerprint for the electronic structure of the metal ions, resembles

the one reported for oxidized hydrogenase II from *Clostridium pasteurianum*, which harbors $[\text{4Fe-4S}]^{2+}$ clusters (34). Typical features are the resonance in the rising edge and the rather flat maximum followed by a sharp minimum. The extracted fine structure (EXAFS) is dominated by a single frequency with a shift at about 8 \AA^{-1} . The high intensity at wave numbers larger than 10 \AA^{-1} in biological samples indicates the presence of a multinuclear metal center. This is consistent with the peak at about 2.8 \AA in the corresponding Fourier transformation (FT). The high intensity of the main peak at about 2.3 \AA in the FT points towards a homogenous first coordination sphere formed by sulfur ligands. The FT is very similar to the one observed for the $[\text{4Fe-4S}]^{2+}$ clusters mentioned above (34). Models based on the assumption of $[\text{4Fe-4S}]^{2+}$ clusters resemble the data very well (Fig. 5B and 5C). All attempts to replace one of the sulfur ligands in the fit by light atoms such as oxygen or nitrogen lead to artificially long Fe-O/N distances. Thus, recognizable contributions above 10% of the average ligand sphere are excluded. The Fe-S distance of 2.29 \AA and the Fe-Fe distances of 2.74 \AA match the literature values for oxidized $[\text{4Fe-4S}]$ clusters very well (35).

Essential Function of the Fe-S Clusters in ABCE1—By means of biophysical and biochemical analyses, we resolved that ABCE1 from *Sulfolobus solfataricus* contains two diamagnetic $[\text{4Fe-4S}]^{2+}$ clusters. However, the functional impact of the two different Fe-S clusters cannot easily be addressed in archaea. Therefore, we initiated a genetic analysis in *Saccharomyces cerevisiae*, where ABCE1 has been shown to be essential for viability due to its fundamental role in translation initiation and ribosome biosynthesis (9,12,17). By systematic mutation of all conserved cysteine residues, individually or in combination, we addressed the functional role of the Fe-S clusters in *S. cerevisiae* ABCE1. Plasmids encoding wildtype or ABCE1 mutants were transformed into a yeast strain, in which a tetracycline-repressible one replaced the endogenous promoter of ABCE1. After repression of endogenous ABCE1 by addition of doxycycline, we analyzed single clones for viability.

Remarkably, only five out of the eight conserved cysteines (C16, C25, C55, C61 and C65; pos. 1/3/5/7/8) were found to be essential for cell survival (Fig. 6A). To our very surprise the C21S, C29S and C58S mutants (pos. 2/4/6) are still viable (Fig. 6A). It should be mentioned

that the C21S mutant shows a slow growth phenotype. Since it is known that serine residues can coordinate Fe-S clusters in certain cases, we subsequently mutated each of these three cysteine residues to alanine. Here, C29A and C58A (pos. 4 and 6) were still viable, but the C21A mutant (pos. 2) was lethal (Fig. 6B). In conclusion, six coordinating cysteines, of which serine at position can partially be accepted, are strictly required for the formation of the Fe-S clusters and cell survival. The inviability of the C25S and C61S mutant is in agreement with previous studies, which further demonstrated that substitution of these cysteines had no effect on the expression level and stability of the protein (9).

Interestingly, the viable yeast C58 mutant corresponds to the C54S mutant in *S. solf.* Biophysical and biochemical analyses indicate that this mutant contains a $[4\text{Fe-4S}]^{2+}$ and a paramagnetic $[3\text{Fe-4S}]^+$ center. In conclusion, the cysteine at position 6 is not essential for the assembly of the Fe-S cluster and vital function of ABCE1.

The viability of the C29 mutants remained enigmatic, since the corresponding mutant in ABCE1 from *S. solf.* (C24S) showed a defect in Fe-S cluster assembly (see Fig. 1 and 2). We excluded that the adjacent S28 rescues the C29 mutation (Fig. 6B). However, by *in silico* analysis, we noticed that, in contrast to most archaeal homologues, all ABCE1 in eukarya carry an extra cysteine in close proximity to the iron-sulfur centers. This corresponds to C38 in *S. cerevisiae* ABCE1. In a process called ligand swapping, such a cysteine, originally not involved in Fe-S cluster coordination, can take over the function of a missing or mutated cysteine residue. To test this hypothesis, we generated the double C29A/C38A mutant. Indeed, this double mutation was lethal, whereas cells with the double mutation C58A/C38A as a control grew normal, demonstrating a site-specific ligand swapping between C29 and C38 (Fig. 6B).

Finally, double and triple mutants comprising the dispensable cysteines were generated. Notably, any combination of the otherwise viable mutations shows an additive effect, leading to a lethal phenotype (Fig. 6C).

DISCUSSION

The presence of Fe-S clusters discriminates the evolutionary highly conserved protein ABCE1 from all other members of the ABC

superfamily. In this study, we determined the type, coordination and functional relevance of the Fe-S clusters in ABCE1 of archaea and eukarya. For detailed biophysical and biochemical analyses, we used ABCE1 from the hyperthermophilic crenarchaeote *Sulfolobus solfataricus*, which contains only the eight conserved cysteine residues, putatively coordinating Fe-S clusters. By means of a novel expression system, ABCE1 was over-expressed and isolated from the homologous host, which ensured the complete machinery for Fe-S cluster assembly. Expression in *E. coli* was used to examine various mutants efficiently. The functional role of the Fe-S clusters was however addressed in yeast, where ABCE1 is essential for cell viability (9,12,17).

The combination of structural and functional analyses clearly demonstrates the presence of two diamagnetic $[4\text{Fe-4S}]^{2+}$ clusters in ABCE1 and further highlights the essential role of the conserved cysteines for Fe-S cluster assembly. Sequence comparison shows that the Fe-S cluster coordination in ABCE1 (Fig. 7A) partially resembles those of 8 Fe ferredoxins, e.g. in *Desulfovibrio africanus* ferredoxin III or *Azotobacter vinelandii* ferredoxin I (36,37). We therefore conclude that ABCE1 contains one ferredoxin-like $[4\text{Fe-4S}]^{2+}$ cluster formed by the cysteines at position 4/5/6/7. Indeed, this cluster perfectly matches the ferredoxin-type consensus sequence $\text{CPX}_n\text{CX}_2\text{CX}_2\text{C}$ (Fig. 7B). The coordination of the second Fe-S cluster in ABCE1 (cysteines 1/2/3/8) has not been described in any other protein. Hence, we propose a unique ABCE1-type $[4\text{Fe-4S}]^{2+}$ cluster with the consensus sequence $\text{CXPX}_2\text{CX}_3\text{CX}_n\text{KCP}$. This model shall be clarified by a high-resolution structure of the full-length protein.

Both clusters are equally present, but have a slightly different electronic environment as demonstrated by Mössbauer spectroscopy (see Fig. 4). Based on the quadrupole splitting, species 1 ($\delta_1 = 0.43 \text{ mms}^{-1}$, $\Delta E_{Q1} = 1.32 \text{ mms}^{-1}$) is typical for a ferredoxin-like cluster (38,39), whereas species 2 ($\delta_2 = 0.42 \text{ mms}^{-1}$, $\Delta E_{Q2} = -0.86 \text{ mms}^{-1}$) should reflect the ABCE1-type cluster. Additional atoms, such as oxygen or nitrogen from e.g. aspartate, histidine or serine residues, do not contribute to the cluster coordination in wt ABCE1 and the C54S mutant, according to both XAS and ESEEM analysis.

The systematic mutagenesis of all conserved cysteines in ABCE1 revealed that, surprisingly,

three cysteine-to-serine mutants (C21S, C29S, C58S) are not lethal. The C21S mutant has a slow growth phenotype, demonstrating that serine at position 2 can partially substitute cysteine in coordination and assembly of the Fe-S clusters. Nevertheless, four sites (position 1/2/3/8) are strictly required for formation of the ABCE1-type cluster and ABCE1 function (see Fig. 6).

In contrast, position 6, which is part of the ferredoxin-like cluster, is dispensable for the essential ABCE1 function. Strikingly, this cluster can also exist in a $[3\text{Fe-4S}]^+$ state. Although interconversion between $[4\text{Fe-4S}]$ and $[3\text{Fe-4S}]$ clusters has been reported, as e.g. in ferredoxin II from *Desulfovibrio gigas* (39) or ferredoxin III from *Desulfovibrio africanus* (36), we have presently no evidence, whether this state exists for wt ABCE1 *in vivo*. Remarkably, the mutant at position 6 was extremely labile towards oxidation, resulting in a loss of iron and acid-labile sulfur. These findings further support the “all-or-nothing” behavior of the two Fe-S clusters in ABCE1, meaning that they assemble simultaneously and depend on each other (9). Double and triple mutants of the dispensable positions display additive effects resulting in lethality (see Fig. 6). The fact that the Fe-S clusters in ABCE1 are stable down to redox-potentials of approx. $E^\circ' = -560$ mV and that the ferredoxin-like cluster is functional in different states indicates a structural rather than redox-catalytic role for this cluster, similar to *E. coli* endonucleases III (40). In this enzyme, the Fe-S cluster serves as a scaffold for proper positioning catalytic amino acids involved in DNA recognition and binding. Notably, the N-terminal Fe-S domains of ABCE1 are rich in conserved basic residues, which could, similarly to the *E. coli* endonuclease III or MutY, sense and modify nucleic acids (40-42). Despite the potential role in scaffolding a ligand-binding site, the Fe-S clusters of ABCE1 are not required for the

folding and the structural integrity of the twin ABC ATPase domains (14). From the x-ray structure it was anticipated that the two NBDs perform an ATP-driven clamp-like motion. Nevertheless, the impact of the Fe-S domain on conformation changes and the ATP-hydrolysis cycle of ABCE1 needs to be addressed in future experiments.

The dispensable cysteine at position 4 of yeast ABCE1(C29A or C29S) is remarkable, since the corresponding mutation in *S. solf.* ABCE1 (C24S) completely abolishes the incorporation of iron and acid-labile sulfur (see Table 1, Fig. 1/2). Strikingly, all eukaryotic ABCE1 proteins contain a conserved, extra cysteine within the N-terminal Fe-S cluster domain, which can rescue C29 (position 4) by ligand swapping. This extra cysteine, absent in most archaea, explains why the mutation at position 4 (C24S) in *S. solf.* ABCE1 showed no assembled Fe-S clusters. Noteworthy, mutation of C38 (extra cysteine) has no effect on ABCE1 function in yeast. It is therefore questionable if ligand swapping occurs *in vivo*.

ABC-type proteins are evolutionarily highly conserved molecular machines, coupling ATP binding and hydrolysis to conformational changes (43,44). The smallest functional unit appears to be an ABC dimer, which operates in a processive engagement/disengagement cycle (44-46). These chemomechanical engines drive not only membrane translocation but also a variety of other crucial biological processes, such as DNA repair and chromosome segregation. The fundamental role of ABCE1 in RNase L inhibition, HIV capsid maturation, translation initiation and ribosome biosynthesis (8,12,13,15-17), suggests that the two essential diamagnetic $[4\text{Fe-4S}]^{2+}$ clusters identified in this study are involved in recognition and modification (chemical or conformational) of RNA assemblies.

ACKNOWLEDGEMENTS

We would like to thank Volker Müller and Beate Averhoff (Institute of Molecular Biosciences, Goethe-University Frankfurt) for the possibility to use the *Sulfolobus solfataricus* fermentation facility and the anaerobic chamber, Eckhard Boles (Institute of Molecular Biosciences, Goethe-University Frankfurt) for many helpful comments. We are also grateful to Bernd O. Kolbesen and Claudia Rittmeyer (Institute of Inorganic and Analytical Chemistry, Goethe-University Frankfurt) for TXRF measurements. We thank Thomas Prisner (Institute of Physical and Theoretical Chemistry, Goethe-University Frankfurt) for the access to the EPR instrumentation. We further acknowledge Chiara Presenti for excellent assistance. Financial support by the Center for Membrane Proteomics (CMP) at the Goethe-University Frankfurt is kindly acknowledged.

¹ **The abbreviations used are:** ABC, ATP binding cassette; cw, continuous wave; EPR, electron paramagnetic resonance; ESEEM, electron spin echo envelope modulation; EXAFS, extended X-ray absorption fine structure; Fe-S, iron-sulfur; TXRF, total X-ray reflection fluorescence; wt, wildtype; XANES; X-ray absorption near edge structure spectroscopy; XAS, X-ray absorption spectroscopy.

REFERENCES

1. Beinert, H., Holm, R. H., and Munck, E. (1997) *Science* **277**, 653-659
2. Howard, J. B., and Rees, D. C. (2006) *Proc Natl Acad Sci U S A* **103**, 17088-17093
3. Khoroshilova, N., Popescu, C., Munck, E., Beinert, H., and Kiley, P. J. (1997) *Proc Natl Acad Sci U S A* **94**, 6087-6092
4. Pierrel, F., Douki, T., Fontecave, M., and Atta, M. (2004) *J Biol Chem* **279**, 47555-47563
5. Zheng, L., and Dean, D. R. (1994) *J Biol Chem* **269**, 18723-18726
6. Lill, R., and Muhlenhoff, U. (2006) *Annu Rev Cell Dev Biol* **22**, 457-486
7. Lill, R., Fekete, Z., Sipos, K., and Rotte, C. (2005) *IUBMB Life* **57**, 701-703
8. Kispal, G., Csere, P., Prohl, C., and Lill, R. (1999) *Embo J* **18**, 3981-3989
9. Kispal, G., Sipos, K., Lange, H., Fekete, Z., Bedekovics, T., Janaky, T., Bassler, J., Aguilar Netz, D. J., Balk, J., Rotte, C., and Lill, R. (2005) *Embo J* **24**, 589-598
10. Braz, A. S., Finnegan, J., Waterhouse, P., and Margis, R. (2004) *J Mol Evol* **59**, 20-30
11. Zhao, Z., Fang, L. L., Johnsen, R., and Baillie, D. L. (2004) *Biochem Biophys Res Commun* **323**, 104-111
12. Yarunin, A., Panse, V. G., Petfalski, E., Dez, C., Tollervey, D., and Hurt, E. C. (2005) *Embo J* **24**, 580-588
13. Chen, Z. Q., Dong, J., Ishimura, A., Daar, I., Hinnebusch, A. G., and Dean, M. (2006) *J Biol Chem* **281**, 7452-7457
14. Karcher, A., Buttner, K., Martens, B., Jansen, R. P., and Hopfner, K. P. (2005) *Structure* **13**, 649-659
15. Bisbal, C., Martinand, C., Silhol, M., Lebleu, B., and Salehzada, T. (1995) *J Biol Chem* **270**, 13308-13317
16. Zimmerman, C., Klein, K. C., Kiser, P. K., Singh, A. R., Firestein, B. L., Riba, S. C., and Lingappa, J. R. (2002) *Nature* **415**, 88-92
17. Dong, J., Lai, R., Nielsen, K., Fekete, C. A., Qiu, H., and Hinnebusch, A. G. (2004) *J Biol Chem* **279**, 42157-42168
18. Albers, S. V., Jonuscheit, M., Dinkelaker, S., Urich, T., Kletzin, A., Tampé, R., Driessen, A. J., and Schleper, C. (2006) *Appl Environ Microbiol* **72**, 102-111
19. Jonuscheit, M., Martusewitsch, E., Stedman, K. M., and Schleper, C. (2003) *Mol Microbiol* **48**, 1241-1252
20. Schleper, C., Kubo, K., and Zillig, W. (1992) *Proc Natl Acad Sci U S A* **89**, 7645-7649
21. Martusewitsch, E., Sensen, C. W., and Schleper, C. (2000) *J Bacteriol* **182**, 2574-2581
22. Albers, S. V., Szabo, Z., and Driessen, A. J. (2003) *J Bacteriol* **185**, 3918-3925

23. Fish, W. W. (1988) *Methods Enzymol* **158**, 357-364
24. Beinert, H. (1983) *Anal Biochem* **131**, 373-378
25. Schünemann, V., and Winkler, H. (2000) *Rep Prog Phys* **63**, 263-353
26. Korbas, M., Marsa, D. F., and Meyer-Klaucke, W. (2006) *Rev Sci Instr* **77**, article number 063105
27. Korbas, M., Vogt, S., Meyer-Klaucke, W., Bill, E., Lyon, E. J., Thauer, R. K., and Shima, S. (2006) *J Biol Chem* **281**, 30804-30813
28. Hughes, J. D., Estep, P. W., Tavazoie, S., and Church, G. M. (2000) *J Mol Biol* **296**, 1205-1214
29. Khoroshilova, N., Beinert, H., and Kiley, P. J. (1995) *Proc Natl Acad Sci U S A* **92**, 2499-2503
30. Orme-Johnson, W. H., and Orme-Johnson, N. R. (1982) Iron-sulfur proteins. In: Spiro, R. G. (ed). *Iron-sulfur proteins*, Wiley, New York
31. Elsasser, C., Brecht, M., and Bittl, R. (2002) *J Am Chem Soc* **124**, 12606-12611
32. Agarwalla, S., Stroud, R. M., and Gaffney, B. J. (2004) *J Biol Chem* **279**, 34123-34129
33. Seemann, M., Wegner, P., Schunemann, V., Bui, B. T., Wolff, M., Marquet, A., Trautwein, A. X., and Rohmer, M. (2005) *J Biol Inorg Chem* **10**, 131-137
34. George, G. N., Prince, R. C., Stokley, K. E., and Adams, M. W. (1989) *Biochem J* **259**, 597-600
35. Stout, C. D. (2001) Ferredoxins containing two different Fe/S centers of the form [4Fe-4S] and [3Fe-4S]. In: Messerschmidt, A., Huber, R., Wieghardt, K., and Poulos, T. (eds). *Handbook of Metalloproteins*, Wiley, New York
36. Busch, J. L., Breton, J. L., Bartlett, B. M., Armstrong, F. A., James, R., and Thomson, A. J. (1997) *Biochem J* **323 (Pt 1)**, 95-102
37. Tilley, G. J., Camba, R., Burgess, B. K., and Armstrong, F. A. (2001) *Biochem J* **360**, 717-726
38. Emptage, M. H., Kent, T. A., Huynh, B. H., Rawlings, J., Orme-Johnson, W. H., and Munck, E. (1980) *J Biol Chem* **255**, 1793-1796
39. Moura, J. J., Moura, I., Kent, T. A., Lipscomb, J. D., Huynh, B. H., LeGall, J., Xavier, A. V., and Munck, E. (1982) *J Biol Chem* **257**, 6259-6267
40. Kuo, C. F., McRee, D. E., Fisher, C. L., O'Handley, S. F., Cunningham, R. P., and Tainer, J. A. (1992) *Science* **258**, 434-440
41. Porello, S. L., Cannon, M. J., and David, S. S. (1998) *Biochemistry* **37**, 6465-6475
42. Thayer, M. M., Ahern, H., Xing, D., Cunningham, R. P., and Tainer, J. A. (1995) *Embo J* **14**, 4108-4120
43. Hopfner, K. P., and Tainer, J. A. (2003) *Curr Opin Struct Biol* **13**, 249-255
44. Schmitt, L., and Tampé, R. (2002) *Curr Opin Struct Biol* **12**, 754-760
45. Janas, E., Hofacker, M., Chen, M., Gompf, S., van der Does, C., and Tampé, R. (2003) *J Biol Chem* **278**, 26862-26869
46. van der Does, C., and Tampé, R. (2004) *Biol Chem* **385**, 927-933

Table 1: Incorporation of iron and sulfur in ABCE1

TABLE 1

Iron and sulfur determination from ABCE1 (1 nmol)

	Iron [nmol]		Inorganic sulfur [nmol]	Total sulfur [nmol]
	Ferrozine	TXRF	Methylenblue	TXRF
WT (<i>S. solf.</i>)	7.2 ± 0.5	6.8 ± 0.3	6.1 ± 0.2	25.0 ± 0.6
WT (<i>E. coli</i>)	6.2 ± 0.2	6.0 ± 0.2	5.5 ± 0.1	21.8 ± 0.6
C54S (<i>E. coli</i>)	4.4 ± 0.1	n.d.	3.1 ± 0.1	n.d.
C24S (<i>E. coli</i>)	n.d.	0.4 ± 0.1	0.0 ± 0.0	12.1 ± 0.6

FIGURE LEGENDS

Fig. 1: Expression and purification of wildtype and ABCE1 mutants. Wt ABCE1 expressed in *S. solf.* (A) and wt ABCE1, C54S and C24S mutants heterologously expressed in *E. coli* (B) were purified under strictly anaerobic conditions via metal affinity chromatography and subsequently analyzed by SDS-PAGE (15%, Coomassie). 0.5-1 mg of ABCE1 was isolated per liter *S. solf.* culture, whereas the yield for the heterologous system was approx. 2 mg/l. (C) wt ABCE1 isolated from *S. solf.* (75 μ M) or from *E. coli* (35 μ M) as well as the C54S mutant (35 μ M) showed a brownish color, except for the C24S mutant (35 μ M).

Fig. 2: UV/VIS absorption spectroscopy of wildtype and ABCE1 mutants. (A) Spectra of wt ABCE1 isolated from *S. solf.* (black line) or from *E. coli* (red line) as well as the mutants C54S (green line) and C24S (orange line) were recorded in the buffer C. Wt ABCE1 isolated from *S. solf.* was incubated with the oxidant potassium ferricyanide (B) or the reductant sodium dithionite (C) at indicated concentrations for 2 min. All spectra were recorded at a protein concentrations of 50 μ M.

Fig. 3: EPR spectroscopy of wildtype ABCE1 and C54S mutant. (A) EPR spectra of wt ABCE1 purified from *S. solf.* (solid line) were recorded in buffer C before (solid line) and after oxidation with a 10-fold excess of ferricyanide (dotted line). The g-tensor principal values of oxidized ABCE1, g(1): 2.031, g(2): 2.017, g(3): 2.002 (error ± 0.002), extracted by numerical simulation (data not shown), are indicative for a $[3\text{Fe-4S}]^+$ cluster. (B) Spectra of wt ABCE1 reduced with 50-fold molar excess of sodium dithionite in 20 mM Tris, 100 mM NaCl, pH 9.0. (C) Spectra of the C54S mutant were recorded in buffer C before (solid line) and after oxidation with a 1:1 molar ratio of ferricyanide (dotted line). The g-tensor determined by numerical simulation (data not shown) yields principal values of: g(1): 2.033, g(2): 2.018, g(3): 2.002 (error ± 0.002). All spectra were recorded at 40 μ M protein concentration with the following parameters: microwave frequency, 9.424 GHz; microwave power, 8 mW, field modulation frequency, 100 kHz, field modulation depth, 5 Gauss (peak to peak); temperature 10 K.

Fig. 4: Mössbauer spectroscopy of ABCE1. Spectra of wt ABCE1 were recorded at 77 K in a zero magnetic field (A) and at 4.2 K in a field of 4 T perpendicular to the γ -beam (B). The solid lines represent simulations with the parameters given in the *Experimental Procedures*. Species 1 and 2, present at equimolar ratio (44% both), are diamagnetic and exhibit parameters typical for $[4\text{Fe-4S}]^{2+}$ clusters. Species 1: $\delta_1 = 0.43 \text{ mms}^{-1}$, $\Delta E_{Q1} = 1.32 \text{ mms}^{-1}$; Species 2: $\delta_2 = 0.42 \text{ mms}^{-1}$, $\Delta E_{Q2} = -0.86 \text{ mms}^{-1}$. Species 3 (12%) is characteristic for unspecific Fe^{3+} and has been disregarded in the simulations shown in (B). ABCE1 isolated from *S. solf.* was analyzed in buffer C at 1.2 mM in iron.

Fig. 5: X-ray absorption analysis of the Fe-S cluster in ABCE1. (A) Fe K-edge X-ray absorption spectra of wt ABCE1 (*S. solf.*) (B) Fe K-edge k^3 weighed EXAFS spectra and (C) the corresponding Fourier transformation. The EXAFS is dominated by two contributions, the Fe-4S signal at $2.29 \text{ \AA} \pm 0.01 \text{ \AA}$ and the Fe-3Fe signal at $2.74 \text{ \AA} \pm 0.01 \text{ \AA}$. The Debye-Waller factors ($2 \sigma^2$) for these contributions were refined to $0.010 \text{ \AA}^2 \pm 0.001 \text{ \AA}^2$ and $0.008 \text{ \AA}^2 \pm 0.001 \text{ \AA}^2$, respectively. EF was $-3 \text{ eV} \pm 1 \text{ eV}$. ABCE1 was analyzed in buffer C at an iron concentration of 1.2 mM.

Fig. 6: Functional analysis of ABCE1 in *S. cerevisiae*. Plasmids of ABCE1 harboring the indicated mutations were transformed into a yeast strain, in which the endogenous promoter was replaced by a tetracycline repressible promoter and plated on minimal agar using histidine as a selection marker. Single colonies were then spread on minimal agar plates containing doxycycline. The plasmid containing wt ABCE1 served as a positive control (wt), and the empty vector as a negative control (-K). (A) Mutation of the eight conserved cysteine residues to serine. (B) Single cysteine-to-alanine mutations of the viable mutants from the first screen, as well as the double mutant S28A/C29A. (C) Mutation of the extra cysteine residue C38 to alanine individually and in combination with selected conserved residues. Double and triple mutants of the viable mutants from the first screen are lethal.

Fig. 7: Model for the structural organization of the Fe-S cluster in ABCE1. (A) Consensus sequence of 8 Fe ferredoxins and the consensus sequence of Fe-S cluster in ABCE1 by comparison (B) Sequence alignment of the N-terminal Fe-S cluster domain of ABCE1 from archaeal and eukaryotic organisms generated by ClustalW: *Sulfolobus solfataricus* (gi:15897231), *Sulfolobus acidocaldarius* (gi:70606479), *Thermophilum pendens* (gi:119719130), *Pyrococcus furiosus* (gi:18977042), *Thermococcus kodakarensis* (gi:57640966), *Pyrococcus horikoshii* (gi:14590719), *Thermoplasma volcanium* (gi:13542329), *Methanococcus maripaludis* (gi:45357945), *Archaeoglobus fulgidus* (gi:11497625), *Halobacterium salinarum* (gi:15791346), *Guillardia theta* (gi:13811968), *Trypanosoma brucei* (gi:21212953), *Leishmania major* (gi:68223887), *Caenorhabditis elegans* (gi:17555800), *Dictyostelium discoideum* (gi:66803577), *Toxoplasma gondii* (gi:111145381), *Schizosaccharomyces pombe* (gi:19113524), *Saccharomyces cerevisiae* (gi:74676343), *Candida glabrata* (gi:50288565), *Kluyveromyces lactis* (gi:50306045), *Oryza sativa* (gi:115485837), *Triticum aestivum* (gi:16755057), *Arabidopsis thaliana* (gi:110742163), *Bombyx mori* (gi:112982681), *Drosophila melanogaster* (gi:24661270), *Xenopus laevis* (gi:28302203), *Danio rerio* (gi:63102477), *Gallus gallus* (gi:57530144), *Homo sapiens* (gi:987870). Essential cysteines are marked with an asterisk. Ligand swapping occurs between C29 and the extra C39, conserved among all eukaryotes. C58 is not essential, since this cluster is also functional in a [3Fe-4S] state.

Figure 1

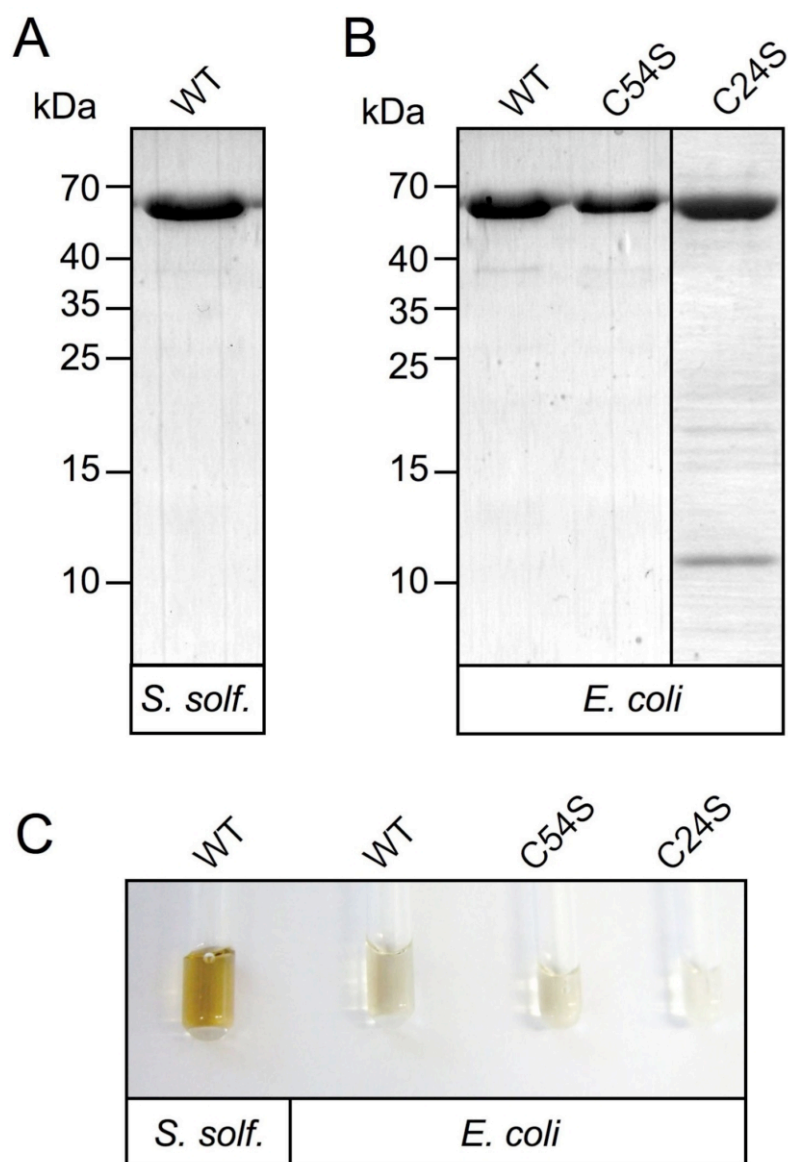


Figure 2:

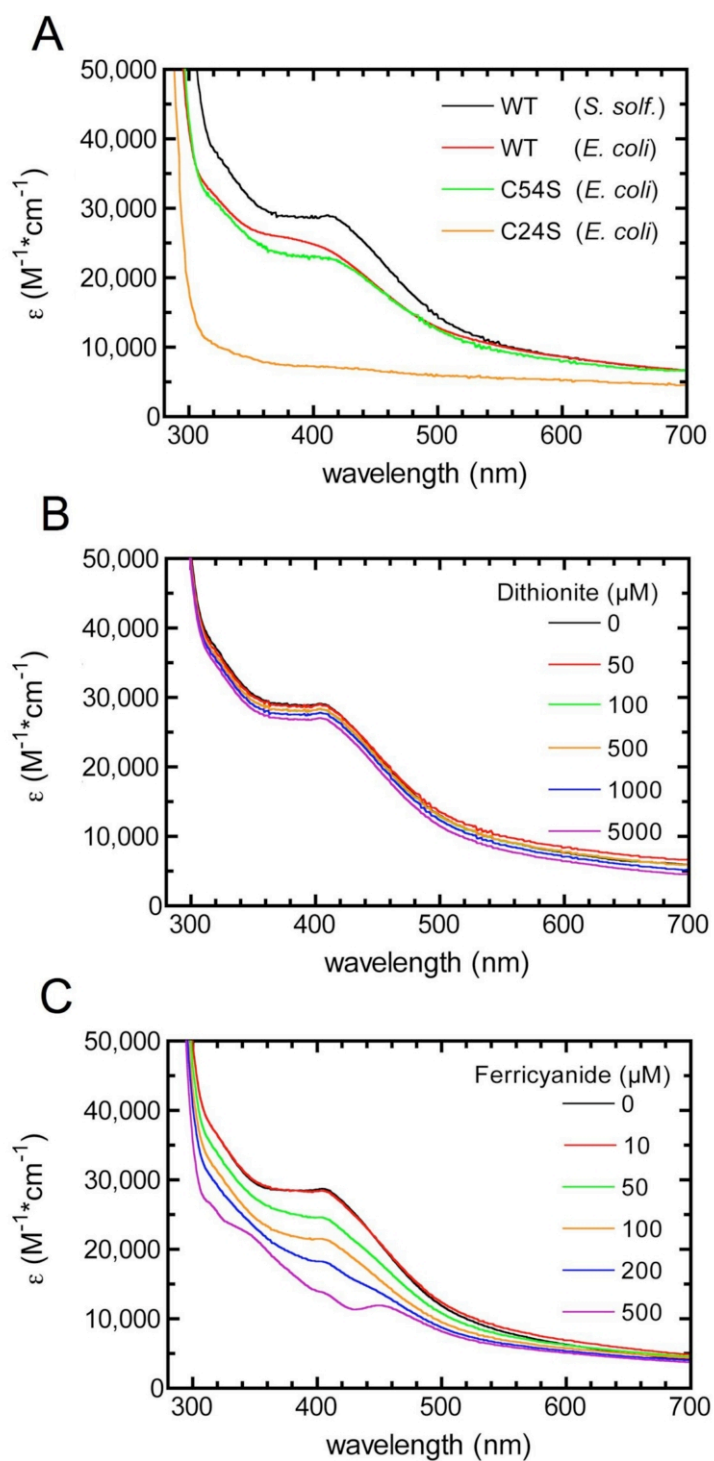


Figure 3:

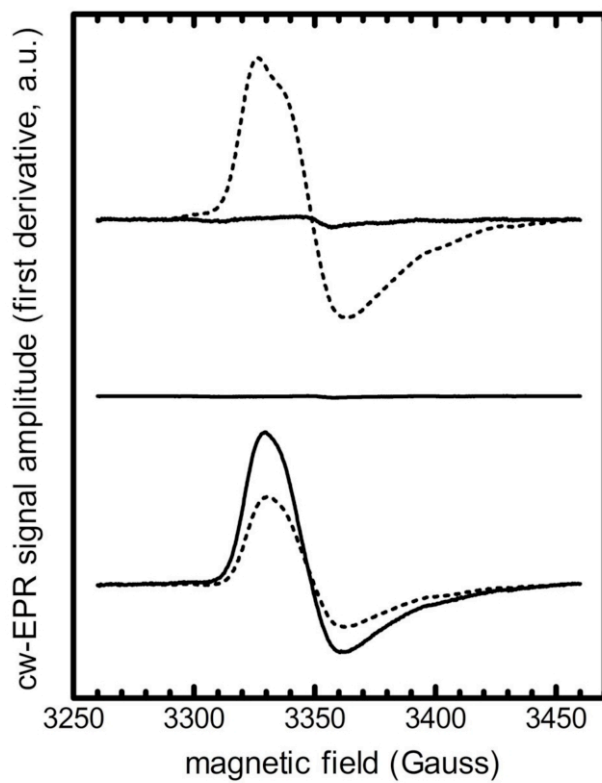


Figure 4:

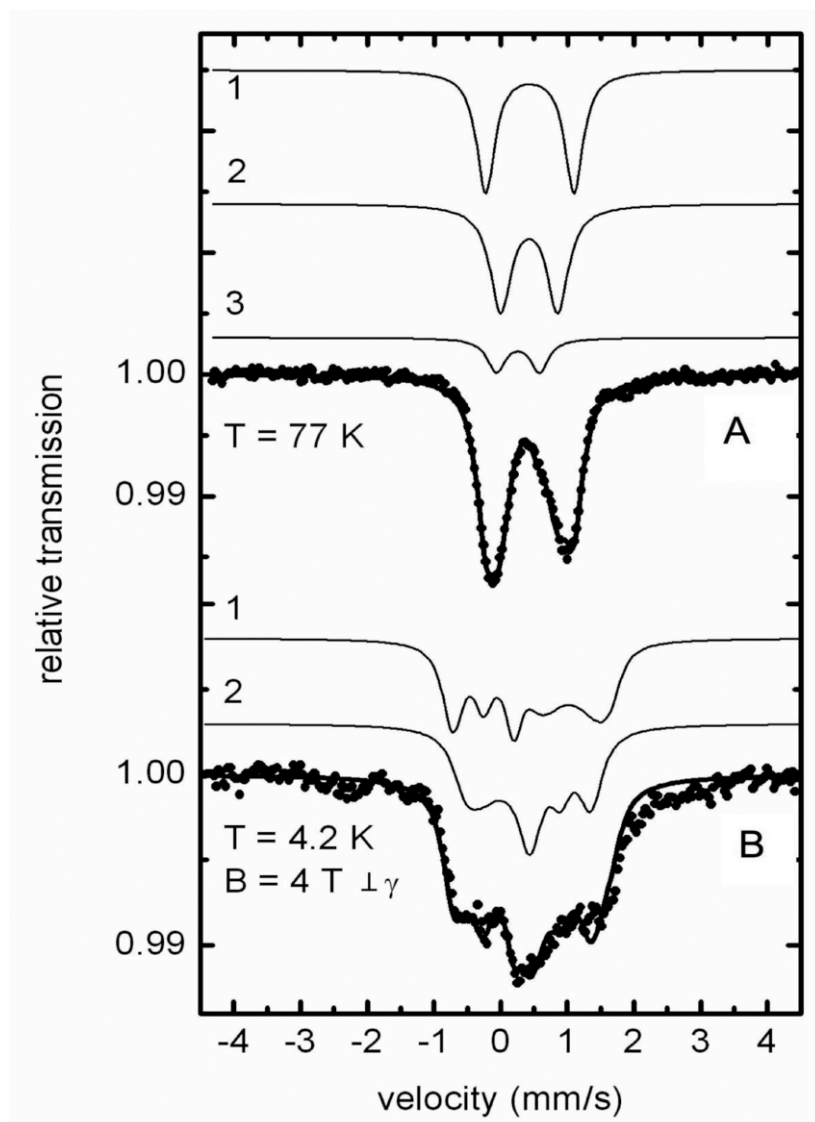


Figure 5:

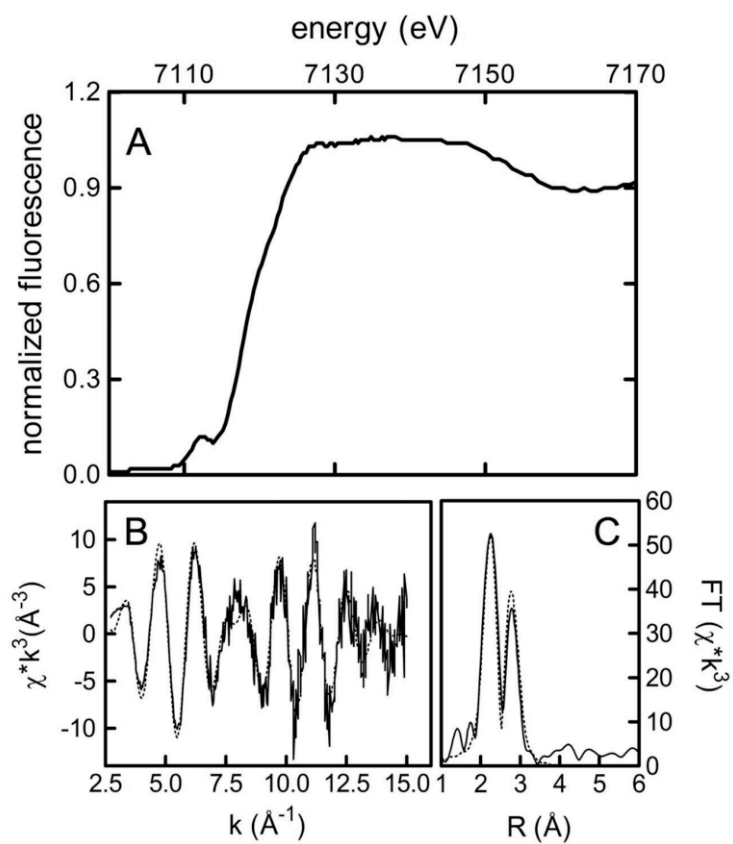
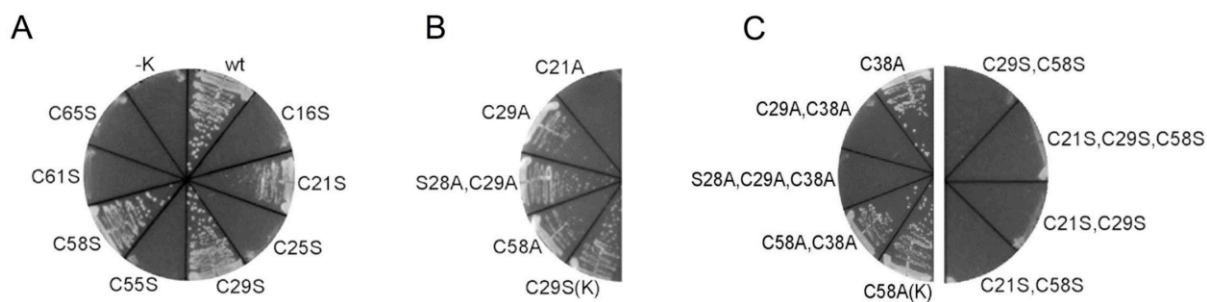


Figure 6:



D Overview-Mutation analysis in yeast

single mutants	double mutants		triple mutants
C16S non viable			
C21S/C21A viable/non viable	C21S, C29S non viable	C21S, C58S non viable	C21S, C29S, C58S non viable
C25S non viable			
S28A n.d.	C29S, C38A non viable	S28A, C29A viable	S28A, C29A, C38A non viable
C29S/C29A viable/viable			
C38A viable	C38A, C58A viable	C29S, C38A non viable	C29S, C38A non viable
C55S non viable			
C58S/C58A viable/viable	C58S, C58A viable	C58S, C58A viable	C58S, C58A viable
C61S non viable			
C65S non viable			



The Crystal Structure of [Fe]-Hydrogenase Reveals the Geometry of the Active Site

Seigo Shima, *et al.*
Science **321**, 572 (2008);
DOI: 10.1126/science.1158978

The following resources related to this article are available online at www.sciencemag.org (this information is current as of July 25, 2008):

Updated information and services, including high-resolution figures, can be found in the online version of this article at:

<http://www.sciencemag.org/cgi/content/full/321/5888/572>

Supporting Online Material can be found at:

<http://www.sciencemag.org/cgi/content/full/321/5888/572/DC1>

This article **cites 31 articles**, 3 of which can be accessed for free:

<http://www.sciencemag.org/cgi/content/full/321/5888/572#otherarticles>

This article appears in the following **subject collections**:

Biochemistry

<http://www.sciencemag.org/cgi/collection/biochem>

Information about obtaining **reprints** of this article or about obtaining **permission to reproduce this article** in whole or in part can be found at:

<http://www.sciencemag.org/about/permissions.dtl>

ined the binding of BiP with a DnaJ-domain mutant of ERdj5 in which histidine 63 in the HPD motif is replaced with glutamine (ERdj5/H63Q) (13). ERdj5/H63Q did not bind to BiP, even in the presence of ATP (Fig. 4A). Thus, ERdj5 interacts through its DnaJ domain with BiP.

We examined the *in vivo* effect of the ERdj5/H63Q mutant on HMW complex formation and on the ERAD of J chains. Accumulation of the J chain HMW complex was considerably decreased 48 hours after transfection with wild-type ERdj5 compared with amounts after mock transfection (Fig. 4B). In contrast, neither transfection with ERdj5/H63Q nor with the ERdj5/SS mutant repressed the accumulation of J chain HMW complexes. Transfection with the ERdj5/H63Q mutant did not accelerate J-chain degradation (Fig. 4C and fig. S3) even though this mutant retains the disulfide reductase activity (fig. S2). Thus, both the reductase activity of ERdj5, which is conferred by its CXXC motifs, and the association of ERdj5 with the molecular chaperone BiP are necessary to prevent multimer formation by the misfolded proteins and also to promote efficient ERAD of such proteins.

We next examined the involvement of ERdj5 in the EDEM-mediated ERAD pathway. EDEM coimmunoprecipitated with both wild-type ERdj5 and the ERdj5/AA mutant in HEK293 cells, which suggests that the binding of EDEM with ERdj5 is CXXC-independent (fig. S8). Acceleration of ERAD by EDEM overexpression is dependent on mannose-trimming and is inhibited by kifunensine, an inhibitor of ER mannosidase I (3). Promotion of ERAD by ERdj5 overexpression was totally abolished in the presence of kifunensine (Fig. 4D), which suggests that ERdj5-mediated ERAD requires EDEM to function.

Thus, ERdj5, either overexpressed or endogenous, can serve as a key component for the ERAD of misfolded proteins. The following are all required for ERdj5-mediated ERAD acceleration: (i) the reductase activity of ERdj5, which is conveyed through its CXXC motif; (ii) the binding of ERdj5, through its DnaJ domain, to the ER-resident Hsp70 family chaperone BiP; and (iii) the functional interaction of ERdj5 with EDEM, a lectin-like molecule that may recognize the Man₈ N-glycan on misfolded proteins to be degraded. ERdj5-mediated cleavage of intermolecular disulfide bridges decreased the accumulation of covalent multimeric forms of misfolded proteins in the ER; such accumulations are expected to hinder the retrograde transport of misfolded proteins through the retrotranslocation channel. ERdj5 may prevent disulfide-linked aggregation and/or misfolding of substrates by maintaining them in reduced states and may enhance their ERAD by increasing retrotranslocation-competent misfolded proteins.

The redox potential of ERdj5 is even more reducing than the ER redox status (16) or the redox potential of PDI (17). ERdj5 has three CXPC motifs, consistent with reports that the redox potential of CXPC motifs contained in thioredoxin superfamily proteins is reducing (18). Its reducing redox potential indicates that ERdj5 is thermodynamically stable in

an oxidized form in the ER redox environment and that ERdj5 can function as a strong disulfide reductase once it accepts electrons from electron donors. Electrons might be transported into the ER from the reducing cytosol or provided from the high ER concentration of the reduced form of nicotinamide adenine dinucleotide phosphate (NADPH) (19). These possibilities remain to be addressed.

Here, we have established the presence of a supramolecular functional ERAD complex, comprising EDEM, ERdj5, and BiP, which have distinct, but linked and concerted, roles (fig. S9). In this model, after the transfer of terminally misfolded proteins from calnexin to EDEM, ERdj5 bound to EDEM cleaves their disulfide bonds, which results in dissociation of the covalent multimeric substrates. At the same time, ERdj5 activates the conversion of the ATP-form of BiP to adenosine diphosphate form, resulting in dissociation of BiP from ERdj5, which, in turn, strongly binds the substrates (20) and holds them in a dislocation-competent state until they are transferred to the retrotranslocation channel.

References and Notes

1. L. Ellgaard, A. Helenius, *Nat. Rev. Mol. Cell Biol.* **4**, 181 (2003).
2. K. Kanehara, S. Kawaguchi, D. T. Ng, *Semin. Cell Dev. Biol.* **18**, 743 (2007).
3. N. Hosokawa *et al.*, *EMBO Rep.* **2**, 415 (2001).
4. Y. Oda, N. Hosokawa, I. Wada, K. Nagata, *Science* **299**, 1394 (2003).
5. M. Molinari, V. Calanca, C. Galli, P. Lucca, P. Paganetti, *Science* **299**, 1397 (2003).

6. Y. Oda *et al.*, *J. Cell Biol.* **172**, 383 (2006).
7. N. Hosokawa, I. Wada, Y. Natsuka, K. Nagata, *Genes Cells* **11**, 465 (2006).
8. A. Mezghrani *et al.*, *EMBO J.* **20**, 6288 (2001).
9. D. Tortorella *et al.*, *J. Cell Biol.* **142**, 365 (1998).
10. Materials and methods are available as supporting material on Science Online.
11. S. Pollock *et al.*, *EMBO J.* **23**, 1020 (2004).
12. P. M. Cunnea *et al.*, *J. Biol. Chem.* **278**, 1059 (2003).
13. A. Hosoda, Y. Kimata, A. Tsuru, K. Kohno, *J. Biol. Chem.* **278**, 2669 (2003).
14. Y. Shen, L. M. Hendershot, *Mol. Biol. Cell* **16**, 40 (2005).
15. L. Ellgaard, L. W. Ruddock, *EMBO Rep.* **6**, 28 (2005).
16. C. Hwang, A. J. Sinskey, H. F. Lodish, *Science* **257**, 1496 (1992).
17. N. J. Darby, T. E. Creighton, *Biochemistry* **34**, 16770 (1995).
18. G. Roos *et al.*, *J. Mol. Biol.* **368**, 800 (2007).
19. S. Picciarella *et al.*, *J. Biol. Chem.* **281**, 4671 (2006).
20. K. Liberek, D. Skowrya, M. Zyliz, C. Johnson, C. Georgopoulos, *J. Biol. Chem.* **266**, 14491 (1991).
21. We thank N. Hosokawa for providing NHK and the EDEM protein plasmids. We also thank R. I. Morimoto and K. Inaba for critical discussions and advice. This work was supported by Grants-in-Aid for Creative Scientific Research (19G50314) and Scientific Research (19058008) (to K.N.) and the Canadian Institutes of Health Research (to D.Y.T.). R.U. was supported by a fellowship from the Japan Society for the Promotion of Science.

Supporting Online Material

www.sciencemag.org/cgi/content/full/321/5888/569/DC1
Materials and Methods
Figs. S1 to S9
References

18 April 2008; accepted 12 June 2008
10.1126/science.1159293

The Crystal Structure of [Fe]-Hydrogenase Reveals the Geometry of the Active Site

Seigo Shima,^{1*†} Oliver Pilak,^{1*} Sonja Vogt,¹ Michael Schick,¹ Marco S. Stagni,² Wolfram Meyer-Klaucke,² Eberhard Warkentin,³ Rudolf K. Thauer,¹ Ulrich Ermler^{3†}

Biological formation and consumption of molecular hydrogen (H₂) are catalyzed by hydrogenases, of which three phylogenetically unrelated types are known: [NiFe]-hydrogenases, [FeFe]-hydrogenases, and [Fe]-hydrogenase. We present a crystal structure of [Fe]-hydrogenase at 1.75 angstrom resolution, showing a mononuclear iron coordinated by the sulfur of cysteine 176, two carbon monoxide (CO) molecules, and the sp²-hybridized nitrogen of a 2-pyridinol compound with back-bonding properties similar to those of cyanide. The three-dimensional arrangement of the ligands is similar to that of thiolate, CO, and cyanide ligated to the low-spin iron in binuclear [NiFe]- and [FeFe]-hydrogenases, although the enzymes have evolved independently and the CO and cyanide ligands are not found in any other metalloenzyme. The related iron ligation pattern of hydrogenases exemplifies convergent evolution and presumably plays an essential role in H₂ activation. This finding may stimulate the ongoing synthesis of catalysts that could substitute for platinum in applications such as fuel cells.

Molecular hydrogen (H₂) is a relatively inert molecule. The dissociation energy of the H-H bond is 436 kJ mol⁻¹, and its pK_a is 35 (1, 2). Despite this, H₂ is used or produced by many microorganisms in their energy metabolism. Indeed, H₂ was one of the earliest energy sources available on Earth when life evolved. H₂/H⁺ interconversion reactions (H₂ ⇌ 2H⁺ + 2e⁻) are catalyzed by hydrogenases that contain nickel and/or iron as key components in

their active sites; these hydrogenases are more efficient catalysts than platinum, which is used industrially to catalyze hydrogenation. H₂ is considered a major fuel in future energy technology, but the amounts of catalyst required for large-scale H₂ production and use will require alternatives to platinum, which is expensive and not abundant. One approach of current research is to learn from hydrogenases (Fig. 1), and model compounds mimicking the metal centers of hydro-

genase have recently been synthesized that can interact with protons and/or H_2 (3–7).

The most prominent hydrogenases are [NiFe]-hydrogenase (in bacteria and archaea) and [FeFe]-hydrogenase (in bacteria and eukaryotes) (8). The structures of their binuclear metal active sites are pictured in Fig. 1, A and B (9–17). In addition to the binuclear metal center, both types of hydrogenases harbor at least one essential [4Fe-4S] cluster. The iron in the binuclear [NiFe] center (Fig. 1A) is redox-inactive and low-spin (18), as probably is the iron proximal to the [4Fe-4S] cluster in the binuclear [FeFe] center (19) (Fig. 1B). The third type of hydrogenases, the [Fe]-hydrogenase—formerly named iron-sulfur cluster-free hydrogenase or H_2 -forming methylenetetrahydromethanopterin (methylene- H_4 MPT) dehydrogenase (20)—contains a mononuclear iron center (Fig. 1C) and is found only in some hydrogenotrophic methanogenic archaea, where it catalyzes one step involved in CO_2 reduction to methane (Fig. 2). Each subunit of the homodimeric enzyme contains one iron (which is not redox-active) and no iron-sulfur clusters.

In [Fe]-hydrogenase, the iron center is the catalytically active constituent of an iron guanylyl pyridone cofactor (FeGP cofactor), which can be extracted from the enzyme by denaturation in the presence of mercaptoethanol and used for reconstitution of the active enzyme from inactive heterologously produced apoenzyme (21). The FeGP cofactor is light- and temperature-sensitive (22), which hampers purification to homogeneity. Observed decomposition products are guanylyl pyridone (see below), two CO molecules, and one iron ion (23). Infrared (IR) spectroscopic analysis (24) revealed two CO molecules as iron ligands; x-ray absorption analysis (25) predicted two CO, one sulfur, and one or two N/O ligands at coordination distance to iron; Mössbauer spectroscopic data (26) identified the iron as low spin, either in the Fe(0) or Fe(II) oxidation state; and x-ray structure analysis of the [Fe]-hydrogenase without the FeGP cofactor (apoenzyme) established the overall architecture of the enzyme (27) (Fig. 3). Here, we describe the structure of the [Fe]-hydrogenase–FeGP complex (holoenzyme) at 1.75 Å resolution (Fig. 3A) (28). This allows a detailed three-dimensional view of the structure and binding of the intact FeGP cofactor—the site of H_2 activation—and thereby integrates previous biochemical and biophysical data into a comprehensive and consistent picture.

To elucidate the holoenzyme structure, we reconstituted the heterologously produced apoen-

zyme of *Methanocaldococcus jannaschii* with the labile FeGP cofactor under completely anaerobic and red-light conditions and crystallized the reconstituted enzyme. The crystal structure of [Fe]-hydrogenase contains the FeGP cofactor with a high occupancy embedded in front of the C-terminal end of the parallel β sheet of both Rossmann fold-like peripheral units and capped by an α -helical subdomain (Fig. 3). The specific amino acid residues involved in binding of the FeGP cofactor

to the enzyme are shown in fig. S1. The guanosine monophosphate moiety functions to anchor the FeGP cofactor, and its binding mode essentially corresponds to the adenosine monophosphate moiety of dinucleotide binding proteins (Fig. 4). The catalytically relevant iron-center moiety is located close to the intersubunit clefts (Fig. 3) and consists of a mononuclear iron atom surrounded by a distorted square pyramidal or an octahedral ligation shell dependent on the enzymatic state (Fig. 5).

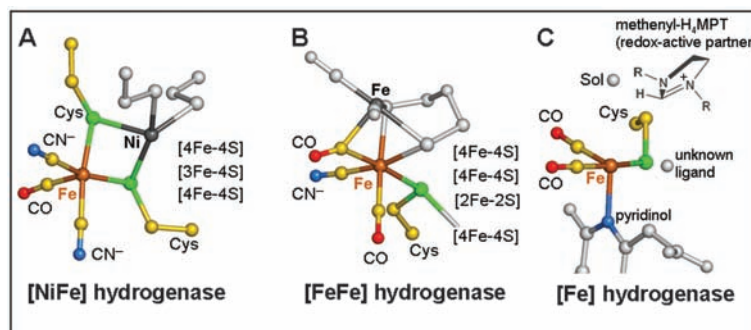


Fig. 1. Superimposed active-site structure of the three phylogenetically unrelated hydrogenases. (A) [NiFe]-hydrogenase from *Desulfovibrio gigas* (9, 12). (B) [FeFe]-hydrogenase from *Clostridium pasteurianum* (13) and *Desulfovibrio desulfuricans* (14, 16). (C) [Fe]-hydrogenase from *Methanocaldococcus jannaschii* (this work). In [Fe]-hydrogenase, the fifth and sixth ligation sites are marked by gray spheres. All three hydrogenase types have in common a low-spin iron (brown) ligated by thiolate(s), CO, and cyanide or pyridinol (considered as cyanide functional analog), which acts together with a redox-active partner (dark gray). The partners—Ni, the distal iron, and methenyl- H_4 MPT⁺ (modeled), respectively—take over the electrons or the hydride and perhaps play a role in the heterolytic cleavage of H_2 .

Fig. 2. Reaction catalyzed by [Fe]-hydrogenase in methanogenic archaea. The heterolytic cleavage of H_2 by the enzyme is dependent on the presence of methenyl- H_4 MPT⁺, whose methenyl C14a has carbocation character and is therefore an excellent hydride acceptor. H_4 MPT, tetrahydromethanopterin.

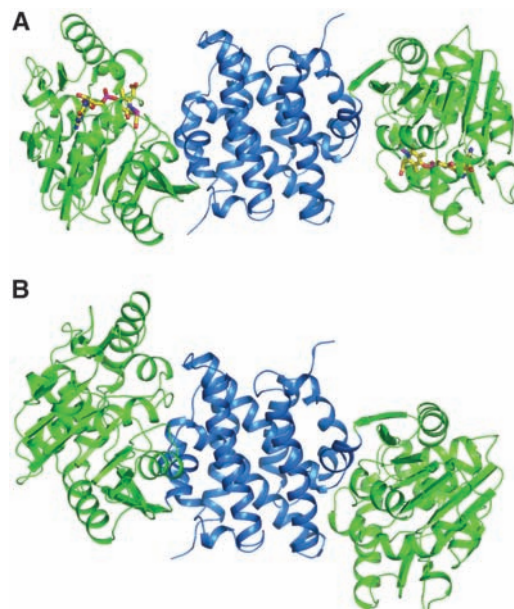
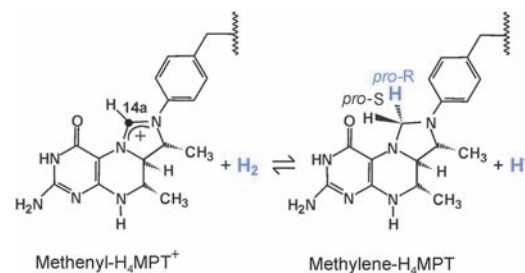


Fig. 3. Ribbon diagrams of the [Fe]-hydrogenase of *M. jannaschii*. The homodimeric enzyme is composed of three folding units. The two peripheral units (N-terminal segments) consist of a Rossmann fold-like domain (green) which can be further subdivided into a classical Rossmann fold, an extension ($\beta\alpha\beta$), and an α -helical insertion region. The unique central unit (in blue) constitutes an intertwined helix bundle formed by the C-terminal segments of both subunits (27). The structure of the holoenzyme (A) is in an open conformation and that of the apoenzyme (B) is in a closed conformation with respect to the cleft between the central and the peripheral units (27). The rotation angle between the states is 37°. The FeGP cofactor is bound to the peripheral units and is depicted as a color-coded stick model.

¹Max-Planck-Institut für Terrestrische Mikrobiologie und Laboratorium für Mikrobiologie, Fachbereich Biologie, Philipps-Universität Marburg, Karl-von-Frisch-Straße, D-35043 Marburg, Germany. ²EMBL Hamburg, Notkestr. 85, D-22603 Hamburg, Germany. ³Max-Planck-Institut für Biophysik, Max-von-Laue-Straße 3, D-60438 Frankfurt/Main, Germany.

*These authors contributed equally to this work.

†To whom correspondence should be addressed. E-mail: ulermier@mpibp-frankfurt.mpg.de; shima@mpi-marburg.mpg.de

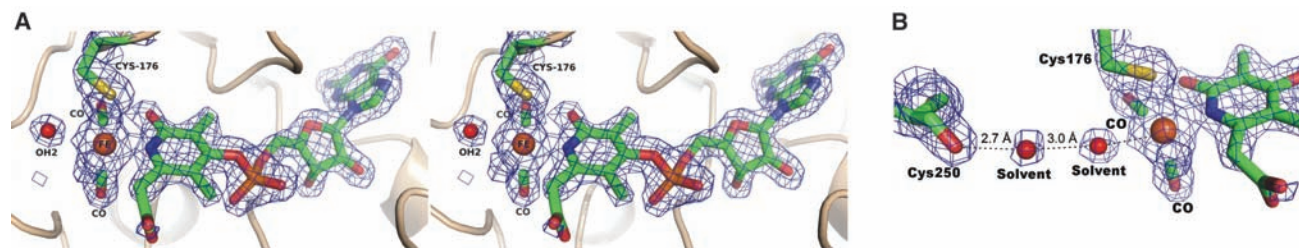


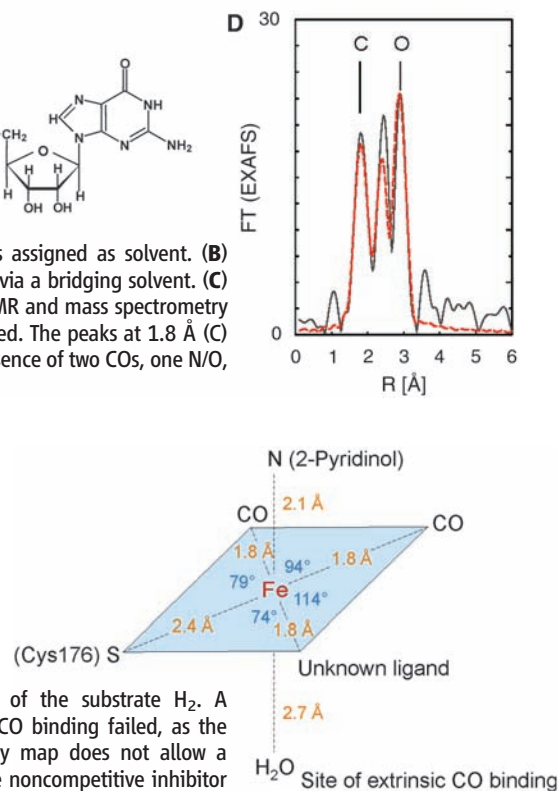
Fig. 4. The FeGP cofactor. **(A)** Stereoview of electron density (in blue) ($\sigma = 1.2$) of the FeGP cofactor bound to [Fe]-hydrogenase. The density fits almost perfectly (from right to left) to a guanine, a ribofuranose, a phosphate, and a pyridinol (with its carboxymethyl and two methyl substituents), which are covalently connected with each other via a β -N-glycosidic bond and a phosphodiester bond, respectively. The pyridinol nitrogen, two diatomic ligands, most certainly CO, the sulfur of Cys¹⁷⁶, and an unknown ligand have been identified as iron ligands. A spherical electron density 2.7 Å apart from the iron was assigned as solvent. **(B)** Electron density map of the solvent close to the iron that interacts with the carbonyl of Cys²⁵⁰ via a bridging solvent. **(C)** The structure of the guanylylpyridone (in its 2-pyridinol tautomeric form) as determined by NMR and mass spectrometry in the enzyme-free state (23). **(D)** Fourier-transformed EXAFS of [Fe]-hydrogenase as crystallized. The peaks at 1.8 Å (C) and 2.9 Å (O) are dominated by the CO contribution. The fit is, at best, compatible with the presence of two COs, one N/O, one S ligand, and of another not fully occupied first-shell ligand (see table S1).

One iron ligand is the pyridinol nitrogen atom, which links the organic guanylylpyridinol molecule with the iron center (Fig. 4). The hydroxylate and carboxylate substituents of pyridinol are not used as iron ligands, although the latter is partly disordered and must be analyzed with caution. Because of its planarity, the heterocyclic ring is present in a pyridinol and not in a pyridone tautomeric form (Fig. 4C), and therefore the nitrogen atom is in a π -accepting sp^2 configuration. The pyridinol group—in particular, if the hydroxyl group is in a deprotonated state—might have ligand back-bonding properties similar to those of cyanide (29, 30), which acts as an iron ligand in the [NiFe]- and [FeFe]-hydrogenases. Further ligands are two CO molecules that are optimally accommodated between several nonpolar atoms of the polypeptide chain. The CO molecules form an angle of 90°, in agreement with the interpretation of the IR spectrum of the holoenzyme (24). The sole proteinaceous ligand originates from the thiolate sulfur of Cys¹⁷⁶ that points toward the iron from a loop following strand 169:174 at the bottom of the intersubunit cleft.

The chemical nature of the fifth ligand is unknown, and its electron density cannot definitely be assigned as a monatomic or diatomic ligand, although it is clearly connected with that of the iron and of relatively high occupancy (i.e., corresponds to a completely occupied water molecule). The electron density ($\sigma = 1.2$) at the position of the unknown ligand (fig. S2) is increased (by a factor of 1.6) after soaking of the crystals with 3 mM cyanide, which suggests that this is the binding site of the reversible and noncompetitive inhibitor cyanide (22).

The vacant sixth coordination site of the iron contains a spherical electron density interpreted as a monatomic solvent molecule (i.e., a completely occupied water molecule) that is, however,

Fig. 5. Coordination of the iron in the active site of [Fe]-hydrogenase. The iron sits in the plane of the square spanned by the Cys¹⁷⁶ sulfur, two COs, and the unknown ligand; the nitrogen is at the top of the pyramid. The sixth ligation site trans to the pyridinol nitrogen is presumably the binding site of the competitive inhibitor CO (according to IR spectroscopy data) and of the substrate H₂. A structural confirmation of the extrinsic CO binding failed, as the quality of the resulting electron density map does not allow a distinction between a water and CO. The noncompetitive inhibitor cyanide presumably occupies the binding site of the unknown ligand as derived from x -ray crystallographic studies (fig. S2). Note that the iron, one of the intrinsic COs, the unknown ligand (or the cyanide), and probably the extrinsic CO are located in the plane of the pyridinol ring. The distances and angles between the irons and ligands are drawn in, except for those between the four ligands in the plane and the pyridinol's nitrogen and the nearby solvent assigned as water [N/S, 86°; N/CO (left), 102°; N/CO (right), 91°; N/cyanide, 94°; H₂O/S, 90°; H₂O/CO (left), 72°; H₂O/CO (right), 91°; H₂O/cyanide, 90°]. The distances between iron and the four identifiable ligands agree well with those determined in parallel by EXAFS spectroscopy (Fig. 4C and table S1).



at a distance of 2.7 Å too far away to be considered as a ligand (Fig. 4). We predict this site to be the binding position of extrinsic CO (Fig. 5) known to inhibit [Fe]-hydrogenase, as the Fourier-transformed IR spectrum of the CO inhibited enzyme predicts a perpendicular orientation of the extrinsic CO relative to the two intrinsic COs (24). Because CO is a competitive inhibitor with respect to H₂, the latter most likely also binds to this site (Figs. 1 and 5). The solvent close to the iron interacts with a second solvent molecule, which in turn is linked to the carbonyl group of the strictly conserved Cys²⁵⁰ (Fig. 4A). Interestingly, the Cys²⁵⁰ → Ala mutant shows reduced enzyme activity (table S2).

A comparison of the active-site metal centers of the three hydrogenase types reveals unexpected common features (Fig. 1) previously recognized for the two binuclear hydrogenases. All three types

contain a redox-inactive low-spin iron, presumably in the oxidation state II, that is asymmetrically ligated by five or six ligands arranged as a distorted square pyramid or octahedron. Moreover, three π -accepting ligands comprising CO, cyanide, or pyridinol (considered as a cyanide functional analog) are oriented perpendicular to each other in a geometrically related manner, and a thiolate sulfur always coordinates the iron trans to a diatomic molecule (Fig. 1). All three iron centers act together with a redox-active partner—methenyl-H₄MPT⁺ in the case of [Fe]-hydrogenase, the distal iron in the case of [FeFe]-hydrogenase, and nickel in the case of [NiFe] hydrogenase—whose spatial position relative to the other ligands is also similar. Apparently, these related iron centers, with unusual nonproteinaceous ligands thought to be synthesized by three different enzymatic machineries (31) and embedded into three architecturally different hydro-

genase structures, evolved independently. Remarkably, hydrogenases are the only metalloenzymes that use toxic CO and cyanide (or pyridinol) as metal ligands. Thus, hydrogenases are an impressive example of convergent evolutionary development as a consequence of specific biological and/or chemical restraints. However, the intrinsic physicochemical properties of the unique iron ligation pattern are not yet understood, nor are their implications for the technologically important H₂ activation reaction.

Despite the related low-spin iron centers, the enzymatic mechanism of [Fe]-hydrogenase differs fundamentally from that of the other types because of the different nature of the redox-active partner and the accompanying electron delivery mode. In [NiFe]- and [FeFe]-hydrogenases, the electrons of H₂ reduction flow one by one through the redox-active metals and several iron-sulfur clusters over a large distance to an electron acceptor. The active-site structures essentially remain fixed during H₂ cleavage, and H₂ reaches the deeply buried active site by a long diffusion channel. In [Fe]-hydrogenase, however, the found ternary reaction mechanism and the exchange between H₂ and protons of water solely in the presence of methenyl-H₄MPT⁺ (32) (see partial structure in Fig. 2) suggests that methenyl-H₄MPT⁺ directly accepts the hydride from H₂. This conclusion is supported by the x-ray structure, as the cleft between the peripheral and central units can accommodate the bulky methenyl-H₄MPT⁺ molecule and the C14a atom can be positioned sufficiently close to the iron without causing severe clashes with the polypeptide chain (fig. S3). Because the intersubunit cleft in the holoenzyme is, in fact, too large for an optimal methenyl-H₄MPT⁺ adjustment, we assume that its binding is accompanied by an induced-fit movement constituting the catalysis-competent active-site before each turnover. The expected large-scale conformational changes are reflected in the different positions of the peripheral unit relative to the central unit found in the structures of the holo- and apoenzymes (Fig. 3), mainly induced by crystal forces. H₂ can readily reach the solvent-exposed Fe center, which is probably encapsulated upon methenyl-H₄MPT⁺ binding.

The most attractive hypothesis for the mechanism of H₂ cleavage in [Fe]-hydrogenases is based on a concerted action of the strong hydride acceptor methenyl-H₄MPT⁺ and the Lewis acid Fe(II) that lowers the pK_a value of H₂, preferably when bound in a side-on conformation. The polarized H₂ ligated to the postulated binding site (Fig. 5) is attacked from the adjacent carbocation C14a of methenyl-H₄MPT⁺ from the *Re*-face of the ring system (see Fig. 2), generating methylene-H₄MPT. Acceptors for the released proton within 6.5 Å from the iron include the Cys¹⁷⁶ thiolate ligand, the pyridinol nitrogen, oxygen, and carboxyl oxygen as well as two conserved histidines, His¹⁴ and His²⁰¹ (for the position of the two histidines relative to the iron, see fig. S1B). A His¹⁴ → Ala mutation drastically reduces the hydrogenase activity of the enzyme, whereas His²⁰¹ → Ala has only a minor effect (table S2).

Although there are still many questions to be answered, the crystal structure allows us to draw the following conclusions: (i) The active-site iron is definitely mononuclear, not dinuclear as in the [FeFe]- and [NiFe]-hydrogenases. (ii) The presented structural data, together with results of studies using various spectroscopic methods [nuclear magnetic resonance (NMR), mass, IR, Mössbauer, and extended x-ray absorption fine structure (EXAFS) (23–26)] and information from mutational analysis (25), converge to a coherent result. (iii) The structures of the [Fe]-, [FeFe]-, and [NiFe]-hydrogenases are completely different but share features in their active site that can only have evolved convergently (Fig. 1). (iv) The detailed three-dimensional structure will allow density functional theory (DFT) calculations of energy profiles, which will help to exclude some of the proposed mechanisms of H₂ activation. (v) Model complexes can be constructed on the basis of the iron center of [Fe]-hydrogenase, and their analysis will provide further insight into its essential but not yet understood function in H₂ activation (3–7).

References and Notes

1. D. M. Heinekey, W. J. Oldham, *Chem. Rev.* **93**, 913 (1993).
2. G. J. Kubas, *Catal. Lett.* **104**, 79 (2005).
3. C. Tard *et al.*, *Nature* **433**, 610 (2005).
4. T. Liu, M. Y. Darensbourg, *J. Am. Chem. Soc.* **129**, 7008 (2007).
5. A. K. Justice *et al.*, *Inorg. Chem.* **46**, 1655 (2007).
6. S. Ogo *et al.*, *Science* **316**, 585 (2007).
7. X. Hu, B. S. Brunswig, J. C. Peters, *J. Am. Chem. Soc.* **129**, 8988 (2007).
8. P. M. Vignais, B. Billoud, J. Meyer, *FEMS Microbiol. Rev.* **25**, 455 (2001).
9. A. Volbeda *et al.*, *Nature* **373**, 580 (1995).
10. E. Garcin *et al.*, *Structure* **7**, 557 (1999).
11. H. Ogata *et al.*, *J. Am. Chem. Soc.* **124**, 11628 (2002).
12. A. Volbeda *et al.*, *J. Biol. Inorg. Chem.* **10**, 239 (2005).
13. J. W. Peters, W. N. Lanzilotta, B. J. Lemon, L. C. Seefeldt, *Science* **282**, 1853 (1998).

14. Y. Nicolet, C. Piras, P. Legrand, C. E. Hatchikian, J. C. Fontecilla-Camps, *Structure* **7**, 13 (1999).
15. B. J. Lemon, J. W. Peters, *Biochemistry* **38**, 12969 (1999).
16. Y. Nicolet *et al.*, *J. Am. Chem. Soc.* **123**, 1596 (2001).
17. Z. Chen *et al.*, *Biochemistry* **41**, 2036 (2002).
18. M. Frey, *ChemBioChem* **3**, 153 (2002).
19. A. Silakov, E. J. Reijerse, S. P. J. Albracht, E. C. Hatchikian, W. Lubitz, *J. Am. Chem. Soc.* **129**, 11447 (2007).
20. S. Shima, R. K. Thauer, *Chem. Rec.* **7**, 37 (2007).
21. G. Buurman, S. Shima, R. K. Thauer, *FEBS Lett.* **485**, 200 (2000).
22. E. J. Lyon *et al.*, *Eur. J. Biochem.* **271**, 195 (2004).
23. S. Shima *et al.*, *Angew. Chem. Int. Ed.* **43**, 2547 (2004).
24. E. J. Lyon *et al.*, *J. Am. Chem. Soc.* **126**, 14239 (2004).
25. M. Korbas *et al.*, *J. Biol. Chem.* **281**, 30804 (2006).
26. S. Shima, E. J. Lyon, R. K. Thauer, B. Mienert, B. Bill, *J. Am. Chem. Soc.* **127**, 10430 (2005).
27. O. Pilak *et al.*, *J. Mol. Biol.* **358**, 798 (2006).
28. See supporting material on Science Online.
29. J. M. Rawson, R. E. P. Wimpenny, *Coord. Chem. Rev.* **139**, 313 (1995).
30. S. Wolfe, N. Weinberg, Y. Hsieh, *Theor. Chem. Acc.* **118**, 265 (2007).
31. A. Böck, P. W. King, M. Blokesch, M. C. Posewitz, *Adv. Microb. Physiol.* **51**, 1 (2006).
32. S. Vogt, E. J. Lyon, S. Shima, R. K. Thauer, *J. Biol. Inorg. Chem.* **13**, 97 (2008).
33. Supported by the Max Planck Society, the Fonds der Chemischen Industrie, and the Bundesministerium für Bildung und Forschung (BioH₂ project). We thank H. Michel for continuous support, and the staff of beamline PXII at the Swiss Light Source for help during data collection. Coordinates of [Fe]-hydrogenase and [Fe]-hydrogenase complexed with cyanide have been deposited in the Research Collaboratory for Structural Bioinformatics Protein Data Bank under accession codes 3DAG and 3DAF.

Supporting Online Material

www.sciencemag.org/cgi/content/full/321/5888/572/DC1
Materials and Methods
Figs. S1 to S3
Tables S1 to S3
References

10 April 2008; accepted 5 June 2008
10.1126/science.1158978

Manipulating the Metazoan Mitochondrial Genome with Targeted Restriction Enzymes

Hong Xu, Steven Z. DeLuca, Patrick H. O'Farrell*

High copy number and random segregation confound genetic analysis of the mitochondrial genome. We developed an efficient selection for heritable mitochondrial genome (mtDNA) mutations in *Drosophila*, thereby enhancing a metazoan model for study of mitochondrial genetics and mutations causing human mitochondrial disease. Targeting a restriction enzyme to mitochondria in the germline compromised fertility, but escaper progeny carried homoplasmic mtDNA mutations lacking the cleavage site. Among mutations eliminating a site in the cytochrome c oxidase gene, *mt:Col^{A302T}* was healthy, *mt:Col^{R301L}* was male sterile but otherwise healthy, and *mt:Col^{R301S}* exhibited a wide range of defects, including growth retardation, neurodegeneration, muscular atrophy, male sterility, and reduced life span. Thus, germline expression of mitochondrial restriction enzymes creates a powerful selection and has allowed direct isolation of mitochondrial mutants in a metazoan.

A typical animal cell contains hundreds to thousands of copies of the mitochondrial genome (mtDNA), which encodes 13 essential subunits of the electron transport

chain complexes and RNAs (2 rRNAs and 22 tRNAs) required for mitochondrial translation (1, 2). It is not clear how the genetic integrity of this amitotically distributed genome is main-



The crystal structure of C176A mutated [Fe]-hydrogenase suggests an acyl-iron ligation in the active site iron complex

Takeshi Hiromoto^a, Kenichi Ataka^b, Oliver Pilak^a, Sonja Vogt^a, Marco Salomone Stagni^c, Wolfram Meyer-Klaucke^c, Eberhard Warkentin^d, Rudolf K. Thauer^a, Seigo Shima^{a,*}, Ulrich Ermler^{d,*}

^aMax-Planck-Institut für Terrestrische Mikrobiologie, Karl-von-Frisch-Straße, D-35043 Marburg, Germany

^bBielefeld University, Department of Chemistry, Universitätsstraße 25, D-33615 Bielefeld, Germany

^cEMBL Hamburg, Notkestraße, 85, D-22603 Hamburg, Germany

^dMax-Planck-Institut für Biophysik, Max-von-Laue-Straße 3, D-60438 Frankfurt/Main, Germany

ARTICLE INFO

Article history:

Received 20 November 2008

Revised 30 December 2008

Accepted 5 January 2009

Available online 20 January 2009

Edited by Hans Eklund

Keywords:

Hydrogenase

Iron–guanylylpyridinol-cofactor

Methanogenic archaea

Iron complex

X-ray crystal structure

X-ray absorption spectroscopy

ABSTRACT

[Fe]-hydrogenase is one of three types of enzymes known to activate H₂. Crystal structure analysis recently revealed that its active site iron is ligated square-pyramidally by Cys176-sulfur, two CO, an “unknown” ligand and the sp²-hybridized nitrogen of a unique iron–guanylylpyridinol-cofactor. We report here on the structure of the C176A mutated enzyme crystallized in the presence of dithiothreitol (DTT). It suggests an iron center octahedrally coordinated by one DTT-sulfur and one DTT-oxygen, two CO, the 2-pyridinol’s nitrogen and the 2-pyridinol’s 6-formylmethyl group in an acyl-iron ligation. This result led to a re-interpretation of the iron ligation in the wild-type.

© 2009 Federation of European Biochemical Societies. Published by Elsevier B.V. All rights reserved.

1. Introduction

The reversible oxidation of molecular hydrogen, which serves many microorganisms as electron supplier or electron sink in their energy metabolism, is catalyzed by hydrogenases from which three basic types have been discovered [1]. [NiFe]- and [FeFe]-hydrogenases use a binuclear [NiFe] and [FeFe] center for H₂ activation, respectively, and several Fe/S clusters for electron delivery (H₂ ⇒ 2H⁺ + 2e⁻) [2]. [Fe]-hydrogenase contains a mononuclear iron center that somehow facilitates the generation of a hydride (H₂ ⇒ H⁺ + H⁻) to be abstracted by methenyl-tetrahydromethanopterin (methenyl-H₄MPT⁺) [3]. Despite their different protein architectures and not being phylogenetically related the active sites reveal amazing similarities as result of a convergent evolu-

tionary process presumably provoked by special chemical requirements for H₂ activation [1,4,5]. In all three types the iron (in [FeFe]-hydrogenase the iron proximal to the 4Fe–4S cluster) is redox-inactive, low-spin, presumably present in the oxidation state II, and ligated by at least one sulfur and three unusual π-accepting ligands such as CO, cyanide and/or a pyridinol that are arranged similarly in a square-pyramidal or octahedral geometry [1]. However, why these ligands and this arrangement are applied for the heterolytic cleavage of H₂ is not well understood. Large efforts are undertaken to elucidate the catalytic mechanism because H₂/H⁺ interconversion is considered as one of the major reactions in future energy storage/transformation processes [3].

[Fe]-hydrogenase catalyzes a reaction involved in many methanogenic archaea in CO₂ reduction to methane by reducing methenyl-H₄MPT⁺ to methylene-H₄MPT at the expense of H₂ [3]. The enzyme consists of a homodimer of 38 kDa per monomer built up of the C-terminal segments of both subunits forming a central helical unit and of two peripheral N-terminal domain units adopting a Rossmann-like fold [6] (Fig. 1A). Each of the latter domains binds at the C-terminal end of their parallel β-sheet a unique iron–guanylylpyridinol (FeGP)-cofactor whose catalytically competent iron complex points into the reaction site located inside a

Abbreviations: methenyl-H₄MPT⁺, methenyl-tetrahydromethanopterin; methylene-H₄MPT, methylene-tetrahydromethanopterin; FeGP, iron–guanylylpyridinol; EXAFS, extended X-ray absorption fine structure; ATR-IR, attenuated total reflection infrared; DTT, dithiothreitol; r.m.s., root-mean-square; GP, guanylylpyridinol

* Corresponding authors. Fax: +49 69 6303 1002 (U. Ermler), +49 6421 178109 (S. Shima).

E-mail addresses: shima@mpi-marburg.mpg.de (S. Shima), ulermler@mpibp-frankfurt.mpg.de (U. Ermler).

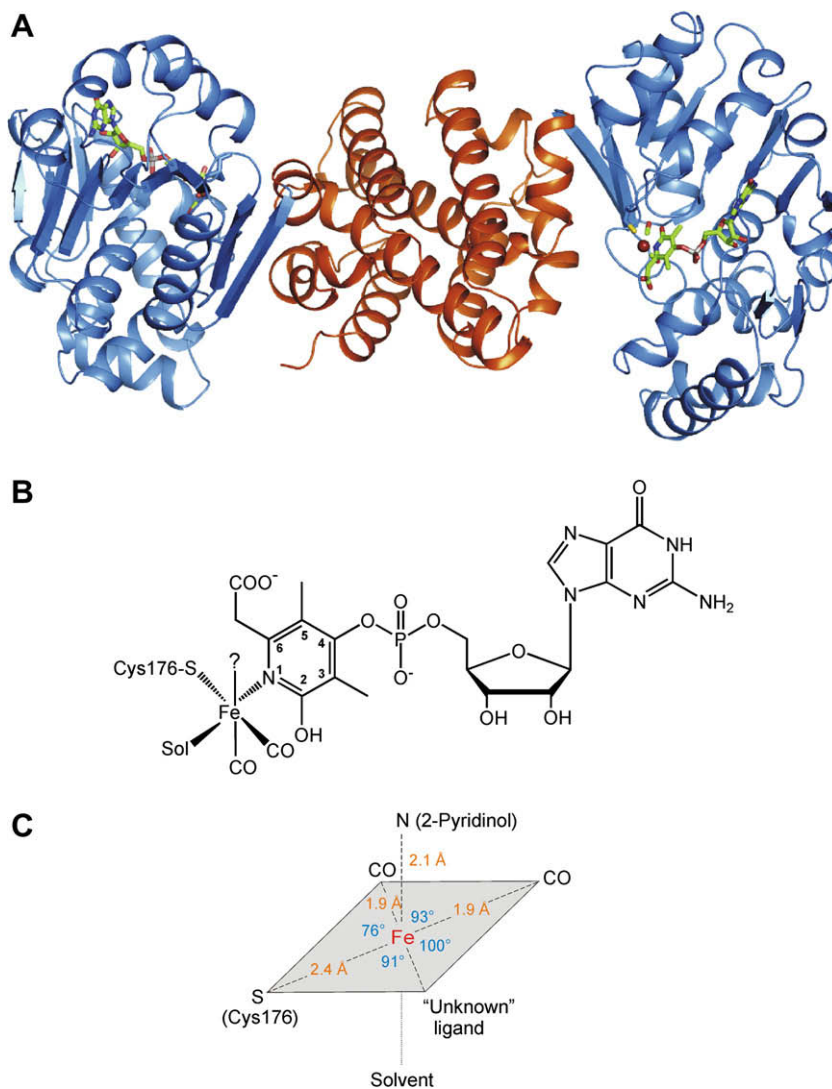


Fig. 1. Iron-ligation structure of wild-type [Fe]-hydrogenase and of its iron-guanylylpyridinol-cofactor as proposed previously [1]. (A) Ribbon diagram shows that the dimeric enzyme is composed of one central (orange) and two peripheral (blue) units. The two active sites are located within the two clefts between these units. (B) Structure of the FeGP-cofactor when it covalently binds to the enzyme via Cys176 as published [1]. (C) Schematic representation of the iron square-pyramidally ligated to the Cys176-sulfur, an “unknown” ligand, two CO and the pyridinol’s sp^2 -hybridized nitrogen. A solvent is associated to the iron trans to the pyridinol’s nitrogen. Bond length was derived from the X-ray crystallographic data [1].

cleft between the central and the peripheral units [1]. Based on the interpretation of IR, Mössbauer, extended X-ray absorption fine structure (EXAFS) and X-ray crystallographic data from the holoenzyme (apoenzyme reconstituted with FeGP-cofactor) the iron complex consists of a low-spin iron square-pyramidally ligated by Cys176-sulfur of the polypeptide chain, two CO, an “unknown” ligand and the sp^2 -hybridized nitrogen of the cofactor’s pyridinol nitrogen [1,7–11]. The sixth position appears to be occupied by a hydrogen-bonded solvent molecule, however, too distant to be a direct ligand (Fig. 1B and C).

We report here on the crystal structure at 1.95 Å resolution of the holoenzyme of [Fe]-hydrogenase from *Methanocaldococcus jannaschii* in which the active site Cys176 was mutated to an alanine. It revealed that the Cys176 sulfur and the “unknown” ligands of the iron complex of the wild-type enzyme are replaced in the C176A enzyme by the dithiothreitol (DTT) present in the crystallization solution. The obtained electron density prompted us to reinterpret the iron ligation structure recently published for the wild-type enzyme [1]. A better fit was obtained when the 2-pyridinol moiety contributes two rather than one ligands to the iron, the

sp^2 -hybridized nitrogen and the 6-formylmethyl group, the latter in an acyl-iron ligation. The modified iron-ligation pattern in the C176A mutated enzyme is compatible with the previously obtained IR and EXAFS data of the mutated and wild-type enzymes.

2. Materials and methods

2.1. C176A holoenzyme preparation, crystallization and X-ray structure determination

The C176A mutant from *M. jannaschii* was prepared as described previously [7]. The apoenzyme was overproduced in *Escherichia coli* BL21(DE3) cells, purified and reconstituted with FeGP-cofactor [12]. The resulting catalytically inactive holoenzyme was crystallized and diffraction data were collected at the Swiss Light Source beamline PXII (Villigen). The data were processed and scaled with the programs HKL [13] and XDS [14] (Table 1). The obtained isomorphous crystals allowed a straightforward structure determination using the wild-type enzyme model solved previously [1]. Model refinement was performed with REFMAC5 [15]

Table 1
Data collection and refinement statistics.

Data set	[Fe]-hydrogenase C176A	[Fe]-hydrogenase wild-type
<i>A. Data collection</i>		
Wavelength (Å)	0.992	0.992
Space group	I4 ₁ 22	I4 ₁ 22
Unit cell parameter		
<i>a</i> , <i>c</i> (Å)	96.4, 166.6	95.9, 165.8
Resolution range (Å) (highest shell)	41.7–1.95 (2.0–1.95)	26.2–1.75 (1.80–1.75)
Redundancy	7.9 (7.7)	5.2 (3.6)
Completeness (%)	96.9 (95.8)	95.5 (81.6)
<i>R</i> _{merge} (%)	6.4 (70.1)	5.6 (50.8)
<i>I</i> / σ (<i>I</i>)	17.2 (4.2)	16.0 (2.6)
<i>B. Refinement</i>		
Resolution limit (Å)	40.0–1.95	25.0–1.75
<i>R</i> _{work} / <i>R</i> _{free} (%)	16.5/20.5	17.3/20.5
Number of Residues	345	344
Number of solvent molecules	169	238
Rmsd bond lengths (Å)	0.016	0.016
Rmsd bond angles (°)	1.6	1.6
Cruickshank's DPI (Å)	0.13	0.10
Average B (Å ²) protein/FeGP/solvent, DTT	37.5/28.2/46.4, 40.2	32.8/26.7/43.2

and model building/manual inspections with COOT [16]. The *R*_{work} and *R*_{free} factor converged to 16.5% and 20.5% in the resolution range 1.95–40.0 Å (Table 1). Figs. 1A–3A are produced by PYMOL (DeLano Scientific). The coordinates of the C176A mutated enzyme model and the re-refined wild-type enzyme model were deposited at the RCSB Protein Data Bank under the PDB accession codes 3F46 and 3F47.

2.2. Infrared spectroscopy

Attenuated total reflection infrared (ATR-IR) spectroscopy was performed using Bruker VERTEX 70 IR spectrometer with Liquid nitrogen cooling system for the MCT detector equipped with Sili-

cone Prism (DuraSample/R™, SENSIR TECHNOLOGIES) under red light. Five microliters of the C176A and wild holoenzyme (20 mg/ml) was dried on the window of the prism under an argon stream at 20 °C. During drying IR spectra were continuously recorded thereby averaging 1280 scans for each spectrum. The enzyme recovered from the crystallization drops were analyzed in the same manner.

2.3. X-ray absorption data re-analysis

The extracted iron K-edge (mutants: 25–680 eV; wild-type: 25–800 eV) EXAFS data were converted to photoelectron wave vector *k*-space and weighted by *k*³. The spectra were refined with EXCURV98 [17]. The program calculated the theoretical EXAFS for defined structural model. In addition to single scattering contributions, multiple scattering linear units were defined for Fe–C=O. The potential acyl group in the vicinity of the iron has been modelled by a single carbon ion, because its other atoms do not contribute to multiple scattering by a linear orientation towards the iron and therefore they are not identifiable in the EXAFS. Parameters of each structural model, namely the atomic distances (*R*), the Debye–Waller factors ($2\sigma^2$), and a residual shift of the energy origin, were optimized, minimizing the fit index.

3. Results

3.1. Iron-coordination in the C176A holoenzyme

The overall structure of the C176A enzyme is highly similar to the wild-type enzyme, reflected in the root-mean-square (r.m.s.) deviation of 0.2 Å using 344 C_α atoms. Significant differences were exclusively found around the mutated residue and the FeGP-cofactor whose occupancy is nearly 100%.

The structure of the iron complex is primarily characterized by the ligation of DTT (present in the crystallization solution) in a bidentate manner (Fig. 2). The eliminated iron-coordinating

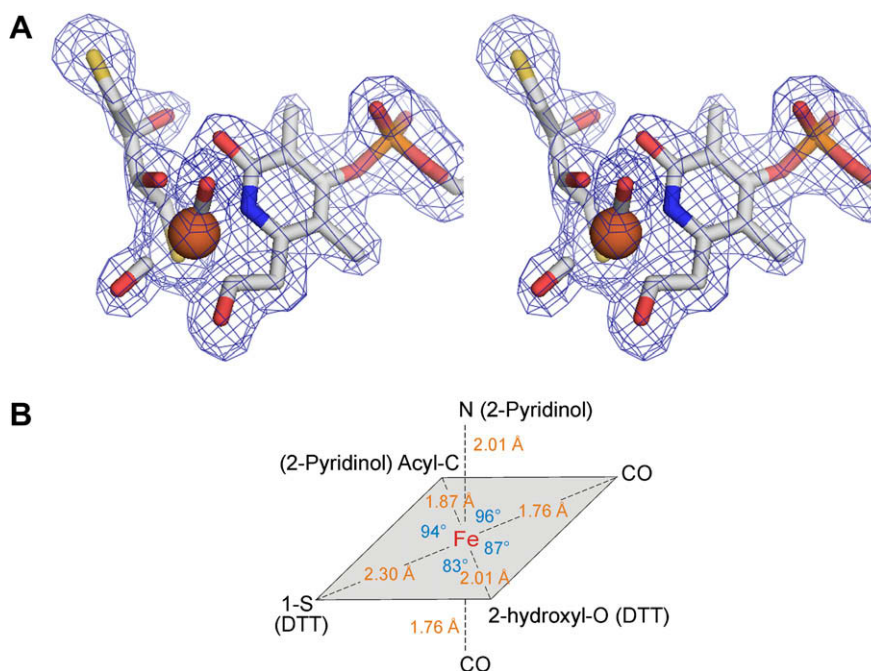


Fig. 2. Iron-ligation structure of C176A mutated [Fe]-hydrogenase. (A) *F*₀–*F*_c omit electron density map around the iron complex contoured at the 3.0σ level (in blue). (B) Schematic representation of the iron octahedrally ligated to a dithiothreitol (DTT)-sulfur, a DTT-oxygen, two CO and the pyridinol's nitrogen and pyridinol's acyl carbon. Bond length was derived from the EXAFS data (see Table 2).

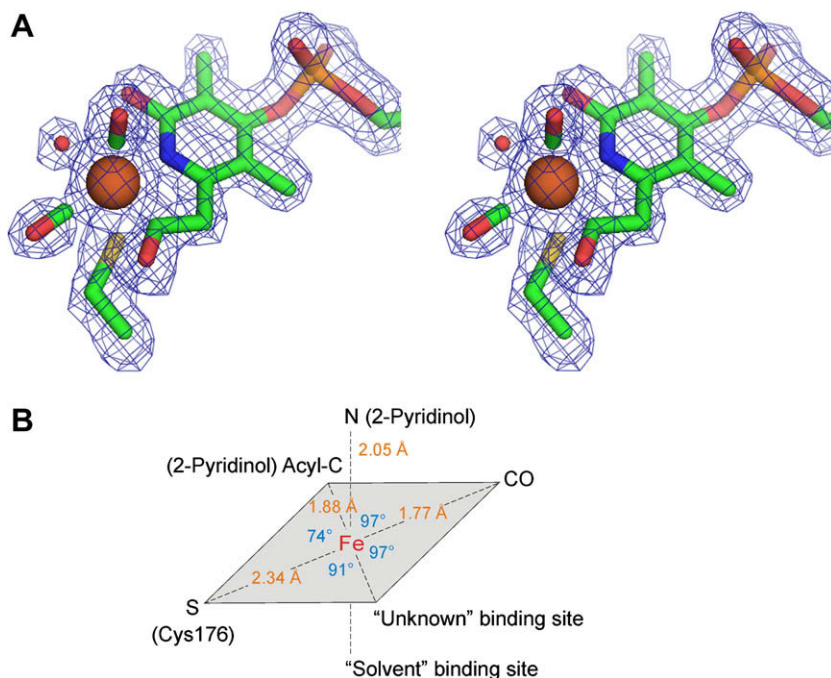


Fig. 3. Re-interpreted iron-ligation structure of wild-type [Fe]-hydrogenase (A) F_o-F_c omit electron density map around the iron complex contoured at the 2.8σ level (in blue), shown in the same orientation as in Fig. 2A. (B) Schematic representation of the iron octahedrally surrounded by the pyridinol's nitrogen, the pyridinol's formylmethyl-acyl carbon, one CO, and the Cys176 sulfur ligands as well as by the "unknown" and "solvent" binding sites. According to the current data the second CO more likely sits at the "solvent" binding site (see Sections 3.2. and 4). Bond length was derived from the EXAFS data (see Table 2).

Cys176-sulfur is replaced by the 1-sulfur of DTT and its 2-hydroxyl group also ligates to the iron from that site which was occupied in the wild-type enzyme by the "unknown" ligand (Fig. 1) [1]. The entire molecule of DTT is clearly visible in the electron density and its temperature factor is only moderately higher than that of the polypeptide (Table 1). The 3-hydroxyl group of DTT is anchored to the protein matrix via a hydrogen bond to the hydroxyl group of Thr13 and the 4-thiol group of DTT interacts with hydrophobic regions of the surrounding residues.

The binding of DTT to the iron creates a serious problem in that the 2-hydroxyl group of DTT severely interferes with the 6-carboxymethyl substituent of the pyridinol ring if assumed to be in the conformation of the wild-type enzyme (Fig. 1B) [1]. This prompted us to rotate the pyridinol ring of FeGP-cofactor by 180° compared to the orientation reported for the wild-type enzyme. The shape of the electron density in the rotated conformation, however, did not allow the incorporation of a carboxylate group with an oxygen as the iron ligand but it did allow the modeling of an acyl group with an iron-ligating carbon. In this arrangement the acyl oxygen is linked to the polypeptide chain by a hydrogen bond with the amide group of Ala176. In the rotated conformation the pyridinol's hydroxyl group points towards the cleft between the central and peripheral unit. The hydroxyl group fits well into the electron density and interacts with the imidazole group of His14 and the 2- and 3-hydroxyl group of DTT.

While one of the intrinsic CO-binding sites corresponds to that reported for the wild-type enzyme the second CO-binding site now appears to be positioned trans to the pyridinol's nitrogen in the C176A enzyme (Fig. 2A). ATR-IR measurements before and after crystallization of the C176A enzyme verified the existence of the two CO ligands in an angle of 90° as previously found in the wild-type (Supplementary Fig. S1).

Based on the presented X-ray structure a re-analysis of the C176A holoenzyme's EXAFS data was performed (Table 2 and Supplementary Table). The EXAFS spectra are dominated by sulfur and CO contributions (Supplementary Fig. S2) but additional backscat-

tering from similar light atoms could be identified already in the previous study [7]. However, EXAFS data analysis is hampered by the destructive interference of similar ligands at slightly different distances yielding to an underestimation of their occupancy. This effect is well established for metal-metal contributions [18,19]. Accordingly, the best fit between experimental and simulated data was previously obtained when the light atoms in the C176A mutant were assigned to two O/N atoms. The presence of a carbon as iron ligand is atypical and had not been considered in former models. The application of the new iron-ligation structure containing three light atoms (N and acyl C from pyridinol, O from DTT) improves the fit index and yields typical bond lengths [20–23]. A minor improvement is possible if the occupancy of one CO ligand of the C176S and C176A enzymes is lowered by 0.25 or 0.5, respectively. The slightly better refinement value points towards a labile ligand. Thus the re-analysis of EXAFS data from C176 mutants supports the presence of the coordinating acyl group in solution. Its identification in a standard ab-initio data analysis would require a data range up to ~ 2000 eV above the edge, which is almost impossible to achieve for metalloproteins.

3.2. Re-interpretation of iron-coordination in the wild-type holoenzyme

Taking into account the unprecedented iron-ligation pattern in the C176A enzyme the structure of the wild-type enzyme was re-refined. And indeed, the resulting electron density also fits better to the reversed orientation of the pyridinol ring and to an acyl-iron ligation (Fig. 3). A re-inspection of further [Fe]-hydrogenase structures (the cyanide or CO inhibited enzyme) based on different diffraction data also argue for the postulated acyl-iron coordination (data not shown). While the interactions between the protein and the acyl group are identical in the C176A- and wild-type enzymes, the pyridinol's hydroxyl group of the wild-type enzyme is not hydrogen-bonded to His14 but to a solvent molecule that is anchored to the protein matrix via Thr13.

Table 2

Structural parameters extracted from the EXAFS refinement for wild-type [Fe]-hydrogenase, and C176A and C176S mutated enzymes. For alternative models compared to the data see Supplementary table. The numbers (*n*) of ligand atoms (L) to the iron, their distance to the iron (*R*), the respective Debye-Waller factor ($2\sigma^2$), the C–O or C–N bond length (*RCX*), the Fermi energy for all shells (*EF*), and the fit index (Φ), indicating the quality of the fit are shown.

<i>n</i>	Fe	L	<i>R</i> (Å)	$2\sigma^2$ (Å ²)	<i>R</i> _{CO} (Å)	<i>EF</i> (eV)	$\Phi \times 10^3$
<i>Wild-type enzyme</i>							
2	Fe	C ^a	1.769(5)	0.0050(7)	1.170(8)	−10.6(5)	0.1664
1	Fe	C ^b	1.88(1)	0.0020(1)			
1	Fe	O	2.052(9)	0.014(2)			
1	Fe	N	2.052(9)	0.014(2)			
1	Fe	S	2.335(4)	0.0064(7)			
2	Fe	O ^c	2.939(3)	0.0025(4)			
<i>Mutated enzymes</i>							
<i>C176A</i>							
1.5	Fe	C ^a	1.76(1)	0.010(3)	1.16(2)	−12(1)	0.2758
1	Fe	C ^b	1.87(7)	0.0038(3)			
1	Fe	O	2.01(1)	0.005(1)			
1	Fe	N	2.01(1)	0.005(1)			
1	Fe	S	2.303(7)	0.005(1)			
1.5	Fe	O ^c	2.922(7)	0.004(1)			
<i>C176S</i>							
1.75	Fe	C ^a	1.75(1)	0.017(8)	1.16(2)	−10.4(8)	0.3685
1	Fe	C ^b	1.83(2)	0.0029(2)			
1	Fe	O	1.997(8)	0.005(1)			
1	Fe	N	1.997(8)	0.005(1)			
1	Fe	S	2.295(7)	0.0048(9)			
1.75	Fe	O ^c	2.91(1)	0.003(2)			

^a Carbon of CO.

^b Carbon of acyl group.

^c Oxygen of CO.

The previous interpretation of the electron density was biased by the lack of imagination concerning the possibility of an acyl group as iron ligand and on the subsequent conclusion that the orientation of a negatively charged carboxylate group towards the rather unpolar protein interior is unlikely. Moreover, the hydroxyl group of the pyridinol ring in van der Waals contact to the iron-ligating CO group is almost isoelectronically and structurally identical to a formylmethyl substituent resulting in a related electron density. In the wild-type holoenzyme there is a second conformation of the Cys176-sulfur unanchored to the FeGP-cofactor suggesting reduced occupancy of its iron that complicates ligand modelling.

On the basis of EXAFS data the acyl coordination can only be identified when the slight differences in backscattering for the three light elements (C, N, and O) are considered (see above). These ligands are typically indistinguishable by this method. Based on the new coordination model an improved refinement was also possible for the wild-type enzyme (Table 2 and Supplementary Table), yielding a coordination by 5 or 6 ligands instead of 4–5 ligands as in our previous models [1,7]. Both, the incorporation of the nitrogen ligand of the cofactor identified before and the carbon from the acyl group improved the fit index. However, the presence of the oxygen ligand (perhaps from a solvent) cannot be judged on the basis of these data. The refinements of wild-type and mutant enzymes are of similar quality although the energy range for the wild-type enzyme is longer than for the mutant samples (Table 2). Thus in solution the iron in wild-type enzyme is coordinated by two CO, the sulfur from C176, the nitrogen and the acyl-carbon of the cofactor, and potentially an easily removable oxygen ligand from the solvent.

4. Discussion

In the new model the pyridinol moiety contributes two ligands to the iron, the sp^2 -hybridized nitrogen and the 6-formylmethyl group in an acyl-iron ligation (Fig. 3). This bidentate iron-ligation

may better explain the stability of the protein free FeGP-cofactor in 10 mM EDTA at pH 8 [12].

The proposed acyl group as iron ligand, although not extracted from previous IR, EXAFS and even X-ray crystallographic data, is not in contradiction to them but has still to be unambiguously confirmed in future studies. The existence of the acyl group is consistent with the results of the NMR and mass spectroscopic analysis of the guanylylpyridinol (GP) part, which was derived from the light sensitive FeGP-cofactor. Upon light inactivation, the proposed acyl-iron bond in FeGP-cofactor could be converted into the 6-carboxymethyl group of GP by hydrolysis [10]. Alternatively, photolysis of iron carbonyl complexes containing an acyl-iron bond has been shown to be associated with a decarbonylation of the acyl group [24]. In this respect it is of interest that the enzyme bound FeGP-cofactor decomposes under acid condition (5% HClO₄) at 60 °C into a GP, an iron and 2.4 ± 0.2 CO per one iron [8]. An acyl carbon-iron bond is also compatible with IR spectroscopic data as the FeGP-cofactor in the active enzyme shows CO stretching frequencies at 2011 cm^{-1} and 1944 cm^{-1} in water [8] and at 1996 cm^{-1} and 1928 cm^{-1} in the dried state (Supplementary Fig. S1). These CO stretching frequencies are similar to those from (η^5 -cyclopentadienyl)dicarbonylacetyliron complexes in organic solvents or in the dried state [24,25]. Apparently, the electronic state of iron in both complexes is related arguing for an acyl-iron ligation in the FeGP cofactor of [Fe]-hydrogenase. Therefore, from now on acyl-iron complexes should be included in the list of possible biomimetic compounds for [Fe]-hydrogenase. Interestingly, an acyl group as metal ligand (to nickel) in an enzyme has so far only been reported for the acetyl-CoA synthase/decarbonylase reaction as possible intermediate in the formation of acetyl-CoA from CO and a methyl group [26,27].

The positions of the Cys176-sulfur and of the intrinsic CO arranged trans to the Cys176-sulfur are not changed by the re-interpretation. This leaves the positions of the “unknown” ligand and of the “solvent” in the previous wild-type enzyme model (Fig. 1C) as possible binding sites for the second intrinsic CO (Fig. 3). While the C176A structure favors the “solvent” binding site for the second intrinsic CO its position in the wild-type enzyme cannot be identified on a structural basis. The electron density at the “solvent” binding site, although compatible with a (partially bound) intrinsic CO is not clearly connected to that of the iron and the weaker electron density of the “unknown” binding site is not sufficiently shaped.

A definitive assignment of the second intrinsic CO-binding site is difficult since the C176A enzyme structure is not active and that both of the mutant and the wild-type structure might be modified during the structure determination process especially at the solvent-exposed “unknown” ligand and “solvent” binding sites because of the instability of the FeGP-cofactor.

Acknowledgements

This work was supported by the Max Planck Society, the Fonds der Chemischen Industrie and the BMBF (BioH₂ project). We thank Hartmut Michel for continuous support and the staff of PXII at the SLS for help during data collection.

Appendix A. Supplementary data

Supplementary data associated with this article can be found, in the online version, at doi:10.1016/j.febslet.2009.01.017.

References

- [1] Shima, S., Pilak, O., Vogt, S., Schick, M., Stagni, M.S., Meyer-Klaucke, W., Warkentin, E., Thauer, R.K. and Ermler, U. (2008) The crystal structure of [Fe]-hydrogenase reveals the geometry of the active site. *Science* 321, 572–575.

- [2] Fontecilla-Camps, J.C., Volbeda, A., Cavazza, C. and Nicolet, Y. (2007) Structure/function relationships of [NiFe]- and [FeFe]-hydrogenases. *Chem. Rev.* 107, 4273–4303.
- [3] Shima, S. and Thauer, R.K. (2007) A third type of hydrogenase catalyzing H₂ activation. *Chem. Rec.* 7, 37–46.
- [4] Volbeda, A., Charon, M.H., Piras, C., Hatchikian, E.C., Frey, M. and Fontecilla-Camps, J.C. (1995) Crystal structure of the nickel-iron hydrogenase from *Desulfovibrio gigas*. *Nature* 373, 580–587.
- [5] Peters, J.W., Lanzilotta, W.N., Lemon, B.J. and Seefeldt, L.C. (1998) X-ray crystal structure of the Fe-only hydrogenase (Cpl) from *Clostridium pasteurianum* to 1.8 Å resolution. *Science* 282, 1853–1858.
- [6] Pilak, O., Mamat, B., Vogt, S., Hagemeyer, C.H., Thauer, R.K., Shima, S., Vonrhein, C., Warkentin, E. and Ermler, U. (2006) The crystal structure of the apoenzyme of the iron-sulfur cluster-free hydrogenase. *J. Mol. Biol.* 358, 798–809.
- [7] Korbass, M., Meyer-Klaucke, W., Vogt, S., Lyon, E.J., Thauer, R.K. and Shima, S. (2006) The iron-sulfur cluster-free hydrogenase (Hmd) is a metalloenzyme with a novel iron binding motif. *J. Biol. Chem.* 281, 30804–30813.
- [8] Lyon, E.J., Shima, S., Boecher, R., Thauer, R.K., Grevels, F.W., Bill, E., Roseboom, W. and Albracht, S.P.J. (2004) Carbon monoxide as an intrinsic ligand to iron in the active site of the iron-sulfur-cluster-free hydrogenase H₂-forming methylenetetrahydromethanopterin dehydrogenase as revealed by infrared spectroscopy. *J. Am. Chem. Soc.* 126, 14239–14248.
- [9] Lyon, E.J., Shima, S., Buurman, G., Chowdhuri, S., Batschauer, A., Steinbach, K. and Thauer, R.K. (2004) UV-A/blue-light inactivation of the 'metal-free' hydrogenase (Hmd) from methanogenic archaea: the enzyme contains functional iron after all. *Eur. J. Biochem.* 271, 195–204.
- [10] Shima, S., Lyon, E.J., Sordel-Klippert, M.S., Kauss, M., Kahnt, J., Thauer, R.K., Steinbach, K., Xie, X.L., Verdier, L. and Griesinger, C. (2004) The cofactor of the iron-sulfur cluster free hydrogenase Hmd: structure of the light-inactivation product. *Angew. Chem., Int. Ed.* 43, 2547–2551.
- [11] Shima, S., Lyon, E.J., Thauer, R.K., Mienert, B. and Bill, B. (2005) Mössbauer studies of the iron-sulfur cluster-free hydrogenase: the electronic state of the mononuclear Fe active site. *J. Am. Chem. Soc.* 127, 10430–10435.
- [12] Buurman, G., Shima, S. and Thauer, R.K. (2000) The metal-free hydrogenase from methanogenic archaea: evidence for a bound cofactor. *FEBS Lett.* 485, 200–204.
- [13] Otwinowski, Z. and Minor, W. (1997) Processing of X-ray diffraction data collected in oscillation mode. *Meth. Enzymol.* 276, 307–326.
- [14] Kabsch, W. (1993) Automatic processing of rotation diffraction data from crystals of initially unknown symmetry and cell constants. *J. Appl. Cryst.* 26, 795–800.
- [15] Murshudov, G.N., Vagin, A.A. and Dodson, E.J. (1997) Refinement of macromolecular structures by the maximum-likelihood method. *Acta Crystallogr. D* 53, 240–255.
- [16] Emsley, P. and Cowtan, K. (2004) Coot: model-building tools for molecular graphics. *Acta Crystallogr. D* 60, 2126–2132.
- [17] Binsted, N., Strange, R.W. and Hasnain, S.S. (1992) Constrained and restrained refinement in EXAFS data-analysis with curved wave theory. *Biochemistry* 31, 12117–12125.
- [18] Gu, W.W., Seravalli, J., Ragsdale, S.W. and Cramer, S.P. (2004) CO-induced structural rearrangement of the C cluster in *Carboxydotherrmus hydrogenoformans* CO dehydrogenase – evidence from Ni K-edge X-ray absorption spectroscopy. *Biochemistry* 43, 9029–9035.
- [19] Ha, S.W., Korbass, M., Klepsch, M., Meyer-Klaucke, W., Meyer, O. and Svetlitchnyi, V. (2007) Interaction of potassium cyanide with the [Ni-4Fe-5S] active site cluster of CO dehydrogenase from *Carboxydotherrmus hydrogenoformans*. *J. Biol. Chem.* 282, 10639–10646.
- [20] Harding, M.M. (2006) Small revisions to predicted distances around metal sites in proteins. *Acta Crystallogr. D* 62, 678–682.
- [21] Kolbener, P., Hung, H.U., Bosch, H.W., Sontag, C. and Berke, H. (1990) Acyl migration in d⁶ iron complexes. *Helv. Chim. Acta* 73, 2251–2262.
- [22] Petz, W. and Neumüller, B. (2007) Reaction of [Fe₂(CO)₆(μ-COLi(THF)₃)₂] with Me₃SiCl – crystal structure of [Fe₂(CO)₆(μ₃-COSiMe₃)(μ₃-COLi(THF)₃)]. *Z. Anorg. Allg. Chem.* 633, 2032–2036.
- [23] Wong, W.K., Chiu, K.W., Wilkinson, G., Galas, A.M.R., Thorntonpett, M. and Hursthouse, M.B. (1983) Electrophilic attack on the [μ₃-acetyl-C¹(Fe¹:Fe²)O(Fe¹:Fe³)]-nonacarbonyl-triangulo-triferrate(1-) anion by fluoroboric acid and methyl fluorosulfate. Carbon-oxygen bond-cleavage to give μ₃-etyldyne and μ-methoxy-groups. X-ray crystal-structures of Fe₃(CO)₉(μ₃-MeCO)(μ-H), Fe₃(CO)₉(μ₃-CMe)(μ₃-OMe), and Fe₃(CO)₉(μ₃-CMe)(μ₃-COMe). *J. Chem. Soc., Dalton Trans.*, 1557–1563.
- [24] Belt, S.T., Ryba, D.W. and Ford, P.C. (1991) Reactive intermediates in the photolytic decarbonylation of the acyl complex (η⁵-C₅H₅)Fe(CO)₂(COCH₃) as studied by time-resolved infrared spectral techniques. *J. Am. Chem. Soc.* 113, 9524–9528.
- [25] Baranowska, E., Danikiewicz, W., Pakulski, Z. and Zamojski, A. (1995) Fragmentation of (η⁵-cyclopentadienyl)dicarbonylacetyliron complexes under electron-impact. *J. Mass Spectrom.* 30, 158–162.
- [26] Ragsdale, S.W. (2007) Nickel and the carbon cycle. *J. Inorg. Biochem.* 101, 1657–1666.
- [27] Svetlitchnyi, V., Dobbek, H., Meyer-Klaucke, W., Meins, T., Thiele, B., Romer, P., Huber, R. and Meyer, O. (2004) A functional Ni-Ni-[4Fe-4S] cluster in the monomeric acetyl-CoA synthase from *Carboxydotherrmus hydrogenoformans*. *Proc. Natl. Acad. Sci. USA* 101, 446–451.

Characterization of the optically excited state of a bis (μ -oxo)-dicopper(III) species mimicking the hemocyanin and tyrosinase active sites

Stephan Binder², Marco Salomone-Stagni¹, Roxana Haase³, Benjamin Schulz², Andreas Eich², Gerald Henkel³, Michael Rübhausen², Sonja Herres-Pawlis³, and Wolfram Meyer-Klaucke^{1,*}

¹ EMBL, Outstation Hamburg, Notkestr. 85, 22603 Hamburg, Germany

² Institut für Angewandte Physik, Universität Hamburg, Jungiusstr. 11, 20355 Hamburg and Center for Free Electron Laser Science, Notkestr. 85, 22603 Hamburg, Germany

³ Department Chemie, Anorganische Chemie, Universität Paderborn, 33098 Paderborn, Germany

Email: wolfram @ embl - hamburg.de

Abstract. Optical excited molecules play an increasingly important role in research at light sources. Here we compare two approaches to structurally characterize such states, pumped-XAS and an innovative combination of EXAFS spectroscopy and resonant Raman scattering. The later combination allows to study efficiently charge-transfer complexes in their ground and excited state. The design of the experimental setups for pumped-XAS and resonant Raman scattering at different temperatures as well as results obtained are presented. We receive two-fold information on the structural and electronic properties of both states elucidating the alterations upon induced charge transfer in the Cu_2O_2 -core of a system mimicking the active site of tyrosinase and hemocyanin.

1. Introduction

The availability of new photon-sources with pulse lengths in the fs-regime will permit fascinating research on triggerable compounds [1]. The relaxation of excited states into the ground state will provide new insights into the dynamics of the systems under study. Of particular interest to the molecular biological and bioinorganic communities will be the dynamics of metal-donor interactions. Excited states of biomolecules can be made available to the structural and spectroscopic analysis by a variety of strategies, ranging from optical pumping to stabilization of chemical mimics. Here, we focus on a system mimicking the Cu_2O_2 -core in hemocyanin and tyrosinases. Hemocyanin serves in many arthropods as an oxygen carrier, similar to hemoglobin in vertebrates. The enzyme tyrosinase is present in plant and animal tissue and shares the dinuclear copper binding site as well as most of the structural features of hemocyanin. In fact, many hemocyanins even exhibit tyrosinase activity [2]. Tyrosinase catalyses the oxidation of phenols, required for the production of melanin and other pigments. This phenol oxidase activity is of considerable interest for industrial applications [3].

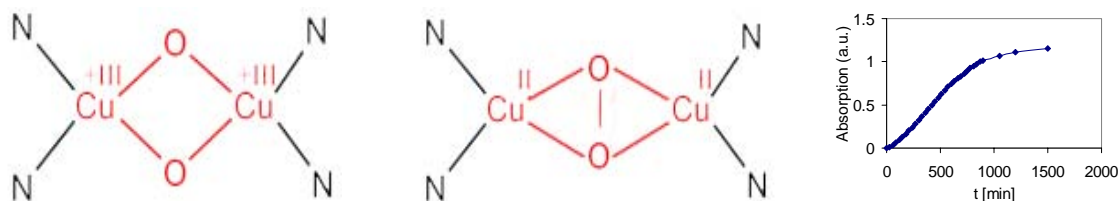


Figure 1. Potential Oxo-form (O-state, left) and Peroxo-form (P-state, center) of complexes modelling hemocyanin and tyrosinase active sites. Formation of $[\text{Cu}_2\text{L}_2(\mu\text{-O})_2]\text{I}_2$ (right) upon oxidation of $[\text{Cu}(\text{L})\text{I}]$ with dioxygen at 25 °C monitored by the absorption intensity for λ_{max} (366 nm).

In both metalloproteins molecular oxygen is binding to two copper ions in the side-on peroxo mode (P-state) [4]. Each of these copper ions is stabilised by three histidine groups. Complexes modelling these features have the potential to serve as highly specific oxidation catalysts [3]. In these complexes the biomimetic donor ligand has the function to stabilize the complex after reaction with molecular oxygen either in the P- or O-state: with a peroxo-dianion or two μ -oxo donors bridging the Cu ions, respectively (Figure 1). Typically, these systems are stable at cryogenic temperatures only [5].

Recently, we presented the first system stabilizing the O-state at room temperature [6]. It is formed by the reaction of molecular oxygen with the Cu(I)-complex, $\text{Cu}(\text{L})\text{I}$ with $\text{L} = (\text{B}(\text{TMPip})\text{G}_2\text{p})$ [7] within several hours as visualized by the increasing absorption at 366 nm (Figure 1, right). In its ground state the complex comprises an O-state as shown by XAFS data, collected at 20 K in fluorescence mode at beamline D2 (EMBL Hamburg, DESY, Germany) [6]: A Cu-dimer with terminal N-donors at 2.00(4) Å, two bridging μ -oxo donors at 1.93(1) Å and a Cu-Cu distance of 2.84(1) Å could be identified in the EXAFS. Such systems typically can be optically excited by UV-light [5]. Here, we compare strategies to characterize this excited state either by optical-pumping or by resonance Raman spectroscopy.

2. Material and Methods

$[\text{Cu}_2\text{L}_2(\mu\text{-O})_2]\text{I}_2$ has been synthesised as described before [6]. For Raman and EXAFS measurements, the following Cu(I) solution was prepared for subsequent oxygenation: 0.05 mmol of $\text{B}(\text{TMPip})\text{G}_2\text{p}$ (33 mg) in 5 mL of THF were added under stirring to a solution of 0.05 mmol of CuI (9 mg) in 5 mL of THF. The resulting concentration is 5 mmol/L which corresponds to 3.1 g Cu/L.

For optical excitation a custom designed UV-LED source with a 1 mm focal spot has been installed at beamline C (HASYLAB, DESY, Hamburg, Germany). This source is based on a NSSU100A LED (NICHIA, Tokyo, Japan) with optics comprising 3 UV-transparent lenses ($f=9\text{mm}$, $f=100\text{mm}$ and

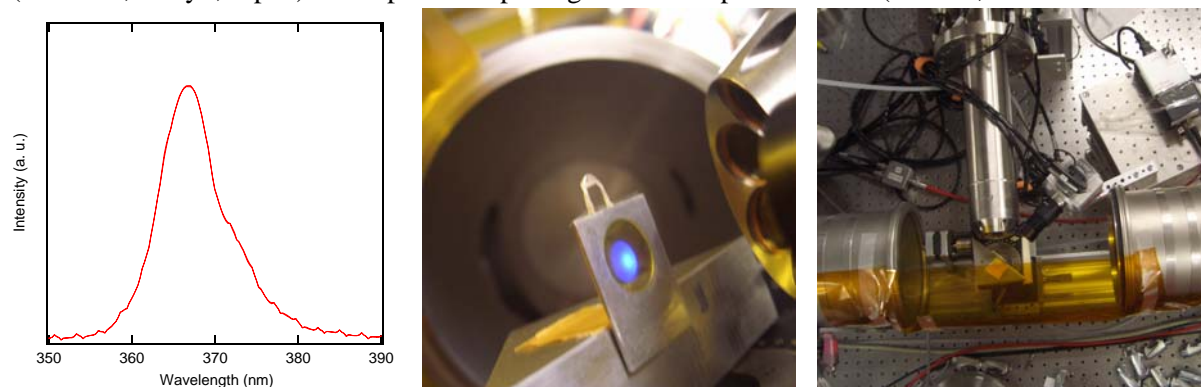


Figure 2. Spectral distribution of the light emitted by our UV source (left). Setup for the XAS experiments on optical excited solution of $[\text{Cu}_2\text{L}_2(\mu\text{-O})_2]\text{I}_2$ with optics of the UV-source (black), multi-element fluorescence detector, safety shield (Kapton, orange), and UV-excited sample in an Al-sample holder with Mylar windows. (center: in direction of the x-ray beam, right: top view).



Figure 3. Axially symmetrical sketch of the custom-made cuvette for temperature dependent measurements (left). Setup for the temperature dependent Raman experiments on solution of $[\text{Cu}_2\text{L}_2(\mu\text{-O})_2]\text{I}_2$ (center: picture of the cuvette, right: top view on the cryostat).

$f=50\text{mm}$). The maximum wavelength at 365nm is in line with the Raman active transition [6]. The resulting total power is 14.5mW , of which 70% are localized in the spot. Cuvettes were sealed with Mylar windows, because it is transparent at this wavelength. Kapton, in contrast, strongly absorbs this UV-light and thus has been used for safety precautions (Figure 2).

Resonant Raman experiments were performed using a custom made UV resonance Raman spectrometer with a completely reflective optics being located in a cleanroom [8]. Because all other compounds mimicking the O-state are unstable at room temperature we compared the quality of Raman spectra collected at different temperatures. A custom-build cuvette was mounted within a liquid helium cryostat (KONTI cryostat Spectro 6111, Cryovac). A suprasil window defines the sample volume of $200\ \mu\text{l}$. The solution was inserted through a small hole that was closed by a screw afterwards (Figure 3).

3. Results and Discussion

The ground state of $[\text{Cu}_2\text{L}_2(\mu\text{-O})_2]\text{I}_2$ has been characterized by Cu-K edge fluorescence XAS at $20\ \text{K}$ (Figure 4, left). Upon optical excitation at room temperature the x-ray transmission signal at $8990\ \text{eV}$ increases immediately (Figure 4, center), whereas the fluorescence signal follows with a few seconds delay. The reasons for these observations are enigmatic: The UV-light might heat up the sample causing lower absorption of x-rays in the 1mm thick cuvette. The second effect causing higher x-ray absorption after switching off the UV light source could not be identified so far. Maybe due to the high concentrations of the Cu-complex a small percentage precipitated prior to the experiment and dissolves at elevated temperatures. Anyhow, difference in the fluorescence XANES with and without UV-light illumination could not be identified for a variety of concentrations indicating a too low UV-photon intensity. Based on the width of the resonance Raman profile of the first and second order Raman peaks, the lifetime of the excited state is estimated to $\Delta t \approx h/\Delta E \approx h/0.2\ \text{eV} \approx 20\ \text{fs}$. At the given UV intensity $\sim 10^{16}$ photons are generated per second; considering the absorption probability of $\sim 40\%$ for the 1mm thick cuvette only a small fraction of the 10^{15} Cu ions elucidated by the $1 \times 1\ \text{mm}^2$ x-ray beam are optically excited when the pulsed synchrotron beam hits the sample.

Thus optical excitation is only feasible for such complexes with the help of a synchronized, pulsed UV-source, because a several orders of magnitude more intense UV-source would evaporate the sample and cause even more artefacts. But even in this case the total power absorbed by the sample will potentially lead to effects similar to the ones shown in figure 4.

For these reasons we looked into a more elegant and instrumentally less demanding approach: the utilization of a method elucidating the structural change induced upon charge-transfer. The Raman spectrum of $[\text{Cu}_2\text{L}_2(\mu\text{-O})_2]\text{I}_2$ exhibits strong vibrational excitations that can be assigned to the bending vibration of the copper-oxygen core at $114.3\ \text{cm}^{-1}$ and its integer multiples. For a given local symmetry the structural change is calculated from the Huang-Rhys parameter given by the intensity

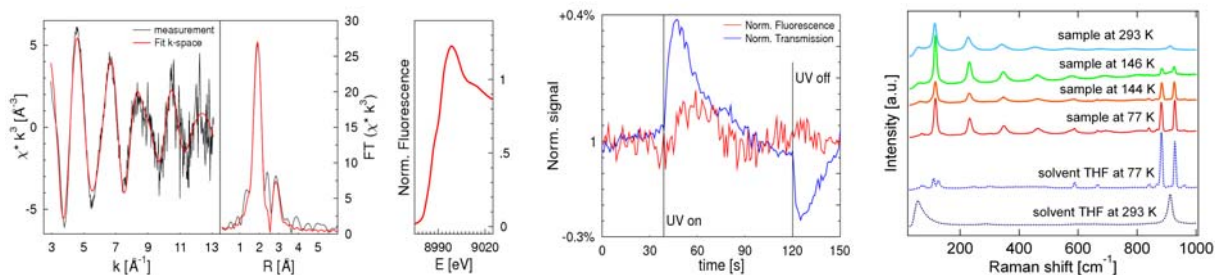


Figure 4. left: EXAFS and corresponding FT plus XANES; center: Normalized transmission and fluorescence at 8990 eV; right: Raman spectra of $[\text{Cu}_2\text{L}_2(\mu\text{-O})_2]\text{I}_2$ and THF at 350.7 nm. For data at 293 K and 77 K 10 minutes were given to reach stable temperature. Data around the melting point of THF (165 K) were taken while cooling down (144K/145K). Offset was added for better visualization.

decrease in the Raman spectra [5, 6]. This results in a change of the copper-oxygen distance by +0.01 Å and of the oxygen-oxygen distance by -0.13 Å [6].

Up to now to the limited stability of such complexes restricted such measurements to cryogenic temperatures. Here, a direct comparison of cryogenic and room temperature conditions is possible. Below the freezing point of the solvent THF (165 K) additional contributions become apart (green curve). These signals can be assigned to THF (dotted blue line)(Figure 4). Due to the huge relative difference in intensity and similar energy transfers no difference spectra were calculated to avoid artifacts. Interestingly, in contrast to X-ray absorption experiments, where due to the decreasing Debye-Waller factor a higher radial resolution is obtained at lower temperatures, no significant difference in resolution was detected in the Raman experiments.

This combination of resonant Raman spectroscopy and X-ray absorption spectroscopy gives direct access to structural and electronic (not shown) parameters of optical excited systems. In future, resonance Raman experiments at copper M-edges at free electron laser sources such as FLASH will provide new experimental tools to go even beyond the characterization presented here.

References

- [1] Bressler C, Milne C, Pham VT, Elnahhas A, van der Veen RM, Gawelda W, Johnson S, Beaud P, Grölimund D, Kaiser M, Borca CN, Ingold G, Abela R and Chergui M 2009 *Science* **323** 489
Schweigert IV and Mukamel S 2008 *J. Chem. Phys.* **128** 184307
Paulsen H, Grünsteudel H, Meyer-Klaucke W, Gerdan M, Grünsteudel HF, Chumakov AI, Ruffer R, Winkler H, Toftlund H and Trautwein AX 2001 *Europ. Phys. J. B* **23** 463
- [2] Decker H, Schweikardt T, Nillius D, Salzbrunn U, Jaenicke E, Tuczek F 2007 *Gene* **398** 183
- [3] van Eldik, R and Reedijk J, *Advances in inorganic chemistry – homogeneous biomimetic oxidation catalysis*, 1 ed., vol. 58, Academic Press, 2006
- [4] Magnus KA, Hazes B, Ton-That H, Bonaventura C, Bonaventura J and Hol WG, 1994 *Proteins* **19** 302
- [5] Henson MJ, Mukherjee P, Root DE, Stack TDP and Solomon EI 1999 *J. Am. Chem. Soc.* **121** 10332
- [6] Herres-Pawlis S, Binder S, Eich A, Haase R, Schulz B, Wellenreuther G, Henkel G, Rübhausen M and Meyer-Klaucke W 2009 *Chemistry – A Europ. J.* accepted
- [7] Herres-Pawlis S, Neuba A, Seewald O, Seshadri T, Egold H, Flörke U and Henkel G 2005 *Eur. J. Org. Chem.* **22** 4879
- [8] Schulz B, Bäckström J, Budelmann D, Maeser R, Rübhausen M, Klein MV, Schoeffel E, Mihill A and Yoon S 2005 *Rev. Scient. Instr.* **76** 073107

Extended X-ray absorption fine structure of the [Fe]-hydrogenase Hmd active site

This article has been downloaded from IOPscience. Please scroll down to see the full text article.

2009 J. Phys.: Conf. Ser. 190 012197

(<http://iopscience.iop.org/1742-6596/190/1/012197>)

View [the table of contents for this issue](#), or go to the [journal homepage](#) for more

Download details:

IP Address: 192.109.31.138

The article was downloaded on 31/05/2010 at 10:14

Please note that [terms and conditions apply](#).

Extended X-ray absorption fine structure of the [Fe]-hydrogenase Hmd active site

Marco Salomone-Stagni¹, Sonja Vogt², Seigo Shima², and Wolfram Meyer-Klaucke^{1,*}

¹ European Molecular Biology Laboratory (EMBL), Outstation Hamburg, Notkestr. 85, 22603 Hamburg, Germany

² Max-Planck-Institut für terrestrische Mikrobiologie, Karl-von-Frisch-Straße, D-35043 Marburg, Germany

Email: wolfram @ embl - hamburg.de

Abstract. Hydrogenases are enzymes that catalyze the reversible oxidation of molecular hydrogen. Although their structure and catalytic mechanism are of considerable applied interest as models for the development of efficient catalysts for hydrogen fueled processes, the understanding of how hydrogenases react with H₂ is only in its infancy. Two of the three known types of hydrogenases are iron-sulfur proteins that contain a dinuclear metal center, either [NiFe] or [FeFe]. In contrast, [Fe]-hydrogenase is the only mononuclear hydrogenase and thus a perfect system for studying the structural and electronic determinants of these enzymes. Here we summarize recent improvements in modeling based on the EXAFS signal and the geometric structure of this metalloenzyme in its as isolated or reconstituted form. The individual contributions to the EXAFS resulting in two different structural models are presented and discussed. Inspired by the new crystal structure, we show an advanced EXAFS model for the enzyme from *Methanothermobacter marburgensis*.

1. Introduction

Many microorganisms utilize the reversible oxidation of molecular hydrogen as an electron supply or electron sink. This reaction is catalyzed by hydrogenases of which three basic types have been discovered [1, 2]. [NiFe]- and [FeFe]-hydrogenases use a dinuclear active site for activation of H₂ and typically a chain of Fe/S clusters for electron delivery ($H_2 \rightleftharpoons 2H^+ + 2e^-$) [2]. In contrast, [Fe]-hydrogenase activity depends on a unique cofactor, iron-guanylyl pyridone (FeGP), forming the active site of the enzyme, which catalyzes reversible hydride transfer from H₂ to 5,10-methenyltetrahydromethanopterin [3].

These three enzymes reveal several similarities although neither being phylogenetically related nor sharing major motifs in the protein architecture: In [FeFe]-hydrogenase, the iron ion proximal to the Fe/S cluster is redox-inactive and present in the formal oxidation state II. It is ligated by three sulfur and three π -accepting ligands such as carbon monoxide and cyanide. The Fe-ion in [NiFe]-hydrogenase is coordinated by a very similar set of ligands: two sulfur ligands, three carbon monoxide / cyanide donors and a yet not fully identified bridging ligand X (Figure 1).

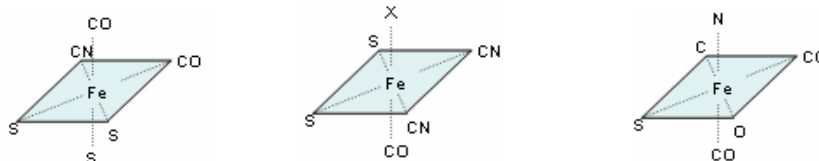


Figure 1. Fe-coordination for the Fe ion proximal to the FeS-clusters in [FeFe]-hydrogenase (left), the Fe-ions in [NiFe]-hydrogenase (center) and [Fe]-hydrogenase (right). The position of the CO ligand trans to N, and O trans to acyl-C in [Fe]-hydrogenase are not assigned unambiguously in the crystal structure.

Mononuclear [Fe]-hydrogenase shares several features with these enzymes: the initial EXAFS characterization of the enzyme isolated from *Methanothermobacter marburgensis* (mHmd) identified a single sulfur ligand bound to the iron ion of the FeGP-cofactor. Site directed mutagenesis studies on all three cysteine residues of [Fe]-hydrogenase from *Methanocaldococcus jannaschii* (jHmd) (*i.e.*: C10A, C176A, C176S, C250A), together with EXAFS studies on these mutants and on a Se-Cys form, determined that the sulfur donor is provided by Cys176 [4]. In addition, two CO-donor groups were clearly visible in the EXAFS and the corresponding Fourier transform in line with earlier IR studies [6]. Interestingly, the contribution of the remote oxygen ion from carbon monoxide to the EXAFS is in jHmd as well as in mHmd much stronger than that observed for [NiFe]-hydrogenase HoxC [7]. Following a conservative approach for *ab initio* EXAFS data analysis, the remaining FT signal bracketed by the CO and sulfur contributions were refined as oxygen groups, because the backscattering potentials are highly similar for the donor types oxygen and nitrogen.

Recent structural information obtained by EXAFS and protein crystallography allows an advanced analysis of these data: In the C176A-mutant of jHmd in addition to the nitrogen donor of the pyridinol group of the FeGP-cofactor its acyl-carbon donor is modeled to be bound to the iron ion. Re-analysis of the jHmd wild type EXAFS shows that this model better fits both crystallographic electron density

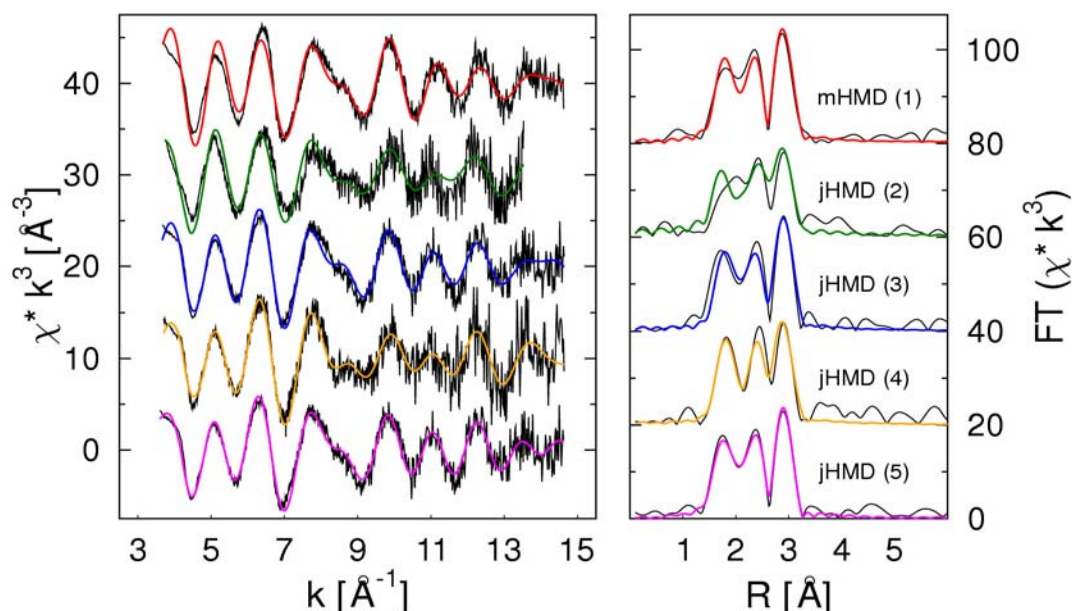


Figure 2. EXAFS and corresponding Fourier transform for mHmd and wild-type jHmd isolated under different conditions and refined with different structural models (black: measurements): mHmd(1): Hmd from *M. marburgensis* modelled as tetrahedral Fe-coordination as initially published [4]; jHmd(2): Hmd apoenzyme from *M. jannaschii* heterologously produced in *E. coli* and reconstituted with FeGP-cofactor with pentacoordination as published in [4]; jHmd(3): a sample similar to jHmd(2) but of higher quality and metal concentration with tetrahedral structural model for Fe-coordination [5]; jHmd(4): the protein under crystallization conditions as published in [5]; jHmd(5): advanced, octahedral structural model for jHmd(3) as published in [1]. Note, the sensitivity of jHmd to different buffer conditions.

and EXAFS data [1]. Here, we show that distinguishing between individual contributions of light ligands can improve the fit quality considerably.

2. Material and Methods

The jHmd samples from *M. jannaschii* and mHmd from *M. marburgensis* were prepared as described previously [6, 4, 5]. Whereas the wild type form of Hmd from *M. marburgensis* has been isolated from the organism, for jHmd and its mutants the apoenzyme was overproduced in *Escherichia coli* BL21(DE3) cells, purified and reconstituted with the FeGP-cofactor [8].

All Fe-K edge XAFS spectra were recorded at the EMBL Hamburg EXAFS beamline (DESY, Germany) in fluorescence mode. The extracted iron K-edge EXAFS data were converted to photoelectron wave vector k -space by KEMP [9] and weighted by k^3 . The spectra were refined with EXCURV98 [10]. The program calculated the theoretical EXAFS for defined structural models. In addition to single scattering contributions, multiple scattering linear units were defined for Fe-C=O and Fe-C-N. The acyl group has been modelled by a single carbon ion, because its other atoms do not contribute to multiple scattering by a linear orientation towards the iron and therefore they are not identifiable in the EXAFS. Parameters of each structural model, namely the atomic distances (R), the Debye-Waller factors ($2\sigma^2$), and a residual shift of the energy origin, were optimized, minimizing the fit index (Table 1).

3. Results and Discussion

In our initial study we identified the cysteinic sulfur ligand as well as two CO groups in Hmd from *M. jannaschii* and from *M. marburgensis*. The remaining backscattering contributions at about 2 Å were refined by 1 or 2 oxygen donor atoms, respectively, as shown in Figure 2. The spectrum obtained for the enzyme from *M. jannaschii* overexpressed in *E. coli* and reconstituted with the FeGP-cofactor differs considerably from the mHmd spectrum. This has been modeled by an additional oxygen.

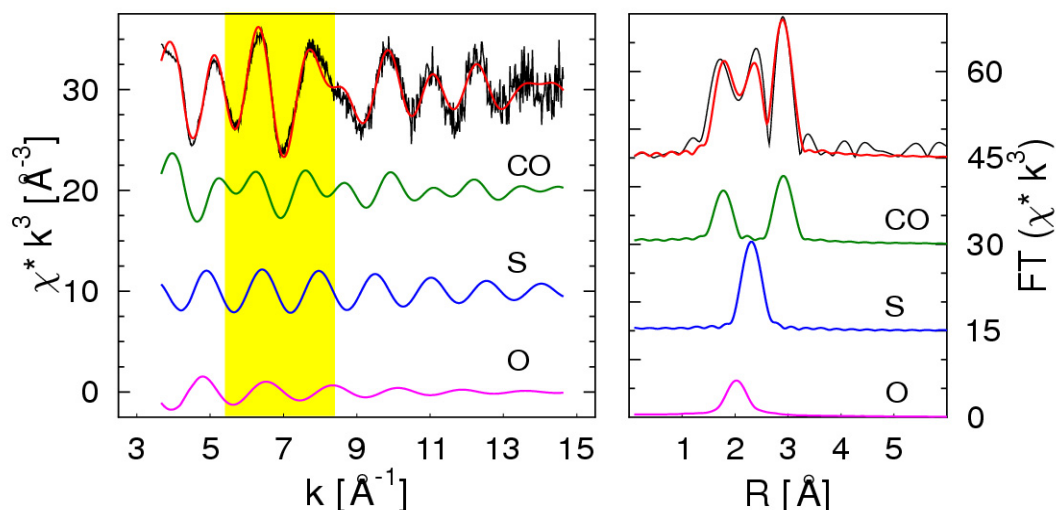


Figure 3. EXAFS and corresponding Fourier transform for reconstituted jHmd(3) (black: measurement, red: refinement) with individual components contributing to tetrahedral EXAFS model (green: one out of two CO, blue: S, magenta: O). Due to the multiple scattering within the CO unit the contribution by the oxygen ions is strongly enhanced. No destructive interference at lower photoelectron wave-vectors (yellow area) for sulphur and oxygen backscattering is observed. At higher waver vectors the oxygen signal is strongly damped due to its nature and the Debye-Waller factor obtained in the refinement (Table 1).

Preparations of jHmd with different buffer conditions yielded different EXAFS traces much more similar to mHmd. This spectrum, jHmd(3), was initially refined as a tetracoordinated Fe-ion (see below) [4]. In the crystal structure of jHmd one ligand could not clearly be identified, prompting the speculation that it might be caused by the buffer conditions. This has been tested by EXAFS on jHmd under such conditions (jHmd(4)). Here, only small changes occur and no additional ligand can be identified by EXAFS [5]. Prompted by the crystal structure of the C176A-mutant of jHmd [1] an octahedral Fe-coordination has been modeled in the corresponding EXAFS as well, assuming for the first time binding of the acyl-carbon to the metal ion. This resulted in an improvement of the EXAFS fit [1]. Based on this structural model the fit for jHmd(3) improves slightly as well.

The individual components contributing to the EXAFS of jHmd using the tetrahedral model are shown in Figure 3: The backscattering from the two CO groups, of which only one is shown, and the sulfur donor are dominating. As visualized in the Fourier transform the oxygen from CO contributes even stronger to the EXAFS than the carbon ion.

This is caused by the focusing of the photo electron wave by the carbon ion. The signals for sulfur and oxygen represent each a single contribution at an average distance with a disorder defined by the Debye-Waller factors. For small photo electron wave vectors these signals are in phase. At higher wave vectors when they get out of phase the oxygen contribution is small, reflecting of the higher Debye-Waller factor obtained in the fit (Table 1).

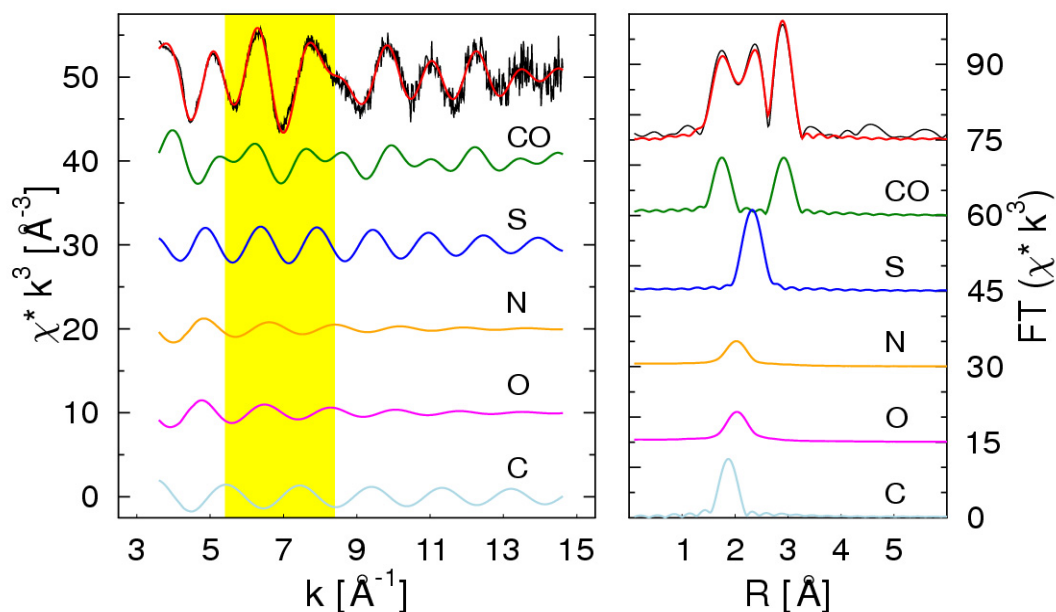


Figure 4. EXAFS and corresponding Fourier transform for reconstituted jHmd(5) (black: measurement, red: refinement) with individual components contributing to octahedral EXAFS model (green: CO, blue: S, orange: N, magenta: O, light blue: (acyl-)carbon). The destructive interference of the carbon ascribed to the acyl-group and the N/O contribution at lower photoelectron wave-vectors (yellow area) results in a quasi-cancellation of these two contributions in this energy range. At higher energies mainly interference with the sulphur contribution can be observed. Here, the O and N contributions are very small due to their higher Debye-Waller factor that we ascribe to a weaker binding of the oxygen donor. In the Fourier transform magnitude the negative interference is not visible.

n	Fe	L	R	$2\sigma^2$	$R_{CX}(\text{\AA})$	EF	Φ
			\AA	\AA^2	\AA	eV	$\times 10^3$
mHmd (1)							
2	Fe	C ^a	1.801 (4)	0.0084 (8)	1.121 (8)	-9.0 (4)	0.01196
1	Fe	O	2.034 (6)	0.007 (1)			
1	Fe	S	2.308 (3)	0.0051 (6)			
2	Fe	O ^a	2.922 (4)	0.0083 (5)			
jHmd (2)							
2	Fe	C ^a	1.813 (5)	0.007 (1)	1.100 (13)	-7.3 (4)	0.4825
2	Fe	O	2.004 (5)	0.007 (1)			
1	Fe	S	2.34 (1)	0.008 (1)			
2	Fe	O ^a	2.923 (8)	0.013 (1)			
jHmd (3)							
2	Fe	C ^a	1.792 (4)	0.0077 (9)	1.142 (8)	-8.9 (4)	0.2005
1	Fe	O	2.040 (9)	0.013 (2)			
1	Fe	S	2.321 (4)	0.0071 (8)			
2	Fe	O ^a	2.934 (4)	0.0081 (5)			
jHmd (4)							
2	Fe	C ^a	1.795 (5)	0.007 (1)	1.12 (1)	-8.3 (7)	0.3643
1	Fe	O	2.03 (1)	0.008 (2)			
1	Fe	S	2.351 (6)	0.007 (1)			
2	Fe	O ^a	2.921 (7)	0.0098 (9)			
jHmd (5) New fit							
2	Fe	C ^a	1.769(5)	0.0050(7)	1.170 (8)	-10.6(5)	0.1664
1	Fe	C	1.88(1)	0.0020(1)			
1	Fe	O	2.052(9)	0.014(2)			
1	Fe	N	2.052(9)	0.014(2)			
1	Fe	S	2.335(4)	0.0064(7)			
2	Fe	O ^a	2.939(3)	0.0025(4)			

Table 1: EXAFS parameters for models shown in this paper. The numbers (n) of ligand atoms (L) to the iron ion, their distance to the iron ion (R), the Debye-Waller factor ($2\sigma^2$), the C–O, the Fermi energy for all shells (EF), and the fit index (Φ), indicating the quality of the fit are shown.

In Figure 4 the individual contributions are shown for the octahedral Fe-coordination. Note that the major contributions to the EXAFS (cysteinic sulfur, carbon and oxygen of the carbon monoxide ligands) differ only marginally from the one for tetrahedral coordination (Figure 3). The residual signal has initially been modeled only by one oxygen contribution, which is based on its small size fully justified. When additional information became available more complex models were considered, allowing for partially destructive interference of these components. Here, the carbon and the oxygen contribution nearly cancel out at small wave-vectors and the carbon backscattering contributes to a much better fit at higher wave-vectors.

This is as well visualized by the corresponding Fourier transform: Measurement and fit match much nicer than for the tetrahedral model. The values resulting from this fit are given in table 1 showing that the other contributions are only marginally affected. Based on these considerations we re-analysed the mHmd (1) data and compared them to the new structural model for the Hmd active site. As shown in table 1 the model again improves slightly. This is inline with the optical representation (Figure 5) and allows concluding that the active sites in mHmd and jHmd are virtually identical. Moreover, this work highlights the need for additional criteria in XAS data analysis. Here, the XANES as well as methods considering target values for bond lengths, bond valance sum, Debye-Waller factors and Fermi energy shift will play an important role [11, 12].

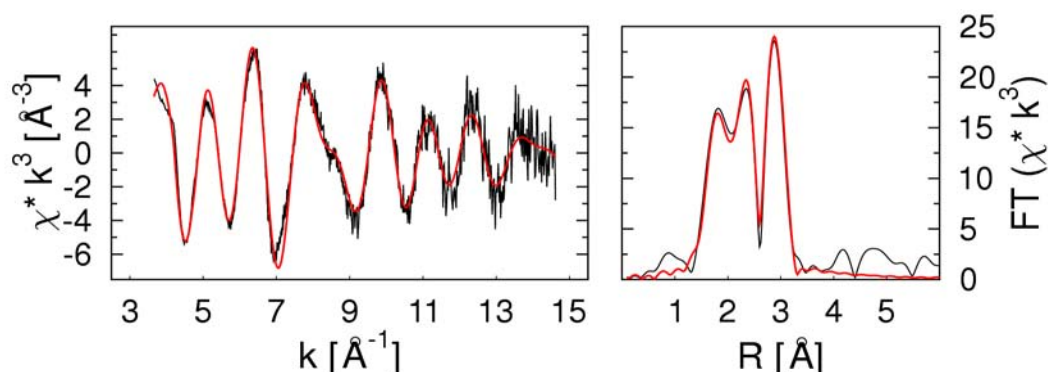


Figure 5. EXAFS and corresponding Fourier transform for mHmd (black: measurement, red: refinement) assuming an octahedral Fe-coordination as indicated in Figure 1.

References

- [1] Hiromoto T, Ataka K, Pilak O, Vogt S, Stagni M S, Meyer-Klaucke W, Warkentin E, Thauer R K, Shima S and Ermler U 2009 The crystal structure of C176A mutated [Fe]-hydrogenase suggests an acyl- iron ligation in the active site iron complex *FEBS Lett* **583** 585-90
- [2] Fontecilla-Camps J C, Volbeda A, Cavazza C and Nicolet Y 2007 Structure/function relationships of [NiFe]- and [FeFe]-hydrogenases *Chem Rev* **107** 4273-303
- [3] Shima S and Thauer R K 2007 A third type of hydrogenase catalyzing H₂ activation *Chem Rec* **7** 37-46
- [4] Korbas M, Vogt S, Meyer-Klaucke W, Bill E, Lyon E J, Thauer R K and Shima S 2006 The iron-sulfur cluster-free hydrogenase (Hmd) is a metalloenzyme with a novel iron binding motif *J Biol Chem* **281** 30804-13
- [5] Shima S, Pilak O, Vogt S, Schick M, Stagni M S, Meyer-Klaucke W, Warkentin E, Thauer R K and Ermler U 2008 The Crystal Structure of [Fe]-Hydrogenase reveals the geometry of the Active Site *Science* **321** 572-5
- [6] Lyon E J, Shima S, Boecher R, Thauer R K, Grevels F W, Bill E, Roseboom W and Albracht S P 2004 Carbon monoxide as an intrinsic ligand to iron in the active site of the iron-sulfur-cluster-free hydrogenase H₂-forming methylenetetrahydromethanopterin dehydrogenase as revealed by infrared spectroscopy *J Am Chem Soc* **126** 14239-48
- [7] Löscher S, Zebger I, Andersen L K, Hildebrandt P, Meyer-Klaucke W and Haumann M 2005 The structure of the Ni-Fe site in the isolated HoxC subunit of the hydrogen-sensing hydrogenase from *Ralstonia eutropha* *FEBS Lett* **579** 4287-91
- [8] Buurman G, Shima S and Thauer R K 2000 The metal-free hydrogenase from methanogenic archaea: evidence for a bound cofactor *FEBS Lett* **485** 200-4
- [9] Korbas M, Marsa D F and Meyer-Klaucke W 2006 KEMP: A program script for automated biological x-ray absorption spectroscopy data reduction *Rev Sci Instrum* **77** 063105
- [10] Binsted N, Strange R W and Hasnain S S 1992 Constrained and restrained refinement in EXAFS data analysis with curved wave theory *Biochemistry* **31** 12117-25
- [11] Burgdorf T, Löscher S, Liebisch P, Van der Linden E, Galander M, Lenzian F, Meyer-Klaucke W, Albracht SPJ, Friedrich B, Dau H and Haumann M. 2005 Structural and oxidation-state changes at its nonstandard Ni-Fe site during activation of the NAD-reducing hydrogenase from *Ralstonia eutropha* detected by X-ray absorption, EPR, and FTIR spectroscopy *J Am Chem Soc* **127** 576-592
- [12] Wellenreuther G and Meyer-Klaucke W 2007 Towards a Black-box for Biological EXAFS data analysis - I. Identification of Zinc finger proteins 2007 *XAFS13 AIP Conference Proceedings* **882** 322-324

This paper is published as part of a *Dalton Transactions* themed issue on:

Bioinspired Catalysis

Guest Editor Seiji Ogo
Kyushu University, Japan

Published in [issue 12, 2010](#) of *Dalton Transactions*

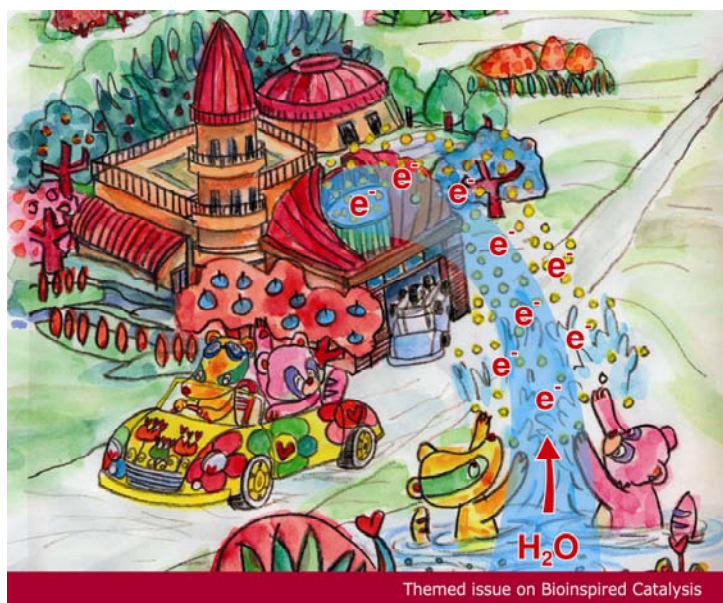


Image reproduced with permission of Seiji Ogo

Articles published in this issue include:

PERSPECTIVES:

[Mimicking Nitrogenase](#)

Ian Dance

Dalton Trans., 2010, DOI: 10.1039/b922606k

[Dual functions of NifEN: insights into the evolution and mechanism of nitrogenase](#)

Yilin Hu, Aaron W. Fay, Chi Chung Lee, Jared A. Wiig and Markus W. Ribbe

Dalton Trans., 2010, DOI: 10.1039/b922555b

[Quest for metal/NH bifunctional biomimetic catalysis in a dinuclear platform](#)

Takao Ikariya and Shigeki Kuwata

Dalton Trans., 2010, DOI: 10.1039/b927357c

COMMUNICATION:

[Chemiluminescence enhancement and energy transfer by the aluminium\(III\) complex of an amphiphilic/bipolar and cell-penetrating corrole](#)

Atif Mahammed and Zeev Gross

Dalton Trans., 2010, DOI: 10.1039/b916590h

Visit the *Dalton Transactions* website for more cutting-edge inorganic and bioinorganic research
www.rsc.org/dalton

The iron-site structure of [Fe]-hydrogenase and model systems: an X-ray absorption near edge spectroscopy study†‡

Marco Salomone-Stagni,^a Francesco Stellato,^b C. Matthew Whaley,^c Sonja Vogt,^d Silvia Morante,^b Seigo Shima,^d Thomas B. Rauchfuss^c and Wolfram Meyer-Klaucke^{*a}

Received 28th October 2009, Accepted 8th January 2010

First published as an Advance Article on the web 28th January 2010

DOI: 10.1039/b922557a

The [Fe]-hydrogenase is an ideal system for studying the electronic properties of the low spin iron site that is common to the catalytic centres of all hydrogenases. Because they have no auxiliary iron-sulfur clusters and possess a cofactor containing a single iron centre, the [Fe]-hydrogenases are well suited for spectroscopic analysis of those factors required for the activation of molecular hydrogen. Specifically, in this study we shed light on the electronic and molecular structure of the iron centre by XAS analysis of [Fe]-hydrogenase from *Methanocaldococcus jannashii* and five model complexes (Fe(ethanedithiolate)-(CO)₂(PMe₃)₂, [K(18-crown-6)]₂[Fe(CN)₂(CO)₃], K[Fe(CN)(CO)₄], K₃[Fe(III)(CN)₆], K₄[Fe(II)(CN)₆]). The different electron donors have a strong influence on the iron absorption K-edge energy position, which is frequently used to determine the metal oxidation state. Our results demonstrate that the K-edges of Fe(II) complexes, achieved with low-spin ferrous thiolates, are consistent with a ferrous centre in the [Fe]-hydrogenase from *Methanocaldococcus jannashii*. The metal geometry also strongly influences the XANES and thus the electronic structure. Using *in silico* simulation, we were able to reproduce the main features of the XANES spectra and describe the effects of individual donor contributions on the spectra. Thereby, we reveal the essential role of an unusual carbon donor coming from an acyl group of the cofactor in the determination of the electronic structure required for the activity of the enzyme.

Introduction

Molecular hydrogen was one of the earliest energy sources available on earth. As a consequence, many microorganisms continue to use it as electron donor.¹ To do so, these organisms rely on the hydrogenase enzymes, which catalyze the production and oxidation of molecular hydrogen. Their active sites exploit first-row transition metals exhibiting turnover rates comparable to that of platinum.^{2,3} Nature's use of the most abundant metal on earth, iron, is obviously attractive,⁴ but synthetic iron catalysts typically are not highly active toward hydrogen.⁵ It is therefore of obvious value to fully characterize the catalytic centres that mediate H₂ heterolysis under mild conditions. This knowledge may lead to new biomimetic methods for the generation and utilization of H₂.⁶

Although the three known classes of hydrogenases are not phylogenetically related, their active sites share striking similarities.^{2,7} [NiFe]- and [FeFe]-hydrogenases feature binuclear 3d-transition metal centres, complemented by iron-sulfur clusters.⁸ The third class, the [Fe]-hydrogenases, lacks FeS clusters.⁹ This enzyme has been found exclusively in some methanogenic archaea and it exploits only one metal-ion incorporated in FeGP-cofactor.^{2,10} In all three hydrogenases, this iron centre is ligated by at least one thiolate sulfur and three potential π -accepting ligands, consisting of CO and CN⁻ molecules in the [NiFe]- and [FeFe]-hydrogenases and of two COs and an acyl-carbon in case of [Fe]-hydrogenases.^{2,11,12} These commonalities point towards convergent evolution, indicating specific ligand structures that facilitate H₂ activation by iron.

The first step of enzymatic H₂ activation is heterolysis, giving a proton and a hydride, which is bound to the metal. This transformation is well known to proceed with the help of low-spin iron centres.^{13,14} Although it is understood that ligands on Fe must stabilize the low-spin ferrous state, specific electronic roles of the various ligands in facilitating hydrogen activation are not well understood.

Even though extensive studies over the past decade have advanced our understanding of the electronic structure and the catalytic mechanism of [NiFe]- and [FeFe]-hydrogenases,⁸ our understanding of the mononuclear [Fe]-hydrogenase is still rather primitive. This situation is due to the fact that only recently its active site structure has been described (Fig. 1).^{2,15} Due to the presence of a single metal ion and the absence of other

^aEMBL Outstation c/o DESY, Notkestraße 85, D-22603, Hamburg, Germany. E-mail: wolfram@embl-hamburg.de; Fax: +49 40 89902149; Tel: +49 40 89902124

^bPhysics Department and INFN, Università di Roma "Tor Vergata", Via della ricerca scientifica 1, I-00133, Roma, Italy

^cDepartment of Chemistry, University of Illinois, A328 Chemical & Life Science Lab, 600 South Mathews Avenue, IL-61801, Urbana, USA

^dMax-Planck-Institute für terrestrische Mikrobiologie, Karl-von-Frisch-Straße, D-35043, Marburg, Germany

† All the graphs were created using the program KaleidaGraph 4.0 (<http://www.synergy.com>) and structure 1 with Accelrys DS Visualizer v2.0.1.7347.

‡ Electronic supplementary information (ESI) available: Supplementary material. See DOI: 10.1039/b922557a

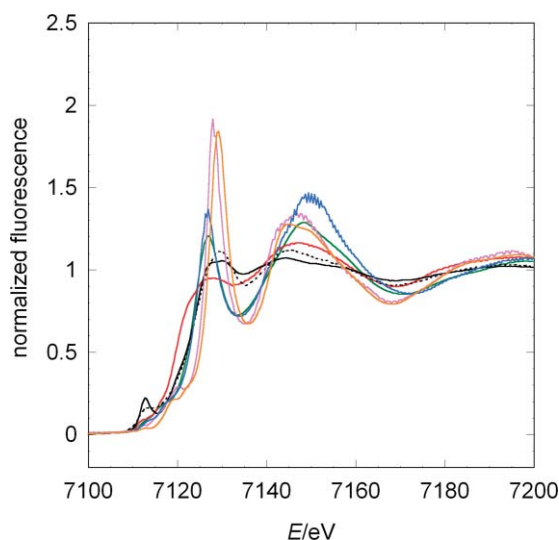


Fig. 2 Comparison among the experimental XANES of the model systems and jHmd-wt. Black line: jHmd-wt; black broken line: jHmd-CN; red line: Fe(II)(edt)(CO)₂(PMe₃)₂ (**A**); blue line: [K(18-crown-6)]₂[Fe(0)(CN)₂(CO)₃] (**B**); green line: K₄[Fe(0)(CN)(CO)₄] (**C**); orange line: K₃[Fe(III)(CN)₆] (**D**); purple line: K₄[Fe(II)(CN)₆] (**E**).

the white-lines [Footnote: In XAS the white-line denotes the main peak formed by the rising edge and the following minimum] of complexes **D** and **E** are very sharp.²⁸ In accordance with the formal charge, the ferrocyanide compound (**E**) has an edge position at lower energies than the ferricyanide **D**, 7127 eV and 7127.5 eV, respectively (orange and purple lines in Fig. 2).

In compounds **B** and **C**, iron is in the formal oxidation state 0. These pentacoordinate complexes are structurally similar, differing only in the relative ratio of CO/CN⁻ donors. This similarity is reflected by their XANES (green and blue lines in Fig. 2). Compared to the data for **D** and **E**, the white-lines of **B** and **C** are less sharp, indicative of their lower symmetry. As expected, both edge positions are at lower energies with respect to **D** and **E**. The differences observed in the peak intensities might be ascribed to the exchange of one CO by CN⁻: CO is a good σ donor and a strong π acceptor, while CN⁻ is a good σ donor and poor π acceptor, which influences in this case only the matrix element for transitions into the unoccupied orbitals, but not their energy levels.¹⁵

In compound **A**, the Fe(II) ion is bound to two CO ligands, two sulfur and two phosphine donors. The S and P donor ligands mimic to some extent the sulfur ligand bound to Fe in Hmd. The low-symmetry of the iron coordination results in a broadened white-line. Interestingly, the edge is positioned at the lowest energy, despite the formal oxidation state of the iron (red line in Fig. 2). This shift is ascribed to the influence of the phosphine and sulfur atoms. Thus, the nature of the ligands has for these complexes a stronger influence on the absorption edge position than the formal oxidation state.

The model compounds are chosen to illustrate the two competing effects determining the edge position and the metal–ligand distances: metal oxidation state and ligand type. An additional effect becomes apparent: the shape of the XANES depends on the homogeneity of the electron donors. The more cyanides are present in the sample the sharper is the white-line. A confirmation of the

Table 1 Edge positions, pre-edge peak positions and pre-edge peak areas for jHmd-wt, jHmd-CN and the model complexes. For simplicity, only the distances for the donor groups carbon monoxide, cyanide and sulfur from the iron ion are given here. In parentheses the error margins on the last digit are given

Sample	edge position eV	pre-edge peak position eV	1s→3d pre-edge peak area 10 ⁻² eV
jHmd-wt	7119.2(2)	7112.7(2)	60(1)
jHmd-CN	7117.0(2)	7112.7(2)	28(2)
A	7116.0(2)	7112.0(2)	9(2)
B	7124.6(2)	7112.9(2)	8(1)
C	7123.8(2)	7112.6(2)	18(2)
D	7127.4(2)	7112.3(2)	2(1)
E	7126.6(2)	7111.9(2)	1(1)

trend comes from compound **A**. Its coordination is heterogeneous and thus the white-line is small.

jHmd-wt and jHmd-CN

Intriguingly, the XANES-spectrum of jHmd-wt (full black line in Fig. 2) revealed characteristics very similar to compound **A**, with smooth maxima and minima. This similarity makes the latter the spectroscopic model closest to jHmd. Nevertheless, the spectra of jHmd-wt and **A** do not exhibit similar rising edges. The spectrum of jHmd-CN (broken black line in Fig. 2) shares with the wild type the position of the pre-edge peak as well as the maxima and minima above the edge, but not the relative intensities. jHmd-wt and jHmd-CN also share most of the rising edge. Thus, the electronic structures for wild type and the cyanide-inhibited form are similar, consistent with the similarity of the IR spectra in the ν_{CO} region.¹² The higher white-line intensity in jHmd-CN is indicative of a higher symmetry. This is in line with the pre-edge peak area that is much smaller for jHmd-CN than for jHmd-wt (Tab. 1). This feature is frequently used as a measure of the symmetry and homogeneity of the iron coordination.²⁹ Deviation from an ideal octahedral coordination increases the 1s to 3d/4p transition probability and thus the pre-edge peak intensity.

The first derivative of the XANES spectra of the wild type (full line in Fig. 3B) helps identifying features that are smoothed by the energy resolution of the monochromator (~4000 at 7.2 keV; note that its accuracy is ~0.1–0.2 eV). The jHmd-wt derivative is characterized by the splitting of the second peak into three peaks representing unoccupied orbitals (white-line range: from 7115 to 7130 eV, Fig. 3B). This feature is absent in the inhibited form (Fig. S1†). Thus, the presence of the characteristic can be considered as an indicator of the active form of jHmd.

Comparison of the absorption edges

The absorption edges reflect the influence of both the formal oxidation state of the iron centre and its ligands (Fig. 4). The edge positions have the following order: 7118.8 (jHmd-wt), 7119.0 (jHmd-CN), 7119.5 (**A**), 7124.0 (**C**), 7125.0 (**B**), 7127.0 (**E**), and 7127.5 eV (**D**). For the complexes **B**, **C**, **E** and **D**, with only diatomic ligands and oxidation states 0, 0, 2+ and 3+, respectively, the edges shift towards lower energies upon reduction. Interestingly, the edges of **B** and **C** differ by 1 eV from each other, although they are both Fe(0). This difference indicates the sensitivity of the

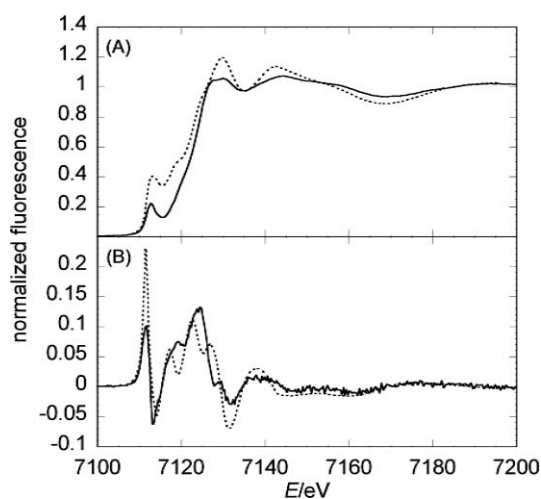


Fig. 3 Comparison between experimental and simulated spectra of jHmd-wt. (A) the XANES and in (B) its 1st derivative is shown. The full lines represent the experimental data, while the broken lines represent the simulations.

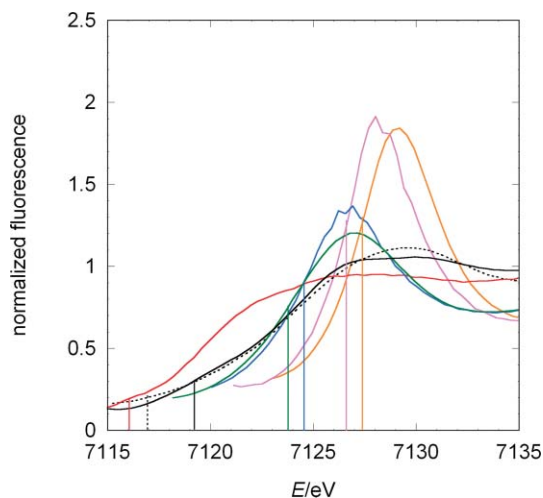


Fig. 4 Comparison between the edge positions of the model compounds, jHmd-wt and jHmd-CN. Black line: jHmd-wt; black broken line: jHmd-CN; red line: Fe(II)(edt)(CO)₂(PMe₃)₂ (A); blue line: [K(18-crown-6)]₂[Fe(0)(CN)₂(CO)₃] (B); green line: K₃[Fe(0)(CN)(CO)₄] (C); orange line: K₃[Fe(III)(CN)₆] (D); purple line: K₄[Fe(II)(CN)₆] (E). For each sample, the edge position—first maximum of the first derivative in the rising edge—is indicated.

effective charges at the metal ion to the donor types. **E** and **D**, which share the same coordination sphere but differ in oxidation state, are separated along the entire rising edges indicating that the corresponding molecular orbitals are only shifted in energy and the matrix elements for the transition from the 1 s orbital are unaffected (Fig. 2, 4). In contrast, compound **A** shows the profound influence of the ligand type. Here, the donors P and S strongly affect the edge position, which is shifted towards lower energies by 7.5 eV from the other ferrous compound **E**. In accordance, the edge positions of jHmd-wt and jHmd-CN are similar to that of **A**, suggesting a comparable effective charge at the iron ion.

Comparison of pre-edge peak intensities

The pre-edge peak intensity correlates with the symmetry of metal binding site: for octahedral sites and homogenous donor types it is lower than for tetrahedral sites and inhomogeneous donor types.²⁹ In line with their octahedral iron-coordination and their homogenous ligand sphere, the hexacyanides **D** and **E** possess the smallest pre-edge peak intensity of about 1 and 2 × 10⁻² eV, respectively. Complex **A** exhibits a pre-edge peak intensity of about 9 × 10⁻² eV, which reflects the heterogeneity of its octahedral ligand set. Complexes **B** and **C** are square pyramidal and as a consequence, the pre-edge peak areas are higher: complex **C**, has an area of about 18 × 10⁻² eV. An interesting exception to the rule is complex **B** with an area of only 9 × 10⁻² eV. This indicates higher symmetry potentially caused by the compensation of π-accepting and π-donating ligands. For jHmd-wt and jHmd-CN the largest pre-edge peak intensities are observed. The heterogeneity and asymmetry of the coordination sphere and likely the steric constraints by the protein environment result in a highly distorted geometry at the iron site. Interestingly, jHmd-wt pre-edge peak intensity (60 × 10⁻² eV) is twice of that of the inhibited form (28 × 10⁻² eV) and considerably higher than that of the isolated cofactor (44 × 10⁻² eV).²¹ These differences suggest a correlation between distortions of the active site geometry and catalytic activity of Hmd. Moreover also a partial occupation of the “oxygen position” can increase the intensity of the pre-edge peak. In fact, our EXAFS refinements without a sixth ligand are only slightly worse than the ones for six-fold coordination (Fig. S4†). Partial occupancy may indicate that ligands at this site are labile. We can conclude that octahedral geometry is consistent with low spin ferrous state and with all experimental results from protein crystallography and spectroscopy. This does not exclude a transient pentacoordination.

Metal-donor distances

The metal-carbon distances of the model systems do not differ significantly for Fe(II) and Fe(0) complexes (Tab. S1); the values are similar to those reported for other iron ions ligated by carbon monoxide.^{23,30} The Fe-CO distances observed in Hmd fall within this region as well (Tab. S1). The iron-sulfur distances obtained in the EXAFS refinement for jHmd-wt (2.33 Å) is closer to the ones of compound **A** and related models with nitrogen donors in place of phosphines (2.31 Å),³¹ than to those calculated by molecular modelling for [Fe]-hydrogenases³² (2.38 Å) and the ones measured for the [FeFe]-hydrogenases (2.25 Å).³³ In general, Fe(II)-S distances are poorly sensitive to oxidation state, but highly sensitive to spin state.^{34,35} For example, the Fe-S distance in Et₃NH[Fe(0)(SPh)(CO)₄] (2.332(5) Å)³⁴ is almost identical to that in Fe(II)H(SPh)(CO)₂[P(OPh)₃]₂ (2.343(3) Å).³⁵

XANES analysis

To gain further insights into the electronic structure of the iron ion in [Fe]-hydrogenases, *in silico* simulations of the XANES spectra of the model complexes and jHmd-wt were carried out with the program FEFF8.2 (see experimental). We analyzed both the XANES and their first derivatives in order to highlight homologies and differences among spectra and withdrawn qualitative information about the iron ion electronic structure.

Structure-based EXAFS refinement

The coordinates used in our simulations were extracted from EXAFS refinements based on crystal structure models reflecting the different geometries of the iron sites (see Fig. 1). The X-ray diffraction coordinates were read into Excurv98 as starting parameters for the refinement of the EXAFS data. Interestingly, the solvent oxygen of jHmd-wt is for this geometry slightly better modelled at 2.49 Å (Fig. S3†), instead of 2.05 Å as presented in Hiromoto *et al.* 2009 for ideal octahedral coordination.¹⁵ Attempts to model the EXAFS with an oxygen contribution at other distances led to poorer fit indexes (Fig. S3†) in line with the periodicity/interference of the EXAFS signal. Besides, we tried modelling this contribution by other elements (*e.g.* phosphorus, sulfur, fluorine, bromine, iodine) and obtaining comparable results for fluorine and bromine (Fig. S4†). These results are indicative for the presence of an atom/molecule at the “solvent oxygen” position but do not allow an unambiguous identification. Thus, we favor oxygen for consistency with the crystallographic model.

XANES simulations of the model systems

Simulations of the XANES for the model systems served as a proof of principles and defined the required cluster size in this study (first two to three shells). The principal features of the spectra have been reproduced: the curves trend matches the experimental data and the sequence of the rising edge positions is reflected by the simulations (Fig. 5). Moreover, the white-lines correlate with the symmetry and homogeneity of the coordination sphere.

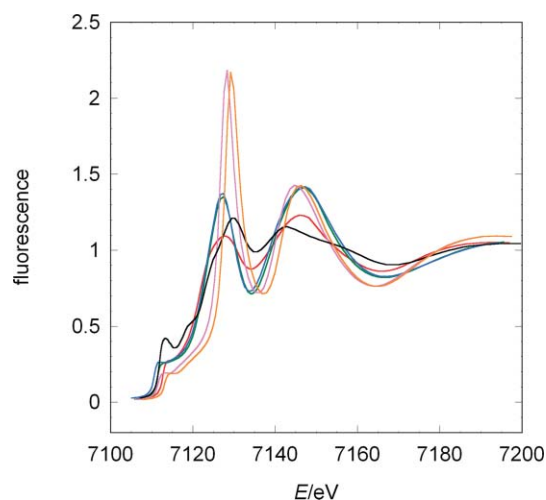


Fig. 5 Comparison among the simulated XANES of the model systems and jHmd-wt. Black line: jHmd-wt; red line Fe(II)(edt)(CO)₂(PMe₃)₂ (A); blue line: [K(18-crown-6)₂][Fe(0)(CN)₂(CO)₃] (B); green line: K[Fe(0)(CN)(CO)₄] (C); orange line: K₃[Fe(III)(CN)₆] (D); purple line: K₄[Fe(II)(CN)₆] (E).

In our simulations, the pre-edge peak regions are not reproduced very well. This problem is connected to the inaccurate calculation of transition probabilities into pre-edge states. Thus, the over intense pre-edge area characteristics are considered as artefacts.

XANES simulations of jHmd-wt

The positions of maxima and minima and the general shape of the experimental data are reproduced indicating the agreement between the electronic states in jHmd-wt and the simulation (Fig. 3A and B). Only the relative intensities and thus the magnitude of the transition matrix element are not adequately modelled. In the first derivative of the simulated spectrum a distinctive three-fold split white-line peak is preserved, highlighting the existence of three narrow energy levels.

Impact of individual donors on the electronic structure

In order to evaluate the impact of individual donors on the electronic structure of Hmd-wt, we successively omitted one of them in the simulations. Now we focused on first derivatives to highlight the impact on the electronic structure induced by systematically removing one metal donor (Fig. 6). Omitting one of the two CO ligands (CO1 and CO2) has a strong influence on most of the XANES spectrum, in the energy interval from 7117 to 7167 eV, in line with their intense multiple scattering contributions (Fig. 6A, B). The differences between these simulations show the importance of the geometry. In the XANES simulations this geometry is taken into account by multiple scattering contributions (from the central iron ion to a donor, continuing *via* the central iron atom to the donor in *trans* position and back to the iron ion); for CO1 this multiple scattering pathway includes the sulfur (2.3 Å away from the iron ion) and for CO2 the nitrogen atom opposite to CO2 (2.0 Å away from the metal ion) resulting in different phase and amplitude of these contributions (Fig. 1). Interestingly, in both spectra the white-line peak splitting is conserved, indicating that these ligands can not strongly contribute to the identity of the three unoccupied orbitals that give rise to this rising edge.

The donors from the pyridinol derivative significantly influence the region from 7115 to 7150 eV, corresponding to the white-line till the following minimum (Fig. 6C, D). The characteristics at 7155 and 7175 eV remain unchanged. Pyridinol-N and acyl-C omissions change the structure of the white-line peak, indicating their function in fine tuning the electronic structure. The sulfur contribution to the white-line feature is rather mild. The region from 7115 to 7120 eV is appreciably affected (first transition to an unoccupied orbital in the XANES) (Fig. 6E). It seems that here the COs and the other ligands give a contribution stronger than found for typical metal binding enzymes, thus diminishing the influence of sulfur. Removing the “solvent-oxygen” in the simulation affected the entire rising edge (Fig. 6F from 7114 to 7128 eV). This influence is small except for the first characteristic of the white-line peak at 7117 eV, which is lost.

The above results highlight the distinctive contribution from each of the six ligands. The differing contributions of the two CO ligands suggest that they play a key electronic role, as expected because of their strong tendency to back-bond.

The comparison of the jHmd-wt XANES with the model complexes identified the ferrous complex A as a mimic for the enzyme's electronic structure. Moreover, jHmd-wt and complex A share the CO and sulfur ligand types. These similarities and the identical absorption edge positions concludes that the enzyme harbours a ferrous ion. The analysis of the pre-edge peak intensities shows that in contrast to complex A the octahedral

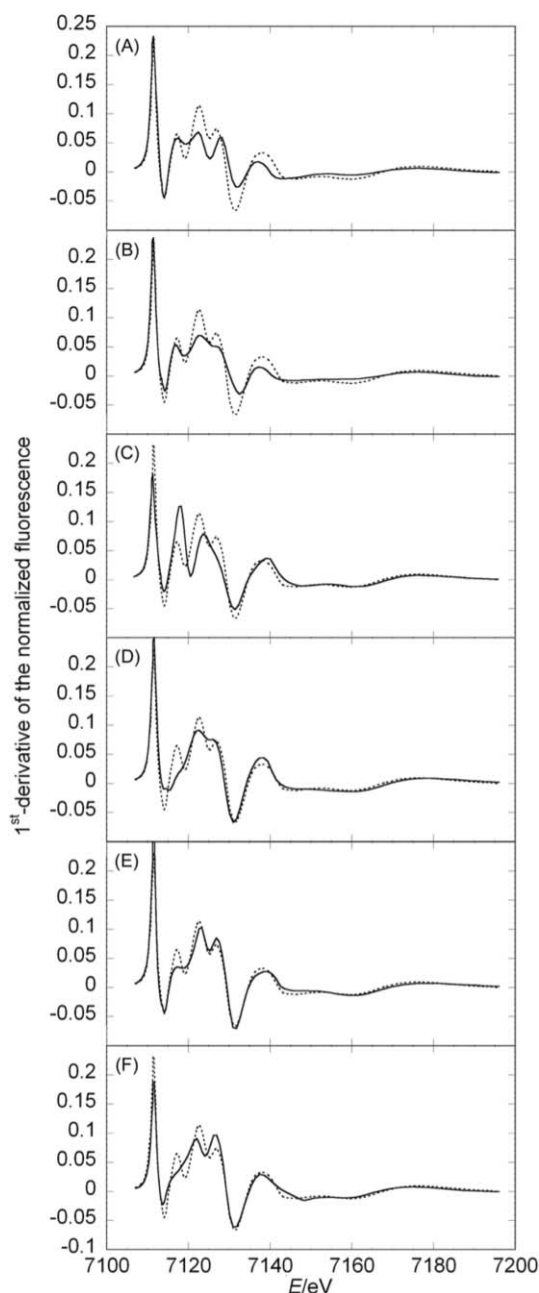


Fig. 6 Comparison between the first derivative of jHmd-wt XANES simulation in the full coordination (dotted lines) and simulations omitting one donor at the time (full lines): (A) CO1 omitted, (B) CO2 omitted, (C) acyl-C of the cofactor omitted, (D) pyridol-N of the cofactor omitted, (E) Cys176-S omitted, (F) oxygen omitted. The comparisons for the XANES simulations are shown in Fig. S4.†

symmetry is much more distorted in the enzyme, pointing to a specific tuning of the electronic structure (and thus most likely of the reactivity) by the protein environment, namely by the pockets harbouring the CO groups (Fig. S7†). This hypothesis is supported by the much smaller pre-edge peak intensity observed for the isolated FeGP-cofactor.²¹ An appreciable difference in the symmetry of the iron site in jHmd-wt and in the isolated cofactor could be inferred also from the electric field gradient sensed by the 57-Fe Mössbauer nucleus and the corresponding quadrupole splitting of the Mössbauer spectra (0.65 mm s^{-1} in wt-Hmd and

0.43 mm s^{-1} for FeGP).²² The jHmd-CN experimental XANES showed that the CN^- binding alters significantly the electronic structure of the iron ion. This change, as well as the saturation of the coordination sphere of Fe(II), is relevant to its inhibitory effect.

In the XANES simulations the essential contributions of the acyl-carbon and of the pyridinol nitrogen to the electronic structure were visualized by changes in the three unoccupied orbitals of the rising edge. Indeed, the identity of the feature representing the white-line transitions to unoccupied orbitals vanished when one of these donors was omitted. The ligand *trans* to H_2 is known to have a strong influence on hydrogen back donation, the intra molecular distance and metal-hydrogen bond length.¹³ Herein, we show that this is likely for jHmd-wt, where the acyl-carbon is *trans* to the supposed H_2 binding site. Interestingly, the omission of the oxygen smoothed down the first transition.

Conclusions

A formal 2+ oxidation state is consistent with all the available data on jHmd-wt: Mössbauer spectroscopy²² and our experimental data. The octahedral geometry is compatible with the 2+ oxidation state but not with Fe(0).³⁶ In addition, the rising edge of jHmd-wt's XANES overlaps nicely with that for the HoxC subunit of the hydrogen-sensing [NiFe]-hydrogenase from *Ralstonia eutropha*, which is accepted as Fe(II) (Fig. S6†).³⁷ The experimental and simulated spectra of jHmd-wt are consistent with the recently proposed acyl-carbon ligand. It is interesting that nature has chosen a very low symmetry site for H_2 activation. While the two CO ligands ensure low-spin state, the arrangement of the other four donors tune the reactivity toward H_2 , which is activated at the labile site *trans* to the acyl ligand reminiscent of the CO ligand *trans* to the hydride binding site in the [FeFe]- and [NiFe]-hydrogenases.⁸

Our analysis demonstrates that in the resting enzyme, Fe has an octahedral geometry with a five- to six-fold coordination. This geometry, which was indicated in our recent C176-mutated and DTT-bound enzyme,¹⁵ is incompatible with Fe(0), but is expected for low spin ferrous iron. Collectively, all these findings help to define the features that lead to efficient utilization of H_2 , especially the specific positioning of the three π -accepting ligands. The results of this work may provide a useful guide to the design of new catalysts aiming at cheaper and greener energy processing.

Experimental

Preparation of the samples for XAS analysis

All the samples were homogenized with degassed BN and filled in Hesar glass® cuvettes covered with Kapton® film. After freezing, the samples were stored in liquid nitrogen for the data collection.

Protein samples

All protein samples were prepared in anaerobic condition as described by Pilak *et al.*³⁸ The holoenzyme was reconstituted from the apoenzyme and FeGP-cofactor isolated from Hmd purified from *Methanothermobacter marburgensis* as described by Shima *et al.*²

Model system samples

The model complexes **A**, **B**, **C** were prepared under anaerobic conditions following our published procedures.³⁹ Complexes **D** and **E** were obtained from commercial sources (Sigma-Aldrich).

XAS measurements

XAS data collection of the enzyme samples is described by Korbas *et al.*²¹ XAS data for the model systems were collected in transmission mode at D2 beamline of the EMBL Outstation Hamburg at DESY, Germany. A Si(111) double-crystal monochromator scanned X-ray energies around Fe K-edge (6.8–8.1 keV). Harmonic rejection was achieved by a focusing mirror (cut-off energy at 20.5 KeV) and a monochromator detuning to 50% of its peak intensity. Sample cells were mounted in a two-stage Displex cryostat and kept at about 20 K. For each of these samples three scans were collected and averaged to ensure good statistics. Spectrometer energy was calibrated by recording Bragg reflections from a static Si(220) crystal in back-reflection geometry during each scan.⁴⁰ Data reduction, such as background removal, normalization and extraction of the fine structure, was performed with KEMP²¹ assuming a threshold energy $E_{0,Fe} = 7120$ eV. EXAFS data were analysed in an energy range from 3 \AA^{-1} to 14.5 \AA^{-1} with Excurv98.⁴¹

X-ray absorption near edge structure (XANES) analysis

Qualitative analysis and comparison of the XANES was carried out using the software ATHENA.⁴² The intensities and energies of the $1s \rightarrow 3d$ pre-edge features of the normalized Fe K-edge absorption spectra were quantified using the program WinXAS.⁴³ Spectra were fitted over 13 eV around the pre-edge features and modelled by pseudo-Voigt peak shapes. Energy positions, full width at half maximums (FWHMs) and heights were refined. The background underneath the pre-edge features was modelled as well by a pseudo-Voigt function. The total intensity of the $1s \rightarrow 3d$ pre-edge feature was assigned to the area of the pseudo-Voigt peak at about 7112.5 eV. Features in the rising edge were not included. The absolute edge positions were identified as the first maximum of the first derivatives within the rising edge (Fig. S2†).

FEFF simulations

The XANES spectra were simulated by *ab initio* self-consistent field full multiple scattering calculations with FEFF8.2.²⁷ We used as input for the calculations the atomic coordinates extracted from EXAFS modelling, which was carried out with the program Excurve98 on the basis of the available structures.^{2,15} Attempts to directly use X-ray diffraction coordinates led to less accurate results (data not shown). No corrections or exchange potentials were introduced in the simulation. Attempts to impose a given ionicity on the metal ion yield results where the edge position remains unchanged and the intensities varies less than 2.5%. Thus the simulations of our samples are not sensitive to this feature and this possibility was ignored here. All simulated spectra have been shifted by 3 to 6 eV towards lower energy for comparison with experimental data. This is standard and reflects small inaccuracies in the calculation of the $1s$ -continuum transitions. The simulations

were aligned with respect to the white-line peak positions of the XANES and their first derivatives.

Acknowledgements

SV and SS were financed by an emeritus grant to Rudolf K. Thauer from the Max Planck Society. We also thank him for fruitful discussions and his continuing interest. Moreover, we thank Eckhard Bill (Max-Planck-Institute für Bioorganische Chemie, Mülheim a. d. Ruhr, Germany) for fruitful discussions. TR was financed by the US Department of Energy, Office of Science.

Notes and references

- 1 M. Stephenson and L. H. Stickland, *Biochem. J.*, 1931, **25**, 205–214.
- 2 S. Shima, O. Pilak, S. Vogt, M. Schick, M. S. Stagni, W. Meyer-Klaucke, E. Warkentin, R. K. Thauer and U. Ermler, *Science*, 2008, **321**, 572–575.
- 3 R. Cammack, M. Frey and R. Robson, *Hydrogen as a fuel: Learning from nature*, Taylor & Francis, London, 2001; P. Hoffmann and T. Harkin, *Tomorrows energy*, MIT press, 2001.
- 4 S. Enthaler, K. Junge and M. Beller, *Angew. Chem., Int. Ed.*, 2008, **47**, 3317–3321.
- 5 A. J. von Wangelin, *Iron Catalysis in Organic Chemistry. Reaction and Applications.*, Wiley-VCH (October 13, 2008), 2008.
- 6 F. A. Armstrong and J. C. Fontecilla-Camps, *Science*, 2008, **321**, 498–499; F. Gloaguen and T. B. Rauchfuss, *Chem. Soc. Rev.*, 2009, **38**, 100–108.
- 7 P. M. Vignais, B. Billoud and J. Meyer, *FEMS Microbiol. Rev.*, 2001, **25**, 455–501.
- 8 J. C. Fontecilla-Camps, A. Volbeda, C. Cavazza and Y. Nicolet, *Chem. Rev.*, 2007, **107**, 4273–4303.
- 9 C. Zirngibl, W. Vandongen, B. Schwörer, R. Von Büнау, M. Richter, A. Klein and R. K. Thauer, *Eur. J. Biochem.*, 1992, **208**, 511–520.
- 10 S. Shima and R. K. Thauer, *Chem. Rec.*, 2007, **7**, 37–46.
- 11 A. J. Pierik, W. Roseboom, R. P. Happe, K. A. Bagley and S. P. J. Albracht, *J. Biol. Chem.*, 1999, **274**, 3331–3337.
- 12 E. J. Lyon, S. Shima, R. Boecker, R. K. Thauer, F. W. Grevels, E. Bill, W. Roseboom and S. P. J. Albracht, *J. Am. Chem. Soc.*, 2004, **126**, 14239–14248.
- 13 G. J. Kubas, *Chem. Rev.*, 2007, **107**, 4152–4205.
- 14 W. Lubitz, E. Reijerse and M. van Gestel, *Chem. Rev.*, 2007, **107**, 4331–4365; R. M. Henry, R. K. Shoemaker, D. L. DuBois and M. R. DuBois, *J. Am. Chem. Soc.*, 2006, **128**, 3002–3010.
- 15 T. Hiromoto, K. Ataka, O. Pilak, S. Vogt, M. Salomone-Stagni, W. Meyer-Klaucke, E. Warkentin, R. K. Thauer, S. Shima and U. Ermler, *FEBS Lett.*, 2009, **583**, 585–590.
- 16 E. J. Lyon, S. Shima, G. Buurman, S. Chowdhuri, A. Batschauer, K. Steinbach and R. K. Thauer, *Eur. J. Biochem.*, 2004, **271**, 195–204.
- 17 G. Buurman, S. Shima and R. K. Thauer, *FEBS Lett.*, 2000, **485**, 200–204.
- 18 C. Zirngibl, R. Hedderich and R. K. Thauer, *FEBS Lett.*, 1990, **261**, 112–116.
- 19 T. Hiromoto, E. Warkentin, J. Moll, U. Ermler and S. Shima, *Angew. Chem., Int. Ed.*, 2009, **48**, 6457–6460.
- 20 M. Salomone-Stagni, S. Vogt, S. Shima and W. Meyer-Klaucke, *J. Phys.: Conf. Ser.*, 2009, **190**, 12197.
- 21 M. Korbas, S. Vogt, W. Meyer-Klaucke, E. Bill, E. J. Lyon, R. K. Thauer and S. Shima, *J. Biol. Chem.*, 2006, **281**, 30804–30813.
- 22 S. Shima, E. J. Lyon, R. K. Thauer, B. Mienert and E. Bill, *J. Am. Chem. Soc.*, 2005, **127**, 10430–10435.
- 23 X. F. Wang, Z. M. Li, X. R. Zeng, Q. Y. Luo, D. J. Evans, C. J. Pickett and X. M. Liu, *Chem. Commun.*, 2008, 3555–3557.
- 24 A. M. Royer, T. B. Rauchfuss and D. L. Gray, *Organometallics*, 2009, **28**, 3618–3620.
- 25 A. Arcovito, M. Benfatto, M. Cianci, S. S. Hasnain, K. Nienhaus, G. U. Nienhaus, C. Savino, R. W. Strange, B. Vallone and S. Della Longa, *Proc. Natl. Acad. Sci. U. S. A.*, 2007, **104**, 6211–6216; M. C. Feiters, F. C. Küpper and W. Meyer-Klaucke, *J. Synchrotron Radiat.*, 2004, **12**,

- 85–93; E. D. Risberg, F. Jalilehvand, B. O. Leung, L. G. Pettersson and M. Sandstrom, *Dalton Trans.*, 2009, 3542–3558.
- 26 L. D. Slep and F. Neese, *Angew. Chem., Int. Ed.*, 2003, **42**, 2942–2945; A. Pantelouris, H. Modrow, M. Pantelouris, J. Hormes and D. Reinen, *Chem. Phys.*, 2004, **300**, 13–22.
- 27 A. L. Ankudinov, B. Ravel, J. J. Rehr and S. D. Conradson, *Phys. Rev. B: Condens. Matter Mater. Phys.*, 1998, **58**, 7565–7576.
- 28 A. Mijovilovich and W. Meyer-Klaucke, *J. Synchrotron Radiat.*, 2002, **10**, 64–68.
- 29 T. E. Westre, P. Kennepohl, J. G. DeWitt, B. Hedman, K. O. Hodgson and E. I. Solomon, *J. Am. Chem. Soc.*, 1997, **119**, 6297–6314; C. R. Randall, Y. Zang, A. E. True, L. Que, J. M. Charnock, C. D. Garner, Y. Fujishima, C. J. Schofield and J. E. Baldwin, *Biochemistry*, 1993, **32**, 6664–6673; C. R. Randall, L. J. Shu, Y. M. Chiou, K. S. Hagen, M. Ito, N. Kitajima, R. J. Lachicotte, Y. Zang and L. Que, *Inorg. Chem.*, 1995, **34**, 1036–1039; A. L. Roe, D. J. Schneider, R. J. Mayer, J. W. Pyrz, J. Widom and L. Que, *J. Am. Chem. Soc.*, 1984, **106**, 1676–1681.
- 30 W. K. Wong, K. W. Chiu, G. Wilkinson, A. M. R. Galas, M. Thornton-Pett and M. B. Hursthouse, *J. Chem. Soc., Dalton Trans.*, 1983, 1557–1563.
- 31 J. Takács, L. Markó and L. Párkányi, *J. Organomet. Chem.*, 1989, **361**, 109–116.
- 32 X. Yang and M. B. Hall, *J. Am. Chem. Soc.*, 2008, **130**, 14036–14037.
- 33 S. Löscher, L. Schwartz, M. Stein, S. Ott and M. Haumann, *Inorg. Chem.*, 2007, **46**, 11094–11105.
- 34 W. F. Liaw, C. Kim, M. Y. Darensbourg and A. L. Rheingold, *J. Am. Chem. Soc.*, 1989, **111**, 3591–3597.
- 35 S. A. Wander, J. H. Reibenspies, J. S. Kim and M. Y. Darensbourg, *Inorg. Chem.*, 1994, **33**, 1421–1426.
- 36 K. H. Whitmire, A. T. Kelly and C. Hofmann, in *Comprehensive Organometallic Chemistry III*, ed. M. Bruce, Elsevier, Amsterdam, 2006, vol. 6, pp. 1–76.
- 37 S. Löscher, I. Zebger, L. K. Andersen, P. Hildebrandt, W. Meyer-Klaucke and M. Haumann, *FEBS Lett.*, 2005, **579**, 4287–4291.
- 38 O. Pilak, B. Mamat, S. Vogt, C. H. Hagemeyer, R. K. Thauer, S. Shima, C. Vonnheim, E. Warkentin and U. Ermler, *J. Mol. Biol.*, 2006, **358**, 798–809.
- 39 Y. S. Guo, H. X. Wang, Y. M. Xiao, S. Vogt, R. K. Thauer, S. Shima, P. I. Volkers, T. B. Rauchfuss, V. Pelmenschikov, D. A. Case, E. E. Alp, W. Sturhahn, Y. Yoda and S. P. Cramer, *Inorg. Chem.*, 2008, **47**, 3969–3977; C. M. Whaley, T. B. Rauchfuss and S. R. Wilson, *Inorg. Chem.*, 2009, **48**, 4462–4469; J. K. Ruff, *Inorg. Chem.*, 1969, **8**, 86–89; G. A. Goldfield and K. N. Raymond, *Inorg. Chem.*, 1974, **13**, 770–775.
- 40 R. F. Pettifer, C. Brouder, M. Benfatto, C. R. Natoli, C. Hermes and M. F. R. Lopez, *Phys. Rev. B: Condens. Matter*, 1990, **42**, 37–42.
- 41 N. Binsted, R. W. Strange and S. S. Hasnain, *Biochemistry*, 1992, **31**, 12117–12125.
- 42 B. Ravel and M. Newville, *J. Synchrotron Radiat.*, 2005, **12**, 537–541.
- 43 T. Ressler, *J. Synchrotron Radiat.*, 1998, **5**, 118–122.